Forschungszentrum Karlsruhe
Technik und Umwelt

Wissenschaftliche Berichte
FZKA 5515
EUR 16100 EN

Nuclear Fusion Project Annual Report of the Association Forschungszentrum Karlsruhe/EURATOM

October 1993 - September 1994

Projekt Kernfusion

Januar 1995

Forschungszentrum Karlsruhe
Technik und Umwelt

Wissenschaftliche Berichte
FZKA 5515
EUR 16100 EN

Nuclear Fusion Project Annual Report of the Association Forschungszentrum Karlsruhe/EURATOM

October 1993 - September 1994

compiled by G. Kast
Projekt Kernfusion

January 1995

Als Manuskript vervielfältigt
Für diesen Bericht behalten wir uns alle Rechte vor

Forschungszentrum Karlsruhe GmbH
Postfach 3640, 76021 Karlsruhe

ISSN 0947-8620

Preface

The Research Center Karlsruhe (FZK), the former Nuclear Research Center Karlsruhe (KfK), contributes to the European Fusion Programme in developing the key technologies needed to build the International Thermonuclear Experimental Reactor (ITER) and to design commercial fusion reactors.

The historical basis of the present fusion activity are various nuclear technology projects and accelerator development. Whereas the nuclear projects gave the background for the present fusion related materials programme, blanket - fuel cycle - and safety activities, the earlier accelerator work gave origin to the present disciplines of superconductivity and rf-heating.

Technologies developed for the Next European Torus (NET) are made available to ITER. During the eleven years of existence of the FZK fusion project major test facilities have been built which constitute a considerable potential to test components and systems relevant for ITER in a technical scale. In particular the ITER model coil test facility TOSKA, the in-vessel-handling demonstration facility EDITH, the tritium laboratory TLK and the test arrangement for first wall components FIWATKA shall be named.

One of the important technological missions of ITER will be the qualification of first wall and fuel cycle components, in particular the breeding blankets. Within a European Community wide cooperation FZK elaborates breeding blanket designs for a Demonstration Reactor (DEMO) and conducts the basic r+d to qualify these concepts for implementation as test sections in ITER. Associated to the blanket activities is a programme to develop and qualify structural materials with sufficient lifetimes and reasonable activation properties. The work conducted in this frame necessitates extensive reactor and accelerator irradiations and subsequent hot cell examinations. Reactor irradiations are performed out of site, whereas two cyclotrons combined as Dual Beam Facility provide a unique tool for simulation of irradiation effects and for activation measurements.

The safety related part of the fusion project contributes to the component studies (blankets, superconducting magnets) and investigates the risk of severe accidents of fusion installations in nuclear operation.

The present yearly report of the FZK fusion project compiles the work under contract with the Commission of the European Community. References given on the responsible staff and on available reports may serve to provide the interested reader with more information on our programme.

J.E. Vetter

Contents

Page

Report of the Next Step Technology Programme

Plasma Facing Components and Plasma Engineering 1

PPM 1 Characterization of Graphites and CFCs 2

PPM 3 Numerical Simulation of Off-normal Plasma Material Interaction 4

PPM 4 Ceramics for Heating and Current Drive Systems 5

PPM 6 Erosion, H-Retention, Gas Interaction 7

PDT 1 First Wall Mock-ups and Tests 8

Superconducting Magnets 12

MCOI Model Coil 13

MCON Full-Size 40 kA Conductor 14

MTOS TOSKA Upgrade for Model Coil Testing 16

MBAC High Field Operation of NbTi at 1.8 K 20

Vacuum and Fuel Cycle 21

TPV 2 Optimization of Cryogenic Vacuum Pumping of Plasma Exhaust 22

TEP 2 Permeation und Catalytic Cracking 30

TEP 3 Tritium Storage and Transportation 35

TRIT-1 Tritium Supply and Management: Calorimetric Measurements 37

Nuclear Engineering / Basic Blanket

NDB 1 Neutronics Data Base 38

T 16 Preparation of Neutronics Experiments and Measuring Technologies 42

Remote Handling / Maintenance 46

RHB 1 RH Common Subsystems 47

RHT 1 Articulated Boom Transporter 48

T 43 Remote Pipe Welding and Cutting (former task RST 2) 56

Safety and Environment 57

SEA 3 Analysis of Reference Accident Sequences 58

SEP 2 Environmental Impact of Tritium and Activation Products 61

Study Contracts for ITER / NET 63

I_c vs. Strain Test on Nb_3Sn Strands 64

Investigation of Cryo-Cascade-Concept for ITER and Definition of Test Requirements 65

ITER Coil and Model Coil Design and Analysis 70

Quench Analysis for Magnet Safety Assessment 71

ITER Shielding Analysis 72

Long Term Program for Materials Development 74

LAM 2	Nuclear Data Base for Low Activation Materials Development	75
LAM 3	Development of Low Activation Martensitic Steel	77
MANET 1.1	Characterization and Optimization of MANET-II-Steel	83
MANET 2.3	Diffusion Welding	84
MANET 3.2	Pre- and Post-Irradiation Fatigue Properties of MANET Steel	85
MANET 3.4	Pre- and Post-Irradiation Fracture Toughness	88
MAT 5	Ion-Beam Irradiation Fatigue and Creep Fatigue Tests	91

Test Blanket Development 94

BS - Solid Breeder Test Blankets 95

BS DE-D 1	Solid Breeder Test Blanket Design	95
BS BE-D 1	Beryllium	104
BS BR-D 1/D 2	Preparation and Characterization of Ceramic Breeder Materials	107
BS BR-D 3	Irradiation Testing and Post Irradiation Examination	108
BS BR-D 4	Tritium Release	113
BS BR-D 8	Characterization of Lithium Orthosilicate: Adsorption of Water	114
BS NN-D 1	Helium Blanket Test Loop	115
BS NN-D 2	Non Nuclear Tests	117
BS NN-D 3	Tritium Extraction from a Solid Breeder DEMO Blanket	120

BL - Liquid Metal Test Blankets 122

BL DE-D 1	Liquid Metal Test Blanket Design	122
BL PC-D 2	Active and Inactive Impurities and Clean-up of Molten Pb-17Li	125
BL EI-D 1	Electrical Insulation and Coatings	126
BL MH-D 1	Liquid Metal MHD	130
BL SA-D 1	Reliability Assessment	135
BL SA-D 2	Safety Analysis of Self-cooled LM Breeder Blankets	136

Development of ECRH Power Sources 139

Appendix I: Allocation of Tasks 147
Appendix II: Table of NET Contracts 149
Appendix III: FZK Departments Contributing to the Fusion Project 150
Appendix IV: Fusion Project Management Staff 151

Plasma Facing Components and Plasma Engineering

Introduction:

A limited, but highly ITER-relevant, number of tasks has been continued in the reporting period. They deal with a further qualification of First Wall protection materials both with regard to strength (PPM 1) and tritium interaction (PPM 6), the thermocyclic testing of mock-ups (PDT 1) and the modelling of the impact of plasma disruptions on divertor materials (PPM 3). In addition the data base for the design of ECRH windows has been largely expanded (PPM 4).

H.D. Röhrig

PPM 1 Characterization of Graphites and CfCs

Bending strength measurements on CfC-materials were continued with a new batch of Sepcarb N112 provided by NET. Specimens were cut in two directions. The high-temperature and room-temperature strength data are plotted in fig. 1. An increase of strength with temperature is obvious up to 1400°C. The strength data differ in both directions by a factor of about 2.

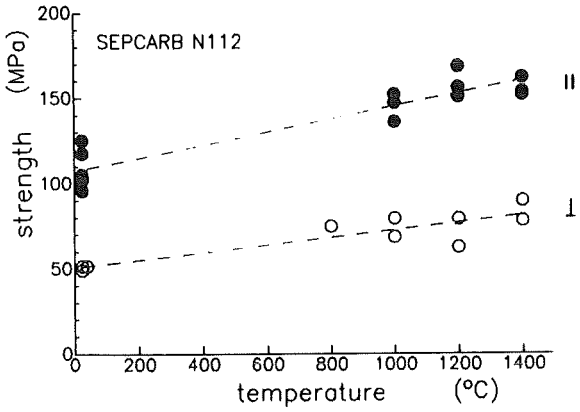

Fig. 1: Bending strength of SEP N112 as a function of temperature

Cyclic tests were performed in a cantilever bending arrangement with load application by loudspeakers. Despite the large scatter of the data points in the Wöhler plot the following relation between the numbers of cycles to failure N_f and the bending stress σ can be derived:

$$N_f = A\,\sigma_{max}^{-76}$$

with lgA = 145.04 for σ_{max} in MPA.

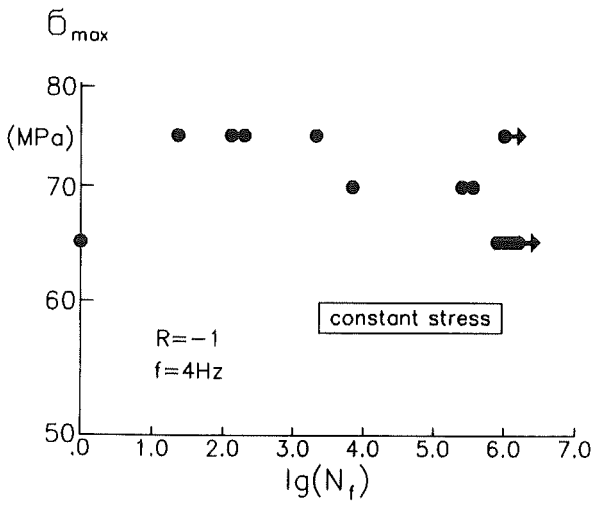

Fig. 2: Cyclic fatigue data in a Wöhler plot

Staff:

T. Fett
H. Schneider

The experimental determination of Thermophysical properties of CfC-composites is finished regarding the thermal diffusivity, thermal expansion and specific heat of Sepcarb N 112 Fig. 3 shows the thermal diffusivity α of N 112 samples taken from different batches.

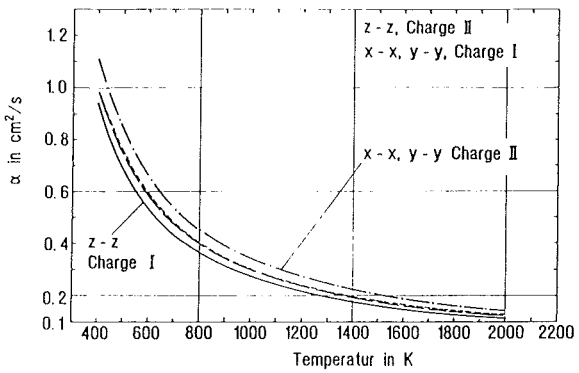

Fig. 3: Thermal diffusivity of Sepcarb N 112 x-x-y, z-z-Fiber orientation with respect obviously no heat flow

There is a difference of about 10% between the results of different batches. Fig. 4 gives the thermal conductivity λ calculated from thermal diffusivity, density and specific heat.

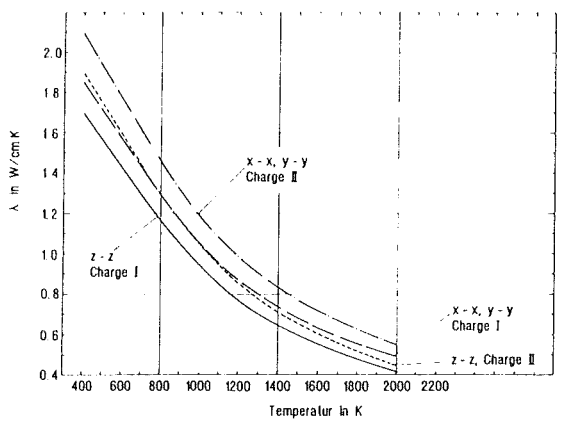

Fig. 4: Thermal conductivity of Sepcarb N 112

Also the determination of the thermal diffusivity of FMI-CfC-composites has been finished for large samples. The investigation of a possible dependence of thermal diffusivity

on sample thickness will close the examination of thermophysical properties of CfC-composites.

The work on the hot cell laserflash-equipment for routine measurements will be finished in the next weeks. Many constructive details for such measurements had to be undertaken in cooperation with HVT/HZ.

Staff:

G. Haase
P. Mangai
B. Schulz
P. Severloh
Ch. Zeisluft
H. Ziegler

PPM 3 Numerical Simulation of Off-normal Plasma Material Interaction

During the thermal quench phase of a plasma disruption and during ELMs the divertor plates are hit by an intense plasma flow consisting of electrons and ions. In ITER this flow has the following parameters particle energy around 10 keV, pulse duration larger than 100 µs, energy density up to 150 MJ/m^2 for disruptions and up to 10 MJ/m^2 for ELMs [1]. The high divertor heat load results in sudden evaporation of a thin layer of divertor plate material which acts as vapor shield and protects the divertor from further excessive evaporation. Formation and effectiveness of the vapor shield and material erosion are calculated in one dimensional planar geometry with the radiation hydrodynamics code FOREV [2]. The hydrodynamic motion is calculated along and across magnetic field lines. Heat conduction into the bulk target, erosion and melt front propagation into the target and beam energy deposition by ions and Maxwellian distributed electrons are modeled. Momentum deposition of the ion component of the incident plasma flow is taken into account. Multifrequency radiation transport is described by Planck and Rosseland opacities. For the multigroup emissivities LTE plasma, optically thin plasma and a realistic approach based on escaping factors was used [3].

The FOREV results for high Z materials with emissivities for LTE plasma are in satisfactory agreement with results from simulation experiments. Line radiation is unimportant and erosion remains small in comparison with melt layer evolution [4]. For the low Z materials beryllium and carbon emissivities with escaping factor correction have to be used to describe the observed temperature in the plasma edge [5]. The multigroup approach is inappropriate for the radiative energy transfer. It neither allows to appropriately calculate the transmission of hot photons from the plasma edge to the target through a cold dense plasma layer, nor it takes the interaction of these photons with the plasma ions into account. A self consistent method being presently under development has to be used for these cases. The erosion values for beryllium and carbon as given in [5] therefore are preliminary.

Literature:

[1] G. Janeschitz et al., 11th Int. Conf. on Plasma Surface Interactions in Controlled Fusion Devices, Mito, May 23 - 27, 1994.

[2] I. Landman et al., Proc. Int. Conf. on Phenomena in Ionized Gases, ICPIG-21, Sept. 21 - 24, 1993, Bochum, Vol, II, p. 201.

[3] B. Bazylev et al., 21. EPS Conf. on Controlled Fusion and Plasma Physics, Montpellier, June 27th - July 1st, 1994.

[4] H. Würz et al., 11th PSI Mito, May 23 - 27, 1994.

[5] I. Landman, H. Würz, 18th SOFT 1994, Aug. 22 - 26, 1994, Karlsruhe.

Staff:

B. Goel
W. Höbel
H. Würz

PPM 4 Ceramics for Heating and Current Drive Systems

Subtask 3: Performance fo ECRH Windows under NET/ITER Conditions

The two major approaches for high power ECRH windows are based on cryo-windows (cryogenically-cooled Sapphire) and on conventionally-cooled alternative windows (special Silicon and Diamond grades). The dielectric property measurements at 145 GHz focused on these reference materials and persued to consolidate the design relevant data base.

For the cryo-window approach, one of the major open problems is the radiation effect on the torus window. Efforts were continued to corroborate the previously proposed tolerable level of neutron fluences of 10^{21} n/m² (E>0.1 MeV). Therefore Sapphire specimens from the related "ambient temperature" irradiation at GKSS Geethacht ($T_{irr} \approx 320$ K) were studied also in the extraordinary ray which is the complementary orientation to the 'ordinary ray' used in window design. Even though the overall dielectric loss for the extraordinary ray is lower by a factor of 2, again radiation-induced changes only occurred in the specimen irradiated to 10^{22} n/m², but not at lower fluence levels (Fig. 1). The absence of marked orientation effects gives further evidence of rather general damage structures that are responsible for the degradation of dielectric loss in Sapphire.

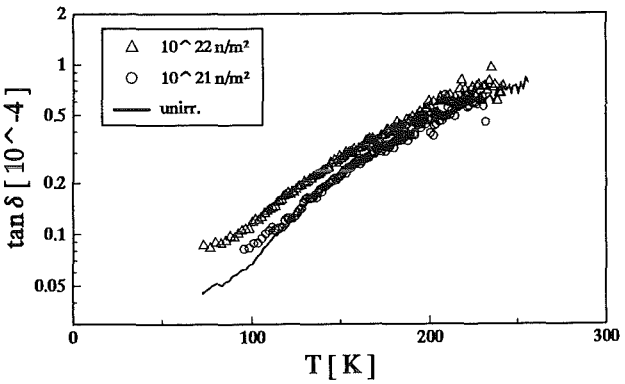

Fig. 1: The influence of neutron-irradiation on the dielectric loss at 145 GHz in Sapphire (extraordinary ray)

The "cryogenic irradiation" was prepared at HFR Petten to settle the importance of the temperature effect at low temperatures on the relevant defects causing degradation of the dielectric and thermophysical properties. The specimen set, mainly consisting out of Sapphire (HEMEX and Union Carbide grades), were supplied to Petten where the irradiation facility was established for irradiation near 77 K. However, the test of the irradiation capsule made some revisions necessary. Therefore the envisaged date of the irradiation could not be kept in summer. At present, the irradiation is expected to start in October.

Despite of the promising property profile of CVD Diamond with respect to thermal crack formation, the true potential of this alternative material had not been clear because of previously observed excessive dielectric loss levels. Consequently dielectric loss measurements have so far been limited to grades in as-received conditions. Translucent grades could be obtained which showed significantly improved losses as compared to black grades (Fig. 2). In the first translucent material, a strong temperature dependence above 250 K still gave evidence of free charge carrier absorption. When a related impurity could be kept out of the production process, a grade was received with loss levels below 10^{-4}.

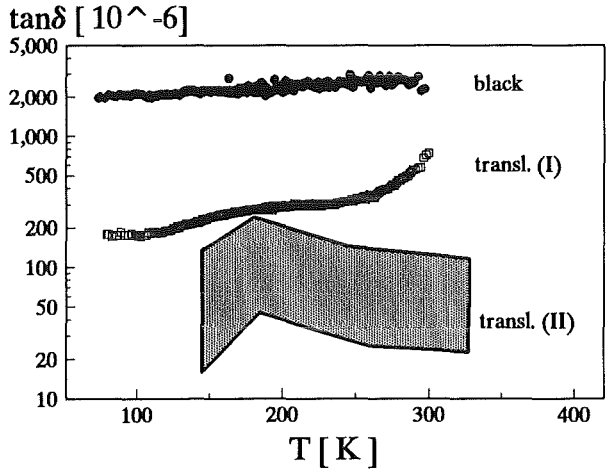

Fig. 2: The dielectric loss at 145 GHz of various grades of CVD diamond.

The investigations of special Silicon grades have been reintensified since it could been shown that the major problems of high resistivity Silicon, namely sensitivity to ionizing radiation and increased dielectric losses below room temperature, could be strongly reduced by structural defects produced by electron irradiations. In cooperation with the Institute of Applied Physics /Nizhny Novgorod (RF), it was shown that reduced dielectric loss levels could be achieved in the temperature range below 300 K by gold doping. Apparently free charge carriers can then be blocked with a similar efficency as with structural defects. By this method of materials optimization, specimens were obtained with the lowest loss levels so far found at 145 GHz (Fig. 3).

In addition, amorphous and monocrystalline quartz grades were inspected for temperature and radiation effects on the permittivity in the context of their use in broadband windows in EC wave diagnostics. Much smaller temperature coefficients (by a factor of 10) than in Sapphire were found. Permittivity was not affected at neutron fluences up to 10^{22} n/m², which compares well with Sapphire.

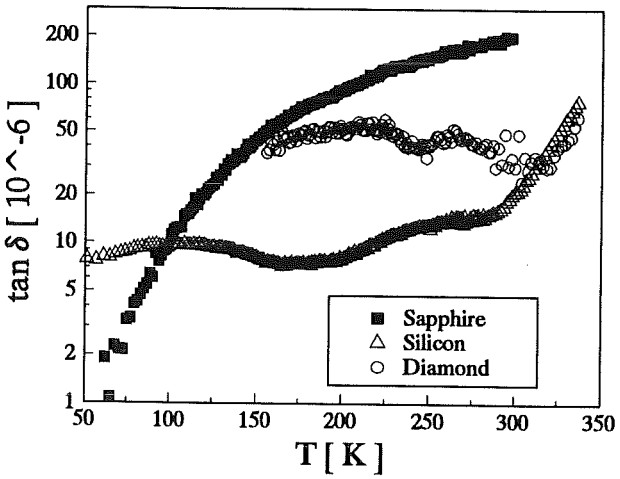

Fig. 3: The dielectric loss at 145 GHz of the best presently measured reference materials for ECRH windows.

Literature:

[1] R. Heidinger; Dielectric Property Measurements on CVD Diamond Grades for Advanced Gyrotron Windows, 19th Int. Conf. on Intrared and Millimeter Waves, Sendai (J), 17 - 24.10.94

[2] J. Molla, A. Ibarra, R. Heidinger, E.R.Hodgson; Electron-irradiated silicon: An optimized material for gyrotron windows, accepted for publication in J. Nucl. Mater.

[3] R. Heidinger, G. Link; Dielectric measurements on amorphous and nonocrystalline quartz grades for EC wave broadband windows, 18th Symp. on Fusion Technology, Karlsruhe, 22 - 26.08.94

Staff:

M. Blumhofer
J. Bürkin
R. Heidinger
S. Nazaré
H. Zimmermann

PPM 6 Erosion, H-Retention, Gas Interaction

Subtask 2: H/T Retention Studies in Neutron Irradiated Graphites, CFCs and Doped C Composites

Carbon-based materials as well as beryllium are considered for protection of plasma facing components of fusion reactors. Previous experiments indicate a huge (factor hundred) increase of tritium trapping capacity in carbon-based materials induced by neutron damage [1]. A check of these results and a better understanding of neutron irradiation effects on tritium retention in these materials is urgently required.

A common NET/ECN/KfK program has been initiated [2,3]. Irradiated carbon-based materials (irradiated up to 3.5 dpa) and Be samples (irradiated up to 4×10^{22} 1/cm^2 fast fluence) are available. An equipment capable of heating the samples to 1300°C for loading with tritium (in a stagnant H_2/T_2 atmosphere) and for annealing the loaded tritium by purging with He+0.1% H_2 has been installed.

In contrast to previous studies [1], where the tritium trapping in graphite was found to increases by a factor ten with increasing damage from 0.01 to 0.1 dpa, in this work only a minor increase of several ten percent (ECN) or no increase (FZK, former KfK) was observed in this damage range.

Before studying tritium behavior of the irradiated Be samples, the tritium generated during irradiation by fast neutrons was annealed. Release kinetics was found to be remarkably influenced by the irradiation history: To release most of the tritium within several hours the high-fluence samples ($\geq3\times10^{22}$ 1/cm^2) had to be heated to 850°C, but the low-fluence samples (0.8×10^{11} Bq/q up to about 900°C. Huge amounts of tritium (2×10^{11} Bq/q for the 3.9×10^{22} 1/cm^2) as compared to unirradiated samples. It has to be checked if the number of irradiation-induced trapping sites is decreased by annealing.

Literature:

[1] R.A. Causey et al., Fusion Technology 19 (1991), 1585.

[2] H. Kwast et al., "The Effect of Neutron Irradiation on the Trapping of Tritium in Carbon-Based materials", ICFRM-6, Stresa, Sept./Oct. 1993.

[3] C.H. Wu et al., "Neutron Irraddiation Effects on the Properties of Carbon Materials", ICFRM-6, Stresa, Sept./Oct. 1993.

Staff:

T. Eberle
M. Glugla
J. Lebkücher
M. Möschke
K.H. Simon
H. Werle

PDT 1 First Wall Mock-up and Tests

Subtask 4: Thermomechanical Tests on Specimens Protected by Mechanically Attached Carbon Based Tiles

First wall/blanket concepts may utilize compliant layers between protection tiles and the structural material in areas of moderate heat fluxes. The compliant layer is to improve the thermal and electrical contacts between components where the bare rigid partners would be in point contact only; it also makes tiles amenable to repair by remote maintenance.

The compliant layer needs to be flexible in order to provide thermal contact even if the components deform differently under heat load. As a design basis the mechanical and thermal properties of the compliant layer material and the resulting heat transmittance must be known; of special interest is the question whether the heat transmittance changes under cyclic heat loads.

The problem was investigated experimentally for Papyex, a laminated graphite of Le Carbone Lorraine, as a compliant layer between CFC protection tiles and a NET first wall mockup (TS1).

1. Compliant Layer Deformation Characteristics

The Papyex material (see Fig.3 for data) was characterized by measuring the compressive stress/strain curve at three different temperatures with a universal material testing machine; saturation was reached after between two and roughly 30 load cycles depending on stress amplitude and temperature. As a result the Young's modulus at saturation was evaluated and is plotted in Fig.1.

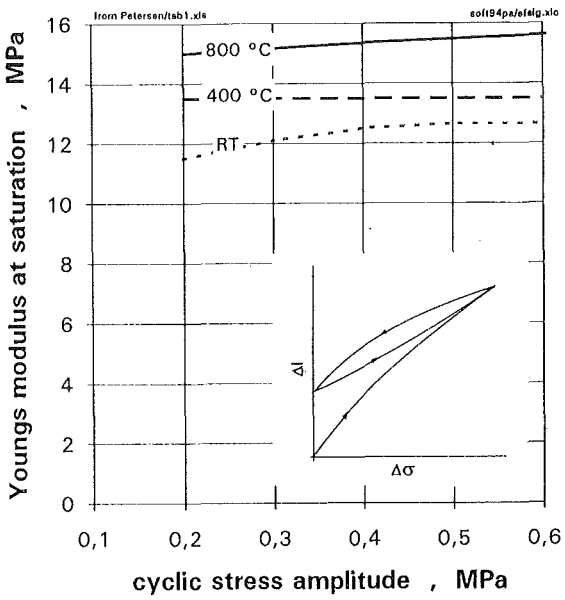

Fig. 1: Young's modulus of the compliant layer

It is almost constant with stress and it slightly increases with temperature. Fig. 2 shows that out of the total compressive deformation the elastic portion, which is available for keeping the thermal contact at deformation of the components, is on the order of 100 to 200 µm depending on stress and temperature; it also shows that the permanent portion strongly increases with temperature, indicating that the compliant layer shrinks when it is heated up under pressure.

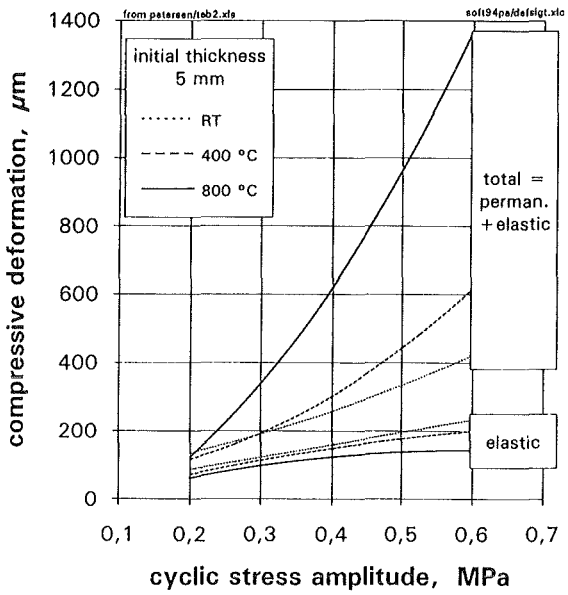

Fig. 2: Deformation of the compliant layer

2. Compliant Layer Transmittance

The heat transmittance h' through the compliant layer consists of the three steps (a) contact heat transfer from the tile's backside to the layer, (b) heat conduction through the layer, and (c) contact heat transfer from the layer to the first wall. h' was determined experimentally by running heat-flux tests with a tile-protected specimen in the First Wall Test Facility Karlsruhe (FIWATKA) 1.

2.1. Experimental setup

Fig.3 shows how stripes of Papyex as a compliant layer were placed between square protection tiles and a water-cooled first wall mockup. The tile was pressed to the mock-up via a central attachment stud and with a conical nut of TZM. The stripes covered one half of the area of the tile and were located close to the underlying coolant channels; the contact pressure at mounting of the tile was set to 0.5 MPa and remained constant until the first heat-up. The tile was instrumented with TCs in locations as indicated.

The specimen faced the high-temperature resistance heater of the FIWATKA facility and received a heat flux qz" of up to 38 W/cm² for the results reported in the following section; qz" was determined calorimetrically with the cooling water. Data were obtained from steady-state tests whereas

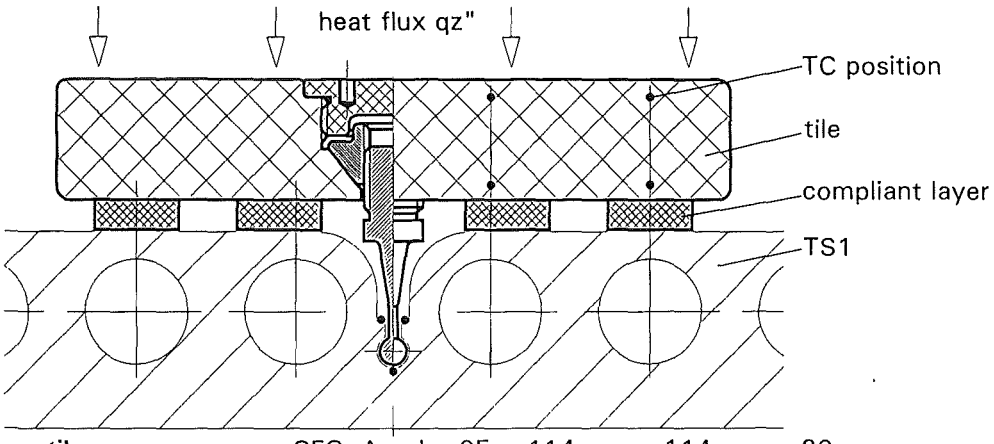

tile :	CFC Aerolor 05 , 114 mm x 114 mm x 20mm
compliant layer :	Papyex, special type, 5 mm thick, density 0.4 g/cm³
attachment stud :	TZM
TS1 :	SS 316L, FW mockup, water-cooled

Fig. 3: Experimental setup showing the tile attachment and listing of the materials

alternating thermal loads were generated by 4-minutes-power-on and 4-minutes-power-off cycles.

2.2. Results

A typical temperature profile through the tile, the compliant layer, and into the mockup shown in Fig. 4 may be constructed with the known data of the two temperatures in the tile, the temperature of the water and its heat transfer coefficient at the channel surface, and the thermal conductivities of the steel and the tile material.

The temperature drop across the compliant layer includes the two contact resistances; it is rather large and dominates the temperature level at the tile; together with the locally increased heat flux it is the basis for calculating the heat transmittance h' across the compliant layer.

Fig. 5 shows that the transmittance h' is on the order of 0.1 W/cm²K and slightly increases with heat flux which is probably due to the conductivity of Papyex that increases with temperature. h' appears rather uniform since for eight different locations in the tiles very similar values were found.

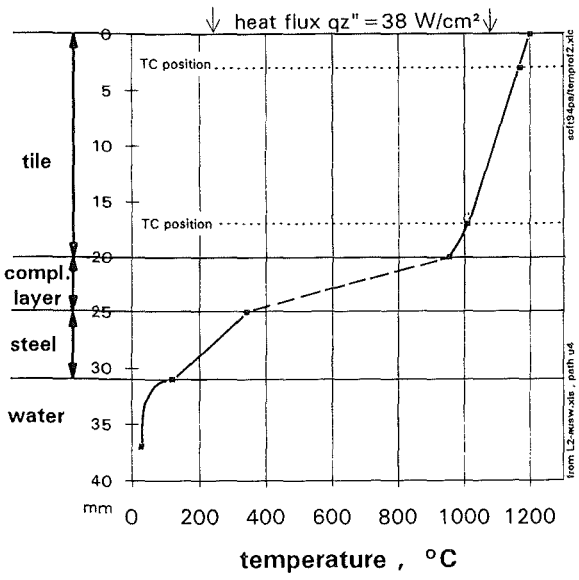

Fig. 4: Temperature profile through specimen

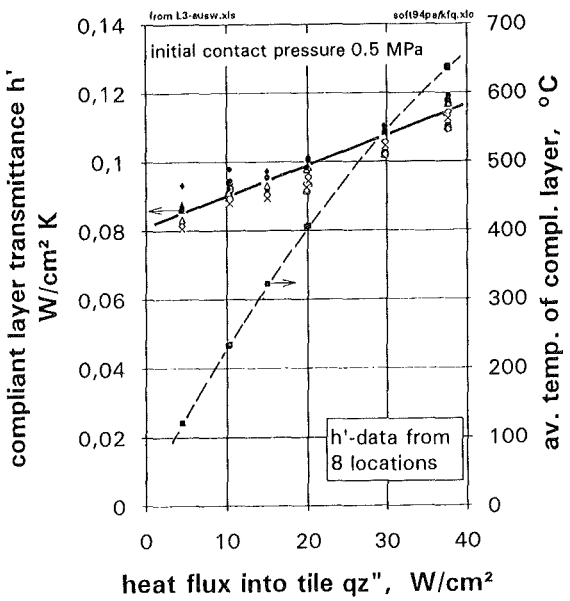

Fig. 5: Compliant layer thermal transmittance

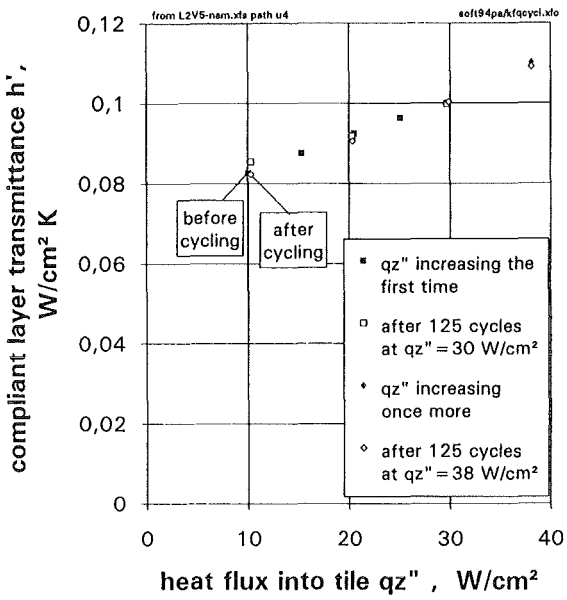

Fig. 6: Influence of thermal cycling on h'

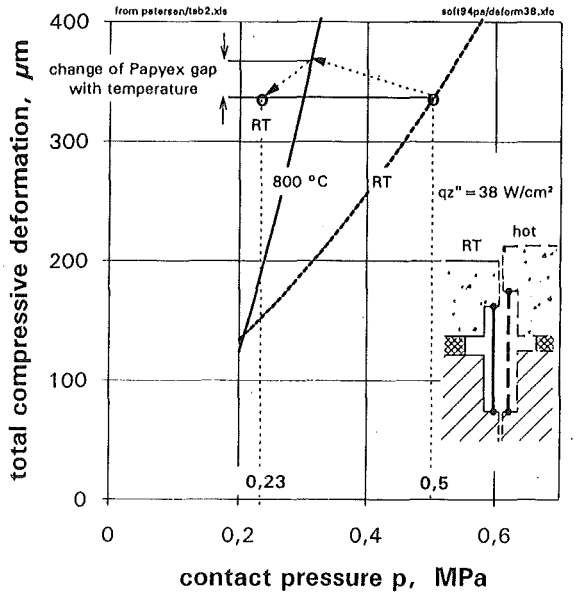

Fig. 7: Change of contact pressure under thermal load

Fig. 6 offers an answer to the question whether h' deteriorates as a result of thermal load cycles: after increasing the load to qz" = 30 W/cm² and running 125 cycles at this level h' remained unchanged; also, increasing the load to qz" = 38 W/cm² and once more running 125 cycles did not change h'. The compliant layer transmittance seems unaffected by the load cycles; the reason may be understood from the following paragraph since a decreasing contact pressure is the only mechanism suspicious of being able to reduce h`.

The contact pressure relaxes automatically in the course of each test as demonstrated in Fig. 7 which uses two curves out of Fig. 2 :

The tile mounted at RT applies a pressure of 0.5 MPa to the layer and compresses it by 340 µm. Heating up will (a) narrow the gap in which the layer lies by roughly 30 µm due to several thermal expansions participating, and (b) ask for application of the 800°C deformation curve with a larger permanent portion; hereby the pressure is reduced to roughly 0.3 MPa. Later cool-down will reopen the gap to its initial size and let the Papyex expand elastically which again reduces the pressure according to the modulus, resulting in a final pressure at RT of about 0.23 Mpa.

A similar remaining contact pressure of 0.15 MPa was measured after a test shown in Fig. 8; in spite of the heavy reduction in contact pressure the heat transmittance did not change, as the experimental data from the figure prove.

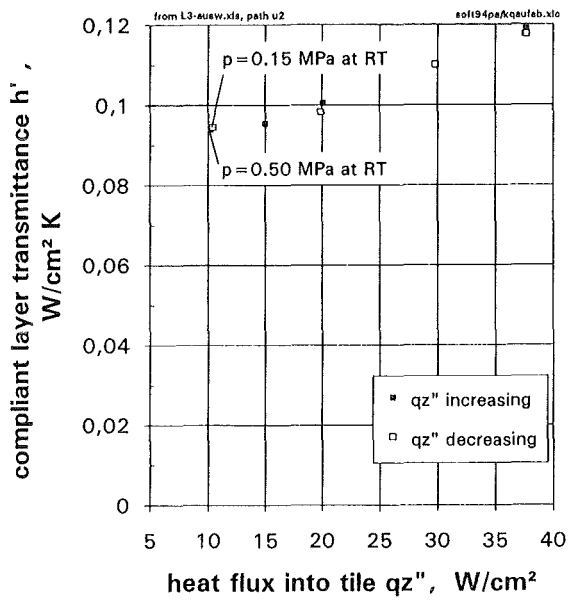

Fig. 8: h' before and after application of a heat load which reduces the contact pressure

3. Conclusions

A compliant layer made from 5mm thick Papyex caused a relatively high temperature drop due to its poor thermal conductivity. But the contact behavior appears entirely unproblematic; if the initial contact pressure at mounting is sufficiently high to cause nestling between the soft layer and its rigid partner surfaces, the pressure may change later to low values without influencing the heat transmittance. The compliant layer thickness may be reduced such that it provides just enough elastic deformability for the geometrical and heat load conditions of a specific design.

Literature:

[1] G. Hofmann and E. Eggert, The First Wall Test Facility FIWATKA , KfK 5381 (1994)

Staff:

E. Diegele
E. Eggert
G. Hofmann
G. Rizzi
C. Petersen
B. Schinke
G. Schweinfurther

Superconducting Magnets

Introduction:

The confinement of plasma in ITER relies on a superconducting magnet system consisting of 24 D-shaped toroidal field coils, a central solenoid to drive the plasma current and a set of poloidal field coils for plasma stabilization. KfK is together with the EC Home Team and other associated European laboratories involved in the development of these magnet systems. Components of ITER conductors, subsize conductor assemblies are examined for their performances. Materials to be used in coil construction are qualified for their application under cycling load. Cryogenic loops and components are developed to establish stable forced flow conditions to cool the magnets. An important task is now the upgrading of the magnet test facility TOSKA for the testing of the ITER TF model coil manufactured by industrial methods, which will be applied for the construction of the ITER plant.

The safety of superconducting magnets is analyzed by computer code still under development and by experimental studies of effects, potentially initiating a sequence of events leading to an accident.

H. Knuth

MCOI Model Coil

Subtask 1: Monitoring Manufacture of the Toroidal Field (TF) Model Coil

The aim of the subtask is the support of the home team in the fabrication of the ITER model coils.

In the beginning of 1994 according to the "Request for Task Proposal" of the JCT the elaboration of a toroidal field (TF) model coil specification was started by the EU Home Team. The elaboration of the specification is the task of the EFET industry consortium in collaboration with the European superconducting magnet laboratories CEA Cadarache, KfK Karlsruhe and ENEA Frascati where CEA Cadarache is the responsible laboratory for guiding the model coil design. About 8 meetings were held till September to push the TF model coil specification. KfK Karlsruhe contributed to it by the model coil test programme, the hydraulic flow sheet design of the model coil cooling circuit, model coil high voltage testing, and model coil instrumentation (cooling circuit, quench detection). The TF model coil is a joint collaboration of European Union and the Russian Federation. In two meetings in St. Petersburg the work distributions were discussed. Further model coil work is described in Task MTOS-1.

Subtask 3: Basic Development for High Voltage Technique for Components used in the Model Coil and Test Facility (feedthroughs, insulation breaks, current leads, etc.)

The aim of the subtasks is the transfer of the know how in the development of high voltage components gained in the Polo project to the ITER model coils.

The experience gained by partial discharge measurements of the Polo coil (see Task MTOS-1) indicates that this method shall also be used for assessing the electricial properties of the model coil. Work about a network diagram for calculation of the model coil reactance was started.

Staff:

M. Irmisch
P. Komarek
Ch. Sihler
A. Ulbricht
G. Zahn

MCON Full-Size 40 kA Conductor

Subtask 3: I_c Characterization and FBI Upgrade

The aim of the sub-task is the critical current characterization of Nb_3Sn strands and subcables under the effects of field and external strain in the high field test facility FBI. The task is funded in the 1989-91 program. It is still continued caused by difficulties in the strand fabrication combined with delay in delivery. The final report of the subtask 3 was transmitted to the EU Home Team. The subtask MCON 3 is concluded.

1. Testing of ITER Subsize Conductors

1.1 ENEA/LMI conductor

The investigations of this CIC conductor has been started in 1993 and finished in 1994. At three samples including the basic Nb_3Sn strands I_c vs B, I_c vs ε, σ vs ε, and the N values have been tested with the FBI facility. First results and a description of the conductor have been presented in [1] and all results are shown more in detail in [2] . Here the most important result, i.e. I_c as a function of static and cyclic strain, will be reported (ENEA-3, Fig. 1).

First I_c vs ε was obtained by statically straining under stressed and unstressed conditions up to $\varepsilon=0.52\%$ (run 11) and the residual value of $\varepsilon=0.06\%$ (run 12), respectively. Then the sample was cycled 10^3 times between $\varepsilon=0.06\%$ and ($\sigma=0$) and $\sigma=0.31\%$ ($\sigma=230$ MPa), and after that the static tests continued according to run 14 to run 22 (23). In this final strain range around ε_m one observes a degradated I_c curve resulting to $\varepsilon'_m=10.0$ kA in comparison to the expected $I_{cm}\approx 10.6$ kA obtained for the other uncycled samples, as indicated by the dashed curve (Fig. 1). Both ε_m and ε_{Irr} seem to be uneffected by cycling, which is valid also for the stress-strain curve (not shown here). Comparable former cycling tests on CIC conductors did not show any influence onto the I_c vs ε characteristic.

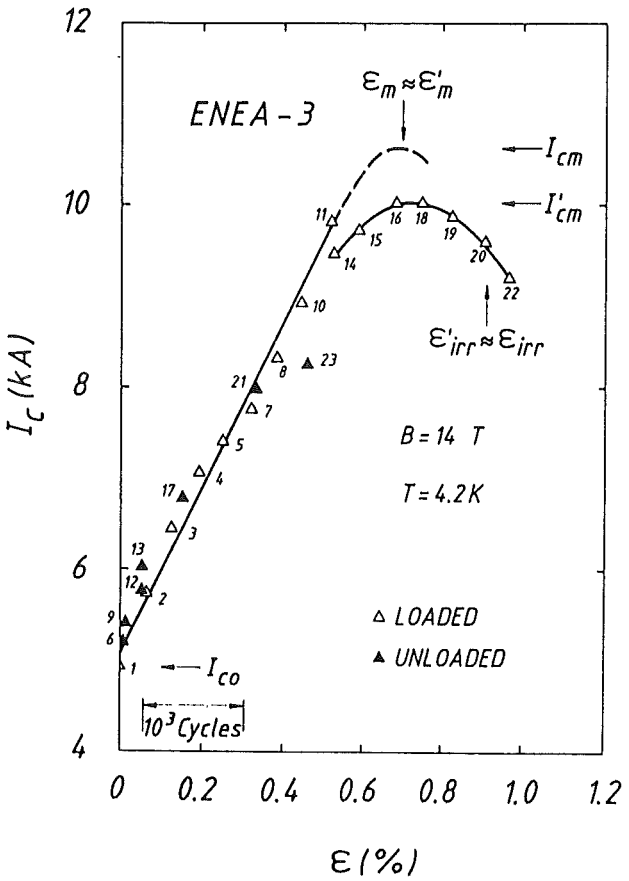

Fig. 1: I_c vs. ε under static and cyclic straining of ENEA/LMI conductor

1.2 CEA/Dour Metal subsize conductor with Ti jacket

Most CIC conductors investigated up to date consist of a steel jacket which degradates I_c drastically due to axial prestress onto the Nb_3Sn filaments. This again results from the higher thermal contraction of steel ($\alpha=16\times10^{-6}$/K) in comparison to that of Nb_3Sn ($\alpha=7.6\times10^{-6}$/K) during cooling from reaction to LHe temperature. A closer matching of α between jacket material and Nb_3Sn would enhance I_c considerably. Therefore CIC conductors consisting of an outer Titanium jacket ($\alpha=5\times10^{-6}$/K) and an inner 36 Nb_3Sn strand cable have been prepared by CEA/Dour Metal and tested at KfK.

In Fig. 2 the normalized critical current, I_c/I_{cm}, versus intrinsic strain, ε_o ($=\varepsilon-\varepsilon_m$), is shown for CIC samples with Ti jacket (C - Ti2) and for comparison with SS jacket (C - SSI) housing the same Nb_3Sn cable as C - Ti2. (The other results shown in Fig. 2 are not relevant in this context). Note, at $\varepsilon_o=-\varepsilon_m$ the degradation of the critical current I_{co}/I_{cm}, amounts to 0.49 for the steel and only 0.94 for the Ti sample at B = 12.5 T. That means, without applied strain the Ti jacketed conductor

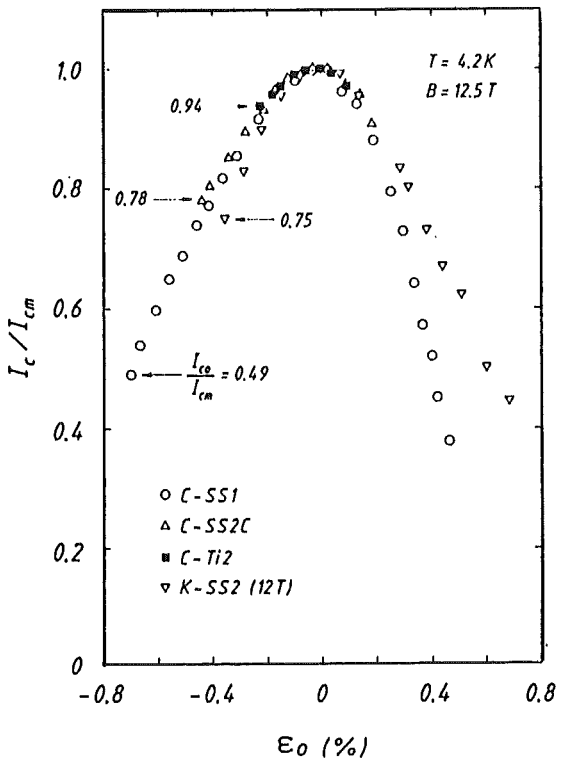

Fig. 2: Comparison of SS and Ti jacketed CIC conductor with respect to the strain effect on I_c.

carries about a factor of two higher current [3]. One disadvantage of using Ti is the lower mechanical strength compared to steel.

2. FBI Test Facility

- The 14 T split coils showed premature quenching after about one year operation. It has been repaired by the supplier and is available now again.

- The big cryostat has been shipped to Messer Griesheim for repairing a leak between the containments of LN_2 and vacuum.

- The LHe transfer lines for both cryostats of the facility are successully in operation.

- The upgrading of the data acquisition is still in progress.

Literature:

[1] Nuclear Fusion Project, Annual Report of the Association KfK/EURATOM, Oct. 1992 - Sept. 1993, KfK 5288, EUR 15466 EN, p. 20, Dec. 1993

[2] W. Specking, Final Report, European Fusion Technology Program, 1984-1991, MCON 3, Feb. 1994

[3] W. Specking and J.L. Duchasteau, to be presented at ASC, Boston, Oct. 16-21, 1994

Staff:

H. Kiesel
W. Specking

MTOS TOSKA Upgrade for Model Coil Testing

Subtask 1: Preparation of TOSKA Facility for the test of the ITER TF Model Coil

The aim of the task is the upgrading of the TOSKA facility for testing the ITER TF model coil. An intermediate step is the testing of the LCT coil at 1.8 K up to 11 T field level in the task MBAC. Useful basic component developments and testing methods which can be transferred later on to ITER model coils are running in the Polo project (previous tasks M4, M8 and MTOR).

The "Task Agreement" for upgrading of the TOSKA facility for testing the ITER TF model coil was signed by the ITER Director and EU Home Team Leader.

The JCT (Joint Central Team) settled the configuration where the ITER-TF model coil is tested adjacent to EURATOM LCT coil and where the joint region shall be in the straight section of the race track coil, the first priority.

The first test phase of the Polo coil was successfully performed from March to May 1994. It was concluded by a high voltage fast discharge of 22 kV from 14.5 kA resulting in a peak power of 320 MW.

1. The TOSKA Facility for Testing the ITER TF Model Coil

The JCT sent out the "Request for Task Proposals" for the ITER model coil end of 1993. In preceding meetings the ITER Director and the Home Team Leaders agreed about the work sharing between the parties for the model coil task. The central solenoid (CS) model coil will be designed and constructed by Japan and the United States while the toroidal field model coil will be the task of the European Union and the Russian Federation. Taking into account that the mechanical and electrical loading of the model coil can only reach in some parameters the 100% values of the loading of the full scale coil, the discussion between the ITER partners led to the creation of an alternate configuration in which the ITER shear key system is tested. Beside the existing parallel configuration (Fig. 1) a configuration in which the model coil is tested in the bore of the LCT coil (Fig. 2) was elaborated whereby the racetrack shaped model coil was assessed more suitably for both configurations compared to the earlier proposed D-shape version. Making the model suitable for both options a sophisticated joint arrangement in the racetrack coil curved region is the consequence which is not representative for the full scale TF coils. Both coils shall meet the interface of the TOSKA facility. Only differently shaped superconducting busbars should be necessary to connect the coil with current leads. The interface document was adapted to both configurations. Contributions to the model coil work were described in Task MCOI-1.

The comparison of both test options led to the decision of the JCT that the parallel configuration having the joints in racetrack coil straight sections is the reference configuration with the first priority.

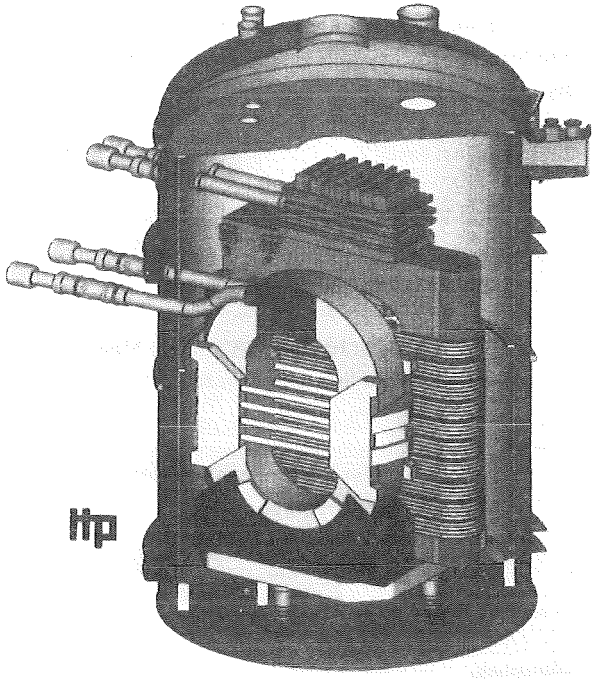

Fig. 1: The so called "Parallel configuration" where the ITER TF model coil is tested adjacent to the LCT coil.

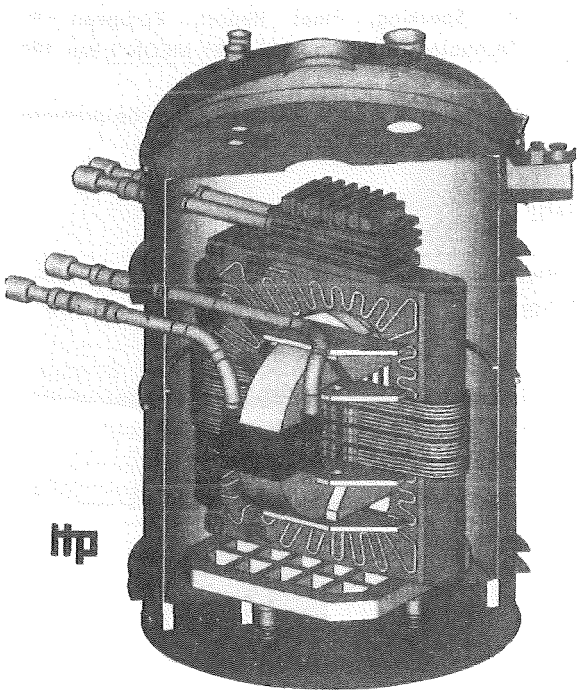

Fig. 2: The so called "Orthogonal configuration" where the ITER TF model coil is tested in the bore of the LCT coil for testing the ITER shear key system.

Status: The parallel operation of the 50 kA and 30 kA resulting in a 80 kA power supply were taken into operation and the control circuit was tested up to 8 kA with a resistive coil. A proposal of testing the 80 kA power supply together with the

Polo coil up to 20 kA was prepared. An arc chute switch capable of breaking 80 kA up to 1.2 kV voltage was identified.

The 80 t crane was installed end 1993 in TOSKA. The control circuit for synchronized operation with the 30 t crane was taken into operation. The crane passed the acceptance test of the German authority TÜV.

Experiments and fabrication investigations for solving the problem areas at the warm and cold end of the 80 kA current lead are running.

The cold lines between TOSKA and the 2 kW refrigerator were installed as far as possible in the present stage. Also the valve box was installed. Cold lines and valve box passed the acceptance test. The remaining installation work will be completed after the Polo test.

The measuring and control system as well as the data acquisition will be exchanged after the Polo test. The status is already described in MBAC.

2. The Test of the Polo Model Coil

2.1 Test conditions and instrumentation

The Polo model coil was developed and constructed by KfK in collaboration with industry and tested in TOSKA (Fig. 3). The goal was to demonstrate that a superconducting poloidal field coil can withstand the typical tokamak field transients like fast ramp up, plasma control and disruption if those are taken into account in the coil design. These typical operation modes were simulated by a special discharge circuit (Fig. 4). Field transients and mechanical loading are generated by fast discharge modes (Fig. 5).

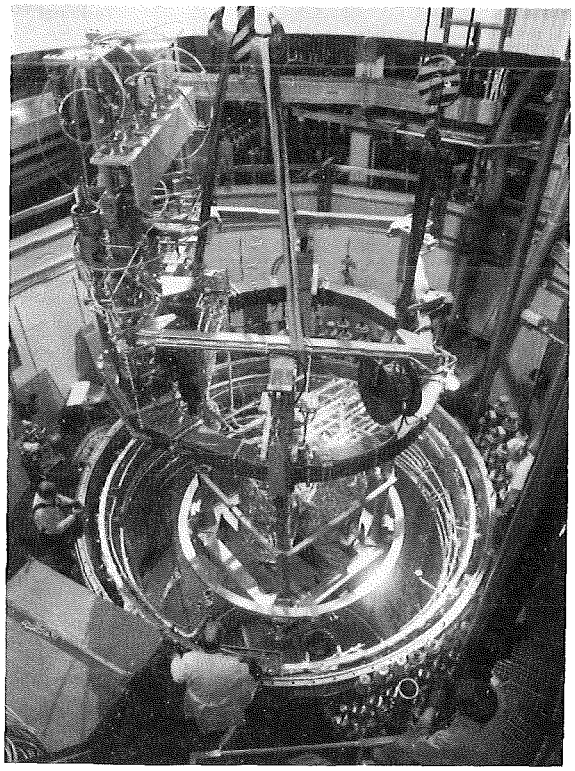

Fig. 3: The Polo coil during installation in the TOSKA vacuum vessel.

- Fast discharge at 23 kV, 15 kA corresponds to decreasing field changes of ~ 140 T/s.
- Fast half coil discharge while one coil half is shorted correspond to increasing field changes up to 588 T/s.
- Fast discharge in a SS-short circuit ring beneath the coil causes coil bending between supports (shear stress loading).

The coil is equipped with sensors at ground and high voltage level. Later ones need a specially developed signal conditioning. A special compensation scheme was used for quench detection and diagnostic (Fig. 6). A data acquisition system with three triggers for different sampling rates is necessary for getting sufficient information. The coil was cooled down at its operation temperature in one week and was kept 60 days at this temperature level.

2.2 Test results [1]

2.2.1 High voltage tests

High voltage tests are an indispensible feature for assessing the insulation properties running during the experiment of the coil, namely:.

- High voltage DC tests for measuring the insulation resistance
- High voltage AC tests for partial discharge measurement in order to determine the opening of micro voids in the ground insulation material.
- High voltage pulse tests for testing turn to turn and pancake to pancake insulation as well as transient voltage distribution.

Partial discharge measurement showed significant differences between 293 K and 4 K (Fig. 6). Also at 4 K new effects were observed. Further investigations are needed for a concluding assessment.

2.2.2 Characteristic magnet properties

The current obtained without quenching was 75% of the current scaled from the strand critical current (Fig. 8). The pancake joint resistance was with 0.5 nΩ as expected. The current lead joint was 13 nΩ and about 3 times worse than obtained in the current lead test. Quench tests showed a slightly better stability margin for CuNi tape wrapped subcables than for glass/Kapton/glass wrapped subcables (Fig. 9). The coil was ramped 20 triangle pulses with 1600 A/s and 15 kA peak current without quenching. AC losses were covered by static losses ~ 23 W (estimation: 0.05 Hz, 8.6 W). The mechanical

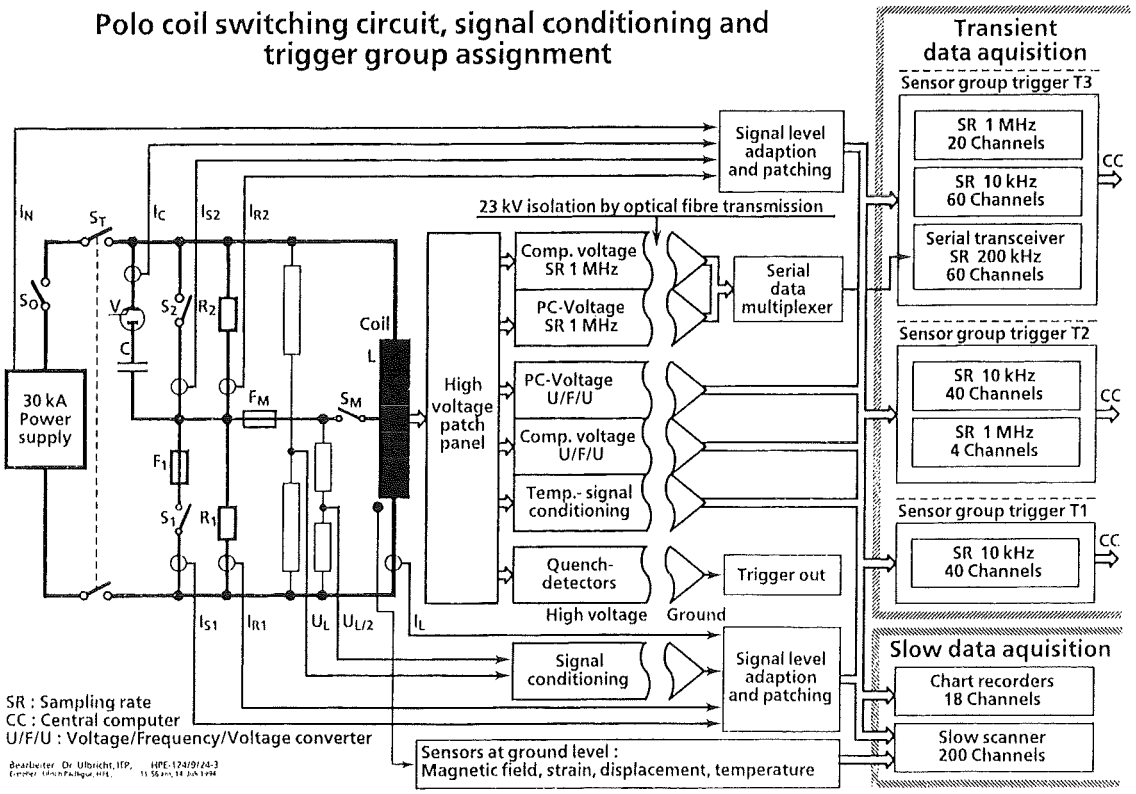

Fig. 4: The block diagram represents the electrical high current supply and switch yard system as well as ground and high voltage level diagnostic.

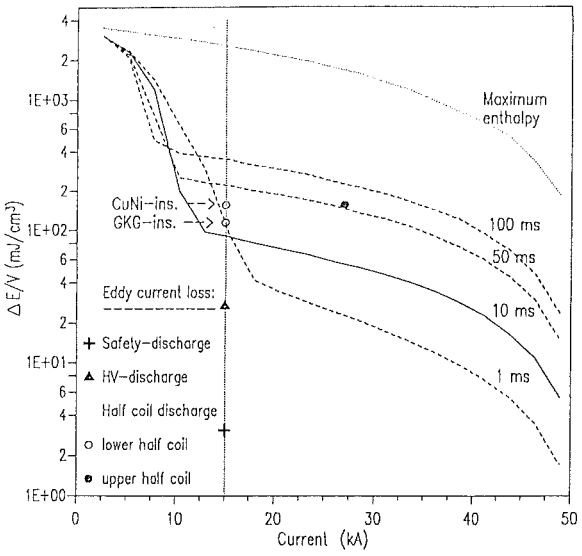

Fig. 5: Calculated specific loss energy versus current released in the Polo cable during the different discharge modes.

properties and the measured diameter extension agreed within 10% with that calculated from a finite element model. During a fast high voltage discharge (Fig. 10) the inner turn experienced 135 T/s decreasing field change without quenching. This agrees with the estimation (Fig. 5). The generated losses are with 38 mJ/cm³ below the stability limit of 100 mJ/cm³.

Summary: The Polo coil is the largest model coil tested before the ITER model coils. High voltage technology was developed

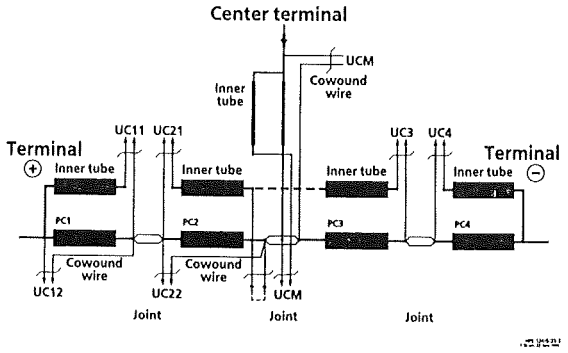

Fig. 6: The insulated inner tube and cowound wire are used for compensation of the inductive voltage part for quench detection and diagnostic.

and applied for a sc-magnet at ITER magnet voltage level. Expected specifications were reached as far as tested. No ramp rate limitations were observed up to now. Progress was obtained in operation experience of the cryogenic and electric systems of TOSKA for the ITER model coil test.

Literature:

[1] H. Bayer et al., Test of the Polo model coil - superconducting poloidal fielcd coil according to the specifications of the tokamak operation - in the KfK TOSKA facility, 18th SOFT, Karlsruhe, Aug. 22-26, 1994.

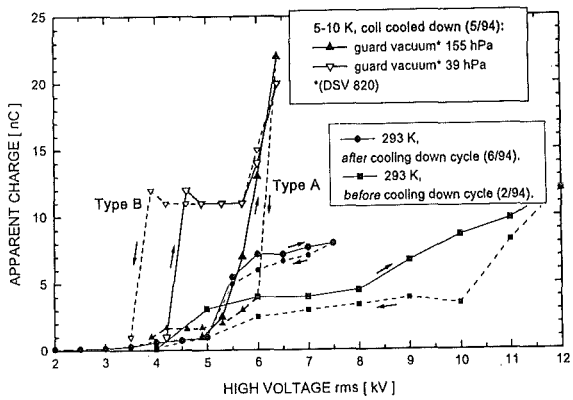

Fig. 7: Type A: App. charge increases already at 4 K at lower voltage levels considerably compared to those measured at 293 K.
Type B: App. charge plateau depends on guard vacuum pressure over a leaking joint box.

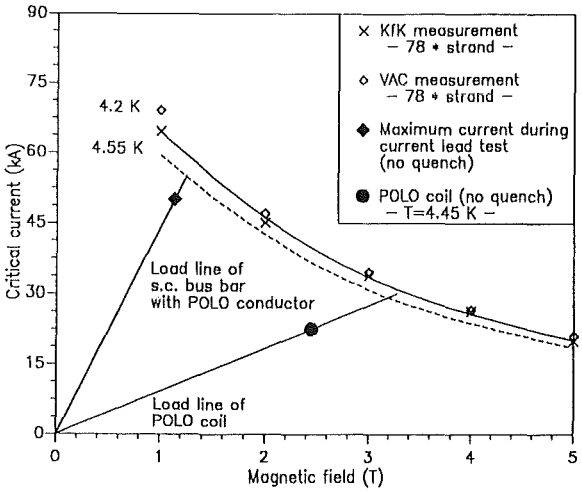

Fig. 8: The Polo coil load line and the critical current limit for 4.2 K resp. 4.55 K derived from the measured strand I_c.

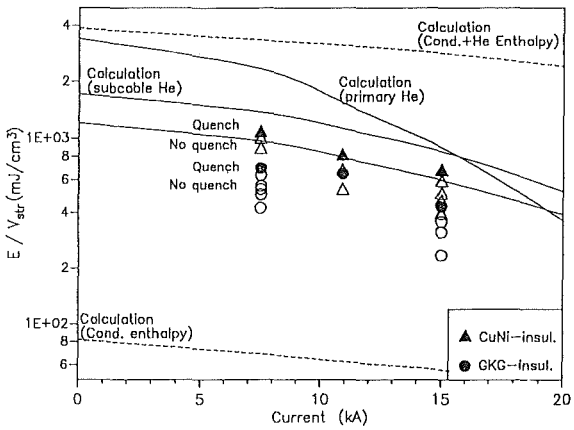

Fig. 9: Estimated specific loss energy input for both cable types used in the Polo coil (CuNi tape wrapped and G-K-G wrapped subcables).

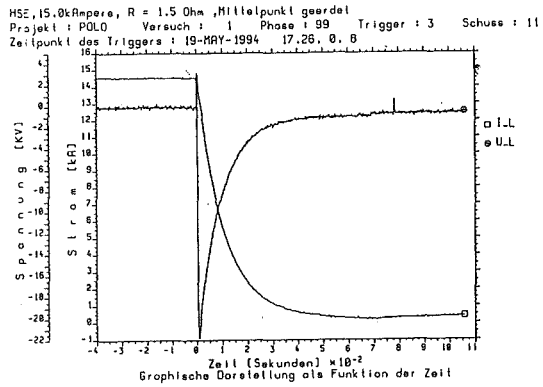

Fig. 10: The 320 MW power pulse during a fast high voltage discharge of the Polo coil.

Staff:

H.Barthel
H. Bayer
F. Becker
S. Darweschsad (since 1.9.93)
P. Duelli
S. Förster (till 31.12.93)
G. Friesinger
A. Götz
P. Gruber
A. Grünhagen
W. Heep
R. Heil
R. Heller
W. Herz
H. Irmisch
H. Kathol
R. Kaufmann
K.-H. Kleiber
P. Klingenstein
W. Lehmann
W. Maurer
G. Nöther
A. Nyilas
U. Padligur
C. Ruf
K. Rietzschel
L. Schappals (till 31.3.94)
C. Schmidt
G. Schleinkofer
K. Schweikert
L. Siewerdt (till 31.3.94)
Ch. Sihler
E. Specht
H.-J. Spiegel
F. Süpfle
F. Süß
M. Süßer
E. Ternig
A. Ulbricht (for 2.)
D. Uhlich
D. Weigert
F. Wüchner
G. Würz
G. Zahn (for 1.)
H.P. Zinecker
V. Zwecker

MBAC High Field Operation of NbTi at 1.8 K

Subtask 1: He II Forced Flow Cooling: 1.8 K Tests of EC LCT Coil plus Development of Circulation Pumps

The 1.8 K cooling technique is indispensible, if technically applicable superconducting materials shall obtain their highest field levels. Therefore the task was started with a programme part for the development of components included in such a cooling circuit and is continued with the operation of a large forced flow cooled fusion magnet, the Euratom LCT coil. The last experiment is an intermediate step in the sequence for upgrading the TOSKA facility for the ITER TF model coil test (Task MTOS).

1. The 1.8 K Test of the Euratom LCT Coil

The preparation of the TOSKA facility for the 1.8 K test of the Euratom LCT is in progress. The test has become more important by the election of the model coil test configuration where the ITER TF model is tested adjacent to the LCT coil (TASK MTOS-1). For the 1.8 K test the design of the flow sheet for the cooling technique is concluded. The switching circuit for the safety discharge of the LCT coil is under construction. Bus-bars, switches and resistors are mounted. A call for tender for the control system of the switches is running and will be ordered in September 94. The extension of the cryogenic measuring and control system is ordered. The order of the visualisation system (software and hardware) and the design of the graphs is running. The configuration of the data base "ORACLE" is in progress. The new installed 80 t crane will ease the installation of the reinforced LCT coil with a weight of about 60 t.

Staff:

H. Barthel
H. Bayer
G. Friesinger
A. Götz
A. Grünhagen
W. Herz
M. Irmisch
W. Maurer
K. Rietzschel
C. Ruf
J. Spiegel
F. Süß
M. Süßer
A. Ulbricht
D. Uhlich
G. Zahn

Vacuum and Fuel Cycle

Introduction:

Our contributions to the optimization of a pumping system for ITER, although largely hampered by the lingering of firm decisions of the ITER-Team on specifications for the ITER-Vacuum System, have been considerable in form of work on several subtasks of TPV 2. Within subtasks 1 and 2 the pumping speed of thin activated charcoal cryosorbent layers has been proven to be compliant with the low tritium inventory requirement. Various activities have been devoted to a qualification of KfK for the development and prototype testing of a complete primary pump for ITER. Within a NET-Contract different cryopump concepts have been evaluated. On the basis of the most promising concept preparations have been untertaken within subtask 7 for the development and small scale testing of critical components using available cryostats, and for the necessary modification of one of these cryostats to house and supply the prototype cryopump for tests.

Within subtask 5 the measurement of pumping characteristics for different combinations of mechanical forepumps has been continued.

Concerning tritium processing the KfK-method based on permeation and catalytic cracking has received full attention by the ITER-Team. The experimental activities within TEP 2 are now concentrated on the demonstration of full tritium operation of the CAPRICE facility. Supporting activities are aimed at the long-term performance of permeators being key components in the process. Another work (TEP 3) is devoted to the investigation of the long-term behaviour of novel tritium storage getter materials. An important aspect in all of the mentioned tritium-related activities is the availability of the Tritium Laboratory Karlsruhe that has officially gone into operation at the end of 1993.

H.D. Röhrig

TPV 2 Optimization of Cryogenic Vacuum Pumping of Plasma Exhaust

Subtask 1: Sorbent Preselection, Cryopanel Development

The investigations into optimization of the sorption properties of thin layer cryopanels were continued. The aim is to develop cryopanels with a high pumping speed for plasma exhaust but with low tritium inventory.

Activated charcoal powders as well as molecular sieve powders were tested with particle sizes in the range between 5 and 160 µm. The following types of powders were included into the test matrix:

Tab. 1: Sorption materials for coating

Sorption material	Type	Supplier
activated charcoal	5963.1	Roth
activated charcoal	114 A	Chemviron
activated charcoal	GFF 30	Chemviron
molecular sieve	Linde Typ 5A	Bayer AG
molecular sieve	Sodalith	Bayer AG
molecular sieve	ZSM - 5	Bayer AG

Each of the selected powders was fixed with the same spraying coating technique and the same type of cement, Thermoguß 2000, on d=50 mm aluminium specimen discs. The coated surface area on these specimen discs is 17.4 cm^2. After the coating procedure layer thicknesses for the sorbent and cement together were measured in the range of <100 µm.

After the thermal cycling tests (77K/420K) at the TARZAN test facility the sorption tests at the HELENE test facility were executed.

For the specimen with the charcoal type GFF 30 supplied by Chemviron the best results in terms of the relative pumping speed (8.8 l/s) were achieved. With the two other types of charcoal powder (114 A from Chemviron and type 5963.1 from Roth) lower results for the pumping speed were measured.

The investigations with the three different molecular sieve powders show lower relative pumping speeds ($\sim 10^{-2}$ l/s) for this material group which do not fulfil the requirements.

In parallel to these activities a new coating facility was designed and constructed for the reproducible fabrication of large panels (Fig. 1). With this apparatus it is now possible to fabricate cryosorption panels having sorbent/bonding layers with a thickness in the range of 0.1 to 3.0 mm. The max. possible coating area is 900 mm×900 mm.

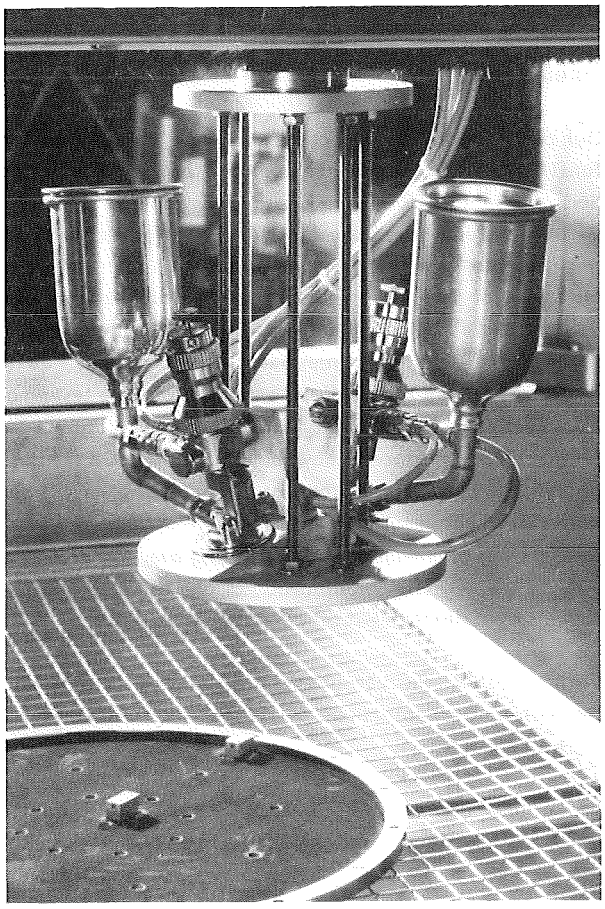

Fig. 1: Coating facility for cryopanels

Subtask 2: Cryopumping Tests

1. Introduction

Cryosorption panels which consist of various material combinations (sorbent/bonding/substrate) for plasma exhaust cryopumping have been developed by KfK [1]. Pumping characteristic measurements have been carried out at the TITAN facility under simulated ITER operating conditions for both compound pumping (three-stage cryopump) and co-pumping (two-stage cryopump) [1,2]. Both cryopump configurations meet the ITER requirements, but the latter takes advantage of its comparatively high conductance for helium.

Another ITER requirement is to minimise the tritium inventory in the cryopump. Therefore a novel coating technique has been developed at KfK. It enables uniform thin and reproducible coating of sorbent powders on large panels.

The sorption characteristics of thick- and thin-layer panels obtained with two exemplary panels in three-stage cryopumping will be discussed.

2. Experimental Procedure

The tests were carried out at the TITAN test facility. The TITAN facility is a cryopump with axial gas flow. Figure 2 shows the cross-section of this system. The cryopump is installed in the upper part of a cylindrical receiver. The gas mixture to be pumped is metered into the lower part of the receiver which is designed in accordance with PNEUROP standards.

In the centre of the pump there is a LHe bath to which the adsorption panel is bolted. The LHe bath is enclosed by a cylindrical LHe shield. This shield is protected from direct incoming flow by a LHe chevron baffle. Between the LHe shield and the warm wall of the vessel there is another LN_2 shield which is also shielded from the incoming flow by a LN_2 chevron baffle. These baffles were installed for the three-stage cryopumping tests. The LHe baffle was omitted for the two-stage crypumping tests. Both baffles have the same geometry. The transmission probability of a single baffle is calculated to be 20% [2] and measured to be 18% in the molecular flow range.

The adsorption panels consist of three layers: Carrier material, bonding and sorbent. The best preselected combinations of materials were used to make panels of 43 cm diameter for the pumping tests at the TITAN facility. The data of the two panels compared are shown in Table 2.

The temperature of the panel and of the two baffles are monitored at two points each (the centre and the edge) by means of calibrated Fe/Rh resistance sensors. In accordance with the PNEUROP standard, the gas pressures are monitored at the inlet dome by means of calibrated BARATRON capacitance diaphragm gauge and BAYARD-ALPERT hot cathode ionization gauge measuring equipment. The gas flows are monitored by MKS mass flow meters.

Prior to each panel test, the entire system was baked out to 150°C for several hours and evacuated simultaneously to $\sim 10^{-8}$ mbar by a turbomolecular pump. The LN_2 shield is filled with LN_2 at least one day before the experiment starts. To cool down the receiver to <80K the LHe shield and LHe bath were filled with LHe. The operating mode was employed by intermittent feeding of gas to be pumped at constant flow rate for a predetermined duration (typically 5 to 15 minutes), followed by an interruption for sufficient time (15 minutes) to allow the system to reach equilibrium. Following the last feeding of gas, the LHe cold surface is heated to 90 K. A gas mixture corresponding to the exhaust gas of ITER was used. The composition of the gas mixture is 0.08 Ar, 0.08 CO_2, 0.16 CO, 0.16 N_2, 0.16 O_2, 1 H_2, 1.12 CH_4, 3 He and 94.24 D_2 in vol. %.

3. Discussion of Results

The pressure in the vacuum vessel is about 10^{-8} mbar before the tests. For a given dosing rate, the pressure first rises rapidly, then becomes almost constant as steady-state is reached. When the gas dosing is interrupted for sufficient time the equilibrium pressure is reached. The pumping speed

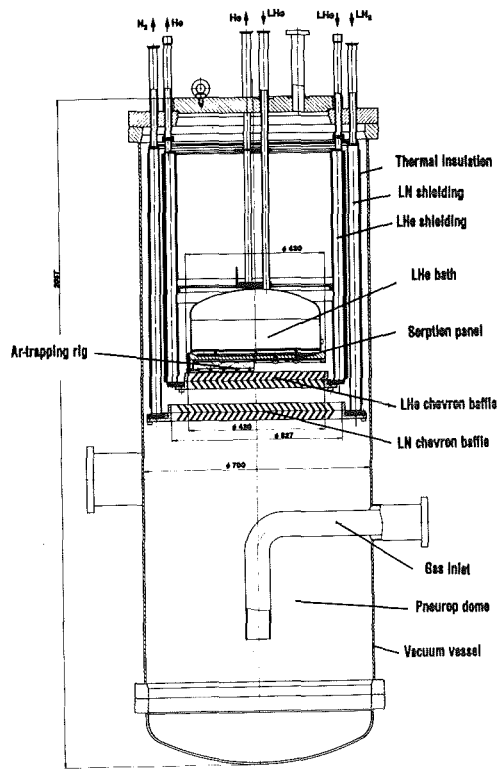

Fig. 2: TITAN cryopump

Tab. 2: Panel data

Panel no.	Sorbent	Bonding	Preparation
12	Activated charcoal CHEMVIRON SC II particles < 3mm	Inorganic cement THERMOGUSS 2000	Sorbent and bonding coated by spraying; thickness <3 mm
19	Activated charcoal CHEMVIRON GFF 30 powder: $d_{vs}=7$ µm	Inorganic cement THEERMOGUSS 2000	Sorbent and bonding coated by spraying; thickness <100 µm

S is calculated from the relation $S=Q/p$ where Q is the gas dosing rate adjusted by means of a mass flow controller and p is the gas pumping pressure measured inside the vacuum vessel, both measured at the temperature of 293 K.

Figure 3 shows the helium pumping speed and Figure 4 the helium equilibrium pressure for thick and thin sorbent layers as a function of gas load related to the activated charcoal cryosurface at the temperature of about 5 K.

Good agreement is observed up to the gas load of 0.1 mbar l/cm². The pumping speed of the thick sorbent layer first

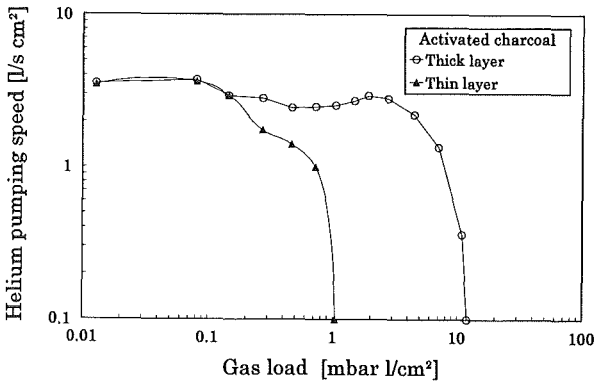

Fig. 3: Helium pumping speed at 5 K.

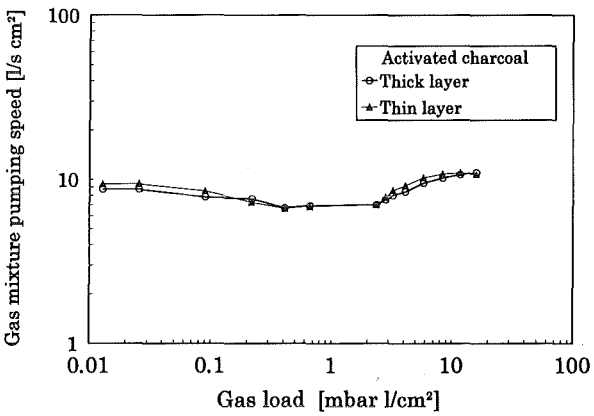

Fig. 5: Pumping speed of the gas mixture.

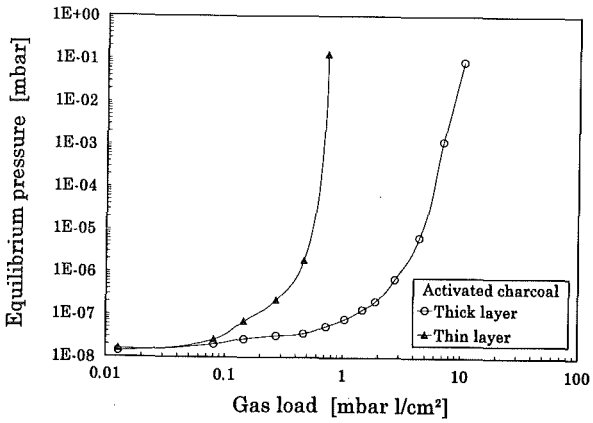

Fig. 4: Helium equilibrium pressure at 5 K.

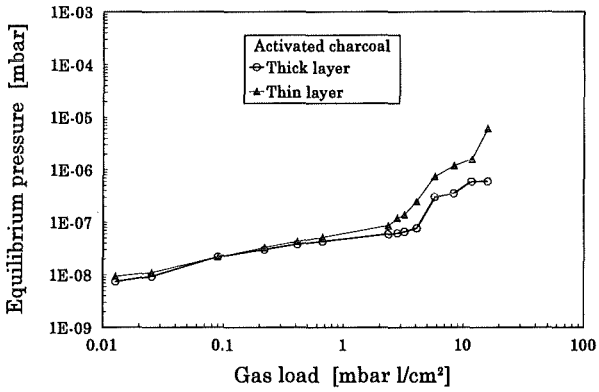

Fig. 6: Equilibrium pressure of gas mixture.

decreases due to the increase of the gas load. After reaching the minimum, the pumping speed increases up to a certain value because the gas flow is changing from molecular flow to the transition and continuum flow regions [3] and then decreases rapidly since the saturation of the cryosurface is reached. In comparison to the thick sorbent layer, the pumping speed of the thin sorbent layer falls continuously to saturation. The ultimate sorption capacity is defined as a specific amount of the adsorbed gas related to the cryosurface for which the pumping speed equals zero. For the thick sorbent layer it is 12 times higher than for the thin sorbent layer. The equlibrium pressure increases slightly at first, then more rapidly with growing of gas load (see Fig. 4).

According to the kinetic theory of gases and the addition theorem [3] for the transmission probability of baffles, the calculated sticking coefficient with a maximum helium pumping speed measured amounts to 56% for the molecular flow region for both thin and thick-layer panels. In contrast to the tests with pure helium, where only adsorption on the activated charcoal cryosurface occurs, tests with the gas mixture lead to both adsorption and condensation of gases since there are condensable and non-condensable gases in the mixture at a temperature of 5 K.

For the gas mixture considered, the pumping speeds and equilibrium pressures as a function of gas load are approx. identical for both panels (see Figs. 5 and 6). The equilibrium pressure increases from 10^{-8} to 10^{-6} mbar in the measured range of gas load up to 10 mbar l/cm².

4. Conclusions

Cryopumps for the torus pumping and fuel recycling system of ITER will be designed by using activated charcoal as sorbent bonded by inorganic cement. For thin- and thick-layer panels coated by activated charcoal and operating at a temperature level of 5 K the following conclusions can be summarized:

- Maximum helium sticking coefficient measured was 56%.
- Identical helium pumping behaviour was observed for thick and thin sorbent layers up to the gas load of 0.1 bar l/cm².
- Nearly identical values were measured for gas mixture pumping speed and equilibrium pressure of thick and thin sorbent layers up to the gas load of 10 mbarl/cm².

Subtask 5: Mechanical Pumps

1. Introduction

Upon completion of the tests specified in the test matrix harmonized with the ITER Home Team according to which the

performance of oil free mechanical positive displacement scroll pumps, supplied by NORMETEX (1300 m^3/h, 600 m^3/h and 60 m^3/h), and a bellows pump, supplied by METAL BELLOWS (6 m^3/h), were tested in single and series operation, further tests of the pumping speeds were carried out with different trains of pumps in the FORTE (Forepumps Testing) test facility, i.e. NORMETEX 1300+60 m^3/h at outlet pressures of 600 and 1200 mbar; NORMETEX 1300+60+METAL BELLOWS 6 m^3/h at outlet pressures of 600 and 1200 mbar, and NORMETEX 600+60 m^3/h at an outlet pressure of 1200 mbar.

2. Tests with Two Series Connected Pumps

2.1 NORMETEX 1300+60 Pumps

In these tests the maximum of pumping speeds is shifted towards higher suction pressures compared to earlier tests on series connected pumps (Figs. 7 and 8). Compared with the results of series operation of NORMETEX 1300+600, the pumping speed for N_2 increases at the outlet pressure of 1200 (600) by a factor of 1.05 (1.05). On the other hand, the pumping speed for H_2 drops by a factor of 6.4 (1.27). The ultimate pressure for N_2 deteriorates from 1.1×10^{-5} to 3×10^{-3} (from 6×10^{-6} to 2×10^{-4}) mbar, the ultimate pressure for H_2 increases from 1.1 to 6×10^{1} (from 1.1×10^{-3} to 9.9×10^{-2}) mbar. Consequently, also the compression ratios are clearly worse by orders of magnitude (Tables 3 and 4).

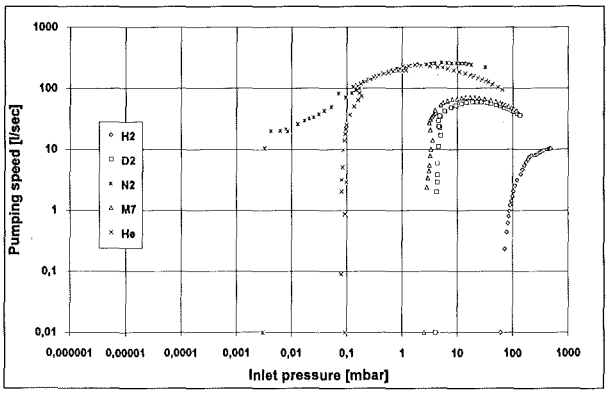

Fig. 7: Pumping speed of NORMETEX-1300+60 pump train for various gases at 1200 mbar exhaust pressure

The qualitative difference in operation of these dual pump trains is reflected by the worse pumping behavior of the train tested here.

2.2 NORMETEX 600+60 Pumps

In this train a pumping speed of 138 l/s was measured which is worse by a factor of 1.9 than the pumping speed in the tests involving the series connected pumps described before, at 1200 mbar outlet pressure for N_2, whereas it is practically unchanged for H_2 (11 l/s) (Table 3). By contrast, the ultimate pressures are only slightly better for N_2 (factor 2) and for H_2

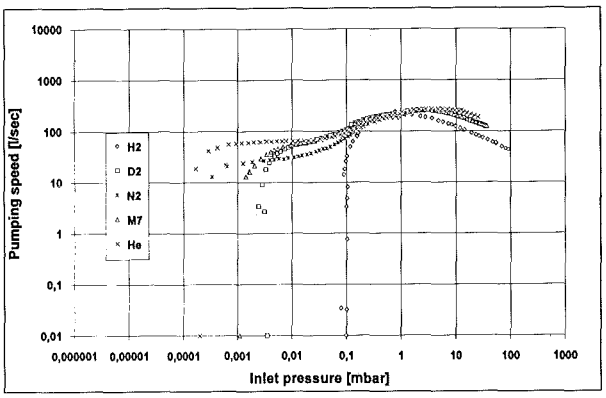

Fig. 8: Pumping speed of NORMETEX-1300+60 pump train for various gases at 600 mbar exhaust pressure

(5.45). Tests at 600 mbar outlet pressure have not been conducted for this pump train.

Tab. 3: Pumping Data of pump trains for various gases at 1200 mbar exhaust pressure

Pump trains	Max. pumping speed (l/s)					Ultimate pressure (mbar)					Compression ratio				
	H2	D2	N2	M7	He	H2	D2	N2	M7	He	H2	D2	N2	M7	He
NORMETEX 1300+60	10	60	261	70	239	6 x E+1	4	3 x E-3	1,1 x E-3	8 x E-2	2 x E+1	3 x E+2	4 x E+5	,09 E+6	1,5 x E+4
NORMETEX 600+60	11	84	138	90	145	1,1 x E+1	3,2 x E-1	1,5 x E-3	1,9 x E-1	7 x E-3	1,1 x E+2	3,7 x E+3	8 x E+5	6,3 x E+3	1,7 x E+5
NORMETEX 1300+60+ METAL BELLOWS 6	258	257	251	255	262	6 x E-6	1,6 x E-5	5 x E-6	5 x E-6	1,6 x E-6	2 x E+8	7,5 x E+7	2,4 x E+8	2,4 x E+8	1,9 x E+6

Tab. 4: Pumping Data of pump trains for various gases at 600 mbar exhaust pressure

Pump trains	Max. pumping speed (l/s)					Ultimate pressure (mbar)					Compression ratio				
	H2	D2	N2	M7	He	H2	D2	N2	M7	He	H2	D2	N2	M7	He
NORMETEX 1300+60	212	258	261	260	271	9,9 x E-2	3,5 x E-3	2 x E-4	1,1 x E-3	2 x E-4	6,1 x E+3	1,7 x E+5	3 x E+6	5,5 x E+5	3 x E+6
NORMETEX 1300+60+ METAL BELLOWS 6	262	260	249	258	271	2,5 x E-6	4 x E-6	3 x E-6	2 x E-6	2 x E-6	2,4 x E+8	1,5 x E+8	2 x E+8	3 x E+8	3 x E+8

3. Tests with three Series Connected Pumps

Extension of the pump train described in Sec. 2.1 by the third pump (NORMETEX 1300+60+METAL BELLOWS-6) brings up at a outlet pressure of 1200 (600) mbar the pumping speed for H_2 to 258 (262) l/s whereas for N_2 a decrease is measured by 10 (13) l/s (Tables 3 and 4). The maximum of pumping speed is attained at 1.2 (1.5) mbar for H_2 and at 4.2 (2.8) mbar for N_2. H_2 is pumped better than N_2 in this pump train (Figs. 9 and 10). Moreover, a clear improvement of the ultimate pressure up to 6×10^{-6} (2.5×10^{-6}) mbar at 1200 (600) mbar outlet pressure can be measured for H_2 which results in a compression rate of 2×10^{8} (2.4×10^{8}) mbar.

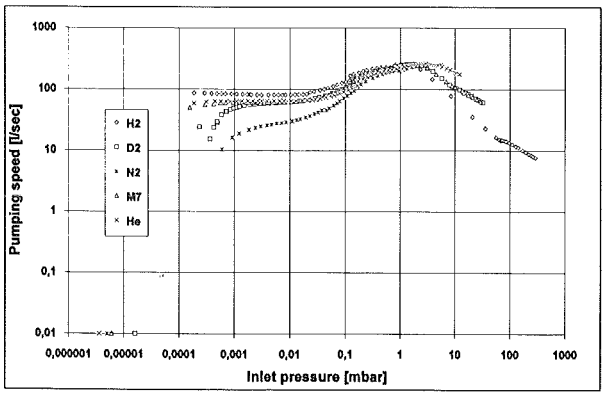

Fig. 9: Pumping speed of NORMETEX-1300+60+METAL BELLOWS-6 pump train for various gases at 1200 mbar exhaust pressure

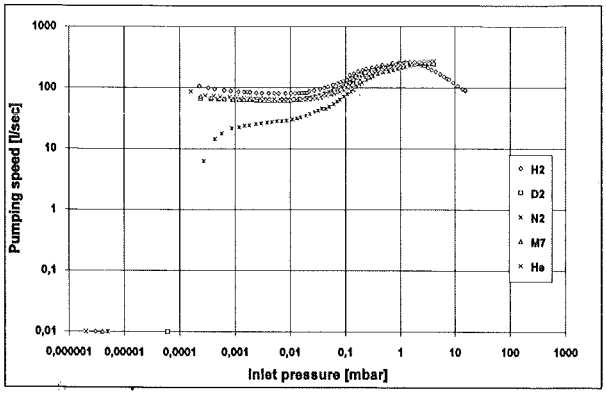

Fig. 10: Pumping speed of NORMETEX-1300+60+METAL BELLOWS-6 pump train for various gases at 1200 mbar exhaust pressure

4. Summary

It has been demonstrated in these tests that also at an elevated outlet pressure of 1200 mbar light gases, e.g. H_2, D_2 and the M7 gas mixture, can be pumped better than nitrogen using the pump train NORMETEX 1300+60+METAL BELLOWS-6 in the range of suction pressures < 10 mbar.

However, compared to the pump trains NORMETEX 1300+600+60 and NORMETEX 1300+600+60+METAL BELLOWS-6 tested earlier, the maxima of pumping speeds are not exactly attained for the individual gases. At 1200 mbar outlet pressure they are lower by 4.6 and 6.6%, respectively, for H_2, by 6.6%, for D_2, and by 4.3 and 5.5%, respectively, for the M7 gas mixture than the values previously measured. At 1200 mbar outlet pressure hydrogen is pumped much better in the range of suction pressures 10^{-1} to 10^{-4} mbar using the three pump trains tested here than with the pump train consisting of three NORMETEX compressors. By contrast, at 600 mbar outlet pressure no difference in performance can be observed.

Subtask 7: Primary pump development, prototype tests

1. Introduction

The general objective of this subtask is the development of components for prototype pumps and valves to be used in the ITER torus pumping and recycling system and testing of prototypes. The activities at KfK are split into two parts:

- development of components (small scale testing)
- testing of prototypes.

The tests are planed to be performed at the two existing test facilities of KfK: TITAN and HELITEX. The work programme consists of the following tasks:

- Proof-of-principle tests for rapid heating/cooling methods of cryopanels.
- Performance evaluation of fuel separation from impurities and helium ash.
- Endurance cycling tests of cryopanels.
- Testing of drives for valves.
- Testing of prototypes of pumps and valves.

2. Development of rapid heating and cooling technology

The proof-of-principle tests for rapid heating/cooling methods of cryopanels are the next to be carried out. The objective is to develop heating and cooling methods for rapid regeneration which should result in minimization of tritium inventory inside the pumping system of ITER.

At the TITAN test facility panels segments in the typical ITER-configuration will be used. Various surface and bulk heating methods will be investigated. At the HELITEX test facility cryopanels will be tested in an ITER representative height (~1500 mm) and width (~300 mm). Cooling of panels is provided by supercriticel helium as coolant.

3. Test facilities

For the experimental investigations the TITAN and HELITEX test facilities will be used.

The TITAN facility (Fig. 2) was designed for tests of plane circular cryosorption panels with a maximum diameter of 430 mm under simulated tokamak operating conditions [4]. The cryopump is mounted in a vertical cylindrical vacuum vessel with a diameter of ~700 mm and a height of ~2200 mm. Its total volume is ~700 l and the max. operating overpressure amounts to 10 bar. The test panel will be installed in a cavity (diameter 580, height 820 mm) shielded by a cylindrical annular LN_2 pool with a max. LN_2 volume of 40 l. The lower part of the cavity is shielded by a 106° chevron baffle (opening diameter 527 mm, thickness 50 mm, sheet thickness

3 mm) made of copper and blackened by a 113 VALVET coating. The baffle is fastened to the annular LN_2 pool.

The gases are metered into the lower part of the vacuum vessel via a tube ND 70.3 mm. This part of the vacuum vessel is designed as a measuring dome with a view to meet the requirements of the PNEUROP Standards.

The HELITEX experimental facility is a high performance facility (up to 600 W/4.4 K) with the coolant supply from a Linde "300 W"-refrigerator. It consists essentially of an 850 l LHe control cryostat which is supplied from the refrigerator and in which the cooling conditions of the test circuit can be set and controlled and of the test cryostat accommodating the object to be tested. The max. possible useful space within the test cryostat is approx. 2 m in diameter and height. Both cryostats are connected via superinsulated transfer lines.

Supercritical helium for forced flow cooling can be circulated either by use of part of the JT flow of the Linde refrigerator or using cold helium pumps within a closed secondary circuit. In this case the control cryostat takes over the function of thermal coupling between the secondary cooling circuit and the primary circuit.

Both helium pumps, a one cylinder piston pump and a one-stage centrifugal pump, are operating while being immersed into the LHe bath of the control cryostat. The piston pump had been developed by KfK under a technology project. The centrifugal pump was developed at the "Walter-Meissner-Institut für Tieftemperaturforschung", Garching, and was modified to fit the applications involving integration in closed circuits.

The main advantages of supercritical helium forced flow cooling are:

- Avoidance of a two phase mixture which gives much more flexibility in piping and layout.

- Flexibility of operation which means that the operation pressure and the mass flow within the circuit can be conveniently set to optimum cooling and stability conditions.

These advantages are of special importance for the test and operation modes required for the cryopump prototypes. Due to the different cryopump operation modes at 5 K, 20 K and 80 K big changes in the density of the supercritical helium have to be expected and cooling instability has to be prevented or at least minimized even under regeneration mode conditions.

Recent investigations on stability of super critical helium forced flow cooling within HELITEX test facility have shown that it is advantageous to circulate helium using a pump with

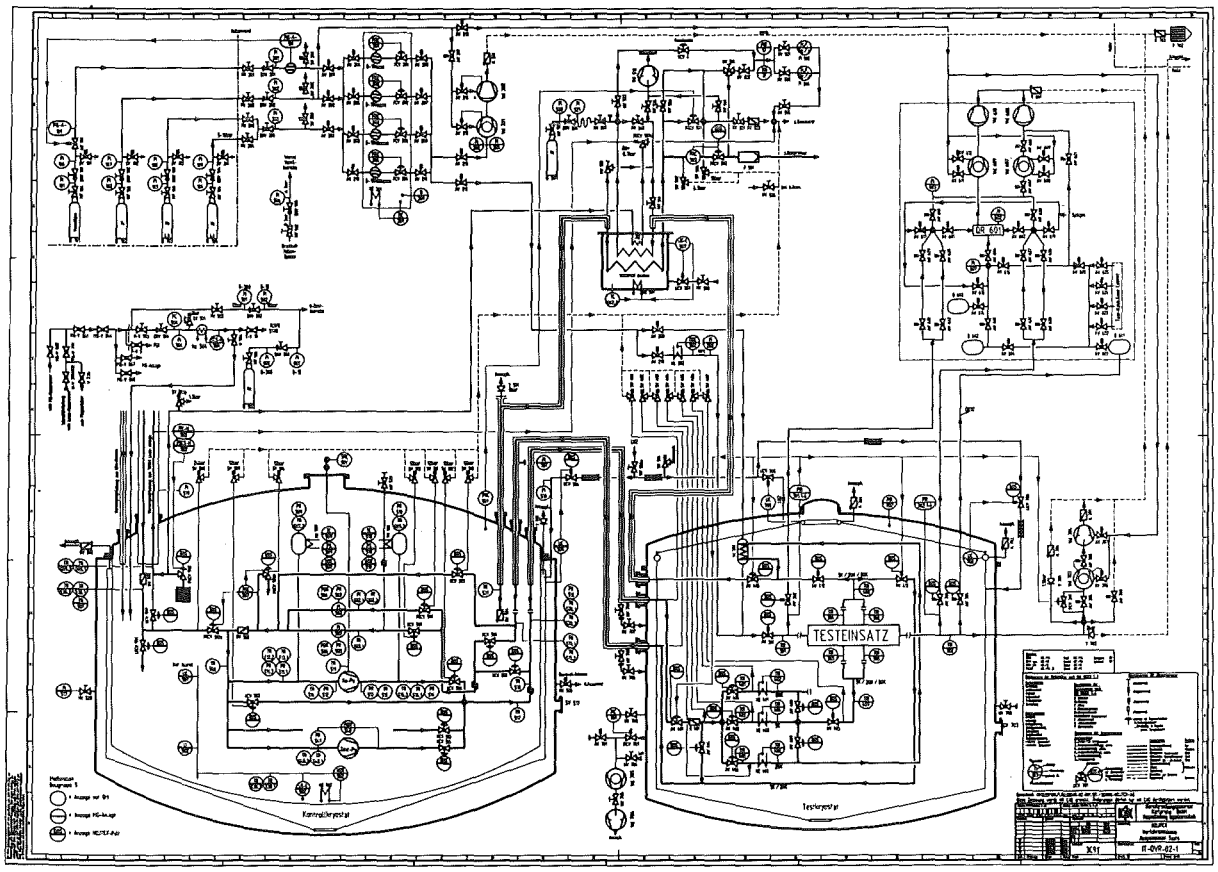

Fig. 11: Flow scheme of HELITEX facility

a steep Δp-m delivery characteristic [5]. This prevents heavy reduction of mass flow in case of disturbing heat loads (regeneration heat) and gives better overall flow stabilization within the cooling circuit.

The HELITEX facility is established with a control room which houses:

- The control desk for setting up and monitoring the operation conditions within the test loops and cryostats and
- the data acquisition and logging system with in maximum 128 measurement channels for pressure, temperature, mass flow, LHe level, pump speed, heat load control.

The HELITEX test facility is integrated within the KfK/ITP helium supply and recovery system. It is connected with the Linde He I/He II refrigerator via the 1.8 K transfer line and can be operated at 4.4 K.

4. Safety studies on hydrogen explosion

The HELITEX test facility has to be modified for safe operation with hydrogen.

For this reason, a study was performed on possible failures caused by a hydrogen-oxygen reaction. Part of the study dealt with failure due to the reaction between the leaking hydrogen condensed on the cooling lines of the test cryostat (Fig. 11) and the incoming air.

4.1 Explosion in the test cryostat

To avoid an explosion due to condensed hydrogen in the test cryostat (Fig. 12), i.e. to prevent the cryostat design pressure from being exceeded in case of occurrence, the limit pressure has to be determined. If the limit pressure is exceeded, all ignition sources installed in the test cryostat such as heaters and pressure transducers have to be switched off.

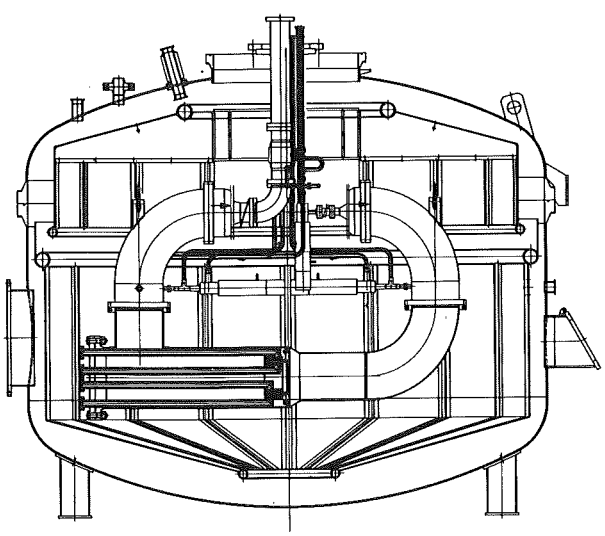

Fig. 12: HELITEX test cryostat

The explosion investigations have been carried out by the Fraunhofer-Institut für Chemische Technologie, Pfinztal.

Using the relationship

$$p = \rho_0 \cdot Es$$

the explosion pressure can be calculated from specific energy and make-up gas density. As the gas composition is unknown at first, expansion of the above formula to the gas mole number n of the mixture has to be performed.

Hence,

$$\rho_o = \frac{(0{,}002016 \cdot n + 4{,}76) \cdot p_o}{(n + 4{,}76) \cdot R \cdot T_0}$$

In the lower range of the mole number, energy can be approximated by

$$E_s = 5{,}5 \cdot 10^5 \cdot n + 1{,}0 \cdot 10^5$$

such that

$$\frac{p}{p_o} = \frac{(0{,}002016 \cdot n + 4{,}76)}{(n + 4{,}76) \cdot R \cdot T_0} \cdot (5{,}5 \cdot 10^5 \cdot n + 1{,}0 \cdot 10^5)$$

With p=7 bar, p_0=1 bar and the boiling temperature of the oxygen of T_0=94.3 K as the most critical value which has already been used previously, expansion of this relation results in the quadratic equation of

$$n^2 + 59{,}1455\, n - 10{,}4286 = 0$$

which leads to n=0.1758. This mole number, however, already is found to be below the lower ignition limit corresponding to n=0.2.

Analog calculation for deuterium yields

$$n^2 + 37{,}7900\, n - 5{,}5904 = 0$$

and n=0.1749<0.2. Consequently, the gas mole number of deuterium also is below the lower ignition limit.

For p_0=1 bar, hydrogen partial pressure at the lower ignition limit amounts to

$$p_{H_2} = 0{,}04 \cdot p_0 = 40\,mbar$$

In safety-related studies, 50% is frequently assumed to be the limit value of the lower ignition limit. This means that the hydrogen partial pressure should not exceed the value of $p_{H_2}=20$ mbar.

For a reaction of this amount of hydrogen in the volume of $V=10\ m^3$, an air partial pressure of $p_L=6.7$ mbar (upper ignition limit) would be required. Hence, the limit pressure could be set, for instance, to $p_{total}=30$ mbar.

This value is safe in two respects: As also air has to be considered as condensed at first, nitrogen will evaporate together with the hydrogen when heat is introduced. Nitrogen, however, renders the hydrogen-oxygen reaction inert, i.e. the reaction of

$$0{,}38\,H_2 + O_2 + 17{,}99\,N_2$$

still would have to be regarded as safe. Here, the hydrogen partial pressure also is $p_{H_2}=20$ mbar, the minimum partial pressure of the oxygen/nitrogen mixture required for a reaction amounts to $p_L=6.7$ mbar. Hence, also in this case a limit pressure of $p_{total} \leq 30$ mbar is obtained.

It is demonstrated by this calculation above that the hydrogen mole number of the mixture with air must not exceed $n_{H_2}=0.175$ to prevent the design pressure of the vessel from being exceeded in the case of occurrence. In addition to the already mentioned nitrogen inertization, however, other criteria are also of decisive importance for a hydrogen-oxygen reaction. These are the lower ignition limit, the upper ignition limit and the minimum oxygen content of the mixture. The permissible hydrogen mole number results in a hydrogen partial pressure of $p_{H_2}=35.46$ mbar. As a reaction equation,

$$0{,}175\,H_2 + n_1 O_2 + n_2 N_2$$

can be used, such that values of

$$\frac{0{,}175}{0{,}175 + n_1 + n_2} = 0{,}75$$

and

$$\frac{n_1}{0{,}175 + n_1 + n_2} = 0{,}05$$

are obtained for the upper ignition limit and the minimum oxygen content, respectively. The solutions of these equations lead to $n_1=0.0117$ and $n_2=0.0466$. Irrespective of the existing inventory, an oxygen partial pressure of $p_{O_2}=50.15$ must not be exceeded. Hence, $p_{H_2}+p_{O_2}=85.6$ mbar could be considered the maximum value. If here again a safety factor of 50% would be assumed, a limit pressure of $p=45$ mbar could be specified. When reaching this value, the plant will be switched off.

Literature:

[1] D. Perinic et al., ISFNT-2, Karlsruhe Germany, 2-7 June Part C (1991)79-84.

[2] D. Perinic et al., 17th SOFT, Roma, Italy, 14-18 Sept., (1992).

[3] R.-A. Haefer, Cryopumping, Theory and Practice, Clarendon Press-Oxford, 1989.

[4] D. Perinic, H. Haas, A. Mack: "Development of cryosorption panels for plasma exhaust cryopumping", Fusion Eng. and Des. 18 (1991) 79 - 84

[5] X. Cheng, W. Lehmann, Investigations concerning the stability of supercritical helium forced-flow-cooling in secondary circuits whith cold helium pumps, CEC/ICMC 1993, Albuquerque

Staff:

A. Edinger
H. Haas
J. Hanauer
T. Höhn
W. Höhn
S. Horn
B. Kammerer
U. Kirchhof
H. Knauß
J. Laier
W. Lehmann
H. Lukitsch
A. Mack
D. Perinic
W. Reeb
R. Rinderspacher
D. Stern
J. Weinhold
D. Zimmerlin

TEP 2 Permeation und Catalytic Cracking

Subtask 1: Permeator Studies

While palladium/silver permeators have withstood without problems years of operation in diverse tritium facilities, they have so far been mostly exposed discontinuously to hydrogen isotopes and tritium gas containing only small amounts of impurities. During plasma exhaust clean-up processing, however, permeators will be subjected to continuous operation in the presence of substantial amounts of impurities in a hard tritium environment. The slowly increasing helium concentration in the permeation membranes produced from tritium that quickly attains steady state concentration in the PdAg membranes during normal operation can have an aggravating effect. It is therefore important to determine the life-time of permeators employing realistic test conditions. The experiment PETRA at the Tritium Laboratory Karlsruhe has been designed to investigate the performance of a "nuclearized" commercial in the presence of tritium and representative type and concentration of fusion fuel cycle impurities permeator during uninterrupted operation.

First long-term integral campaigns with the facility PETRA revealed the need for improvements. In particular, it was observed that

1) the thermocouples used to measure and control the temperature of the permeator were unappropriatly installed,

2) the four sapphire windows of the two infrared cells were blind to infrared radiation on account of metallic film originating from aerosols produced during the welding of the cell bodies,

3) the cooling of the instrumentation rags was insufficient,

4) several pressure sensors were defect, and

5) the number of glove ports was not enough to satisfy the needs of repair and maintenance.

As part of the continuing commissioning tests of the PETRA facility empirical breakthrough curves were determined for the single gases hydrogen and deuterium as well as for various helium/deuterium/hydrogen mixtures as a function of temperature and gas flow rate. Characteristic permeation data describing the effect of temperature are given in Fig. 1.

The permeation data obtained experimentally has been compared with model calculations. On the basis of these empirical permeation curves a technique has been developed for the periodical and indirect control of the mechanical integrity of the permeator during long-term runs with tritium.

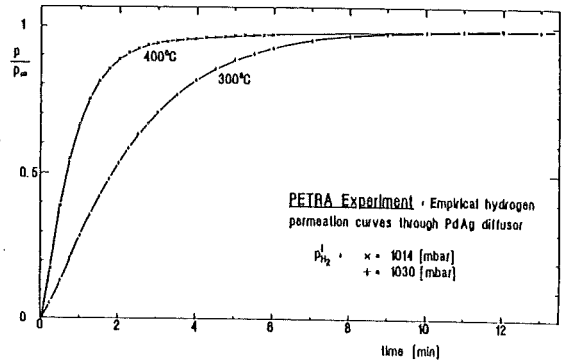

Fig. 1: Typical empirical hydrogen permeation curves through the PETRA AgPd diffusor

With the aim of optimizing the long duration experiments the permeation losses into the isolation vacua of the heated components were determined experimentally under a variety of conditions. The results obtained compared well with model calculations.

All pumps and pump combinations were characterized with respect to achievable vacua and compression ratios using relevant gases and their mixtures. The achievable vacua determined with scroll pumps show a dramatic dependence from exhaust pressure and a significant dependence from the type of gas pumped (see Fig. 2). Metal bellows pumps, on the contrary, produce vacua that are directly proportional to the exhaust pressure and show practically no dependence from the type of gas pumped (see Fig. 3).

Since the infrared analysis integrated into the loop is used to follow the integrity of the permeator and the possible occurance of radiochemical reactions in the gas phase, calibration data for the quantitative determination of pure methane, carbon monoxide and carbon dioxide as well as of their mixtures in helium were obtained.

Fig. 4 shows the effect of deuterium and helium on the infrared analysis of methane. On the basis of these calibrations a good quantitative determination of these gases is possible. The background/signal drift was found to be negligible.

Within the frame of preliminary tests without tritium a permeator operated continuously for a period of about 6 months at 350°C in the presence of hydrogen/deuterium, helium and carbon oxides showed loss of integrity. Metallographic analysis and scanning electron microscopy of the single Pd/Ag permeation tube that failed (long longitudinal rupture) revealed surface segregation at the grain boundary. Preliminary observations, however, indicate that the single tube failure was due to a manufacture defect rather than to a chemically induced process. From this event it is concluded that careful inspection of each permeation tube in permeators envisaged for tritium facilities is necessary.

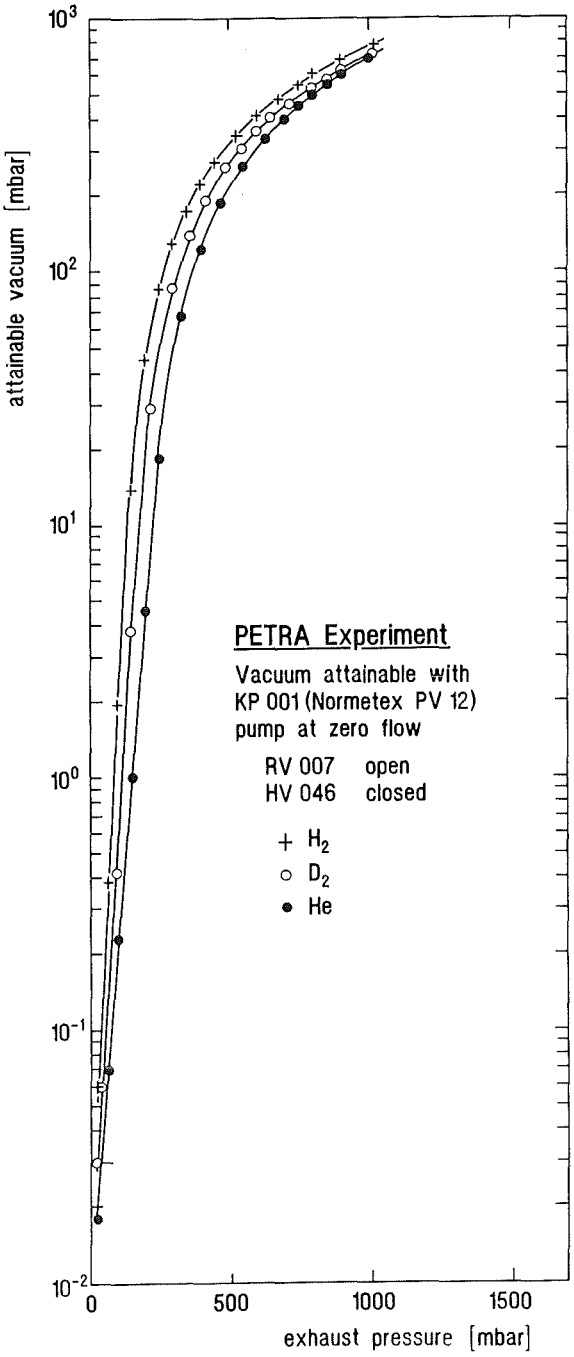

Fig. 2: Performance of the Normetex PV-12 pump

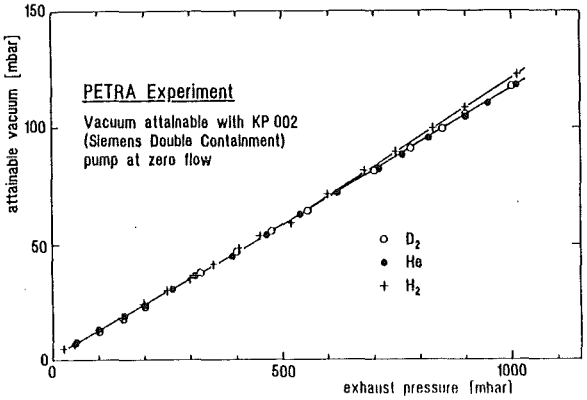

Fig. 3: Performance of the Siemens Double Containment pump

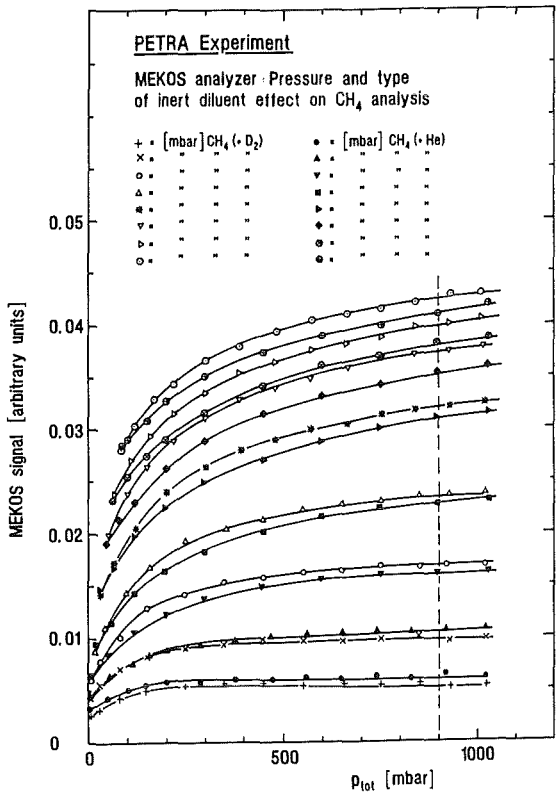

Fig. 4: Effect of pressure with the inert diluents deuterium and helium on the infrared absorption by methane

Numerous tests were carried out to investigate the interaction between TLK infrastructure systems and the PETRA experiment. They included simulation of tritium transfers into the mobile transfer station, tests with the safety system under simulation of temperature and pressure trips, function tests of the glove box, etc. The performance of the tritium retention system integrated into the glove boxes was demonstrated with molecular hydrogen and methane. The glove box cooling system was optimized under simulation of various heat loads.

Provisions to start the operation with tritium have practically been completed. First runs with tritium are anticipated for December 1994 and a full scale long-term run at the beginning of next year.

Some additional activities, complementary to the ones described above are given blow:

After completion of a comparative study at C.E.A. between a commercial permeator from Comptoir Lyon Allemand, France and a permeator supplied by Rosemound, Germany, the former was shipped to Karlsruhe. Work on the "nuclearization" of this permeator is now under way. After

adaption of the french permeator to the local requirements, the C.E.A. permeator will be tested under a tritium atmosphere in the presence of relevant impurities in the PETRA facility at the TLK.

Furthermore, two palladium/silver specimens were implanted at 300°C with 500 and 1000 ppm helium, respectively, employing the KfK dual beam machine. Cylindrical volumes in these specimens were implanted homogeneously at an implantation rate of 0.015 appm He/s. The irradiation spot obtained has a diameter of approx. 5 mm. The specimens were delivered to Ispra in April 1994 for further characterization.

Staff:

U. Bernd
E. Kirste
R.-D. Penzhorn

Subtask 2: Catalytic Cracking Process

A catalytic fuel clean-up process for the recovery of tritium and deuterium from all fusion reactor exhaust streams has been developed at IRCh. The complete process has already been proven with relevant concentrations of tritium at laboratory scale. On the basis of the results obtained the technical facility CAPRICE (*C*atalytic *P*urification *E*xperiment) was developed, and is now under operation at the Tritium Laboratory Karlsruhe (TLK) to demonstrate the process with up to 50% of tritium on a target throughput of 10 mole/h of DT and 1 mole/h of tritiated and non tritiated impurities. With respect to the current design concept adopted for ITER-EDA, CAPRICE has nearly a 1:1 scale.

Full scale experiments with hydrogen and deuterium have been completed to verify the design parameters of CAPRICE and to gain detailed knowledge on the performance of the different subsystems under a variety of experimental conditions. The first runs with about 500 Ci or 1% of tritium in deuterium are scheduled for the end of 1994.

Tests of the main palladium/silver permeator of CAPRICE, which is used to separate the impurities from the molecular hydrogen isotopes, have indicated that break-through of protium and deuterium is shifted to lower flow rates, when the feed gas contains moisture. In spite of this the nominal throughput of CAPRICE could still be attained.

To improve the present concept the following routes are being researched:

- modification of the existing facility to achieve a completely once-through operation instead of the present semi-batch process
- reduction in the number of sensitive components, e.g. the turbo molecular pump
- maximization of the overall decontamination factor, i.e. further reduction of memory effects caused by tritiated water.

A new catalyst reactor (PERMCAT) has been developed for inclusion into the catalytic conversion/permeation based plasma exhaust clean-up process. The reactor directly combines a nickel catalyst with permeation tubes and removes residual amounts of tritium from tritiated species by isotopic swamping with hydrogen at an operating temperature of about 400°C.

Figure 5 shows the basic arrangement of the PERMCAT reactor. It consists of a finger type palladium/silver membrane diffuser used to separate the pure hydrogen isotope stream from the impurity flow. Hydrogen is fed into the reactor at the bottom of the finger via a capillary placed inside of the diffuser. The impurity side is filled with nickel catalyst spheres. The catalyst employed was experimentally shown to be especially effective to promote the isotope exchange reactions between deuterium and methane. Because of the selected counter-current mode of operation the efficiency of the PERMCAT reactor is intensely high.

The PERMCAT reactor should preferably be operated downstream of a "sacrificial" nickel catalyst bed operated at about 480°C. This strictly avoids coking of the isotope exchange catalyst in the PERMCAT reactor by methane cracking or by the disproportionation reaction of a carbon monoxide to carbon dioxide and carbon.

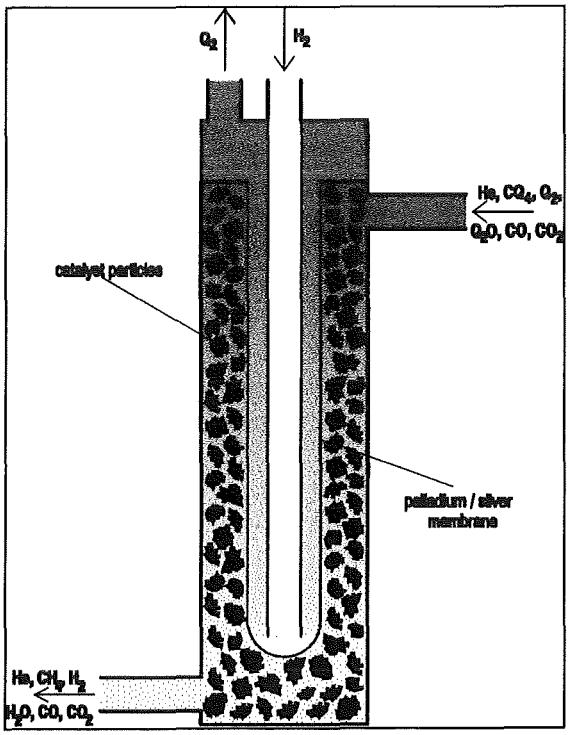

Figure 5: Scheme of the PERMCAT

A mathematical model was developed to simulate the performance of the above described PERMCAT reactor. Presently, modelling is carried out with high partial pressures of methane and molecular hydrogen isotopes to facilitate the experimental verification of the theoretical results with hydrogen and deuterium and deuterated methane.

The mathematical model assumes an instantaneous isotope exchange between impurities and molecular hydrogen on the nickel catalyst and is based on plug flow conditions. Some typical results for a PERMCAT type reactor having an effective permeation area of 1610 cm^2 (the same permeation area as of both CAPRICE permeators) are shown in Figs. 6, 7 and 8. The pressure at the impurity side was taken to be 100 kPa. The assumed flow rates at the impurity side are summarized in Table 1.

Table 1: Parameters for PERMCAT reactor calculations

Molecular hydrogen flow rate	0.003 mol/h
Molecular deuterium flow rate	0.223 mol/h
Molecular tritium flow rate	0.281 mol/h
Methane flow rate	0.230 mol/h
Chemically bonded tritium flow rate	0.255 mol/h
Total tritium flow rate	0.536 mol/h
Total impurity flow rate	4.2 mol/h

As expected, from the results in Figure 6 it is seen that the

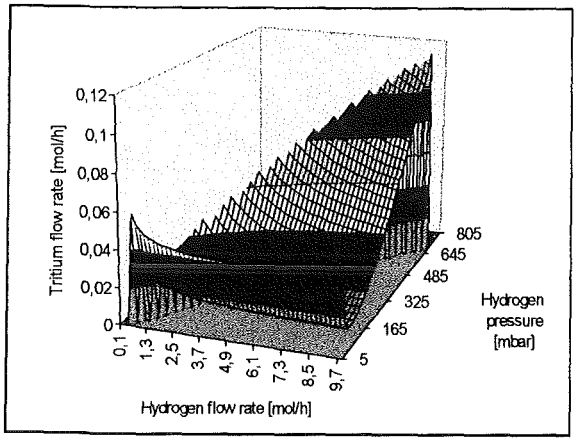

Figure 6: Trtium flow rate at the impurity outlet of the PERMCAT reactor

tritium flow at the outlet of the impurity side decreases with increasing hydrogen feed flow rates at the pure isotope side. At first sight surprising, there is an optimum hydrogen pressure at the pure hydrogen isotope side of about 100 mbar. To understand this result it must be taken into account that higher hydrogen pressures lead to a net permeation flux of hydrogen to the impurity side. The impurity gas stream becomes diluted, the driving force for tritium permeation is reduced and therefore the tritium flow rate at the outlet increases. The tritium flow rate also increases at very low hydrogen pressures because a certain minimum partial pressure of hydrogen is necessary for the isotope exchange reactions to occur. In the above discussed case the optimum hydrogen pressure is about the same as the sum of the partial pressures of hydrogen isotopes at the impurity side.

Figure 7 indicates, that more than 97% of the tritium is

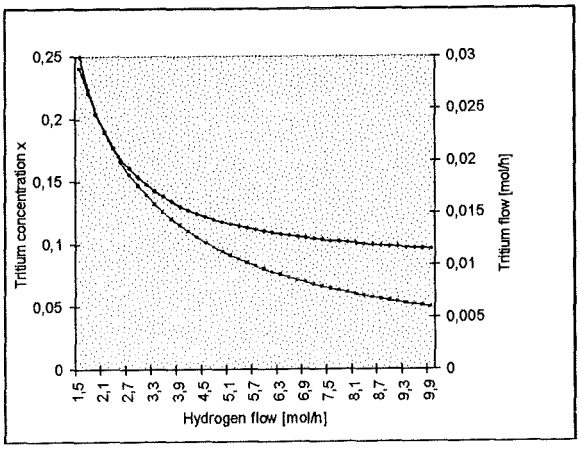

Figure 7: Trtium flow rate at the impurity outlet (upper curve, right scale) and tritium concentration at hydrogen isotope outlet (lower curve, left scale) of the PERMCAT reactor.

removed from the impurity stream, while the tritium concentration in the stream to be sent to the ISS is of the order of 10%. For the given impurity flow rates and the considered permeation surface area an adequate hydrogen feed flow rate is about 5 mol/h.

In Figure 8 the tritium flow rate along the permeation tubes is

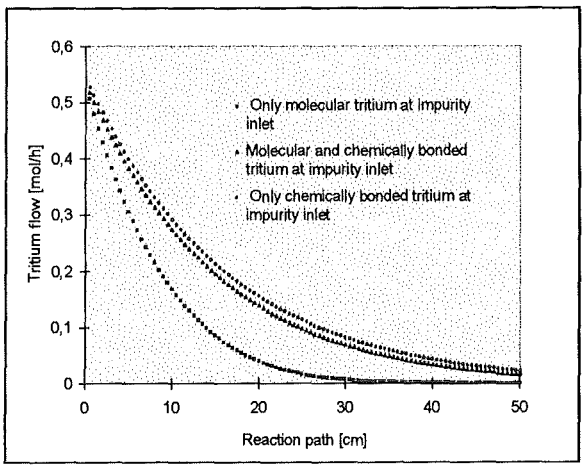

Figure 8: Trtium flow rates within the PERMCAT reactor

plotted. Clearly, molecular tritium (lowest curve) is more easily removed than chemically bonded tritium. This

underlines the necessity of a sacrificial catalyst bed followed by the permeator at the front end of the PERMCAT reactor.

Physical separation of tritium contaminated sections of the PERMCAT reactor from sections with little or almost no tritium contamination is important to minimize memory effects and hence to achieve a high degree of overall decontamination.

An outline of the flow diagram of CAPER, the advanced once-through catalytic exhaust clean-up process proposed for ITER-EDA, is presented in Fig. 9. According to the current design of ITER, 90% of the hydrogen isotopes from the plasma exhaust stream are directly recycled into the torus. The remaining molecular hydrogen isotopes are separated from impurities by a diffuser having a permeation surface area of 0.22 m^2. Downstream of the permeator a small buffer tank is placed to smooth the gas flow. The impurity processing loop is continuously fed; it comprises a nickel catalyst and a permeator and is operated at high circulation flow rates compared to the feed flow rate.

A continuous bleed stream, which mainly contains helium, carbon oxides and some residual molecular as well as chemically bonded tritium is processed through the PERMCAT reactor. Before the gas is finally sent to waste it is passed through another permeator that removes the remaining hydrogen isotopes.

A once-through operation is of particular advantage to achieve high tritium availability and low tritium inventories. With proper process conduction high overall decontamination factors can be accomplished. In addition, a turbo molecular pump is no longer required. The PERMCAT is presently being designed for the operation in a tritium environment and at technical scale. The upgrade version of the "classical" catalytical process concept has been designated CAPER; it gives due consideration to the requirements of ITER-EDA.

Staff:

M. Glugla
K. Günther
T.L. Le
W. Leifeld
R.-D. Penzhorn
K.H. Simon

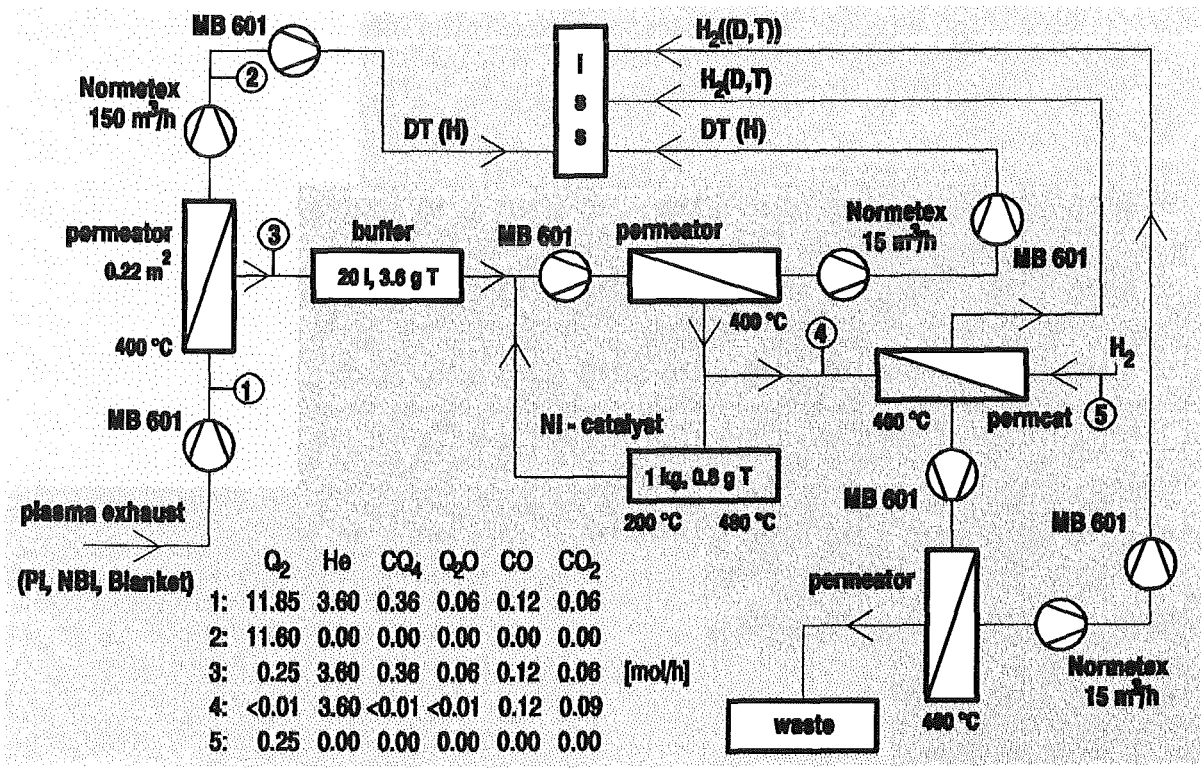

	Q_2	He	CO_4	Q_2O	CO	CO_2
1:	11.85	3.60	0.36	0.06	0.12	0.06
2:	11.60	0.00	0.00	0.00	0.00	0.00
3:	0.25	3.60	0.36	0.06	0.12	0.06
4:	<0.01	3.60	<0.01	<0.01	0.12	0.09
5:	0.25	0.00	0.00	0.00	0.00	0.00

Figure 9: Flow sheet of CAPER, the advanced catalytic clean-up process for ITER-EDA

TEP 3 Tritium Storage and Transportation

Several intermetallic compounds (IMC) that react with molecular hydrogen to yield hydrides with low dissociation pressure a room temperature have been suggested for the storage of tritium. Conceivably, some of these IMC's could also be used for the fast removal of gaseous tritium from a facility during a pressure excursion. Prior to their application in tritium installations, however, they must be characterized with respect to a number of relevant properties. One such property is the gas/solid reaction rate.

The kinetics of the sorption of molecular hydrogen by ZrCo, La $Ni_{4.7}Al_{0.3}$, and $Zr_{0.8}Ti_{0.3}Mn_{1.9}$ was investigated and as a function of temperature at several constant pressures of hydrogen. For the experiments either a "conventional" technique and/or a reactor designed for measurements under near-isothermal reaction conditions, whereby the contribution from the exothermicity of the hydrogen/IMC reaction to the measured rate is minimized. Constant hydrogen pressures were achieved with a fast flow pressure regulator valve.

The sorption rate of hydrogen by zirconium/cobalt at a hydrogen pressure of one bar and isothermal conditions was observed to be much faster than that under non-isothermal conditions. To determine the mechanism of the quasi-isothermal reaction of H_2 with ZrCo the experimental results were fitted to a number of well known gas/solid rate laws. Depending upon the hydrogen pressure three regions were identified (see Fig. 1): a first region at pressures below 25 mbar, a second region at pressures between 25 and 200 mbar and a third one at pressures above 200 mbar. As illustrated in Fig. 2 at p_{H2}>200 bar bar a dissociative hydrogen chemisorption on the metal surface is rate limiting and the best fit is obtained with a mechanism of nucleation with two-dimensional growth. As a result of the change in reaction mechanism the rate constant decreases by a factor of more than 1000 when the hydrogen pressure decreases from 1 to 0.002 bar. At small initial hydrogen pressures an activation energy of approx. 13 kJ/mol was determined using experimentally obtained initial reaction rates with ZrCo.

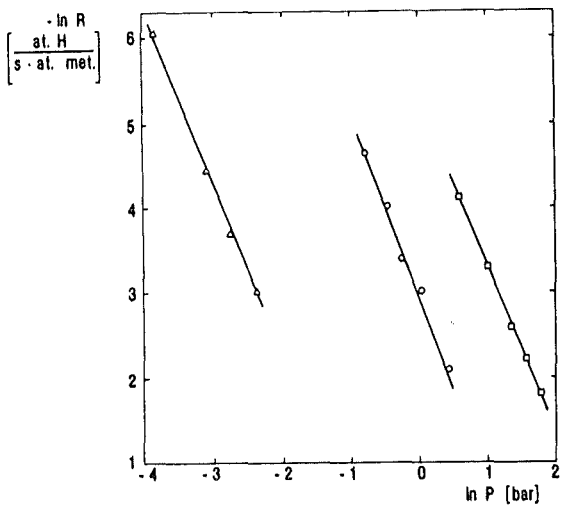

Fig. 2: Comparison between experimental kinetic data for the reaction of molecular hydrogen with ZrCo at 300 K at various constant pressures with result obtained by calculation using known gas/solid laws, i.e. 1) first order chemical reaction or contracting volume, 2) nucleation with two dimensional growth, 3) nucleation with three dimensional growth, 4) two dimensional diffusion and 5) three dimensional diffusion.

A comparison between the isothermal hydrogen sorption rates by ZrCo, $Zr_{0.8}Ti_{0.3}Mn_{1.9}$ and La $Ni_{4.7}Al_{0.3}$ is given in Fig. 3. The hydrogen sorption rate of all three IMC's shows a quadratic dependence from hydrogen pressure.

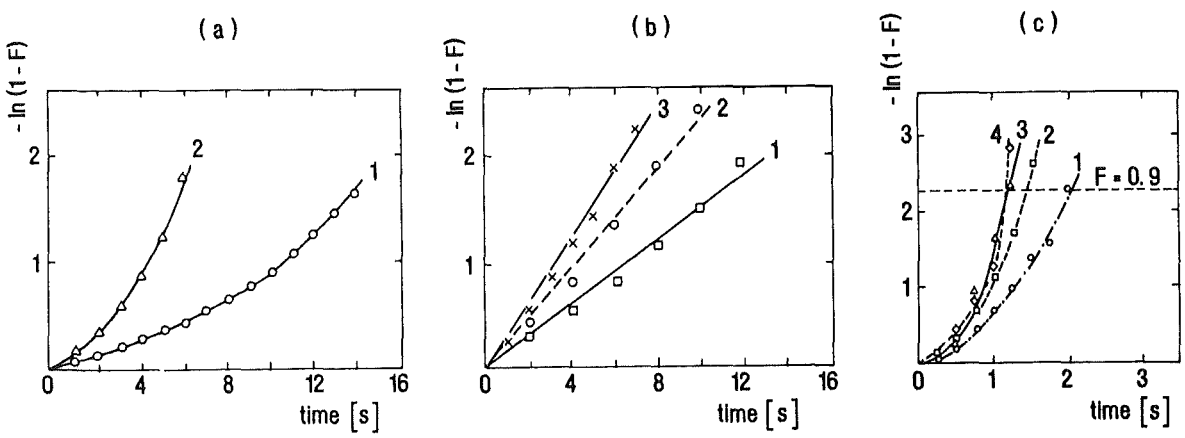

Fig. 1: Kinetic data (F is reacted fraction) for the reaction of hydrogen with ZrCo at 300 K at several constant pressures: a) P=0.004 bar, 2. P=0.006; 1. P=0.05 bar, 2. P=0.07 bar, 3. P=0.10 bar and c) P=0.40 bar, 2. P=0.60 bar, 3. P=0.80 bar, 4. P=1.0 bar.

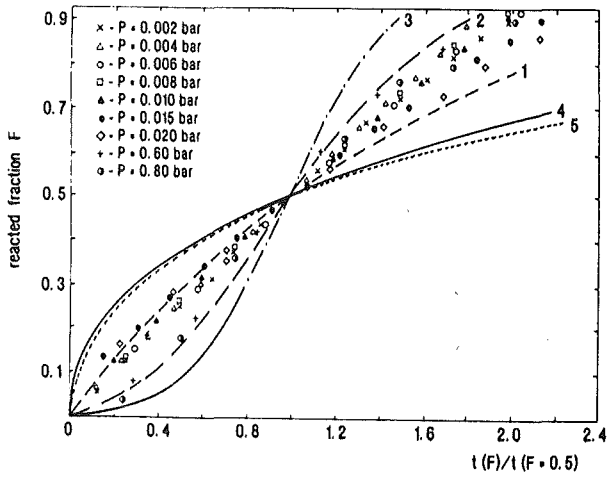

Fig. 3: Pressure dependence of the rate of hydrogen absorption by Δ ZrCo, O $Zr_{0.8}Ti_{0.3}Mn_{1.0}$, and □ $LaNi_{4.7}Al_{0.3}$ at a constant temperature of 300 K.

Staff:

R.D. Penzhorn

A.N. Perevezentsev (guest scientist)

M. Sirch

E. Willin

TRIT-1 Tritium Supply and Management: Calorimetric Measurements

Standard calorimetry is a widely used method in tritium accountancy. Because of the very short penetration of the soft beta rays of tritium a quantitative measurement of the decay heat of tritium, i.e. 324 mW/g, is possible by this technique.

Using two different calorimeters, one developed at KfK, Karlsruhe and one purchased by ETHEL, Ispra, the tritium stored in four commercial Amersham uranium beds loaded with different amounts of tritium (range 0.1 – 2.5 g) were measured. Both calorimeters were calibrated periodically using electrical heat sources that simulate the configuration of the U-beds examined calorimetrically.

With the isothermal microcalorimeter developed at KfK 3 – 4 measurements of extended duration were performed, with each of the four uranium beds. The time of measurement was within the range $59.75 < t < 69.75$ h. Under these conditions and after correction for the decay of tritium ($\lambda = 1.54 \cdot 10^{-4} \pm 5.4 \cdot 10^{-8}$ d^{-1}) the inventories were determined with standard deviations of the order of only 0.009 – 0.09%.

Manufacturer of the isothermal calorimeter of ETHEL was Antech, Ascot, England. In this calorimeter a constant temperature profile is maintained towards its periphery, the temperature of the outer mantle being above that of the room. When a heat source is introduced into the chamber of the calorimeter the temperature control of the calorimeter reduces the heat supply to the inner mantle and keeps the temperature profile constant. The reduction in heat power supply is used by a custom made software, which allows the prediction of the tritium inventory with an accuracy of 2 – 3% after less than half an hour. After 2 – 3 hours an equilibrium fit can be obtained which delivers measurements with an absolute standard deviation smaller than 2 mW. When measurements of longer duration were performed, i.e. >1.6 hours, the standard deviation could be reduced to 0.5 mW.

The intercomparison of the results obtained with the two calorimeters using common tritium samples was highly satisfactory. From the data is is concluded that calorimetry constitutes an important non-destructive tritium management method.

Staff:

H. Kapulla
R. Kraemer
R.D. Penzhorn

NDB 1 Neutronics Data Base

Subtask 1: EFF Development

The objective of this task is the development of a reliable nuclear data base for neutron transport calculations of fusion reactors. To this end nuclear cross-section data evaluations and improvements as well as calculational data tests against integral benchmark experiments are being performed in the framework of the European Fusion File (EFF) project. Within this programme KfK contributes to nuclear cross-section improvements of structural materials in the resonance region and to data test analyses for shielding, structural, breeding and neutron multiplying materials.

Predictability of fluctuations in structural material cross-sections

For the steel components Fe, Cr, Ni resonance parameters are precisely known below a neutron energy of about 0.8 MeV and are included in the data files used in neutron transport and shielding calculations. No resonance parameters are available above 0.8 MeV, but it is well known, and for Fe confirmed by recent high resolution measurements made at Geel, that resonance effects persist and must be included in shielding calculations. The important question is at what energy they become negligible.

In co-operation with CBNM (Central Bureau for Nuclear Measurements) Geel the observed fluctuations were compared with fluctuations calculated from Monte Carlo sampled resonance ladders based on level statistics. Observed and computed fluctuations agree fairly well, see Fig. 1. Furthermore, nuclear reaction theory shows total cross-section variances at zero temperature to be proportional to the difference between compound nucleus formation and resonance-averaged nonelastic cross-sections. Therefore, the variances can be obtained analytically from optical model and Hauser-Feshbach calculations, only higher moments require Monte Carlo methods, see Ref. 1. For structural materials, for

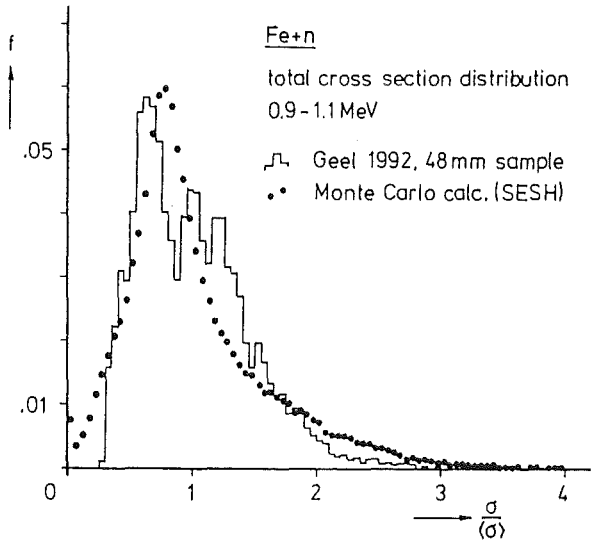

Fig. 1: Experimental and Monte Carlo generated total cross-section distributions for iron around 1 MeV

which Doppler broadening is unimportant, total cross-section fluctuations can thus be predicted quite reliably above the resolved resonance region. For Fe it is found that the relative standard deviations due to fluctuations drop below 10% only above 4 MeV, in agreement with the Geel high-resolution data, see Fig. 2.

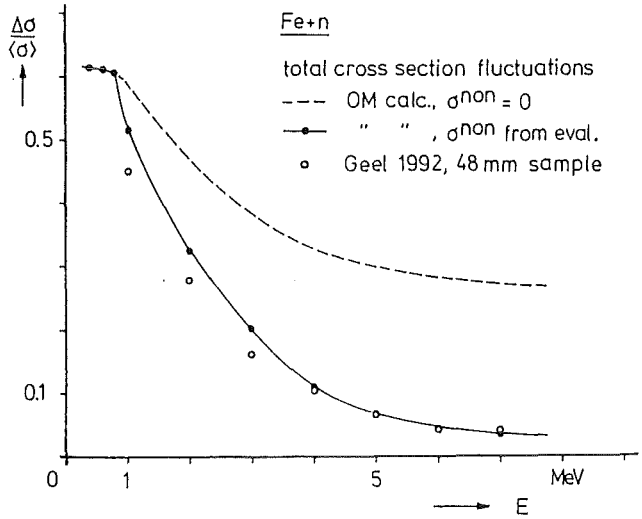

Fig. 2: Experimental and calculated relative standard deviations of the total cross-section distribution of iron. The impact of the inelastic threshold at 0.86 MeV is clearly visible.

EFF benchmark analyses for neutron multiplication and breeding materials

The objective of this sub-task is to validate cross-section data of the latest EFF-2 file for neutron multiplication and breeding materials. To arrive at this goal a three-stages approach is followed. At the first stage the EFF-2 cross-section data are processed and compared with ENDF/B-VI and evaluated data of other sources as well as measured ones. At the second stage transport calculations are performed for simple and clean benchmark problems using different transport codes and cross-section data. At the third stage transport calculations are performed for available 14-MeV neutron transmission experiments. C/E-type information is obtained from the comparison of calculated and measured neutron leakage spectra. Along with the results of the first two stages this information provides the basis for checking and further improving the EFF-2 cross-section data.

A detailed study on the beryllium data evaluations of EFF-1, EFF-2 and ENDF/B-VI has been performed, see Ref. 2. The processed secondary energy and angle distributions (SED/SAD) were compared to each other and to measured differential data. Remarkable differences were found with a strong impact on the neutron transport in beryllium. In particular for EFF-2 there are severe discrepancies with measured double-differential cross-sections at several secondary energy and scattering angles which call for a revision of the evaluated SED/SAD.

Neutron transport calculations were performed for beryllium spherical shell assemblies with the ONETRAN-code using the SN/PL-approximation in the conventional way and the ANTRA1-code applying a direct numerical scheme for the scattering integral without the need to use Legendre polynomials. There is a slight disagreement between the leakage spectra obtained by rigorous ANTRA1- and approximative ONETRAN/PL-calculations for material assemblies with thicknesses of several mean free paths which means that the solution of the S_N/PL - calculation does not converge towards the exact one. The impact of the different beryllium data evaluations, however, is more severe. There are observed very different shapes of the calculated neutron leakage spectra reflecting both the different SED/SAD of the used beryllium data evaluations and the (n,2n) - cross-section which is higher in EFF-1 by about 10% as compared to EFF-2 and ENDF/B-VI, see Fig. 3.

At the third stage transport calculations were performed for 14-MeV neutron transmission experiments on beryllium spherical shells conducted at IPPE Obninsk, KfK and the OKTAVIAN facility (University of Osaka). From the comparison with the analysed integral experiments a preference for the EFF-1 beryllium data evaluation can be deduced (see e. g. Fig. 4 for the KfK KANT experiment). This is in agreement with both the findings of the SED/SAD data tests against differential measurements and computational analyses of total absorptions experiments performed at Idaho National Engineering Laboratory (INEL). This includes a preference for the higher (n,2n) cross-section used in the EFF-1 beryllium data evaluation. With regard to the more recent EFF-2 beryllium data there is a need to improve the SED/SAD and to critically check the (n,2n)-cross-section which is the one of the ENDF/B-VI evaluation.

Literature:

[1] F. H. Fröhner, Proc. International Conference on Nuclear Data for Science and Technology, Gatlinburg, USA, 1994 (in print)

[2] U. Fischer, E. Wiegner: Benchmark analyses of the ENDF/B-VI, EFF-1 and EFF-2 beryllium data evaluations for neutron transport calculations, 3. International Symposium on Fusion Nuclear Technology, Los Angeles, June 27 - July 1, 1994

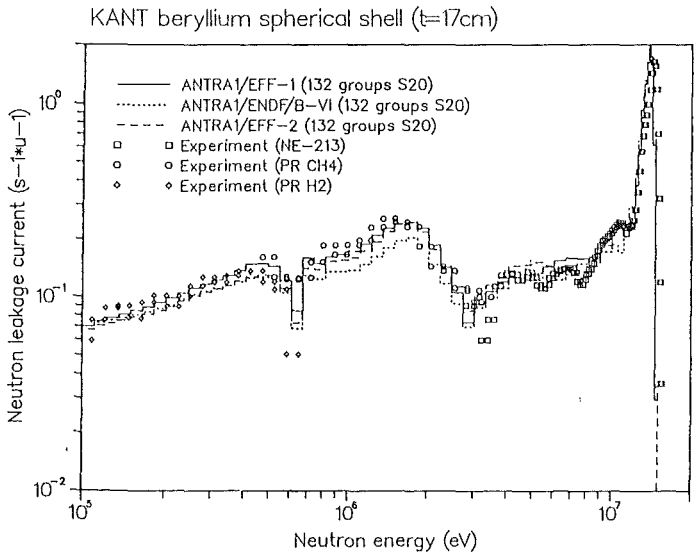

Fig. 3: Secondary energy distribution of ^{9}Be(n,2n) at 14 MeV incident neutron energy: Comparison between evaluated and measured data.

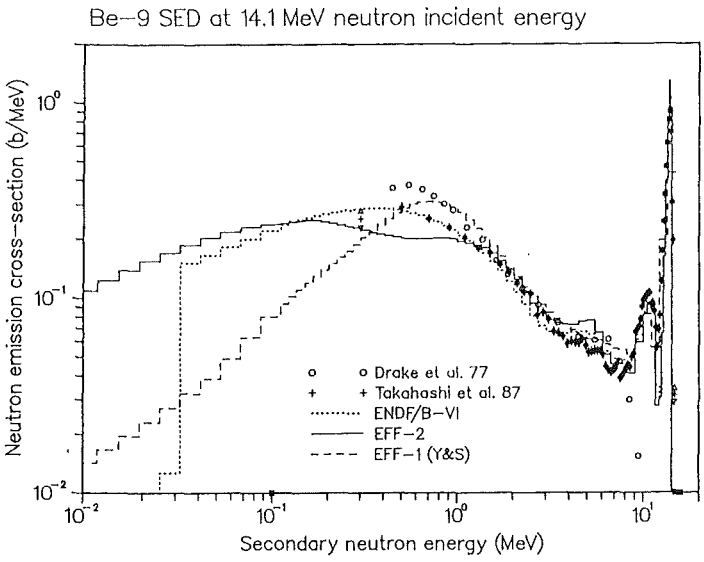

Fig. 4: Calculated and measured neutron leakage spectra of the KfK KANT beryllium shell experiment.

Staff:

U. Fischer
F. H. Fröhner
E. Wiegner

Subtask 2: Shield Penetration Experiments

For fusion reactors as ITER efficient shielding of the superconducting magnets from neutron and photon radiation is one of the problems to be solved in the field of neutronics. The limits formulated for the fluence of fast neutrons in the coils, the number of atomic displacements in the stabilizer, and the nuclear heating in the magnet [1] are determined by the neutron and photon fluxes penetrating the shield blanket. The blanket has several ducts and gaps. The main element of the structural material is Fe. Therefore, Fe slab-assemblies with a gap and without gap were investigated. The thickness of the slabs and the gap geometry were optimized [2] so that the neutron and photon fluxes ($\phi_n(E)$ and $\phi_y(E)$) penetrating the assembly after irradiation with 14 MeV neutrons are sensitive to both the nuclear data of Fe and streaming through the gap.

The geometry of the arrangement is outlined in Figure 5. The Fe slab has a front area of 100 cm×100 cm and a thickness of 30 cm. The distance between source and detector is 349 cm, between source and slab 19 cm. Gap positions are x=10 cm and x=20 cm. The width is b=1 cm and b=5 cm.

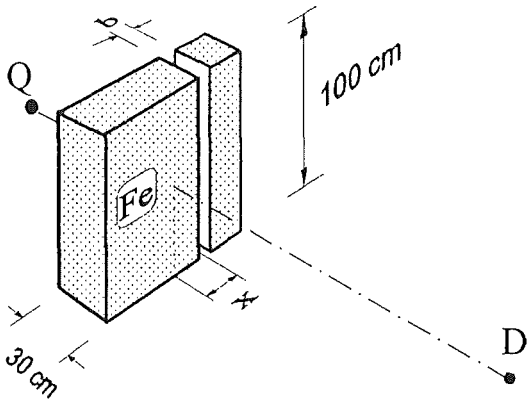

Fig. 5: Geometry of the experiment. Q - neutron source, D - detector, x - gap position, b - gap width

Pulse-height distributions taken from a liquid scintillator (NE 213) are transformed to $\phi_n(E)$ and $\phi_y(E)$ [3,4] for 1 MeV $<E_n<$15 MeV and 0.2 MeV$<E_y<$8 MeV, respectively. The neutron flux for energies E<1 MeV is measured by use of hydrogen-filled proportional counters [5].

To test calculational tools for shielding ϕ_n and ϕ_y are compared with Monte-Carlo-calculations (code MCNP-3B [6], coupled neutron-photon transport) based on the data of the European Fusion File EFF-1 [7].

The measured and the calculated flux spectra for the Fe assemblies with gap parameters b/x=0/0, 5/10 and 5/20 (cm/cm) are presented in Fig. 6. The results for 1/10 and 1/20 are systemically in between.

The $\phi_n(E)$ for E>5 MeV increase systematically from the assembly 0/0 over 5/20 to 5/10. This trend is described. Even the differences of the ϕ_n from the assemblies agree relatively well with the calculated differences. However, for all assemblies the total value of ϕ_n is underestimated. In Ref. [8] is discussed that the forward-peaked neutron emission in this range has to be taken into account for a better description. The largest streaming is measured and calculated for the assembly 5/10 compared to 0/0 in the range of 14 MeV peak.

For E<1 MeV the $\phi_n(E)$ from the three assemblies agree as expected by the calculations. A significant surplus of neutrons is measured compared to the calculated spectra for E<0.2 MeV from all assemblies. It seems to be described. However, from all of the three assemblies the total photon flux is significantly underestimated what may be in conjunction with the more forward-peaked neutron transport compared to the calculation [8].

These investigations were extended to angular fluxes from the assembly which are more sensitive to forward-peaked neutron emissions. The structural material SS316 is used instead of Fe.

Literature:

[1] W. Dänner, ITER Expert Meeting on Shielding Experiment and Analysis, Garching (FRG), 1990, ITER-IL-5-0-5 (1990).

[2] T. Elfruth et al., in Fusion Technology 1992, p. 1341, ed. by C. Ferro, M. Gasparotto and H. Knoepfel, Elsevier Science Publishers, Amsterdam, 1993.

[3] S. Guldbakke et al., in Reactor Dosimetry ASTM STP 1228, ed. by H. Farrar et al., American Society for Testing and Materials, Philadelphia, 1994.

[4] L. Büermann et al., NIM A332 (1993) 483.

[5] D. Albert et al., Kernenregie 20 (1977) 95 and Kernenergie 21 (1978) 82.

[6] J.F. Briesmeister (ed.), Report Los Alamos N.L., LA-7396 (1986).

[7] H. Gruppelaar, Report EFF-Doc-46, Petten.

[8] W. Hansen et al., Proc. Int. Conf. on Nuclear Data for Science and Technology, Gatlinburg (USA) 1994.

Staff:

F. Freiesleben
W. Hansen
D. Richter

K. Seidel
S. Unholzer

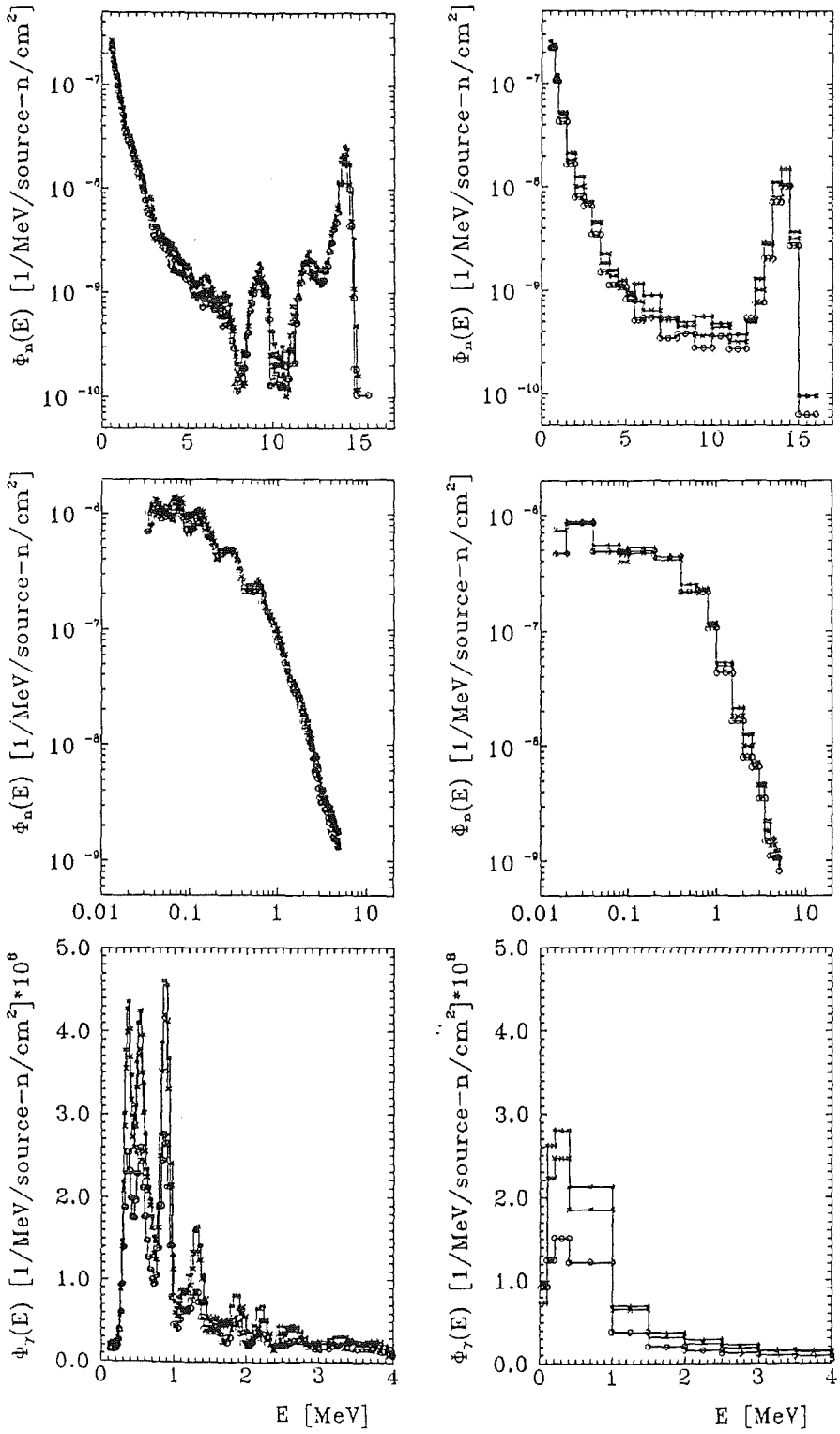

Fig. 6: Measured (left hand) and calculated (right hand) flux spectra for the assemblies with gap parameters b/x(cm/cm) = 0/0 ($_o$), 5/10(*) and 5/20($_x$). a) neutron flux in the high-energy range (upper part), b) neutron flux in the low-energy range (middle part), c) photon flux (lower part).

T 16 Preparation of Neutronics Experiments and Measuring Technologies

1. FENDL-1 Data Validation

The KfK task on FENDL-1 data validation is a sub-task of the ITER R&D task T16. The objective of this task is to qualify and validate FENDL-1 data for shielding and other materials of importance for the ITER design.

The Fusion Evaluated Nuclear Data Library FENDL is a compilation of fusion-oriented data files selected from the nuclear data ENDF/B-VI (USA), BROND (Russian Federation), JENDL (Japan) and EFF (European Union) in an international effort initiated and co-ordinated by the IAEA Nuclear Data Section. The FENDL data file will serve as reference library for design calculations in the Engineering and Development Activities (EDA) phase of the ITER project. Prior to its use in design calculations there is a need to validate the FENDL data base for the relevant fusion reactor materials.

In a first step FENDL validation analyses have been performed for beryllium, lead, iron and copper using the then available multigroup data processed by IAEA/NDS , see Ref. 1 and 2. A three-stages approach has been followed in the data validation analyses comprising checks of the processed FENDL data against other evaluations and against differential experiments, neutron transport calculations for simple clean benchmark problems using different transport methods and codes, and, finally, computational analyses of suitable 14-MeV neutron transmission experiments. In this step, benchmark experiments in simple geometrical configurations - spherical shells with a central 14-MeV neutron source - and one single material were preferred to facilitate the identification of possible deficiencies and/or discrepancies. The selected benchmark experiments were performed at the OKTAVIAN facility (University of Osaka), IPPE Obninsk and KfK. Cross-checking was performed with ENDF/B-VI and EFF-data again applying different computational tools.

In a second step the FENDL multigroup library processed by the Los Alamos National Laboratories (LANL) was used in the data test analyses as this will be the working library for ITER EDA design calculations. In addition, data test analyses were performed for Al, Si, Li and Zr making again use of IPPE Obninsk and OKTAVIAN transmission experiments on spherical shell assemblies, see Ref. 3.

The major results of these analyses may be summarised as follows. For the most important fusion reactor materials the analysed FENDL data have reached a high quality level that allows their reliable use in fusion neutronics applications. In particular the analysed lead and copper data call for only minor improvements. For iron there is a systematic underestimation of the calculated neutron leakages below 1.5 MeV that may be caused by overestimated neutron absorptions due to missing resonance shielding in this energy region. For beryllium improvements of the secondary energy-angle distributions are recommended: in particular there is a strong underestimation of inelastically backward scattered neutrons in the FENDL data. In addition, a preference can be deduced for a higher (n,2n) cross-section as it is used in the EFF-1 evaluation. Based on the results of the analyses both for iron and beryllium further integral experiments in spherical geometry were recommended. Such experiments presently are well underway.

For secondary priority fusion reactor materials (e. g. Al, Si, Zr) the data quality in general is not satisfactory. Figs. 1 and 2 reveal that Si and Zr are primary candidates for improvements in the forthcoming version 2 of the FENDL data file.

Literature:

[1] U. Fischer, E. Wiegner: FENDL benchmark analyses at KfK, IAEA Advisory Group Meeting on Review of Uncertainty Files and Improved Multigroup Cross-section Files for FENDL, Tokai-mura, Japan, November 8 - 12,1993.

[2] U. Fischer, E. Wiegner: FENDL data testing for beryllium, lead, iron and copper, 3. International Symposium on Fusion Nuclear Technology, Los Angeles, June 27 - July 1, 1994

[3] U. Fischer, E. Wiegner, H. Tsige-Tamirat: Status of FENDL data test analyses at KfK, IAEA Advisory Group Meeting on Improved Evaluations and Integral Data Testing for FENDL, Garching, Germany, September 12 - 16,1994.

Staff:

U. Fischer
H. Tsige-Tamirat
E. Wiegner

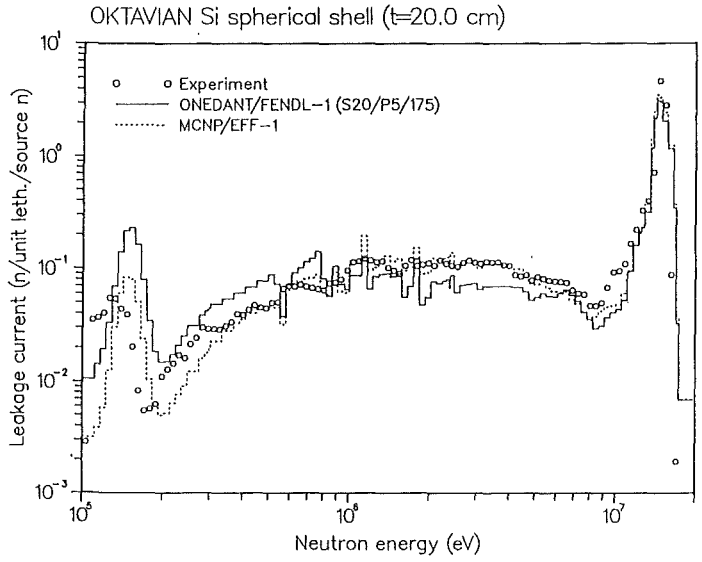

Fig. 1 : Calculated and measured neutron leakage spectra of the OKTAVIAN silicon shell experiment.

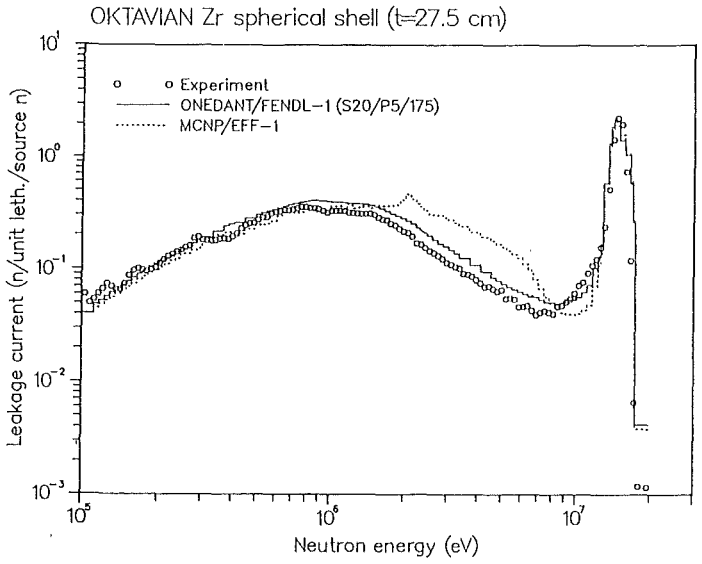

Fig. 2 : Calculated and measured neutron leakage spectra of the OKTAVIAN zirconium shell experiment.

2. Development and Demonstration of Experimental Techniques for Nuclear Heating Measurements

This is a contribution to a joint effort with ENEA Frascati and CEA Cadarache, where thermoluminescence dosimeters and gamma chamber techniques are used for nuclear heating measurements [4].

The objective is to develop methods for measuring heating induced by neutrons and photons with such a high sensitivity that in a blanket model mock-up at positions close to (or in) the material simulating the superconducting coils measurements are possible even with moderate neutron source strength.

Two new methods are investigated. They are based on:

- scintillating optical fibers [5]
- silicon hybrid-minisensors.

1. Scintillating fiber method

Two photomultipliers are coupled to both ends of a scintillating fiber. The energy deposition inside the fiber caused by a traversing particle is determined by the energy-proportional pulses of the left and the right photomultiplier. The position of impact can be derived from the time difference between the signals of both detectors.

The experiments were carried out with the polystyrene-based fiber (5×5 mm^2, 1.2 m length) BICRON BC-408.

For the calibration of the energy scale minimum ionizing electrons were used, characterized by a nearly energy independent value for the energy loss dE/dx in the fiber.

The overall time resolution amounts to typical values of 1.1 ... 1.2 ns (FWHM) which yields a position resolution along the fiber of ± 8.5 ... 9.5 cm.

The experimental arrangement of first measurements is shown in Fig. 3. 14 MeV neutrons from a DT-neutron generator hit the front of the iron slab and produce a neutron/photon radiation field. The fiber is positioned behind the slab at the same height as the neutron source.

Various measurements were carried out with the fiber embedded in iron or polyethylene (PE). The material of the bed and its dimensions were chosen similar to the geometry of the planned test arrangement at Frascati Neutron Generator which consists of alternating layers of steel and Perspex. The dimensions were: 2.0×2.0 cm² for the Pe-bed and 2.5×2.5 for the iron-bed.

The measurements were carried out at a neutron source strength of the order of 10^8 neutrons per second. Typical measuring times were about 20 minutes for the collection of more than 500.000 events.

Significant differences of the spectra collected before, during and after irradiation were registered. It shows the high sensitivity of the method and demonstrates its applicability for after-heating measurements, too.

To understand the measured spectra in detail supporting Monte-Carlo simulations with the code MCNP-4 [6] were carried out. Coupled neutron-photon-electron transport in the real geometry of the measurements is taken into account.

In Fig. 4 an experimental spectrum representing the total energy deposition in a fiber embedded in PE is compared with the calculated share of this distribution caused only by (n,p)-scattering. Evidently for energies above approximately 7 MeV the energy transfer is produced completely by this process. Differences at lower energies are conjectured to arise from photon absorption and (n,α)-reactions on carbon.

In order to determine the amount of nuclear heating quantitatively, the measured spectra have to be extrapolated below the experimental threshold of approximately 800 keV proton energy. Therefore the exact knowledge of the shape of the spectra in the low-energy region has to be determined by simulations including all contributing energy transfer processes. Then the total energy deposited in the fiber is known. This value is pretty close to the nuclear heating in an equivalent volume of Perspex or water.

In addition it will be transformed into nuclear heating in an equivalent Fe-volume. Therefore the ratio of Fe-/PE-heating was already calculated by use of the corresponding KERMA-factors.

2. Silicon minisensor method

A minisensor was tested for the application in gamma-heating measurements in fusion neutronics experiments. The detector from VacuTec Dresden is an integrated chip of dimensions $0.55 \times 0.9 \times 3$ cm³ consisting of a semiconductor Si-detector, charge sensitive preamplifier, pulse amplifier and discriminator. The sensitive volume of the detector is $0.5 \times 0.5 \times 0.03$ cm³. The employment of such detectors is very useful because of its high detection sensitivity, small volume and simple application.

The detector was irradiated with photons from Cs-137- and Co-60-sources for energy calibration and for estimation of the detector response. In Fig. 5 the pulse-height spectra are compared with MCNP-4-calculations.

In a second step this detector was surrounded by iron or polyethylene, placed behind the iron wall assembly as described above and irradiated in the neutron-photon field (see Fig. 3). The measured pulse-height spectra are compared with calculated ones. The energy release from gamma-heating is determined by integration of the measured pulse-height distribution and extrapolation to $E=0$ using the calculated responses.

The ratios of heating in Fe/Si and PE/Si were calculated with the KERMA-factors.

The investigations are in progress; especially the uncertainties of the methods have to be investigated.

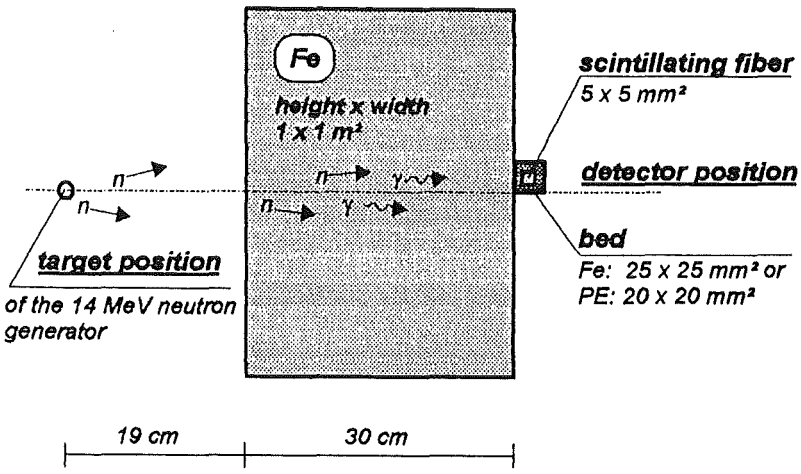

Fig. 3:
Experimental arrangement for the measurement behind a solid iron-block

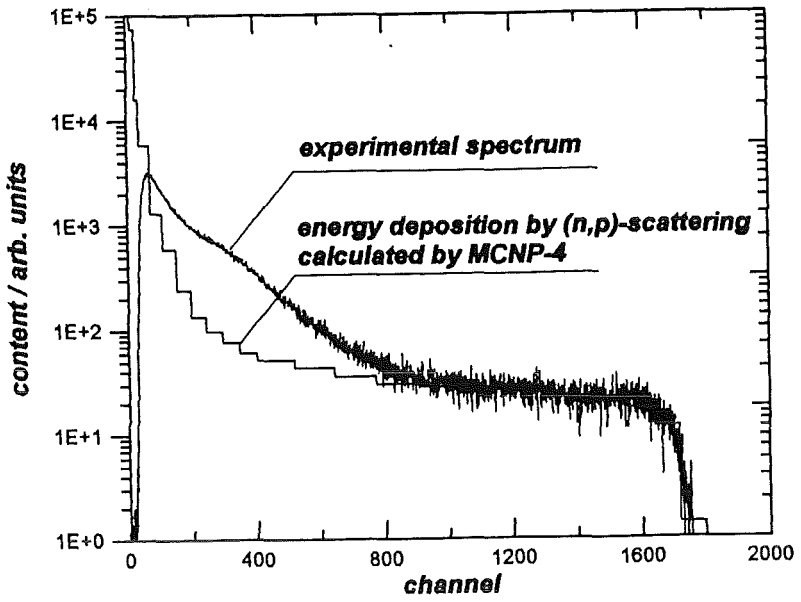

Fig. 4:
Comparison of measured and calculated spectra for the energy deposition inside the fiber (PE-bed)

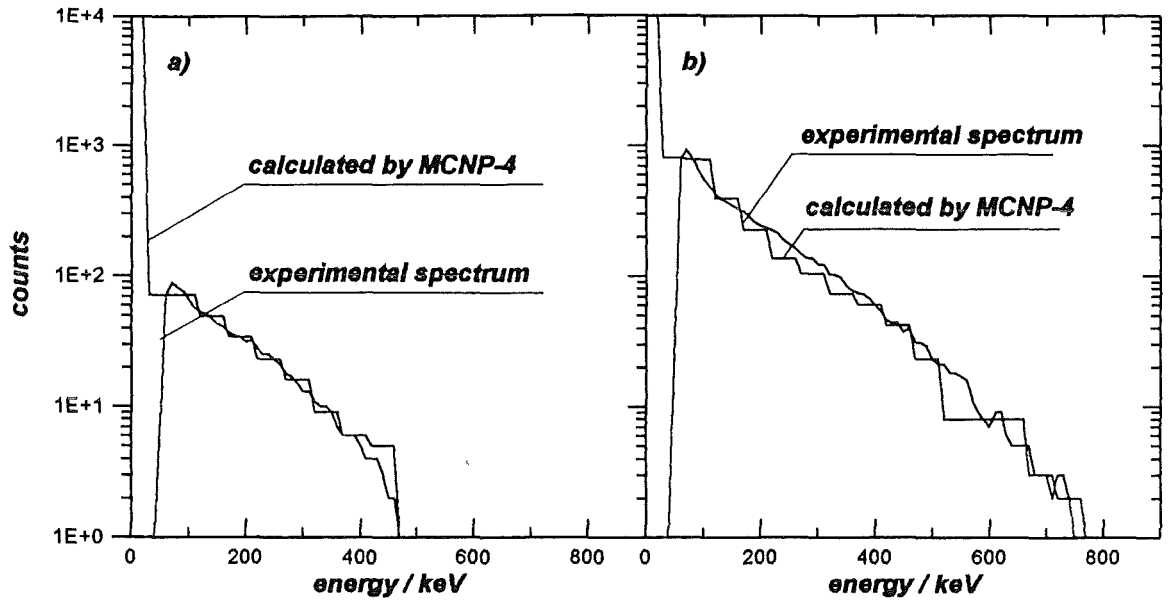

Fig. 5 Comparison of experimental and calculated pulse-height distributions for irradiations from Cs-137 (a) and Co-60 (b)

Literature:

[4] M. Martone et al., Report EFF-DOC-261 (1993)

[5] H. Freiesleben et al., Report EFF-DOC-302 (1994)

[6] J.F. Briesemeister, MCNP - a general Monte Carlo code for neutron and photon transport, LA-7396, Los Alamos (1986)

Staff:

H. Freiesleben
K. Merla
D. Richter
K. Seidel
S. Unholzer

Remote Handling / Maintenance

Introduction:

Due to the activation of most components of a fusion reactor, all operations of inspection, maintenance, connection and disconnection, assembly and disassembly will have to be carried out remotely from the very start of the machine. Hands-on or semi-remote maintenance will be possible only in limited areas and for some peripheral components.

The maintenance of the in-vessel components has been identified as a key problem. The equipment for in-vessel maintenance will have to operate under extreme conditions of radiation and temperature. The large variety of operations to be carried out requires versatile and replaceable tools attached to different work units with large lifting capabilities. The high availability targeted by NET / ITER will require that in-vessel operations have to be carried out with relatively high speed.

Most of the KfK work concentrates on the development and qualification of an in-vessel handling unit (IVHU) with an articulated boom transporter (ABT) and different work units (task RHT 1). This system is primarily, needed for the maintenance or replacement of in-vessel components during short term interventions.

The Experimental Device for In-Torus Handling EDITH is the prototype of this system. It is required to demonstrate that the maintenance of plasma facing components can be carried out with the anticipated reliability and time. It is also needed to optimize the IVHU components and subassemblies and to test different control algorithms.
EDITH is a full scale ABT, supplemented by a full scale mock-up simulating the upper half of a torus sector. The hardening of sensitive IVHU components for NET/ITER typical temperature and radiation levels is being performed in close cooperation with SCK/CEN Mol within EC Task T35.

Task RHT 1 includes now also the further development of a remote handling workstation (RHWS) which can be applied to different remote handling tasks for fusion plant maintenance (former task RHB 1-2).

Most of the work performed within the former task RHS 1 of the 1989-91 programme to standardize and qualify basic machine components for remote handling and to develop remote techniques to assemble and dissassemble these items has been finished, e.g.:

- Electrical connectors (RHS 1-1),
- Pipe connectors (RHS 1-2),
- Fluid connectors (RHS 1-3),
- Welded connectors (RHS 1-4) and
- Welded vacuum lip seals (RHS 1-5).

In 1992-94 KfK concentrated its efforts on the development and qualification of cutting and welding tools for cryo-connectors (EC Task T 43, former subtask RST 2).

A. Fiege

RHB 1 RH Common Subsystems

Subtask 2: Remote Handling Workstation Development

The goal of this task is the development of a general purpose remote handling workstation (RHWS) which can be applied to different remote handling tasks for fusion plant maintenance. The work is based on a NET study contract whose results are documented in [1]. The remote handling workstation supports the operator during task preparation, training, and execution. It also is used as a procedure documentation tool. The RHWS provides the main-machine interface and operational support tools [2]. The RHWS consists of three subsystems (fig. 1) which are connected but which also may be used stand-alone. PEXOS (Procedure Editing, Simulation, Execution, and Monitoring System) is a multimedial electronic handbook interacting not only with the operator but also with the other subsystem and the remote handling devices thus coordinating the whole work according to the planned procedure. The procedures are graphically visualized by action/state networks and described textually, by drawings, photos, video sequences, operator remarks, and KISMET animations. KISMET (Kinematic Simulator, Monitor, and Programming Environment for Tele-manipulation) provides the three-dimensional spatial information for motion planning and monitoring. KISMET device models can be used as master devices for manual control. The DOIF subsystem (Device Operating Interface) provides the graphical operating interfaces for manual device control and monitoring and facilitates manual control of a device or a device group by a macro programming feature. The RHWS is being applied to the EDITH experiment (see task RHT 1) and the EU-TELEMAN-INGRID project for controlling a telemanipulation cell in the Sellafield reprocessing plant.

The RHWS was continuously enhanced according to the experience in the applications. Major subtasks were: (1) subsystem, (2) video overlay facility for KISMET allowing the operator to identify and correct interactively modelling errors, (3) enhancing user friendliness of PEXOS and DOIF, (4) development of a special PEXOS subsystem for instructing the master-slave manipulator operator and coordinating his work, (5) prototypical redesign and implementation of the DOIF subsystem, especially the macro programming feature.

In the context of the remote handling procedure development at JET a KfK delegate applied KISMET which proved to be essential not only in offline feasibility studies and strategy planning, but also during actual remote handling operations. For example: offline studies on KISMET models influenced the design of remote handling equipment for the MARK II divertor exchange. KISMET was employed in the preparation of the successful A2-antenna installation during shutdown work in November '93, where the TARM robot was used for the first time for ex- and in-vessel work. KISMET supplied the main online information for the MASCOT operator during the pumping chamber door mock-up test. Furthermore KfK implemented a camera-control systems operating interface for JET which works reliably controlling five different low-level camera control stations. On the basis of a written procedure documentation the port opening procedure was modelled with PEXOS to demonstrate its usability. PEXOS was evaluated positively by the JET RH group.

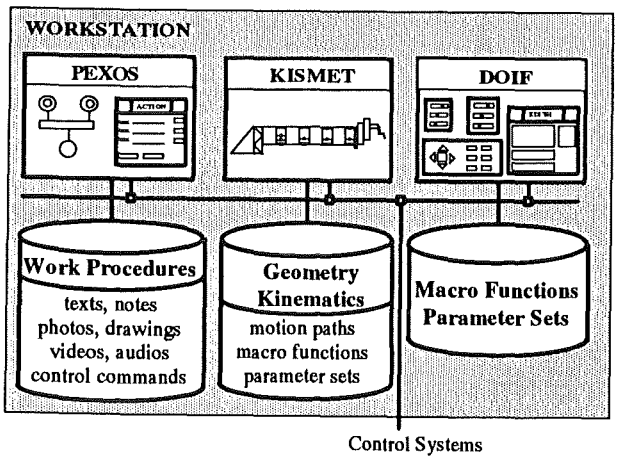

Fig. 1: Architecture of the remote handling workstation

Literature:

[1] K. Leinemann: NET Remote Workstation, KfK-Bericht 4785, KfK, Karlsruhe, Oct. 1990

[2] K. Leinemann, F. Katz, H. Knüppel, W. Olbrich: Synthetic Viewing: Comprehensive Work Representation Making Remote Work more transparent to the Operator. ISFNT-3, 27.6.-1.7.1994, Los Angeles, CA, USA

Staff:

B. Haist
F. Katz
H. Knüppel
U. Kühnapfel
H.G. Krumm
K. Leinemann

RHT 1 Articulated Boom Transporter

Subtask 2: EDITH Prototype Articulated Boom

The objective of this subtask is the qualification of the EDITH prototype in full remote conditions. Testing is being performed with a manipulator end-effector carrying lightweight tools for delicate tasks (e.g. for armour tiles replacement (Fig. 1 or Be-spray) and with a special purpose end-effector to simlate handling of heavy payloads up to 1 ton (e.g. divertor plates or bumper limiters). Operations are simulated in a vessel sector mock-up, scale 1-1, with remote viewing facilities [1 – 3].

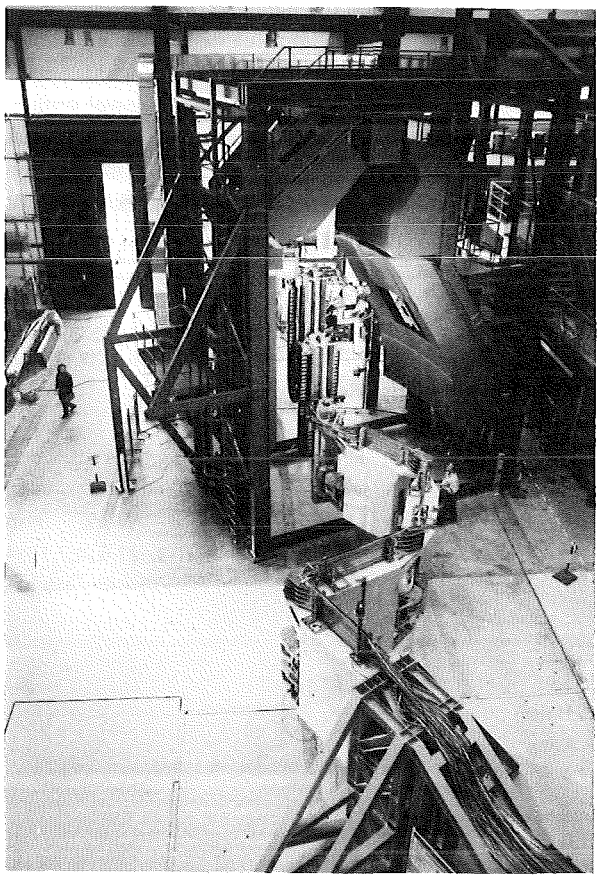

Fig. 1: Articulated boom replacing protective tiles located in the upper torus region of the mock-up

EDITH is being controlled via a multipurpose RH workstation (RHWS).

In continuation of the work performed during the last periods of reporting [4 – 7] the assembly and commissioning of the ABT and the mock-up has been completed in the Remote Handling Laboratory of KfK [8]. Static and dynamic qualification tests have been carried out. The mock-up has been prepared for the demonstration of tile replacement.

Mechanics of the ABT

The ABT (Figure 2) consists of four links which are attached via a cantilever arm to the support structure. At the front link the end-effector positioning unit (EEPU) is mounted which again can be equipped with different end-effectors like the manipulator handling unit (MHU) as a multi-purpose unit or special end-effectors devoted to specific tasks. For the tile replacement the MHU is applied. As an interim end-effector it combines two different electric master/slave manipulators which were available at KfK. The manipulators are connected by means of an adaptation unit which compensates their different geometry and provides an additional roll joint. Between the EEPU and the adaptation unit the manipulator positioning unit is installed which has an additional yaw joint; thus allowing to work with the manipulators radially to the torus. Two overview cameras equipped with pan-and-tilt-heads and two operation cameras mounted at camera arms are part of the viewing system. The system is supplemented by four lamps. The light intensity is variable.

Guidance and Control System

To support the operator in remote task performance a guidance and control system was developed and installed in the EDITH control room providing two working places one for co-ordination and assistance tasks and the other for manual work with servo-manipulators (Figure 3). The overall architecture is shown in Figure 4.

The guidance system is represented by a remote handling workstation (RHWS) [9,10], standard TV monitors, and the master systems of two master-slave manipulators. The RHWS provides the non-conventional man-machine interface and operational support during planning, training, and execution of procedures. The analysis of maintenance procedures showed that three types of maintenance task abstractions are sufficient and convenient for a comprehensive operational support: the representation and simulation of the procedures (handbook information), the representation of the working space geometry including motion paths, and the representation of the device functions. The RHWS consists of three subsystems according to those three aspects: PEXOS (Procedure Editing, Simulation, Execution, and Monitoring System), KISMET (Kinematic Simulator, Monitor, and Programming Environment for Telemanipulation),and DOIF (Device Operating Interface). The RHWS was developed in the task RHB1 and applied to EDITH and the TELEMAN-INGRID project. The work in the last period concentrated on an suitable set-up of the guidance system and its preparation and usage for the various EDITH experiments, especially the tile handling.

The control system is hierarchically organised and consists of a management system (program and parameter management, teach/repeat functions, safety functions), the path control for EDITH, and the camera system control. Main research topic in this area was the fast, precise, and safe motion of the transport arm.

There have been several improvements in the control system. As first one, the dynamic behaviour of the ABS has been enhanced, by implementing a control algorithm, evaluating the deflection of joint gears with respect of joint and motor

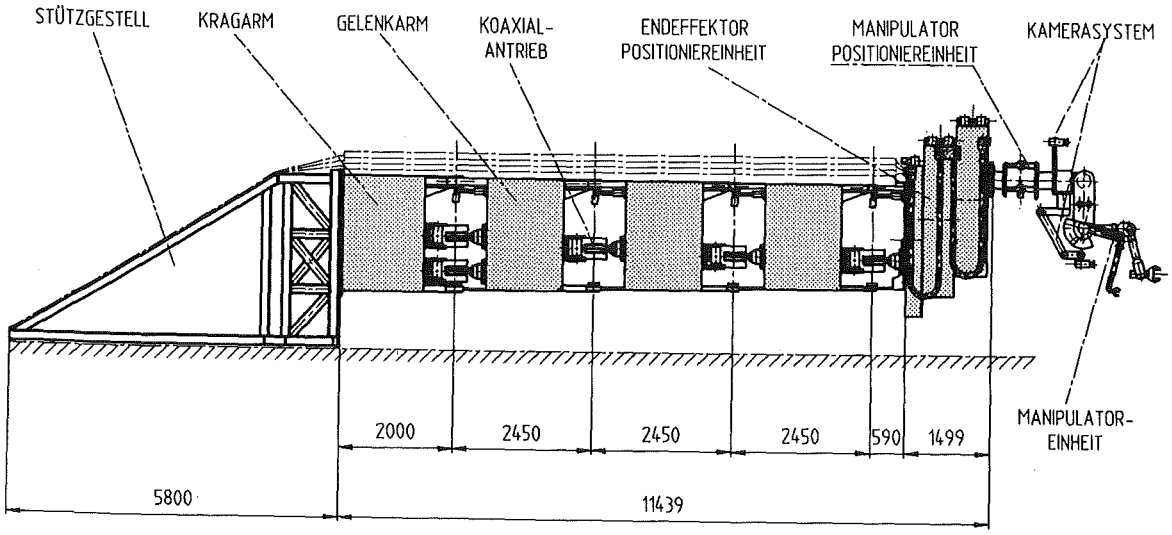

Fig. 2: The articulated boom transporter

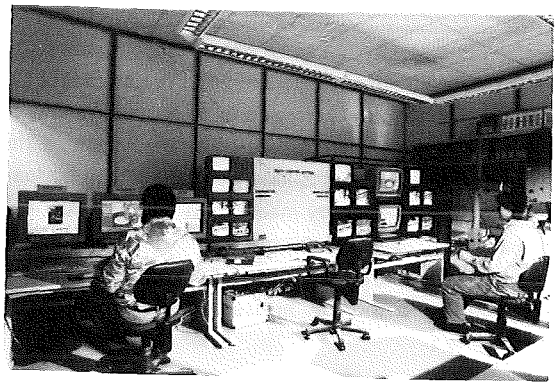

Fig. 3: EDITH control room

positions. Simulations of a state space control design have been processed with success and shall be implemented for handling of heavy loads to improve the accuracy of spatial movements. Also there have been changes to allow the operator a direct access to spatial move commands, which allows him to position the ABS with a higher position accuracy.

With respect to the validation of the dynamic model of the ABS, there has been implemented a fast data acquisition system to record important dynamic system data. Also there has been realized a new monitoring interface, which transfers the position data much faster to the kinematic simulation system KISMET. So it is possible to transfer position data up to the sample rate of the position controller, i.e. 50Hz.

Static and Dynamic Qualification Tests

Within the frame of the ABT qualification the following tests have been performed:

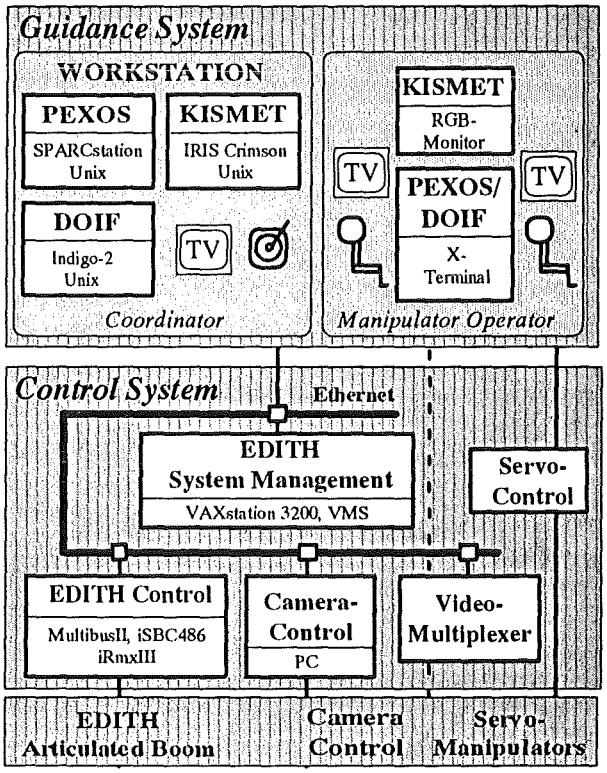

Fig. 4: Architecture of the EDITH guidance and control system

- Static and dynamic load tests to validate the stress analysis and to determine the deflection under load
- Tests to determine the positioning and repeating accuracy
- Experiments to determine the horizontal stiffness to improve the positioning accuracy and the backlash removal of the drive units

- Dynamic load tests in horizontal and vertical direction to achieve data for the validation of the dynamic simulation.

Validation of the stress analysis

Stress measurements using strain gauges and strain gauge rosettes, respectively, have been performed at four link positions in order to determine the maximum load conditions. The measurements have been compared with the results of the stress calculations. The investigations included the straight position of the articulated boom and three positions forming angles where always only one joint (Z2, Z3, Z4) has been forming a knee of 90°.

First static measurements have been carried out at unloaded conditions followed by measurements with an equivalent load of 2200 kg. The equivalent load has been corresponding to a payload of 1000 kg completed by a factor of two for the dynamic influence and additional 200 kg for missing add-on pieces. The evaluation at the lower pressure hinges showed a satisfying compliance with the calculations. At the side walls of the links B1, B2 and B3 the measured bending stresses were too small whilst the shear stresses were too high compared with the calculation. The smaller bending stresses resulted from the assumption of a linear stress distribution between the upper and the lower link chords. More precise calculations performed meanwhile show a strong increase of the bending stresses at the upper and the lower edges of the side walls.

For this reason a strain gauge rosette has been positioned at the lower edge of the link B2 side wall for dynamic measurements. The unloaded articulated boom has been loaded with an additional weight of 200 kg and has then been loaded by 1000 kg which became abruptly free via an electric lifting magnet. The measured stresses at the pressured hinges were comparable with those of the static tests. As to be expected the pressure stress at the side wall of the link B2 has been higher than those at the static measurements and is comparable with the calculated value. On the other hand the shear stress has been smaller. Thus the assumed factor for taking into account the dynamics is in accordance with the stress amplitude under load.

Positioning and repeating accuracy

There have been performed tests that evaluated the repetition accuracy of the Articulated Boom System (ABS). Several movements have been executed repeatedly. The end position of each movement has been measured via the joint resolvers, which are integrated in the ABS, and additionally with an external measurement system. The results gained with the external measurement system have met the specification of the ABS, which was specified as 5mm. The positioning error calculated via forward transformation of the joint resolver values has been much smaller (2mm). The comparison of both results showed, that the differences have been bigger than those, which can be explained with the finite resolution of the resolver system. During further experiments the reason of these differences has been detected as a backlash in the resolver system of about 5×10^{-4} rad. In the worst case, i.e. if the ABS is extended and all the measurement errors add themselves to the greatest error, there must be expected a repetition error of about 14mm, which is mainly (10mm) caused by backlash.During all the experiments such a big error never could be measured. So the probability of it seems to be rather small, but theoretical considerations let seem them to be possible. As measure, the reduction of the backlash to a value of 2 resolver digits may be possible by constructional changes. So the error caused by backlash may be reduced to a theoretical value of about 4mm.

Horizontal stiffness

The horizontal elasticity is caused by

- the drive unit elasticity,
- the drive unit backlash, and
- the joint backlash.

The horizontal elasticity has been determined at a straight position of the ABT. For the measurements the boom tip has been loaded by horizontal forces up to 1 kN orthogonally to the boom orientation in steps of 0.2 kN. The forces at the torque arms of the drive units have been measured by load cells, the boom deflection by means of a laser pointer and scaled marks on the floor. During the test campaign the motors of the drive units were out of operation and their brakes have been locked. The measurement arrangement is shown in Figure 5.

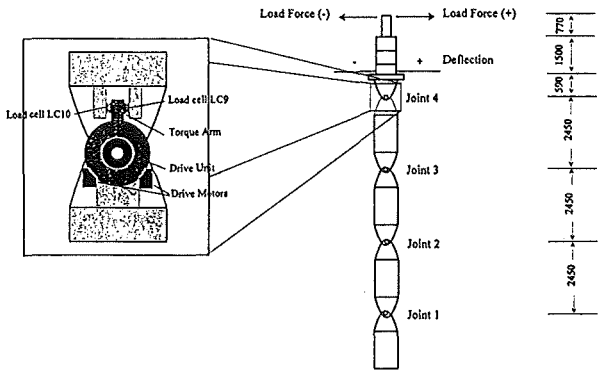

Fig. 5: Measurement arrangement for the horizontal stiffness

The measurement results which are summarized in Table 1 have shown that

- the measured deflection has been approximately twice the calculated one which was based on external measurements at the drive units

- the drive unit backlash is important, and

- a reduction of the torque arm restraint backlash would improve the stiffness substantially.

First tests have shown (Figure 6) that it is possible to reduce the backlash by preloading the drives and by compensating the resulting air gap at the torque arm restraint by fillers. Thus it should be possible to compensate the backlash at the torque arm restraints totally and to achieve a total deflection of about 90 mm.

Validation of the dynamic simulation

The AMBOSS dynamic simulation system has been described already in the previous report and - more detailed - in [8]. One outstanding task has been the validation of the dynamic model that is used in the simulation. This validation is to be performed by comparing simulation results with the data measured during the dynamic qualification tests described above.

Actually, the former dynamic simulations used a model of the ABT which did not comply totally with the experimental conditions. In particular, the EEPU was replaced either by a preliminarily designed model or by a heavy dummy mass. In other simulations, the actual EEPU has been investigated separately, but there has been no combined model of the ABT together with the EEPU.

For comparing simulation results with measured data, the simulation model needs to represent the actual experimental configuration as close as possible. Therefore, the dynamic model had to be re-arranged to the combined model of ABT and EEPU. This task is just now underway. First results that can be compared to the measured data are expected within a few weeks, and the full validation evaluation will be available at the end of 1994.

Subtask 3: Divertor Plate and Armour Tile Handling

Objective of this subtask is the design, manufacture and commissioning of armour tiles and divertor plates handling equipment. The equipment has to be tested, followed by the demonstration of the tile and divertor plate replacement in the mock-up.

Armour tile replacement

For the demonstration of armour tiles work sites in the upper half of the torus mock-up have been arranged. According to the requirements the tiles were fixed by studs and conical nuts. For the replacement two special tools were fabricated, a tile detachment device (TDD) and a tile positioning device (TPD) [7]. Both have been handled with the manipulator handling unit of the ABT. The TDD combines a gripper and two tubular drills, the TPD a gripper and two screw drivers to fasten the plate. The magazines for tools and tiles have been arranged at the floor of the mock-up. The supply lines for the tools were not routed at the ABT. In a final version the supply lines will have to be integrated with the consequence that tools and manipulator will have to be remotely connectable

Table 1: Measured and calculated (in brackets) boom deflections

	Joint 1	Joint 2	Joint 3	Joint 4	Σ
Deflection in mm due to elasticity	40 (24,5.)	31 (26)	11 (10)	2 (1,2)	84 (61.7)
backlash of drive unit and torque arm restraint	23 (2.6)	26 (1.8)	5 (1)	1 (0,2)	55 (5.6)
Total deflection in mm	63 (27.1)	57 (27.8)	16 (11)	3 (1.4)	139 (67.3)

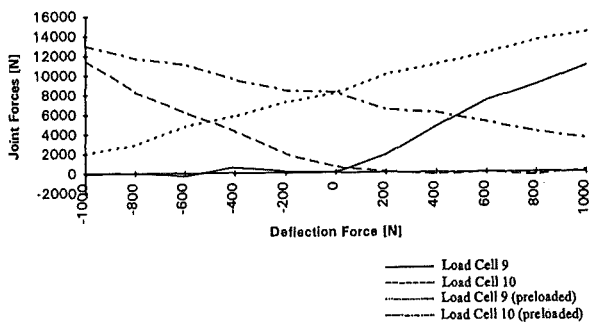

Fig. 6: Comparison of reacting forces at the torque arm of joint 4 under preloaded and not preloaded conditions. The air gap at the torque arm restraint is eliminated.

in order to allow the tool exchange inside the plasma chamber.

The tests were performed remotely without direct view by two operators from the control room. The ABT and the viewing system has been controlled by the co-ordinating operator, the MHU and the tools by the manipulator operator. The main operation steps and the required equipment are listed in Table 2.

During the planning and preparation phase of the tile exchange task the whole procedure was modelled by PEXOS and KISMET. Furthermore the EDITH transportation tasks and the camera positions and viewing directions for the different working positions were taught-in and needed device macro functions were developed using the DOIF system to facilitate application dependent controlling. Video sequences, textual descriptions, photos, and drawings of all relevant working steps were produced and integrated. At the end of these preparation not only a complete multimedia documentation was available but also an executable high-level program

Table 2: Operation steps and required equipment for tile replacement

Operation steps	Required equipment
Grasping the tile to be replaced and trepanning the nuts (Figure 7)	Manipulator handling the tile detachment device
Transfer of the removed tile to a waste magazine for tiles	Manipulator handling the tile detachment device
Removal of the studs and transfer of the removed studs to a waste magazine for studs	Manipulator, no special tools
Picking up of spare studs and positioning them in slots of the first wall.	Manipulator, no special tools
Grasping a spare tile from a magazine and its positioning	Manipulator handling the tile positioning device
Fastening the spare tile	Manipulator handling the tile positioning device

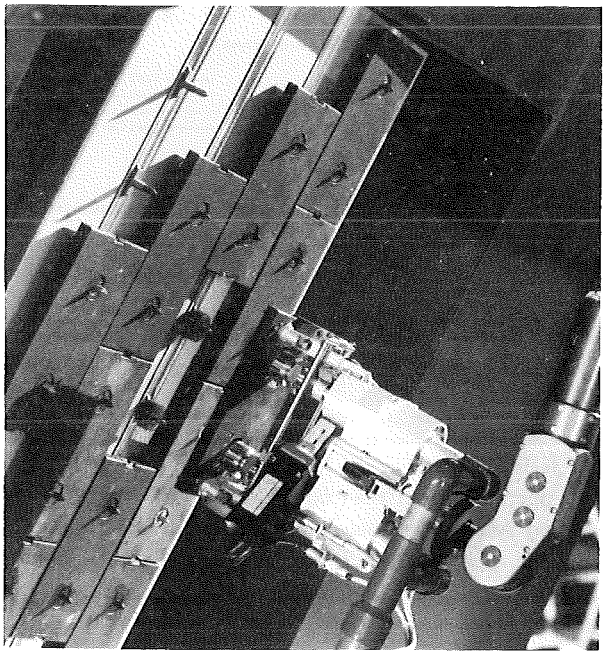

Fig. 7: Tile detachment device with removed tile. At the first wall remained the studs with the nuts and small rings of the divertor plate.

integrating all agents of the task including the operators. During the task execution PEXOS leads the operators step-by-step through the procedure which is visualized graphically by a network of actions and states. The transportation tasks are directly started via PEXOS by the co-ordinating operator and they are monitored using the DOIF subsystem and KISMET. Camera control is reduced to one operator request and probably needed small corrections. The servo-manipulator operator is integrated into the system via a computer screen displaying subtask working instructions and requesting for confirmations of the start and termination of the manual work. Both operators can call for describing information and notices at any time. To cope with unforeseen situations the control system allows to intervene, to leave the planned procedure, and to rejoin it afterwards. Figure 8 shows the PEXOS screen with the graphically visualized tile handling procedure.

Results of the tile handling

For the tile replacement the electric master-slave manipulator EMSM2-B has been used as a multi-purpose handling unit in combination with the TDD and the TPD. The second master-slave manipulator EMSM3 supported the EMSM2-B by carrying the waste storage and the magazine for spare studs.

The trajectories of the ABT to the different pre-defined working positions have been pre-programmed and performed in an automatic mode. The articulated boom could be moved with full speed; the positioning accuracy and repeatability were in accordance with the requirements.

The working sequences for the tile replacement have been carried out by the manipulator operator using the master arm and the integrated viewing system. The replacement did not make any difficulties. The special tools worked well.

The tiles were fixed at the wall with a distance of about 5 mm. The trepanning depth resulted from the plate thickness plus 2 mm and was limited by limit switches. The electrical connections have been sensitive for graphite dust and the trepanning part for different inclinations of tile and handling device.

The camera system was sufficient for working. Nevertheless, some improvements at the camera system are desirable. In particular these are:

- Optimised camera arm lengths to improve the view and to determine the inclination of the wall better which is especially important for fastening the tiles and for the trepanning.
- More powerful motors and changed gear ratios at the camera arms to reduce the time to position the cameras.
- Identification and elimination of a software failure at the camera arm control which did not allow the simultaneous movement of both camera arms.

The complete procedure was successfully co-ordinated and controlled via the remote handling workstation and made possible the reliable and continuous work flow by a combination of manual and automatic operations. The RHWS also provides a comprehensive documentation of the

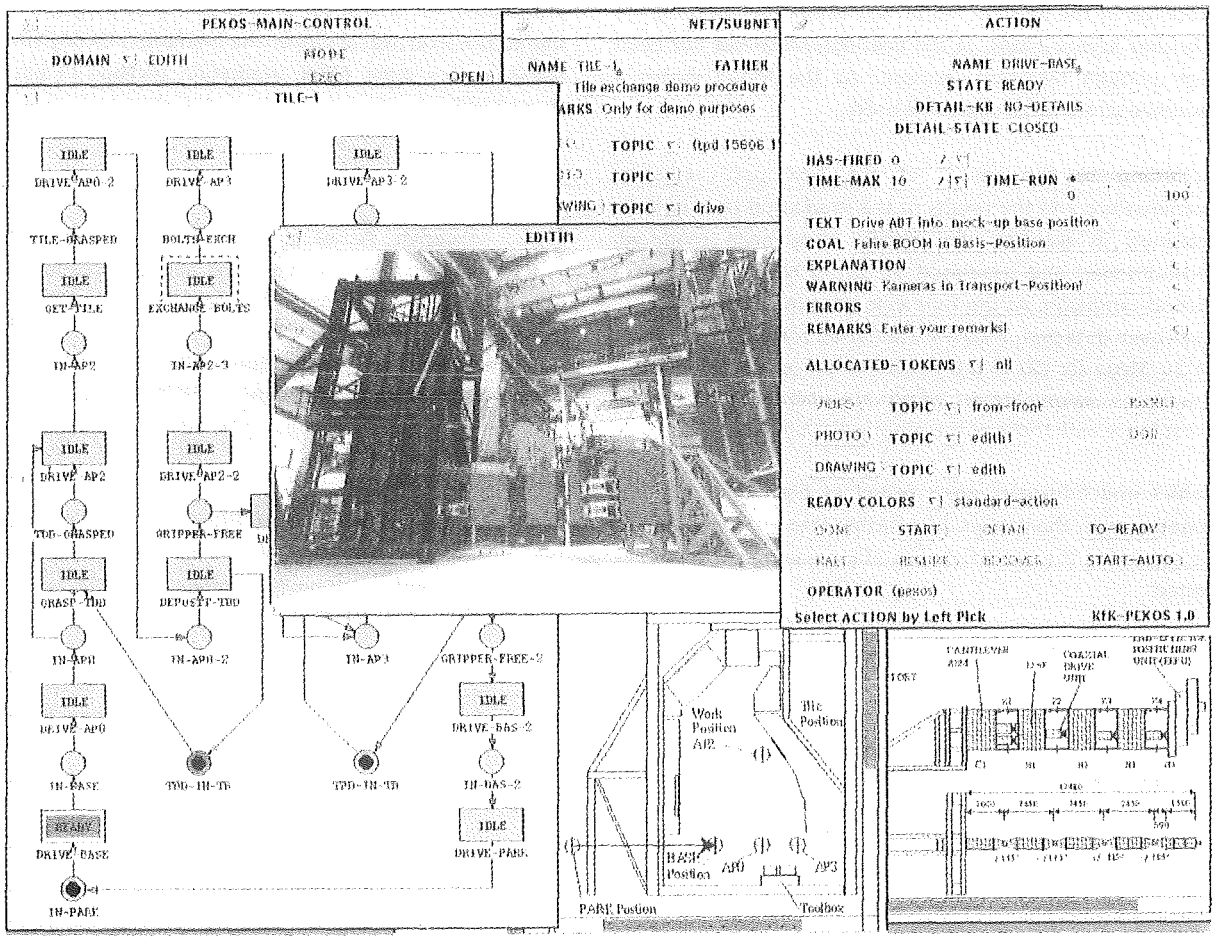

Fig. 8: Example of the PEXOS screen for the tile handling procedure.

procedure including texts, operator remarks, drawings, photos, video sequences, graphical animations, and procedure step related device control commands for the transporter and the camera control system. This documentation guarantees a repetition of the procedure with the same quality.

The required time for the replacement of one tile was approximately half an hour. The most time consuming sequences have been the positioning of the cameras and the trepanning. An improvement could be possible by a modification of the camera system and an optimisation of the trepanning gear ratio to increase the speed of the forward feed.

For the demonstration original tiles and nuts were used which were fabricated from carbon fibre reinforced graphite. Only the studs were fabricated from steel, otherwise the studs would have been to weak. The tests have been performed at daylight as well as in complete darkness using only the camera lightning. In both cases the replacement time was almost the same.

Divertor plate handling

Concerning the divertor plate handling pre-tests without a divertor handling unit are planned for the end of 1994 with the aim to demonstrate the suitability of the ABT to handle loads up to 1 ton safely and reliably. For this purpose a full scale divertor dummy, a simplified device for taking over the dummy and a rack for the storage of the dummy were designed, ordered and will be delivered end of September.

Subtask 4: Manipulator Positioning Unit

Due to the fact that this task is suspended by NET there are no KfK activities in this field.

Subtask 5: Pre- and Post Irradiation Testing of Boom Components

Motors, lubricants, cables

The first irradiation tests with MACCON and MOOG motors were performed during the reporting period 1992/93 and are reported in [7,9]. After having achieved a total γ-dose of 800 Kilo-Gy (Si) at the Maccon motor and 5.9 Mega-Gy (Si) at the Moog motor both motors blocked. Nevertheless, the gamma irradiation has been continued to a total dose of 6.5 Mega-Gy

(Si). Qualitative post-examinations have shown that the blockage of the Maccon motor was caused by applying the lubricant Krytox 240AC at the bearings which has not been high enough radiation resistant. At the Moog motor a loosened screw had blocked the brake.

According to the results of the first post-irradiation examinations and the results of the irradiation tests of basic materials in parallel, the motors have been modified, reconditioned and irradiated up to 10 Mega-Gy (Si) in a second campaign. At the following examinations no failures have been detected. Thus the irradiation will be continued up to 30 Mega-Gy (Si) if the results of the quantitative post-irradiation examinations which are still ongoing are in accordance with those of the pre-irradiation tests.

Cables and lubricants were tested as basic materials and together with the motors. In a further step all motor sizes to be applied at the operational handling equipment should be tested.

Irradiation of Multiturn Resolvers for Remote Handling Systems

The objective of this task is to carry out tests with modified hard-rad resolvers, with view to their precision and resolution data under severe gamma radiation and temperature conditions. From preceding irradiation campaigns in 1992/93 it was known that a restricted number of wires and insulation foils became defective at an accumulated dose of 8 Mega-Gy (Si). Another resolver had failed due to the fact that its ball-bearings had been lubricated inadvertently by the manufacturer. As a consequence, the organic grease had changed its consistency with the on-going gamma exposure and finally formed a totally stiff mass.

Again, multiturn resolvers model GAG-65/GERWAH equipped with SIEMENS angular encoders were chosen and, after receipt of a new series of modified hard-rad multiturn resolvers preparations were started for a second online measurement and test campaign with a couple of pneumatically driven resolvers in early 1994. A test facility was built up comprising most of the components formerly used with the irradiation basket. The pneumatic lines and sealants were renewed and, as well all thermocouples to monitor the resolver's thermal profiles and spot temperatures became exchanged. Provisions were made for an online actuating and measurement system to gain the characteristics and error patterns with the irradiation time and a total gamma dose to up 30 Mega-Gy (Si).

All pre-irradiation tests were successfully terminated in July '94 with both resolvers already mounted in their final positions inside the test basket. In order to provide a reference base, several temperature tests with alternating levels from room temperature to up 150°C were performed and their relevant error margins determined. It was shown that neither the precision nor the reproducibility did exceed the 12 bit error margins.

The start of the second online irradiation campaign is anticipated for 9/94 at the BR2 reactor, MOL/Belgium, and is due to the local availability of the irradiation facility and the schedules for some other irradiation sessions in parallel, respectively.

Literature:

[1] Suppan, A., et al.: The NET Articulated Boom: Preliminary Investigations and Justification for a Full Scale Prototype. KfK 4809, December 1990

[2] Kast, G.: Nuclear Fusion Project - Semi-annual Report of the Association KfK/Euratom - April 1989 - September 1989. KfK 4677, EUR 11397 EN, November 1989

3] Suppan, A., et al.: EDITH - A Prototypical Boom System for NET/ITER. In: Ferro, Gasparotti, Knoepfel: Fusion Technology 1992, Proceedings of the 17th Symposium on Fusion Technology, Rome, 14-18 September 1992, Vol. 2, p. 1599-1603

[4] Kast, G.: Nuclear Fusion Project - Annual Report of the Association KfK/Euratom - October 1989 - September 1990. KfK 4774, EUR 13151 EN, September 1990

[5] Kast, G.: Nuclear Fusion Project - Annual Report of the Association KfK/Euratom - October 1990 - September 1991. KfK 4944, EUR 14015 EN, October 1991

[6] Kast, G.: Nuclear Fusion Project - Annual Report of the Association KfK/Euratom - October 1991 - September 1992. KfK 5099, EUR 14795 EN, October 1992

[7] Kast, G.: Nuclear Fusion Project - Annual Report of the Association KfK/Euratom - October 1992-September 1993. KfK 5288, EUR 15466 EN, December 1993

[8] Suppan, A., et al.: Experimental Device for In-Torus Handling - EDITH Intermediate Report. KfK 5252, October 1993

[9] Leinemann, K.: NET Remote Workstation, KfK-Bericht 4785, KfK, Karlsruhe, Oct. 1990.

[10] K. Leinemann, F. Katz, H. Knüppel, W. Olbrich, W.: Synthetic Viewing: Comprehensive Work Representation Making Remote Work More Transparent to the Operator. ISFNT-3, 27.6.-1.7.1994, Los Angeles, CA., USA

[11] A.Suppan, A.Rahn, M.Englert: Gamma Irradiation Tests with Motors for NET/ITER In-Vessel Handling Equipment. unpublished report, KfK 1993

[12] H.A. Rohrbacher et al.: Radiation- and Temperature Hardened Components for In-Vessel Handling Equipment,18th SOFT Conference, Karlsruhe, August 1994

Staff:

G. Dillmann
B. Dolensky
H. Gutzeit
B. Haferkamp
A. Hinz
W.E. Hörl
J. Hübener
F. Katz
H. Knüppel
H.-G. Krumm
H. Kruse
U. Kühnapfel
K. Leinemann
W. Link
A. Ludwig
G. Müller
W. Müller
W. Olbrich
A. Rahn (KfK-AG Mol)
H.A. Rohrbacher
M. Salaske
U. Schygulla
A. Suppan
J. Woll

T 43 Remote Pipe Welding and Cutting (former task RST 2)

The objectives of this task are to qualify cutting and welding tools to be procured by the NET-Team under the ETA for concentric cryogenic lines and to design and specify the tools for remote weld inspection.

The design, the design description and the call for tender specification of a set of the cutting and welding tools was submitted to the NET-Team at the end of 1993. Early in 1994 a European wide call for tender was performed by the NET-Team. The decision to place the fabrication order with the industry depends now on the approval of the CEC/Brussels and is still open.

The pretest and selection of the inspection tools were finalized. The draft of the specification for procurement of the tools was prepared and submitted to NET. In addition, the IzfP (institute where the tests were performed) prepared an offer for the delivery of a complete set of inspection tools. This offer is also a realistic basis for the later application of the inspection tools to the welding tools to be commissioned after delivery by KfK. The design of the adapters for implementation of the sensor heads in the welding head is in progress.

The FEROS test facility has been prepared for the follow-up commissioning and testing of the prototype tools.

Literature:

[1] Ferro, C., Gasparotto, M., Knoepfel, H., Fusion Technology 1992, Proceedings of the 17th Symposium on Fusion Technology, Rome, Italy, 14 - 18 September 1992, Volume 2, pp. 1574 - 1578.

[2] Kast, G., Nuclear Fusion Project, Annual Report of the Association KfK/Euratom, October 1992 - September 1993, KfK 5288, EUR 15466, Dec. 1993.

Staff:

L. Gumb
P. Heilmann
H. Krause
A. Schäf
M. Selig
D. Stern

Safety and Environment

Introduction:

Within the European Fusion Technology Programme 1992-94 the safety analyses for NET/ITER which are being performed in parallel to the design efforts address mainly two different areas:

Safety Assessment Studies

- Basic Safety Criteria (SEA 1)
- Personnel Safety Assessment (SEA 2)
- Analysis of Reference Accident Sequences (SEA 3)
- Plant Safety Assessment (SEA 4)

and

Plant Related Studies

- Radioactivity Inventories and Source Terms (SEP 1)
- Environmental Impact of Tritium and Activation Products (SEP 2)
- Waste Management and Decommissioning (SEP 3)

The KfK contributions to this program concentrate on:

- Analyses of reference accident sequences in superconducting magnets (subtask SEA 3-2) and

- Calculations of individual and collective doses to the public for routine and accidental releases of tritium and activation products (subtask SEP 2-2).

The investigations on blanket safety are included in the blanket programme.

H. Knuth, H.-D. Röhrig

SEA 3 Analysis of Reference Accident Sequences

Subtask 2: Magnet System Safety

Within the subtask 3.2 KfK investigates the thermal and mechanical behaviour of magnet systems during accidents.

During the period reported here our work on SEAFP has been documented and released [1]. Additionally validation of MAGS [2] and accident analyses for ITER were the main tasks. In terms of MAGS development a new module has been introduced to model arcs in and at coils. Finally due to the requirements of SEAFP and ITER for mailing and reporting a new hard- and software is introduced, and implementation of MAGS on a workstation was started.

a) Thermal analyses for the magnet system

To simulate more realistic transients including arcs a new module SHORTARC has been added to MAGS. Based on the experimental results of Kronhardt [3] the voltage drop for arcs in- and outside of a coil now can be calculated. There are, however, some aspects that still have to be improved: Accidents involving an arc usually do not have the arc as an initial condition, in most cases there are precursors in terms of temperature, current and/or voltage e.g. caused by a short or a fault in the electrical circuit. For these faults one should know better the resistance of a short or the voltage/temperature characteristics of a failing insulation. Additionally a burning arc elongates due to melting of the electrodes, as the length of plasma contributes linearly to its voltage drop these growth characteristics should be known for the conductors investigated. Therefore, presently only parameteric investigations on these accidents can be performed.

In the accident analyses for TF coils it was found that transients inluding a dump of the TF coil system should also consider poloidally closed steel structures that are located close to the coils such as a coil case or shear plates. The induced currents may generate significant amounts of heat that cannot be neglected in all cases.

For accidents including shorts or arcs for the TF system of ITER scoping considerations have been performed. Preliminary results are under discussion.

In the context of verification of MAGS the following activities have been performed. MAGS has been used to recalculate experiments in the test facility HELITEX of ITP. In these tests the transversal heat transfer through a cable in conduit conductor (cicc) has been investigated. A straight conductor having a rectangular cross section was heated on one side with an electrical heater at different power levels and cooled by Helium at different flux rates. It was found that with application of correction factors on the transversal thermal conductance of the cable braid and the heat transfer coefficient from the braid to the He coolant the experiments could be recalculated.

However, with these experiments alone it was not possible to show that the applied corrections reflect the real situation. Therefore, a further assessment is planned to be done with the QUEnch experiments in the STAr facility (QUESTA), being presently under preparation at ITP. In this experiment transversal quench propagation between neighbouring conductor turns in a coil is investigated. The coil consists of one layer and is wound with two conductors in hand to

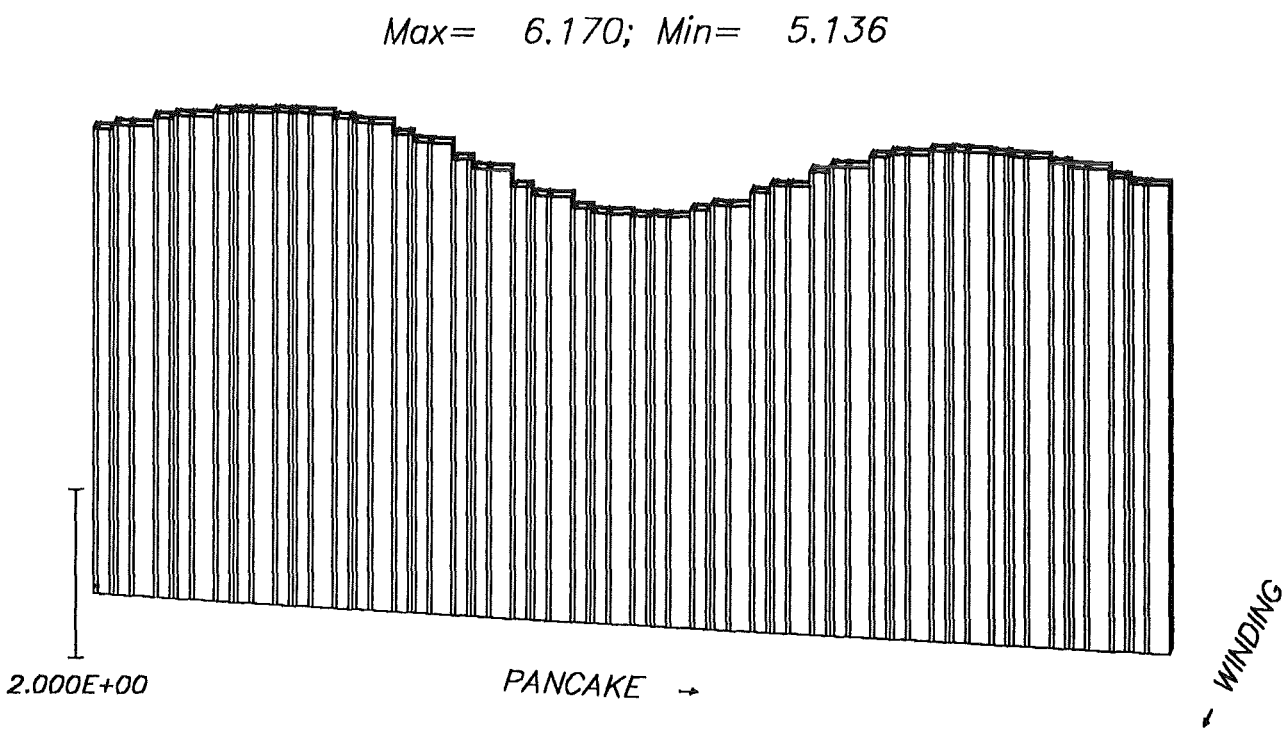

Fig. 1: Absolute value of the magnetic field in mesh elements along the coil axis calculated with EFFI

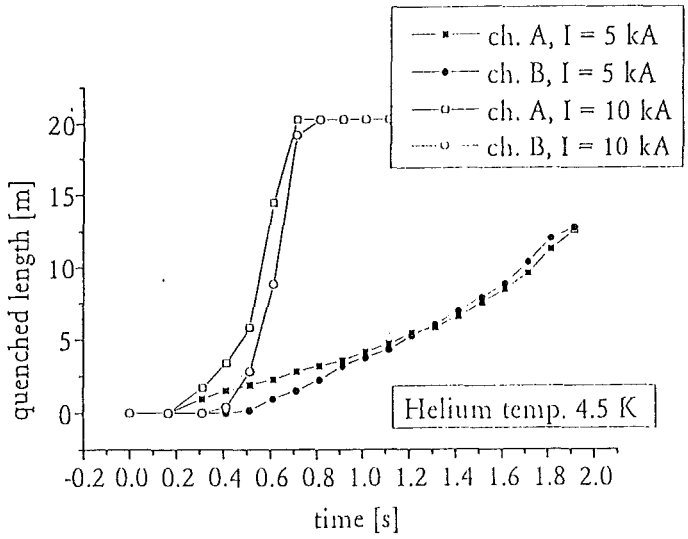

Fig. 2: Quench propagation at different current levels for the QUESTA coil

exclude hydraulic feed back on the transversal quench propagation. The coil is placed in the background field of the STAR facility being controlled independent from the currents in the test coil. Precalculations of the transversal magnetic field for the coil are shown in Fig. 1. Quench is initiated by a hot helium slug in the center of the coil. The evolution of the quenched length in the initiating cable and in the "infected" cable are shown in Fig. 2. One can see that it takes only few seconds to quench the complete coil and the difference quenched length between the two cables is small.

b) Analysis of the mechanical behavior of the coil casings under accident conditions

The mechanical investigations concentrated on the bucking structure which at fault conditions undergoes non-axisymmetrical loadings.

In the former ITER-CDA-design (Fig. 3a) the bucking structure was a vault composed of the wedged straight legs of the TF-coils. The mechanical analysis had to investigate the stability conditions of such a composed vault under asymmetrical loading. For this design connecting elements between the coil legs proved to be crucial constructive elements.

In the new ITER-EDA-design (Fig. 3b) the TF-coil legs are bucked on the central solenoid which is supported by a central bucking cylinder. The cylinder is composed of electrically insulated radial segments. Therefore, from the mechanical point of view the bucking device again is a composed vault, but surrounded by a closed ring which is the central solenoid. In this design the TF-coils are not intended to wedge. They transfer the radial in plane load across the central solenoid onto the bucking cylinder.

Comparing the two designs the last one, due to the thicker vault, seems rather stable. In addition the surrounding closed ring (central solenoid) in principle acts as a hoop and is therefore a vault stabilizing element. But to analyse such a

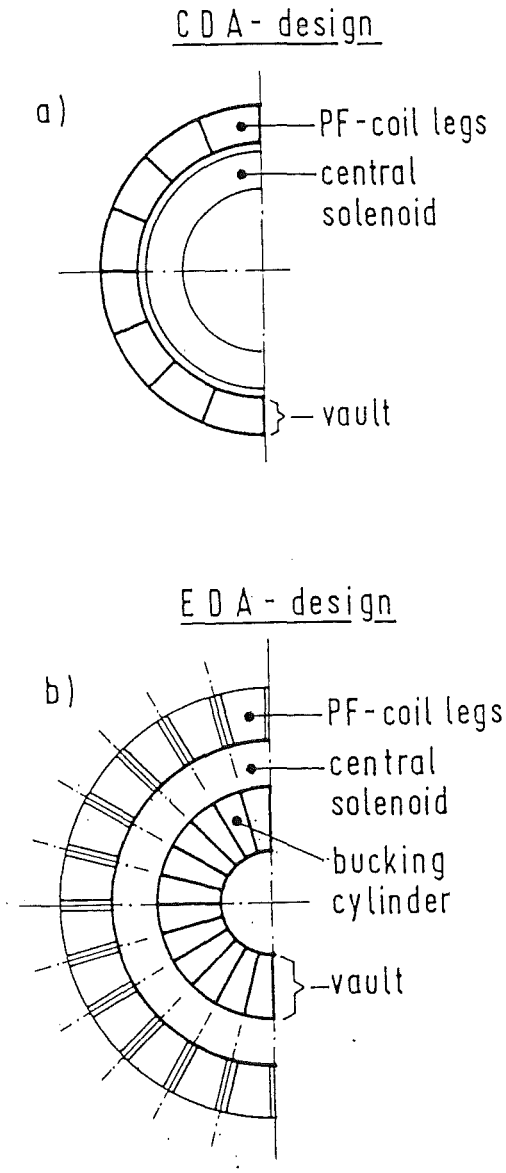

Fig. 3: Bucking structure design

composed structure with many interfaces just under friction contact is rather complicate and beyond standard methods.

In a first step the consequences of several fault loadings of the TF-coils on the bucking structure have been studied. In order to select the most severe loadings and to gain knowledge of the structural behaviour of the composite structure a rather simple model was used. It turned out that a short circuit in one TF-coil during a fast dump leads to the most unfavourable loadings concerning the stability. Hereby the current loading of the central solenoid is of some importance. The results gained so far are under discussion.

In a next step the above mentioned stabilizing effect of the closed ring (central solenoid) on the stability of the bucking structure and the stressing of the solenoid will be investigated. Finally the gained results will have to be checked more rigorously by a detailed FEM calculation for the most critical loading case.

Literature:

[1] W. Kramer, R. Meyder, S. Raff, G. Bönisch: Magnet System safety analysis, SEAFP/R-A5/(93), March 1994.

[2] G. Bönisch, G. Hailfinger, R. Meyder. MAGS: A computer code system to analyse 3d quench propagation in forced flow superconducting magnet systems. IAEA Technical committee Meeting, Toronto 1993.

[3] H. Kronhardt: Einfluß von Kurzschlüssen und Lichtbögen auf die Sicherhehit von Magnetsystemen. KfK 5096, Mai 1993.

Staff:

G. Bönisch
W. Kramer
W. Kuhn
R. Meyder
S. Raff

SEP 2 Environmental Impact of Tritium and Activation Products

Due to the importance of the OBT in nutriment plants, a more detailed photosynthesis model has been developed. This stand-alone model is being tested against experimental data. First results showing a good agreement between plant physiological data from 1993 have been presented in [1]. Further tests with experiments such as the exposure of winter wheat with HTO (closed chamber) will be carried out in the next months. The revised photosynthesis model will be then included in UFOTRI [2].

To have a rough estimate of the radiological impact from nuclides not yet implemented in COSYMA [3], a simplified version of COSYMA had been generated which allows dose assessments with about 290 nuclides. As in this version the ingestion pathways are modelled in a rather simplified way, an improvement is necessary. Calculations with state of the art food chain models such as ECOSYS [4] and FARMLAND [5] will be performed for about 70 fusion relevant nuclides. At the end of 94, the updated nuclide list will be implemented in COSYMA, which allows then to perform dose assessment for the most important materials under discussion for ITER.

With the evaluation program DOSELOOK [6] it is possible to scale and easily combine precalculated dose values of unit releases of up to 290 fusion/fission relevant nuclides for 5 exposure pathways - external irradiation from the ground and cloud, inhalation during plume passage, inhalation of resuspended material and ingestion of contaminated foodstuffs - to get dose estimates for source terms with non-unit release rates. DOSELOOK has been extended with the option to approximately scale the results in the basic data set to other input parameters as used for this run. To this purpose, a scooping tool module offers the possibility to change the release conditions such as building dimensions, stack height, site terrain obstacles, release duration, wind speed, stability class and sigma parameters. Additionally DOSELOOK has been converted to an EXCEL spreadsheet program in Macintosh format.

For accidental releases, both computer codes UFOTRI and COSYMA (partly simplified) have been applied for investigations within SEAFP (Safety and Environmental Aspects of Fusion Power) and ITER. Within SEAFP, dose calculations have been performed for unit releases (1g) of corrosion products from water coolant loops, of first wall erosion products (V-15Ti, MANET2, La12TaLC) and of different coating materials (beryllium and tungsten). Releases of 1g ($3.7 \cdot 10^{14}$ Bq) of tritium in HT/HTO form has been investigated and compared with the releases of the activation products. Additionally, the influence of a prolonged release duration on the individual and the collective dose has been investigated. First results have been presented in [7], a first documentation of the calculations is available in [8] and further documentation will be prepared until the end of the year. Within ITER 19 different release scenarios have been investigated for the two chemical forms of tritium, HT and HTO; 15 cases result from accidental releases, 4 cases are asigned to normal operation conditions. Individual doses have been calculated for the Most Exposed Individual (MEI) at 18 distances from the source. Additionally, the collective dose from 2 km up to 100 km has been obtained. The results are documented in [9]. Parameter studies about the influence of rain on the dose to the most exposed individual at the fence are still under investigations.

The computer code NORMTRI for estimating the doses from tritium releases under normal operation conditions, has been established in a first version in 1993. The documentation is now available [9].

Within SEAFP, dose assessments during normal operation conditions, have been performed for corrosion products from first wall primary coolant loop and for tritium in both chemical forms (HT/HTO) by using COSYMA and NORMTRI, respectively. The results of dose calculations for normal operation effluents will be documented till the end of 1994. Within ITER dose assessments during normal operation conditions have been performed for tritium in both chemical forms (HT/HTO) by using NORMTRI [10].

Within BIOMOVS II (BIOsheric MOdel Validation Study - phase II) study a working group has been established with the aim of testing and validating tritium transfer models. During the last working group meeting in Karlsruhe, May 3 to 6, 1994, the results have been discussed in detail. Modelling of the soil and the dynamics of OBT proved to be the critical points of the models. As the underlaying scenario is not an A-type (= based on experiments) scenario, but artificial, no experimental verification of the model predictions are possible. The report of the model comparison will be ready in the beginning of 1995. As soon as A-type scenarios for testing special processes in the tritium models are ready, calculations will be performed very likely before the end of 1994.

The work on developing models for the assessment of doses to individuals and the public resulting from contamination of waterbodies after an accidental release of radionuclides, has been started last year. A model chain has been outlined, which covers the processes such as run-off, transport of radionuclides in large river systems and the behaviour of radionuclides in lakes. A first version of the integrated model chain has been completed mid 1994 [11]. Validation and tests with run-off data from the Chernobyl accident will be performed to check and improve the quality of the predictions. Additionally the run-off model is participating in a BIOMOVS-II exercise for testing run-off models.

Literature:

[1] Diabaté, S., Müller, J., Raskob, W. and Strack. S.
Short Term Exposure of Crop Plants to Atmospheric Tritium. Experimental Results and Model Development in: Proc. of the '18th SOFT conference', Karlsruhe 20.8.94 - 24.8.94, to be published

[2] Raskob, W.
Description of the New Version of the Tritium Model UFOTRI Including User Guide
KfK-Report 5194, Kernforschungszentrum Karlsruhe (1993)

[3] COSYMA: A New Program Package for Accident Consequence Assessment.
Joint report by Kernforschungszentrum Karlsruhe GmbH and National Radiological Protection Board
Commission of the European Communities, Report EUR-13028 EN (1991)

[4] Müller, H. and Pröhl, G.
ECOSYS-87 a Dynamic model for Assessing Radiological Consequences of Nuclear Accidents.
Health Physics, Vol. 64 (3), pp. 232-252 (1993)

[5] Brown, J., Simmonds, J.R.
Recent validation studies for two NRPB environmental transfer models in: BIOMOVS. Symposium on the validity of environmental transfer models. Swedish Radiation Protection Inst., Stockholm (Sweden) Stockholm: SSI. 1991. pp. 125-135

[6] Meyer, D. and Raskob, W.
User Guide for the PC-Program DOSELOOK
KfK, unpublished Internal Report (to be printed 1994)

[7] Raskob, W.
Dose Assessment for Releases of Tritium and Activation Products Into the Atmosphere Performed in the Frame of Two Fusion Related Studies: SEAFP and ITER-EDA.
in: Proc. of the '18th SOFT conference', Karlsruhe 20.8.94 - 24.8.94, to be published

[8] Raskob, W.
Results for SEAFP-subtask A 10:
Calculations of Individual and Collective Doses to the Public for Routine and Accidental Releases of Tritium and Activation Products.
KfK, Internal Report, Dec. 1993

[9] Raskob, W.
Results of Calculations of Individual and Collective Doses to the Public for Routine and Accidental Releases of Tritium and Activation Products.
KfK, Internal Report, Nov. 1993

[10] Raskob, W.
NORMTRI: A Computer Program for Assessing the Off-Site Consequences from Air- Borne Releases During Normal Operation of Nuclear Facilities.
Report KfK-5364, Kernforschungszentrum Karlsruhe (1994)

[11] Raskob, W., Tkalich, P., Heling, R., Popov, A.
The Modelling Concept for the Radioactive Contamination of Waterbodies in RODOS, the Decision Support System for Nuclear Emergencies in Europe.
in: International Seminar on Freshwater and Estuarine Radioecology Lisbon, Portugal, 21-25 March 1994, to be published

Staff:

J. Ehrhardt
I. Hasemann
D. Meyer
W. Raskob

Studies for ITER / NET

Introduction:

By granting study contracts to KfK, ITER/NET draws upon special expertise available in the laboratory. In contrast to the technology tasks which extend over a longer period of time and consist in most cases of experimental work, study contracts are agreed on short notice and are of limited duration.

I_c vs Strain Tests on Nb_3Sn Strands

The aim of the contract is to get from the running Nb_3Sn wire production for the ITER model coils the necessary data for assessment of the wire production quality and the comparison of the measuring methods.

A) Samples: Within a world-wide action af "Bench Mark Tests" the critical current (I_c), hysteresis losses, RRR, Cr plating thickness and the ratio Cu/non-Cu have been tested on Nb_3Sn strands, described in Tab. 1. In extension of these investigations the axial strain (ε) dependence of I_c has been tested on identical wires within the FBI facility at KfK.

Table 1: Parameter of the Nb_3Sn strands for the bench mark action, according to the Home Teams

	EU	JA	RF	USA
Manufacturer	VAC	Furukawa	Bochvar	TWCA
Technique	Bronze	Bronze	Bronze	Int.Sn
Strand dia. [mm]	0.73	0.92	0.825	0.73
Cu: non-Cu	1.5	1.58	1.22	1.22
Twist pitch [mm]	9	20	7	9.5
Filament alloy	NbTa 7.5	n.a.	Nb	NbTi1
Cr plating [µm]	2	2.5	3	0 (bare)
Heat treatment procedure	570°/144h 650°/200h	625°/312h	560°/150h 650°/180h	185°/120h 340°/72h 650°/200h

B) Apparatus: The 130 mm long straight samples were tested in a tensile test rig, designed for max. loads of axial force and electrical current of 1 kN and 250 A, respectively. The axial strain (ε) was measured in LHe by a capacitive displacement transducer using a gauge length of 50 mm. The magnetic field (B) was supplied perpendicular to the sample axis by a split coil ($B \leq 13$ T, gap=1 cm). An I_c criterion of 1 µV/cm was used for all tests.

C) Results and Discussion: From each manufacturer (party) at least four identical samples have been tested. A typical I_c vs ε characteristic of a VAC wire obtained at B=12 T under loaded and unloaded conditions is represented in Fig. 1. (The numbers indicate the sequence of testing). As expected, I_c shows a maximum as a function of strain. I_{co} and I_{cm} represents the critical current at $\varepsilon=0$ and $\varepsilon=\varepsilon_m$, respectively, and I_{co}/I_{cm} a measure of I_c degradation. I_c behaves reversible up to ε_{irr}, that measured strain under stressed condition, which represents simultaneously the higher ε value tested for the samples from EU, JA and RF. However, in case of the US wire the curve of I_c obtained within unloaded state lies below that one in loaded condition. Therefore is ε_{irr}

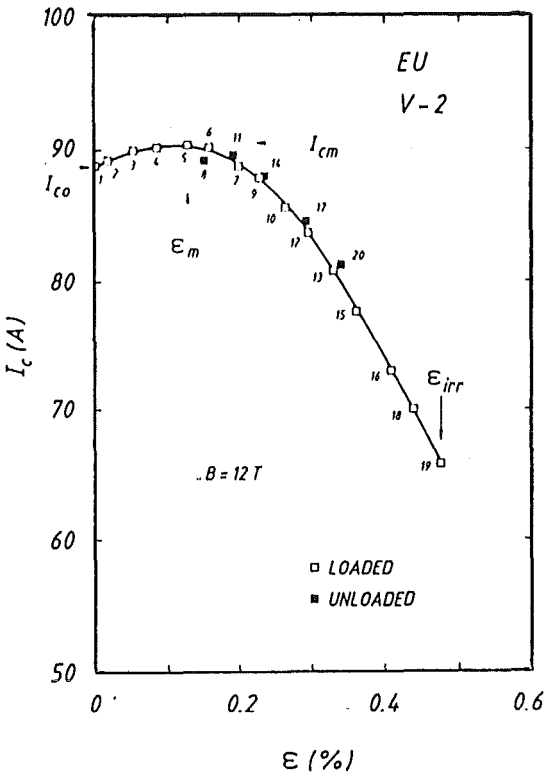

Fig. 1: Strain dependence of crit. current at B=12 T for the EU sample (VAC)

Table 2: Results of I_c vs ε tests at B=12 T

Samples		I_{co} (A)	I_{cm} (A)	I_{co}/I_{cm}	ε_m (%)	ε_{irr} (%)
Party	Quantity					
EU	7	87.6	90.7	0.97	0.13	>0.51
JA	4	228.8	238.8	0.96	0.16	>0.54
RF	5	141.1	151.3	0.93	0.16	>0.51
US	4	121.7	126.2	0.97	0.10	>0.20

of this wire considerably smaller than those measured at the other wires, as shown in Tab. 2, where the average values of several identical samples (quantity 4–7) of all conductors are summarized.

At $\varepsilon=0$ and B=12 T the I_c values show a scattering of up to 38% within the bench mark test action and up to 8% for the FBI tests. The difference may be explained by both the various test facilities used and the different caution of handling of the samples with respect to its high strain sensitivity.

Staff:

H. Kiesel
W. Specking

Investigation of Cryo-Cascade-Concept for ITER and Definition of Test Requirements

1. Task

For the operation of the planned International Thermonuclear Experimental Reactor (ITER) vacuum pumps are required, by means of which the exhaust gases can be pumped under various operating conditions. During the burn and dwell phase, a gas mixture consisting of impurities, helium, fuel (DT) and protium has to be pumped. To enable direct recycling of the hydrogen isotopes into the reactor, the pumping system has to fulfill the task of separating these gas species from the mixture. Pumping of the exhaust gas takes place via the divertor slots to the pump inlet. The available conductance between divertor and pump inlet has to be considered. For safety enhancement, the number and/or size of vacuum vessel penetrations is minimised. This means that the pumps have to be arranged inside the cryostat where they are exposed to high magnetic and irradiation fields. High-speed metal rotors and electric driving units used in conventional mechanical vacuum pump stations cannot be applied in this case.

The validation of the concept of recycling the DT into the torus, the use of cryotransfer pumps for fuel compression and the design of simple valves for regeneration is the focus of the study.

Critical issues and development requirements for components as well as the R+D acitvities for development of prototypes, including proof of principle tests should be defined.

The work is based on the latest data provided informally by the NET TEAM.

2. Requirements

The requirements changed during the ongoing work of the study. The present final report has been reiterated to the data given in Table 1. These data agree with the proposals made during the ITER technical meeting on fuelling and pumping in January 19 - 26, 1994.

Table 5 gives a survey over the divertor pressure, throughput, gas composition, regeneration pressure of primary pump, gas temperature at divertor and pump inlet, number of pumped ducts and the available system conductance between divertor and pump inlet for the burn/dwell mode.

Further requirements for the design of the pumps are:

- Separation of H/D/T from impurities and He during pumping or regeneration
- 99.99% purity for recycling H/D/T into torus
- Total Tritium inventory of the primary and secondary cryopump systems is limited to 60 g

Tab. 1: Requirements for design of primary ITER-cryopump during burn mode

Divertor pressure at 450 K	1×10^{-3} mbar	5×10^{-3} mbar
Throughput at T_N (0°C)	300 mbar l/s	1000 mbar l/s
Gas temperature	450 K	450 K
Gas composition	①	②
Number of pumped ducts	10	10
Required He pumping speed at divertor (450 K)	495 m^3/s	330 m^3/s
+ Available conductance between divertor and pump inlet (450 K He)	≈ 1500 m^3/s	≈ 1500 m^3/s

① 0.5 imp.; 0.25 H_2; 8 He; 91.25 DT (vol.%) D:T 1:1

② 0.5 imp.; 0.25 H_2; 3 He; 96.25 DT (vol.%) D:T 1:1

\+ Status Jan. 1994

- Number of divertor ducts: 24
- Primary and secondary cryopumps are to be located inside the divertor duct
- 90% of the H/D/T should be recycled directly into torus.
- Pressure required for H/D/T recycling: 1200 mbar.
- Temperature of the duct wall: 450 – 600 K

3. Pump concept

The divertor pressure range for the various operation modes is 1×10^{-7} to 1×10^{-1} mbar. That means the pumps must handle the exhaust gas in molecular or transition flow regime. It is possible, that the divertor pressure changes to higher values.

For a given throughput a pump working in the molecular flow condition demands the biggest cross section and the biggest installation volume. At higher divertor pressures the pumping speed of the pump increases. By means of an adjustable throttle valve at the pump inlet the divertor pressure can be kept constant at higher pressure levels.

3.1 Cryocascade concept as primary pump with gas separation ability (separating cryopump)

A simplified arrangement of a three stage cryocascade cryopump working in molecular flow range is shown in Fig. 1. The pump consists of discrete chambers for the pumping of impurities, H/D/T and helium respectively.

The exhaust gas enters the first pump chamber with 450 – 600 K. This chamber can be isolated by two valves for regeneration (Fig. 1, Pos. 1, 4). The inlet valve is assumed as an

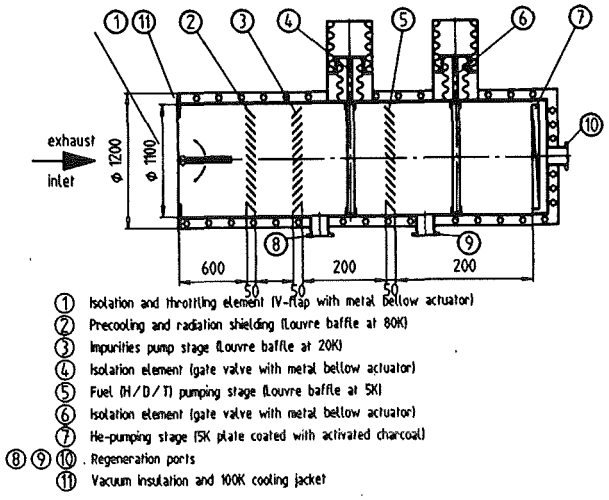

Fig. 1: Cryocascade concept as primary pump with gas separation ability (not to scale)

V-flap, the second valve as a gate valve for example. Other designs are possible.

For cooling down the hot exhaust gases and shielding the 20 K pump structure (Fig. 1, Pos. 3) against the radiation coming from the torus a Louvre baffle is installed in front. The temperature of this baffle is kept at 80 K. This will pump water like impurities. Behind this baffle a second baffle kept at 20 K is arranged. The surface of this baffle serves as pumping area for freezing out the air like impurities.

The pumping panel of the second chamber consists of a Louvre baffle (Fig. 1, Pos. 5) on which the hydrogen isotopes are frozen at 5 K. Isolation of the chamber for regeneration is effected by two cold gate valves (Fig. 13, Pos. 4 and 6).

The third chamber of the pump has to adsorb the remaining amount of helium. The cryopanel is formed as a flat panel (Fig. 1, Pos. 7) coated with activated charcoal and cooled to 5 K.

The pump is installed inside the divertor duct. The cross section has to be adapted to the trapezoidal shape of the divertor duct. The temperature of the duct wall is 450–600 K. To decrease the heat transfer directed to the cryopump a vacuum insulation and a 100 K cooling jacket around the pump vessel is needed.

The V-flap at the pump inlet has to be designed as a throttle valve. It is possible to maintain the divertor pressure constant at higher levels as the pressure inside the pump.

For the actuation of the valves metal bellows operated with pressurized helium are proposed.

3.2 Pump train with primary and secondary pump without gas separation in the primary pump (co-pumping cryopump)

The scheme of the two stage cryopump is outlined in Fig. 2.

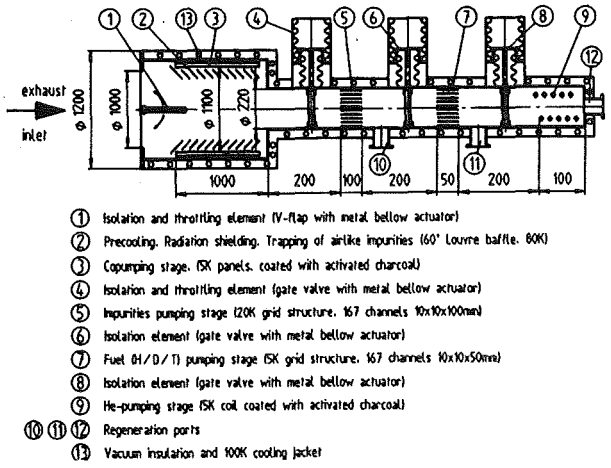

Fig. 2: Scheme of a copumping train (primary and secondary pump)

The primary pump is a copumping unit designed for the molecular flow range. A cylindrical pumping panel is arranged axially. By means of supercritical helium it is cooled to 5 K. The surface of the panel is coated with activated charcoal. The helium and the condensable fractions of the exhaust gas are copumped on this panel. An 80 K Louvre baffle is located upstream of the 5 K surfaces and serves as a radiation shield. It will pump water as well as impurities. The pump inlet is connected with the pumping duct via an adjustable throttle valve. By means of this valve, the divertor pressure can be kept at higher levels as the pressure inside the pump. During regeneration, the inlet of the pump is closed by this valve.

The gas mixture released during regeneration flows to the secondary pump. This is a cryocascade pump conceived for the viscous flow range. It consists of three axially arranged pumping chambers which may be separated from each other by means of valves. The first and second pumping stages have grid structures with the inner surfaces of the individual channels serving as the pumping area. In the first stage, the impurities are condensed at 20 K. Pumping of the hydrogen isotopes takes place in the second stage cooled to 5 K. The uncondensable helium is adsorbed at a 5 K activated charcoal layer in the third stage. For regeneration the valves are closed. Pumping of the impurities and helium is accomplished by an external mechanical forepump system installed outside the cryostat.

The valves are moved by means of metal bellows actuated by pressurized helium. The pump train consisting of a primary and secondary pump shall be designed such that it can be inserted into the divertor duct as a complete unit.

4. Pumping system

On the basis of the design calculations it becomes obvious that the cryocascade pump which is used as primary pump with gas separation ability (Fig. 1) has three major disadvantages:

- The needed inner cross-section of the pump for the burn/dwell mode is 0.88 m^2. If we take into account the space for the vacuum insulation, the 100 K cooling jacket, the device for remote handling, the actuators for the cold valves, the piping for regeneration and mechanical pump down it seems impossible to install this pump inside the duct.

- With a He-pumping probability of 15% the total He-pumping speed amounts to 460 m^3/s for 10 pumps in operation (s.Tab. 2). For the required He-pumping speed of 495 m^3/s at the divertor a conductance of 6505 m^3/s is needed between divertor and pump inlet. This exceeds the now available conductance of 1500 m^3/s.

- The regeneration pressure in the unvented H/D/T-pump chamber amounts to 102 mbar. The pressure level required for H/D/T-recycling is at 1200 mbar. That means that an additional cryotransfer stage is needed for increasing the H/D/T pressure. The ratio of volume of the cryotransfer pump and the H/D/T pump chamber must be at least 1:11.8.

Tab. 2: Design data for He-pumping during burn/dwell at 10^{-3} mbar of cryocascade pump as primary pump with gas separation ability

Number of Pumps in operation		10
Gas composition		He
Pumping probability	[%]	15
Entrance diameter of pump	[cm]	100
Pumping speed for He at pump inlet (rel. to 450 K)	[m^3/s]	46
Inner diameter of cylindrical pump	[cm]	110
Cross section of pump with 50 mm cooling jacket	[m^2]	1.13
Available cross section in duct	[m^2]	1.38
Conductance needed between Divertor and pump inlet	[m^3/s]	6506 +

+ exceeds the available conductance of 1500 m^3/s (Tab. 1)

These disadvantages can be avoided by a pump concept which uses a copumping unit as primary pump and a three stage cryocascade as secondary pump. The design data are given in Table 3.

Tab. 3: Design data for He-pumping during burn/dwell at 10^{-3} mbar for primary pump of pump train with primary and secondary pump

Number of Pumps in operation	[ ]	10
Gas composition		He
Adsorption factor of pumping area	[%]	20
Pumping probability normalized to pump entrance area	[%]	50.7
Entrance diameter of cylindrical pump	[cm]	100
He-pumping speed at pump inlet at 450 K	[m^3/s]	156
Inner Pump diameter	[cm]	110
Cross section of pump with 50 mm cooling jacket	[m^2]	1.13
Available cross section induct	[m^2]	1.38
Conductance needed between divertor and pump inlet	[m^3/s]	724
Total pressure at pump inlet	[mbar]	3.2×10^{-4}
Volume of pump	[l]	1425
Max. Pumping time +	[min]	14.3

+ for 1000 mbar l/s and gas mixture ②

Every pump is installed in one of the trapezoidal shaped ducts. The primary pump has an inner diameter of 110 cm and a length of 100 cm, the secondary pump has a diameter of 21.9 cm and a length of 75 cm. Around this pump there is enough space left for the installation of the peripheric devices.

The maximum pressure in the H/D/T-chamber of the secondary pump amounts to 2650 mbar.

Based on this concept the system shown in Fig. 2 has been proposed. The pumping system comprises 24 units of which 10 are pumping and 10 in regeneration. 4 units are in stand by. 4 mechanical pump units are installed outside the cryostat for initial pumping down and regeneration of He and impurities.

The critical condition for the maximum pumping time is the burn/dwell mode at $5 \cdot 10^{-3}$ mbar divertor pressure and 1000 mbarl/s exhaust gas throughput (related to 273 K). With 10 pumps in operation we have a maximum time of 14,3 min till the max. permissible localized accumulation of 60 g Tritium is achieved. The pumps have to be brought in pumping operation respectively regeneration stepwise with a staggering period of 87 s.

With a given chamber volume of 1425 l the pressure in the unvented primary pump amounts to 17.6 mbar during regeneration. To guarantee the separation efficiency of 99,99% the inlet pressure in the impurity pumping stage of the secondary pump is kept constant at 10^{-1} mbar by means of an adjustable

throttle valve. The gas inventory will be pumped down within five minutes.

If the pump has to deal with higher duct inlet pressures the flow conditions change to viscous range and the pumping speed increases dramatically. As a consequence the pressure at the divertor will be influenced by the oversized pumping speed. To maintain the pressure at the divertor constant on a given level it is necessary to install a throttle valve at the inlet of the pumps by which the pumping speed can be adjusted to the respective working pressure. These throttle valves and the cold isolation valves are not available. They are one of the critical items in this field.

5. Conclusions

The basis for the study are the agreements for the concept of a torus pumping and fuel recycling system for ITER fixed in the minutes of the Technical Meeting on Fuelling and Pumping held on January 19 - 26, 1994 at the Joint Work Site Garching.

The following two pump concepts have been investigated.

a) A three stage cryocascade as primary pump with fuel separation ability (separating cryopump). The primary pumps pump the exhaust gas mixture and separate the fuel. Further fuel compression is done by secondary pumps.

b) A pump train with primary and secondary pump without gas separation in the primary pump (co-pumping cryopump). The plasma exhaust mixture is pumped by the primary pumps without fuel separation. Separation and further compression of the fuel is achieved by the secondary pumps.

The proposed pump system includes 24 pump units, 10 of them are pumping, 10 are in regeneration, 4 are in stand by. The pumping time of a single pump is limited to 14.3 min. by the maximum allowed tritium inventory of 60 g in the pumping system.

The critical operation mode is the burn mode. During this mode the max. total gas throughput amounts to 300 mbarl/s at the divertor pressure of 10^{-3} mbar and for the gas temperature of 450 K which yields the required total pumping speed at the divertor of 495 m^3/s. This value is equivalent to the required max. helium pumping speed. The helium pumping speed available at the pump inlet is 460 m^3/s for the fuel separating primary pumps and 658 m^3/s for the co-pumping primary pumps. To fulfil the pumping requirements at the divertor a total system conductance in between divertor and pump inlet of 6506 m^3/s (for He at 450 K) is required for the fuel separating primary pumping system (a) and 724 m^3/s for the co-pumping primary pumping system (b). This means that the system conductance of the ITER divertor concept is sufficient for a co-pumping pumping system, but it is not sufficient for a system using fuel separating primary pumps.

Comparison of Primary Cryopump Concepts by Monte Carlo Calculations

The helium pumping probabilities have been calculated for both primary pump versions that are technically feasible, i.e. co-pumping cryopump (Fig. 3) and fuel separating cryopump (Fig. 4). This allows the pump concepts to be compared quantitatively.

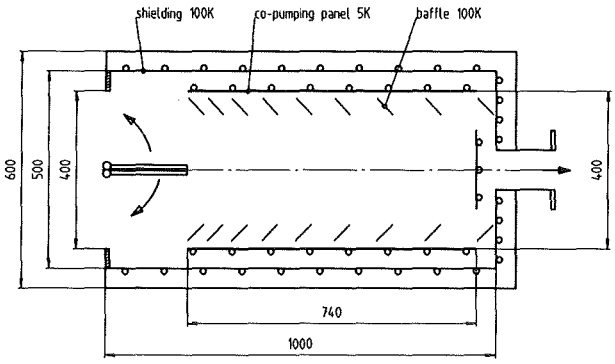

Fig. 3: Schematic representation of the primary co-pumping cryopump

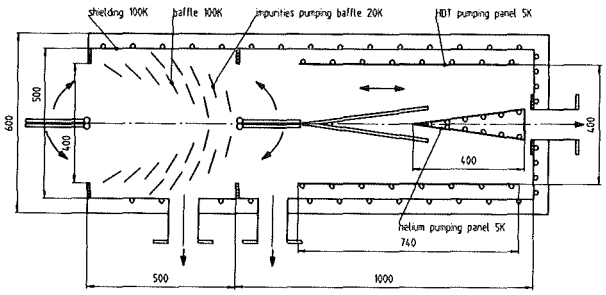

Fig. 4: Schematic representation of the primary fuel separating cryopump

On the basis of the results of the cryosorption panel test performed at KfK [1] the sticking coefficients of the sorption surfaces of these pumps have been determined.

It was assumed that the primary pumps will be installed into the pumping ducts and will have a rectangular configuration (width 600 mm, height 1600 mm). The net pump inlet surface is assumed to have a width of 400 mm and a height of 1400 mm. This yields a cross-sectional area of 0.56 m^2.

Both types of pumps will be equipped with the same shut-off devices. These are centrally fixed double-flap valves that can be opened to the inside or outside. The flaps are designed such that they can be used as throttling devices. Thus, pressure inside the pump will always be below 1×10^{-3} mbar at an initial divertor pressure of 1×10^{-3} - 1×10^{-1} mbar.

For the calculation of the helium pumping probabilities, the MOVAK3D Monte Carlo programme was used [2]. This

programme has been developed by CLASS, KfK and was applied for the calculations of the NET divertor and the LHCD cryopump for JET [3].

The pump inlet surface is defined as the source surface of the simulation volume with a cosine law emission distribution.

For the helium pumping probability calculations, the helium sorption surfaces were assumed to have a sticking coefficient of 0.5. All other surfaces were defined to be diffuse reflectors.

By means of the Monte Carlo computations, the following helium pumping probabilities have been obtained for the two pumps:

- Co-pumping cryopump: $w = 0.340$
- separating cryopump: $w = 0.095$

This yields the following maximum helium pumping speeds for particles at 600 K at the pump inlet:

- Co-pumping cryopump: $S \leq 85.6\ m^3/s$
- separating cryopump: $S \leq 23.9\ m^3/s$

The helium conductance required between divertor and pumps has been determined for the critical operation mode of ITER characterized by the following parameters:

- Initial divertor pressure: 1×10^{-3} mbar
- throughput: 300 mbarl/s at T_N (0°C)
- gas temperature: 600 K

and for 24 primary pumps installed, 10 of which have been in the pumping mode of operation and 10 in the regeneration mode. The helium conductance of $C \geq 2860\ m^3/s$ is needed to obtain the required pumping speed of 659 m^3/s at divertor using co-pumping primary cryopumps. The separating cryopumps can not fulfil the pumping requirements.

For ITER, use of the primary co-pumping cryopumps is recommended, as they meet the pumping requirements and ensure the largest possible specific helium pumping speed.

The Monte Carlo calculations show that co-pumping cryopumps are suitable for use as primary pumps for ITER. In contrast to this, the fuel separating cryopumps fail to meet the ITER requirements. A torus pumping and fuel recycling system consisting of primary co-pumping cryopumps, secondary fuel separating, cryopumps and external mechanical pump system of spiral pumps is proposed for ITER.

There are some critical items which needs further R+D work before designing a prototype pump. These are:

- Separation of fuel (H/D/T) from impurities and helium in the first 20 K pump stage of the secondary pump working in the viscous flow range.
- Separation of fuel (H/D/T) from helium in the 5 K pump stage of the secondary pump.
- Testing of rapid heating and cooling of the pumping panels for quick regeneration.
- Development and testing of metal bellows actuators and sealing configurations for the cold valves.

Component tests concerning the critical items and tests of prototypes can be performed in the HELITEX-facility available at KfK.

Literature:

[1] I. Özdemir, D. Perinic: Comparison of cryosorption on thick and thin sorbent layers for cryopumping of plasma exhaust gases, 18th SOFT, Karlsruhe, Germany, 22 - 26 Aug. 1994

[2] G. Class: 3D Monte Carlo-Simulation der Molekelbewegung und der Wärmestrahlung in Vakuum-Behältern, KfK 4292, Karlsruhe, July 1987

[3] W. Obert, G. Perinic: Pumping speed and thermal load analysis of the JET appendage cryopump by Monte Carlo calculation, Vacuum, vol. 43, No. 1/2, pp. 163 - 166, 1992

Staff:

A. Mack

ITER Coil and Model Coil Design and Analysis

The final report about KfK contributions to the Magnet Workshops in Naka in 1993 was transmitted to the NET/EU-Home Team in January 1994.

The contributions to the ITER coil and model coil design were in four areas.

- Field and force calculations for the TF model coil configuration.
- Electrical quality assurance test specification of the ITER coils.
- Comments to breakdown measurements of fiberglass reinforced epoxy sheets.
- Comments to the bladder system of the Euratom LCT coil used for the equalisation of tolerances between winding and coil case.

While the first and second one were contributions at the ITER magnet workshops in form of papers and presentations, the third and fourth one were comments on request of members of the JCT in Naka.

The final report was accepted by EU Home Team and the contract is therefore concluded.

Staff:

M. Irmisch
W. Maurer
A. Ulbricht
G. Zahn

Quench Analysis for Magnet Safety Assessment

The prediction of the behaviour of the ITER coils (CS and TF) under quench conditions is required as basic part of the magnet safety analysis. When the conductor starts to quench, voltages, transient helium pressures and local temperature gradients develop such that they have the potential to initiate faults.

The analysis of quench requires

- prediction of the one-dimensional helium flow along the conductor,
- tracing of the three-dimensional propagation of quench to adjacent conductors by heat conduction.

Parameter studies have shown that the propagation of the normal zone with time is strongly dependent on the size of the mesh used in the model. Node distances in the order of a few centimeters are necessary to get a well-converged result. Due to the large size of the ITER coils, the number of nodes as well as the number of links become very large.

Despite this fact, as a first attempt a model of two inner layers of the central solenoid of ITER (ITER-CS) has been created having a node distance of 2 meters. The high-grade HP II conductor has been used, and current scenario of the CS as well as hydraulic network of the helium connection lines have been modeled. The initial normal zone (INZ) is located in the center of the first layer (high field region) over a length of 10 meters.

Four cases have been investigated so far:

1. Fault in quench detection system:
   Quench starts at pre-magnetization (t=0), no dump of the coil is initiated.

2. Fault in quench detection system:
   Quench starts at end-of-burn (t=1000 s), no dump of coil is initiated.

3. Fault in power supply circuit, i.e., the voltage at the power supply stays at 1 kV, no discharge of the coil is possible.

4. Short between the coil terminals, no discharge of the coil is possible.

The calculation results obtained so far are as follows:

- Case 1 is the less urgent one because the current of the CS drops with time.
- Cases 2 to 4 are more or less the same because the current stays almost constant.
- After 40 seconds, the maximum conductor temperature reaches 300 K.
  The maximum pressure in the conductor is about 350 bars.

Figure 1 shows conductor temperature in flow path 1 as a function of time for case 4 whereas in Figure 2 pressure in flow path 1 is plotted as a function of time.

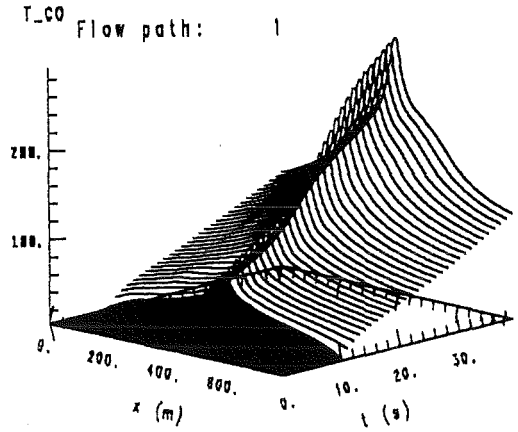

Fig. 1: Conductor temperature along the conductor versus time

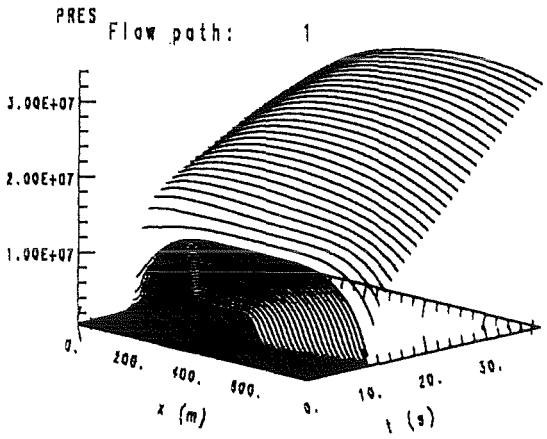

Fig. 2: Helium pressure along the conductor versus time

Staff:

R. Heller

ITER Shielding Analysis

A comprehensive task has been launched by the ITER Joint Central Team to analyse the shielding performance of the ITER device. In a first step the shielding analysis was limited to the machine itself and the effort was distributed to the four ITER parties. A global basis model of the ITER torus had to be developed for providing a common basis for all analyses. This task was accomplished jointly by the US (University of Wisconsin) and the EU (KfK) parties. In addition, the EU part of the shielding analysis covered the complete neutronics analysis of the central part of the ITER torus including a horizontal port at the outboard side equipped with different heating system. The EU-KfK task was devoted to the analysis of an electron cyclotron (EC) heating system.

Global three-dimensional model of the ITER torus

A global torus sector model has been developed with MCNP on the basis of CAD- drawings provided by the ITER-JCT. This model replicates very closely the geometrical configuration of the vacuum chamber, first wall, shielding blanket, vacuum vessel, toroidal field (TF) coil and divertor in a 7.50 torus sector of ITER. The neutron source term is described in a special SOURCE subroutine linked to MCNP. Use is made of the source density distribution provided numerically by ITER on a poloidal-radial grid with 15251 mesh points for the single null plasma shape.

The global torus sector model, developed jointly by the University of Wisconsin and KfK, has been distributed to the other ITER parties, the ITER-JCT and the Euratom Associations contributing to the ITER shielding analysis task. In addition, the model is available as MCNP input deck from the ITER-JCT Garching site including the SOURCE subroutine and the associated source data file.

Torus sector model with horizontal port for heating systems

The torus sector model was further developed for integrating different heating systems of ITER. It was extended to a toroidal angle of 150 and a horizontal port was included at the outboard side. Finally an EC heating system has been integrated into the port that uses optical techniques - a system of waveguides and two copper reflectors, where the antenna system is recessed behind the vacuum vessel - to inject the EC wave power into the plasma. Fig. 1 shows a vertical cross section of the final sector model equipped with the EC heating system. Fig. 2 show a horizontal cut of the outboard section at the poloidal height of the blanket port.

Analysis of the electron cyclotron (EC) heating system

Monte Carlo transport calculations with the MCNP code and cross-section data from the European Fusion File EFF were performed to calculate neutron streaming through the port, the neutron flux and heating rate distributions in the mirrors of the EC system, to provide neutron spectra for subsequent activation and radiation damage calculations and for assessing the radiation loads on the TF-coil adjacent to the port. Use has been made of the importance sampling technique available with the MCNP-code to arrive at statistically reliable scorings in the spatial regions of interest. About 3 million source neutron histories were followed in the final runs for both the EC mirrors and the TF-coil, each consuming 12 to 16h CPU-time on the IBM 3090 mainframe.

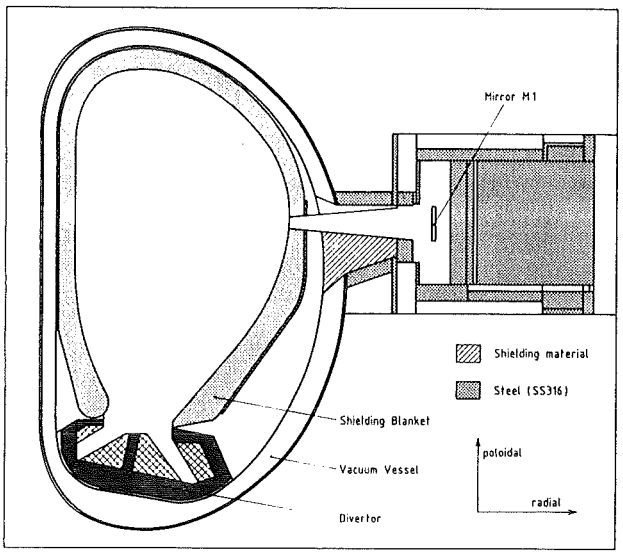

Fig. 1 : Vertical cross-section of the MCNP torus sector model including the EC heating system

At a fusion power of 1500 MW the direct power generation in the copper mirrors M1 and M2 of the EC system (see fig. 2) amounts to 2.34 and 82.6 kW, respectively. The corresponding afterheat contribution is 0.17 and 5.5 kW, the maximum power density is 2.7 10^{-2} and 14.1 W/cm^3, and the peak displacement damage in the copper at 3 full power years is 6.0 10^{-2} and 27 dpa, respectively. Using SS-316 steel as shielding material in the port region results in a sufficient shielding efficiency with regard to the requested radiation design limits. The radiation loads, however, are nearly one order of magnitude higher than those calculated for the properly shielded inboard TF-coil.

Literature:

[1] U. Fischer, M. E. Sawan: Three-dimensional neutronics analysis for the electron cyclotron wave heating system of ITER, 18. Symposium on Fusion Technology, Karlsruhe, Germany, August 22 - 26, 1994

Staff:

U. Fischer

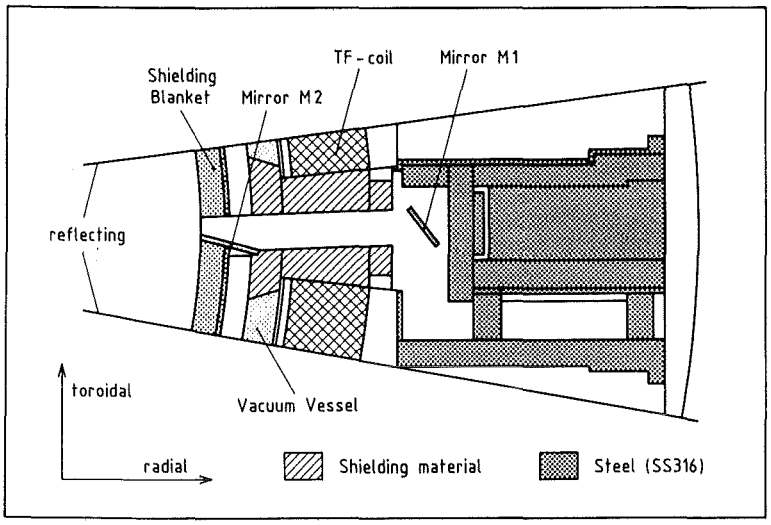

Fig. 2 : Horizontal cross-section through the outboard section of the torus sector model.

Long Term Program for Materials Development

Introduction:

KfK holds a key position in the qualification of martensitic steels and their low-activation variants for application in long term fusion technology.

Within task MANET-1.1 work on the characterization of the MANET-II heat has been completed. The diffusion welding attempts (MANET-3.2) have been very successful, but further optimization will be necessary. Component-related studies will also be continued in the frame of the Blanket Development Programme. Within task MANET 3.2 isothermal fatigue has been determined and the influence of compression hold-times causing creep damage could be identified by fracture surface analysis. Thermal fatigue shows a similar effect of the high temperature half cycles. For thermomechanical fatigue an extrapolation method for the ultimate number of cycles N_f was developed.

The irradiation-induced hardening of martensitic steels was further investigated by impact tests (MANET 3.4). After a complete data set had been established for the SIENA irradiation a new low dose/low temperature irradiation series (MANITU) has been started.

The dual-beam method has been further used to simulate fusion conditions (MANET-5). The experimental activities have in this reporting period been focused on temperature dependence as well as the influence of helium and hydrogen in post-irradiation tensile tests, and on in-beam fatigue tests at 250°C.

Within task LAM 2.1 European activation calculation codes and data files have been further improved. Comparative calculations of dose-rates after fusion reactor shut-down show that the "hands-on" level will never be reached for SiC type materials if sequential reactions are properly taken into account. For V-alloys the low activity potential will depend very much on the impurity content of a technical material.

H.D. Röhrig

LAM 2 Nuclear Data Base for Low Activation Materials Development

1. Code- and Library Developments

The European Activation System (EASY) and the European Reference Code FISPACT, which have been selected in the ITER community as reference codes for calculating radioactivity and other radiological properties have recently been further improved by the introduction of sequential (x,n)-rections with loaded particles at KfK [1]. Fig 1 shows a flow chart of the FISPACT code and indicates the KfK-contributions necessary to include sequential reactions. The spectra and reaction cross sections for charged particles, provided in KFKSPEC and KFKXN were determined by model calculations using ALICE, since experimental data were scarcely available. The differential ranges of loaded particles, collected in the library KFKSTOPP were computed with the well-established code PRAL, further improved and modified by KfK. The files contain data for all elements from hydrogen to curium (Z = 1 – 96). This code development has now been brought to a preliminary end and the most recent data files have been introduced into EASY.

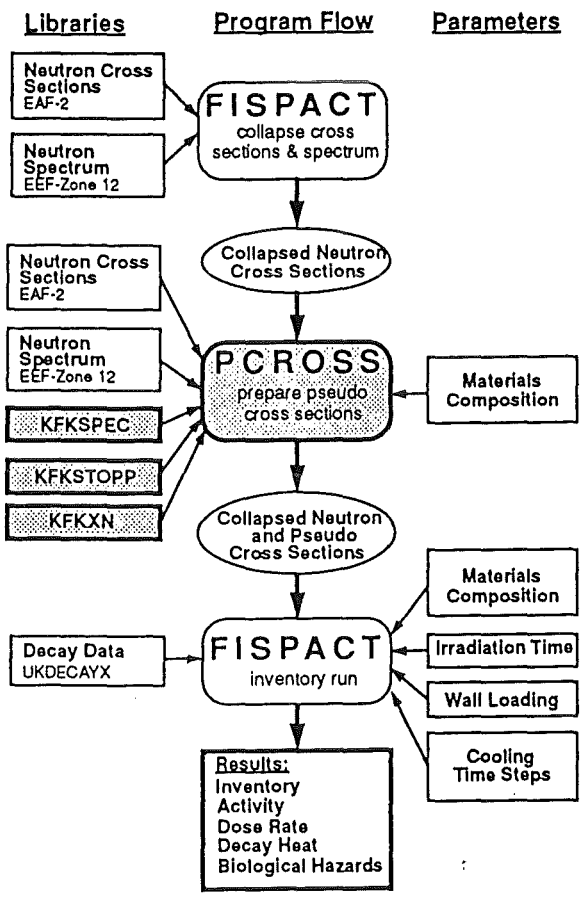

Fig. 1: Flow chart of the FISPACT code including sequential (x,n)-reactions: Hatched areas indicate code modifications by KfK.

2. Consequences of Activation Calculations for Material Development

The detailed calculations have shown that in 17 of 81 investigated elements an increase of at least one order of magnitude for one of the four calculated radiological quantities - activity, dose-rate, decay heat or biological hazard - has been observed by considering the sequential (x,n)-reactions. This is valid for base metals and major alloying elements like vanadium, chromium and manganese, but also for minor alloying elements and impurities like N or Y as a desoxidation medium. So-called "critical elements" like Ag and Bi which have earlier been identified as very important impurities for longterm activation even in very low concentrations, are fortunately not affected by sequential (x,n)-reactions; i.e. their values for maximum allowable concentrations need not be increased. Detailed informations about the effect of sequential (x,n)-reactions in single element inventory calculations on several radiological quantities are given in [2].

A first guide-line for the selection or development of alloys with low longterm activation can be derived from the radiological properties of elements which form the basis for technical materials. As a first criterion the time after shut-down of the reactor, in which the so- called hands-on level of dose rate is achieved can be used. A comparison of dose-rate data is given in Fig. 2 for elements like Si, Ti, V, Fe and others after irradiation corresponding to an integrated wall loading of 12,5 MWy/m². According to these data ceramic composites of type SiC (SiC/SiC$_f$) will never reach the hands-on level of

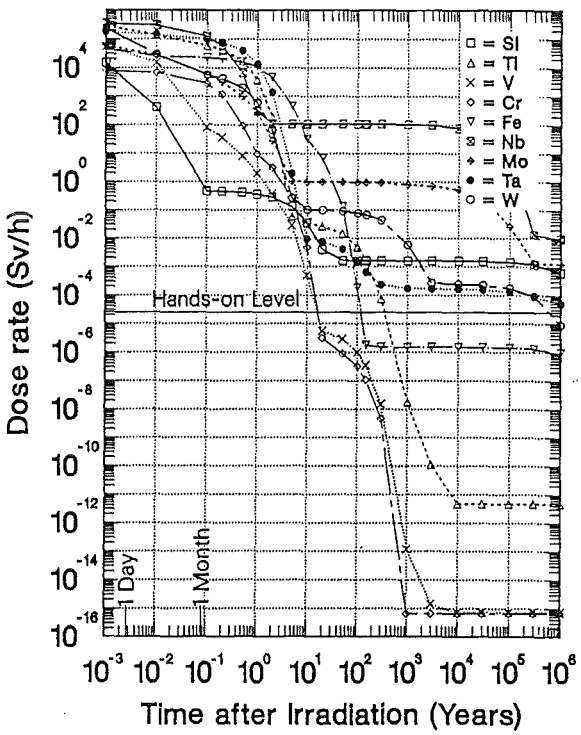

Fig. 2: γ-dose rate after irradiation with neutrons of 12.5 MWa/m².

25muS/h and a similar conclusion can easily be drawn for Al-based alloys.

Iron , the base metal for the best-known class of technical materials, reaches the hands-on level after about 100 years and hence fulfills the requirement for material recycling and waste deposition. The actual behaviour of specific iron-based alloys like ferritic- martensitic steels is, however, more dependent on the appropriate selection of alloying elements like Mo, Nb, W,Ta and others, as has recently been investigated [3]. In Fig. 3 the dose-rate decay data for an optimized ferritic-martensitic steel, denominated as OPTIFER-reference, developed at KfK are compared with those of SiC/SiCf composites and a V- 5Cr-5Ti alloy.

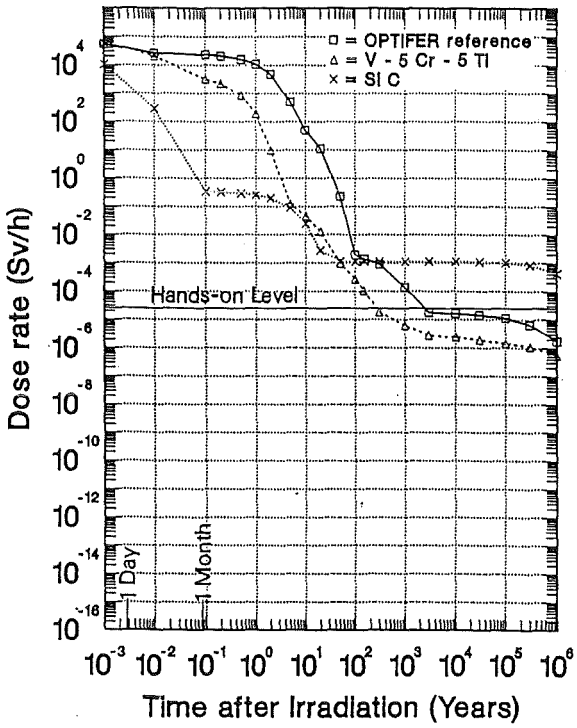

Fig. 3: γ-dose rates for three candidate structural materials.

The class of vanadium-chromium-titanium alloys offers theoretically a break- through to a class of alloys with an extremely low longterm activation, as can be expected, if only the results of the dose-rate calculations for the pure elements in Fig. 2 are taken into account. However, in order to achieve this low level of radioactivity the concentrations of "critical" tramp elements with a high longterm radioactivation have to be extremely low, as has been recently quantified in [2]. If, however, realistic impurity concentrations which can at the best be achieved with present production technique are assumed , the actual advantage of V-Cr-Ti alloys in comparison to the optimized ferritic steel of type OPTIFER is only about one order of magnitude.

In conclusion, the improvement and further development of the methods for calculating important radiological quantities is an important prerequisite for the development of structural and functional alloys with a reduced radioactivity.

Literature:

[1] S. Cierjacks, P. Oblozinsky, S. Kelzenberg and B. Rzehors; Fusion Technology 24 (1993), 277-287

[2] K. Ehrlich, S. Kelzenberg, H.D. Röhrig, L. Schäfer and M. Schirra; J. Nucl. Mat. 212-215 (1994), in press

[3] K. Ehrlich, S. Cierjacks, St. Kelzenberg and A. Möslang; The development of structural materials for reduced longterm activation; 17th. ASTM- Symposium, Sun Valley, Idahoe,USA, June 20-23, 1994, to be published in J. Nucl. Mater

Staff:

K. Ehrlich
S. Kelzenberg
A. Möslang

LAM 3 Development of Low Activation Martensitic Steel

Martensitic chrome steel types with little tendency to activation are being developed as materials for the First Wall and the blanket structures of fusion machines. This requires among others that major alloy elements such as Mo, Ni, Nb and Si, cannot be used. The results of activation calculations have recently been published [1] and have led to the specification of several Fe-Cr-alloys with V, W, Ta as minor alloying elements and Ce and Y as desoxidation media. Five alloys of this OPTIFER-series have been melted in 30 kg quantities by the Saarstahl-Company in a vacuum induction furnace and remelted in a vacuum-arc furnace and the cast ingots were then forged to 25×25 mm rods. Though in the material specification also the max. allowable concentrations of the tramp elements were given, it was clear that such tough specifications could not be fulfilled for these laboratory alloys because necessary high-purity material for the main ingots (esp. Fe) was not available. A comparison of the demanded low concentrations of undesirable elements and their actual concentrations gives a feeling which level of purity can be achieved by using the conventional way of steel making.

In the following first results of the metallurgical and mechanical properties of the OPTFER-alloys are given:

- In Fig. 1 the kinetic of the continuous transformation time diagram, CTT, is given for the CETA- and two OPTIFER alloys. According to these data, an undesirable perlite formation will only be expected, if cooling rates slower than 5°C/min are applied in the relevant temperature range between 800 and 500°C. This guarantees a fully martensitic structure even for thick structures, when applying the usual cooling procedures. In comparison to MANET II a very similar behaviour is observed.

- A further observation is in comparison to MANET II - an increase of the A_{C1}-temperature by 30−50°C. This is advantageous because the tempering temperature can be increased by the same T, which could eventually lower the DBTT.

- The hardening and temper behaviour of the W-containing OPTIFER-alloys corresponds to the CETA-alloy in Fig. 2, whereas the Ta-alloy has a lower hardening level. This can be correlated with the promoted formation of primary Ta-carbides. After tempering at 750°C the hardening of all alloys is very similar.

- The tensile strength data are for the given test temperature range from RT to 650°C higher than for the CETA-alloy, the latter provides higher ductility values, Fig. 3.

- The most important result is the strong improvement of the fracture toughness data of some of the new alloys, as manifested in Fig. 4a,b. In comparison to MANET II and CETA, the OPTIFER-alloys on the basis of CrWVTa (Heats 664 and 667) have a much higher upper shelf energy in impact tests and in addition a much lower DBT-temperature. The alloy based on CrVTa, however, does not show any improvements and can hence be excluded from further examinations.

- Finally in Fig. 5 the results of the chemical analysis of some elements of the OPTIFER-alloys are plotted and compared with the max. allowable concentrations of undesired elements. Most important for the longterm activation is the high concentration of Nb, which exceeds the max. allowable concentration by three to four orders of magnitude and hence governs the longterm activity.

The dependence of the tensile strength upon the tempering temperature and the test temperature was investigated in collaboration with CIEMAT. The long-time resistance against tempering influence ("aging") and creep-rupture tests are running.

The microstructural investigations show, that the grain boundaries are decorated with $M_{23}C_6$ (M = Cr + other metals), and Ce fix the S-impurities and so improves the ductility.

Literature:

[1] L. Schäfer, H. Kempe:
Metallkundliche und mechanische Untersuchungen an dem schwach aktivierbaren martensitischen Chromstahl OPTIFER-IV, Chg. 986489. KfK 5353 (1994).

Staff:

K. Ehrlich
H. Kempe
E. Materna-Morris
W. Meyer
L. Schäfer
M. Schirra

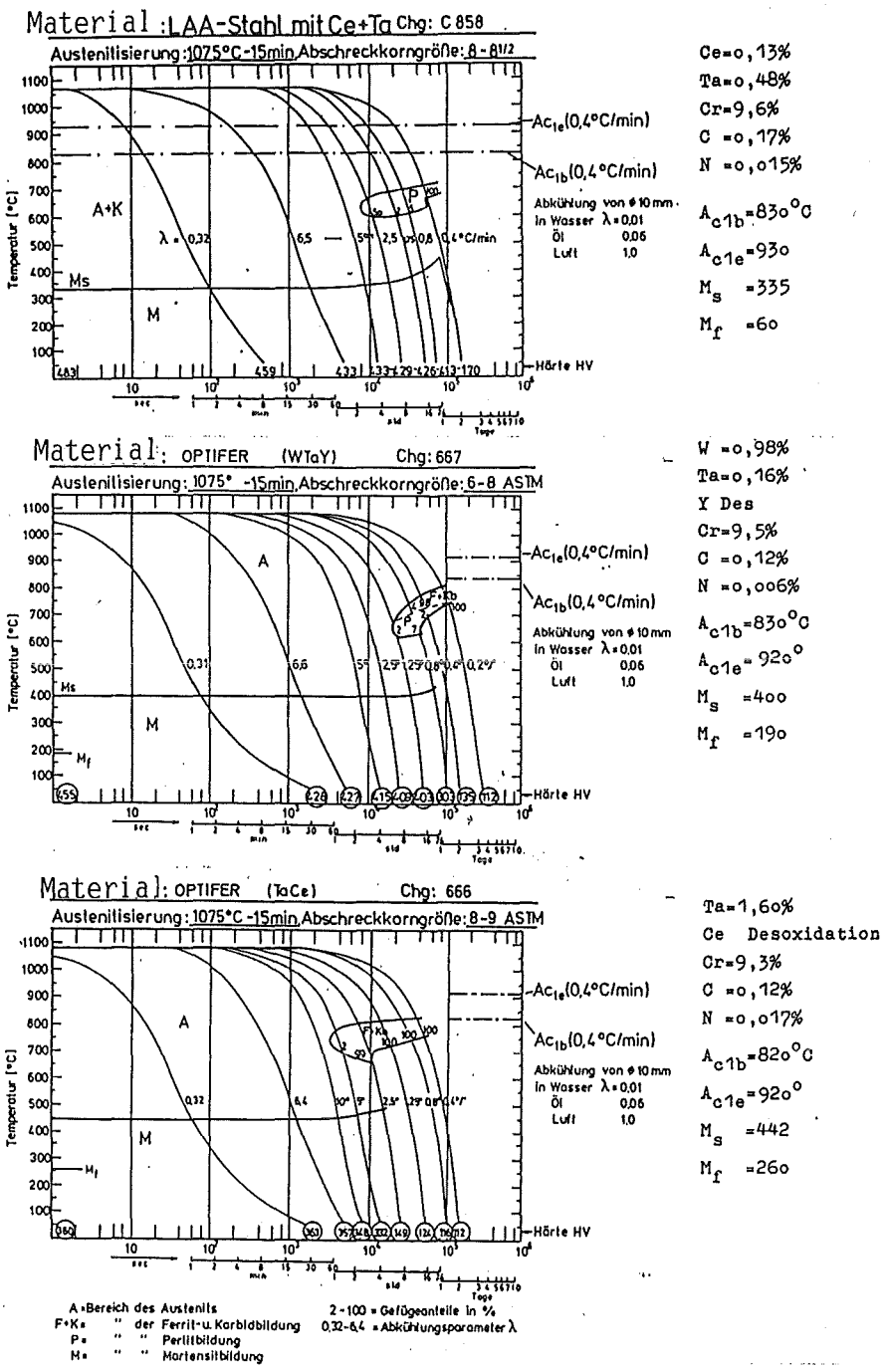

Fig. 1: TTT-diagrams for continuous cooling

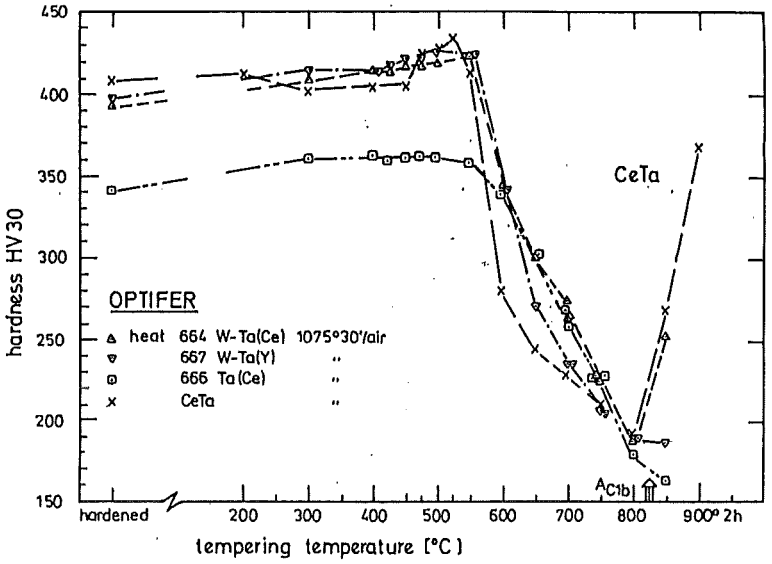

Fig. 2: Tempering-diagram

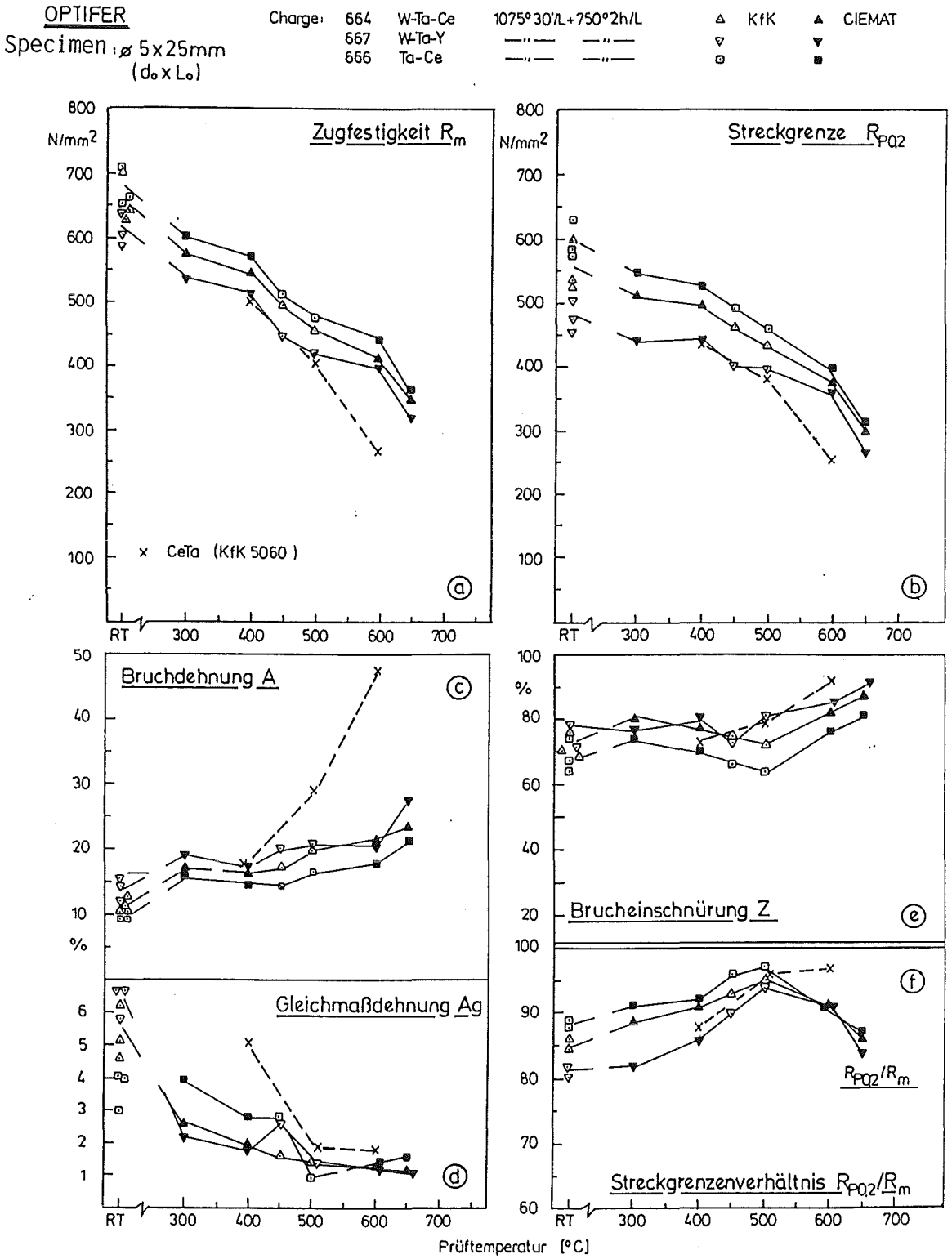

Fig. 3: Tensile-test results vs. test-temperature for OPTIFER-alloys

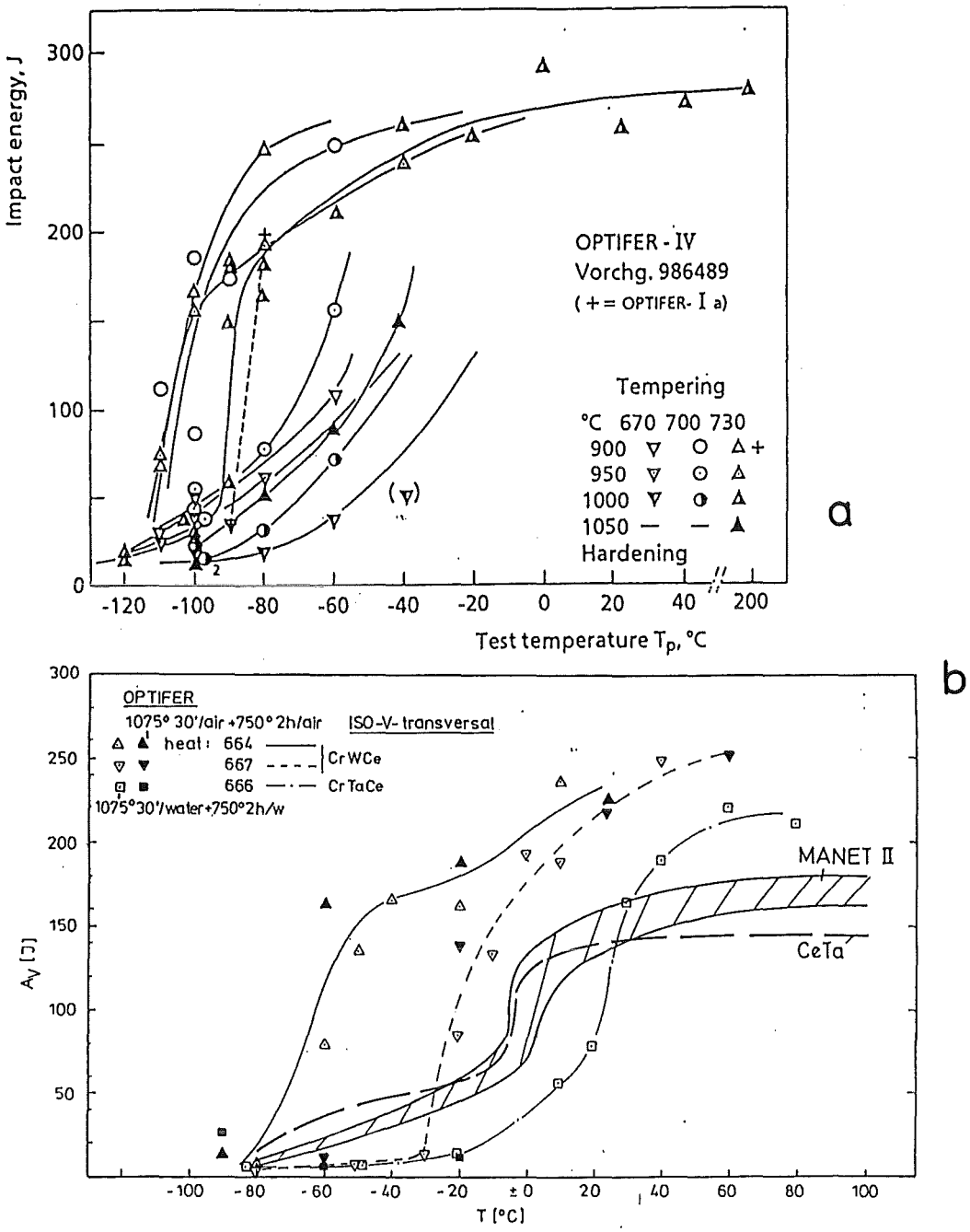

Fig. 4: Impact energy vs. test temperature

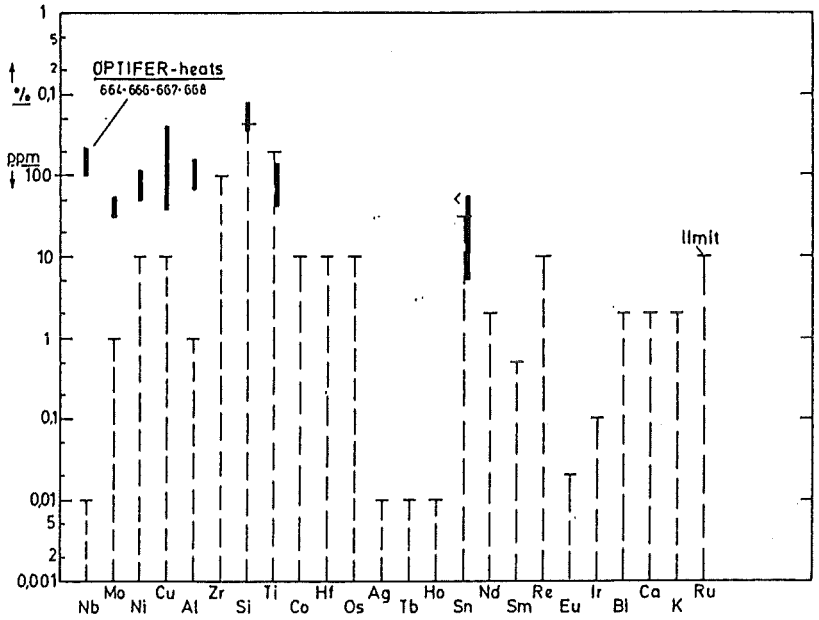

Fig. 5: Undesirable tramp-elements in LA-steels

MANET 1.1 Characterization and Optimization of MANET-II-Steel

A martensitic stainless steel, MANET-II, with 10% chromium has been developed as a material for the first wall and blanket structures of a fusion device. For this application the DBTT of impact tests has to be as low as possible and the 0.2% offset yield strength must be high.The upper shelf energies of MANET-II are sufficient, but the DBTT of the impact energy is still too high (ca. 0°C). Therefore, an improvement of the mechanical properties tested here had been attempted. The austenizing temperature T_{AU} and the annealing temperature T_{AN} had been varied systematically. Figure 1 shows the DBTT=T (A_V=90J) and the 0.2% offset yield strength, $R_{p0.2}$ (500°C), in dependence of the thermal treatment. The most advantageous combination of high strength and low DBTT has been reached using T_{AU}=900°C and T_{AN}=700°C. This tempering improves the DBTT from 0°C to −30°C an the yield strength from 456 to 518 MPa [1].

As is obvious from the notch bar impact tests, the transition temperature attained for the second MANET charge was far better, this may be attributed above all to the reduction of the zirconium content from 0.1% about 0.01%. In MANET I charge, the large Zr (C, N) primary carbides considerably influenced the fracture behaviour. Now, Zr (C, N) still is to be found on the fracture surfaces, fracture behaviour, however, is no longer affected that strongly by it. By addition of zirconium, the adverse effect of MnS could not be reduced, as the sulfur not occur in the form of a mixed crystal with zirconium. Sulfur is captured by Zr (C, N), but as complete MnS. This means that MnS and NbC exist in the form of bead surrounding the Zr (C, N) and again a separation of MnS and the matrix takes place.

Literature:

[1] L. Schäfer: "Kerbschlag- und Zugeigenschaften des Stahles MANET-II und deren Verbesserung durch Optimierung der Vergütung". KfK-Bericht 5245 (1993), Kernforschungszentrum Karlsruhe.

Staff:

E. Materna-Morris
W. Meyer
L.Schäfer
M. Schirra

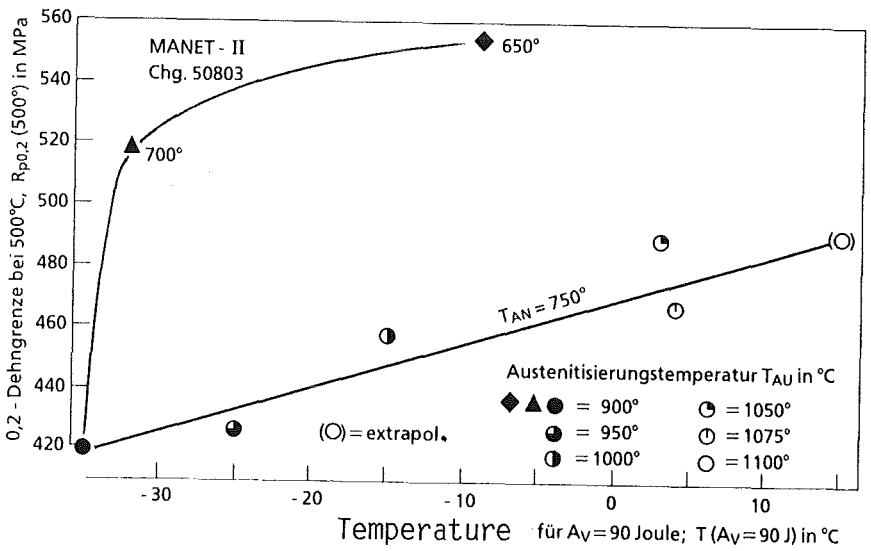

Fig. 1: DBTT≈T (A_V=90 J) and 0.2% offset yield strength $R_{p0.2}$ (500°C) of the steel MANET-II in dependence of the thermal treatment.

MANET 2.3 Diffusion Welding

Within the framework of activities to develop construction elements for highly loaded blanket structures of a DEMO fusion reactor a technique of diffusion bonding is ivestigated which allows structural plates with inner coolant channels to be made from MANET 2.

In two test series the most vavourable diffusion bonding parameters were determined und specimens for quality tests were fabricated. In a first test series involving small specimens provided with coolant and inspection channels, 80 mm in diameter, the most favourable bonding parameters were determined for conditioning the surfaces to be joined - rolled, milled, ground surfaces or surfaces with intermediate nickel layers - as well as for pressure and temperature.

In a subsequent step three specimen plates, 320 mm in diameter (Fig. 1) and provided with a typical first-wall coolant channel geometry, were bonded using the optimum parameters.

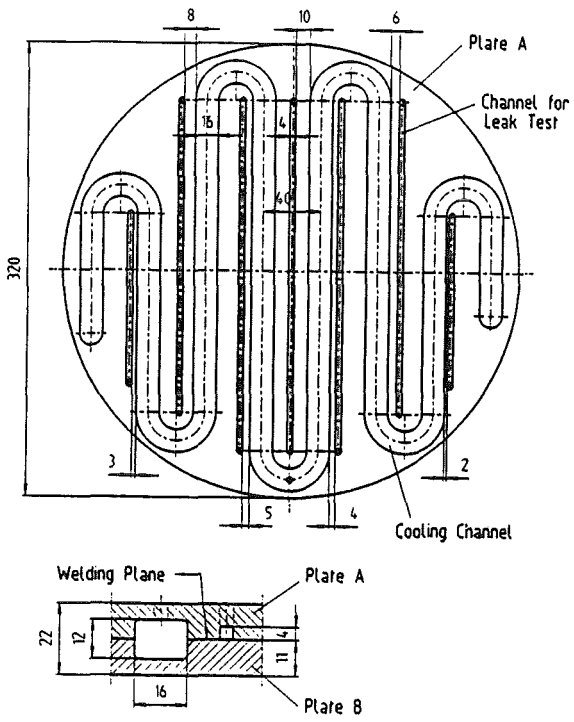

Fig. 1: MANET 2-plates for diffusion bonding tests.

The bonding tests were performed on behalf of KfK by the Forschungsinstitut für Kerntechnik und Energiewandlung, Stuttgart. In the high-vacuum diffusion bonding facility of that institute parts up to 330 mm in diameter can be bonded. Heating is achieved through radiation by a medium-frequency heating system; the maximum temperature attained is 1800°C. The mechanical pressure is supplied by hydraulic displacement of plungers and pressure plates. The distance covered by the plunger is 520 mm so that several pairs of plates can be bonded in one operation.

Results

The best bonding results have been obtained for the specimens with finely ground surfaces - roughness ≤3 µm - and for specimens with an electroplated, about 20 µm thick intermediate nickel layer. The bonding temperature was 980°C and 1050°C, respectively. Bonding was made in two phases of one hour duration each. During the first phase the roughness peaks were adjusted at high pressure - 30 MPa and 18 MPa, respectively - until complete contact of the faces was achieved; this was followed by diffusion bonding at 7 MPa pressure.

Bending tests with these specimens showed that the strength was nearly equivalent to that of the base material.

Figure 2 is a micrograph of a specimen with finely ground faces to be joined. The positions of the faces of the two plates to be joined have been marked by arrows. A regular structure with fine grains can be observed beyond the bonded zone into the base material.

He-leak tests performed on the three 320 mm specimen plates at 80 bar and 150 bar internal pressure of the cooling coils provided evidence of tightness conforming to the detection limit of the instrument used in the leak test. The narrowest bonded line was 2 mm in width.

Staff:

G. Reimann

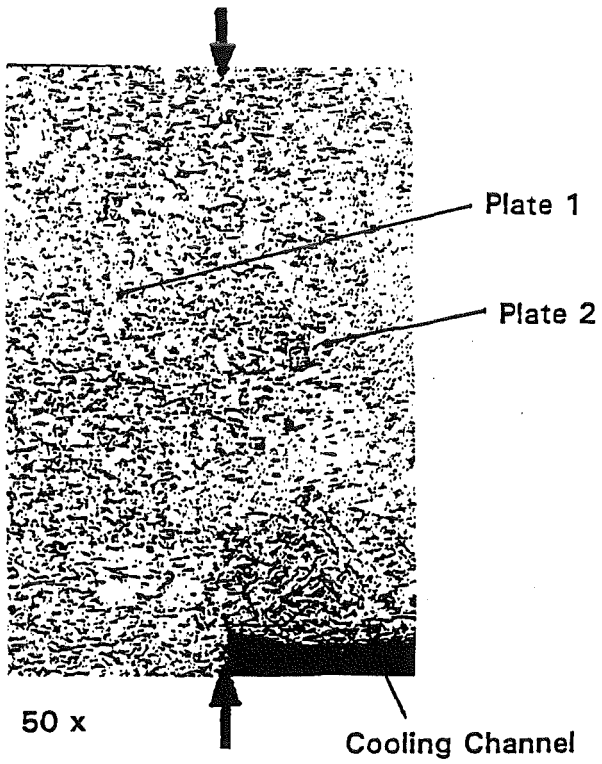

Fig. 2: Micrograph of a diffusion bonded specimen.

MANET 3.2 Pre- and Post-Irradiation Fatigue Properties of MANET Steel

Thermal cycling of large components is a serious problem for the designer. The structure considered in the present case is the first wall of a fusion reactor. Its surface, in the actual design concept, will be subjected to radiation heating from the plasma facing side which may lead to severe thermal stresses. Due to the discontinuous operational mode, thermal cycling will generate oscillating temperature gradients. These, depending on the loading conditions, will cause elastic or elasto-plastic reversed deformation, giving rise to thermal fatigue which at present is considered as the most detrimental lifetime phenomenon for the structure considered. The investigations of MANET 3.2 are devoted to this problem.

The studies to be reported within MANET 3.2 are:

- The influence of temperature and hold-times upon isothermal low-cycle fatigue behaviour of MANET I and II at 450°C and 550°C and a strain rate of 3×10^{-3}/s on S-GRIM specimens.
- Prediction of number of cycles to failure of thermal fatigued MANET I from isothermal LCF data of MANET I.
- Comparison between thermal fatigue data from hourglass shaped and cylindrical MANET II samples.

1. Isothermal Fatigue of MANET

Tests on MANET I with hold-times in tension and compression (symmetrical hold-times) have been finished. The results show, that there is only a small additional decrease of the number of cycles to fracture, compared with results of compression dwell-time tests. In order to minimize test times of further tests on this type of material, it therefore seems to be adequate, to take mainly into consideration compression hold-time tests. An example for the different loading conditions (hold-time = three minutes) is given in Fig. 1 for a test temperature of 450°C. This behaviour can also be observed at 550°C.

Fracture surfaces of MANET I specimens, tested at 550°C with hold-times in tension up to 30 minutes, show characteristic fatigue striations, which mark the position of the crack front after each fatigue cycle. This gives an indication, that - in contrast to austenitic steels - fatigue damage plays the dominating role and consequently the number of cycles to fracture is less reduced for this type of test as compared to compression dwell-time experiments.

In contrast to the above mentioned behaviour, for tests under compression hold-time conditions a structure can be observed, which is predominantly similar to a dimpled fracture. The smaller number of striations is an indication, that for this loading type mainly creep damage is the dominating damage mode. The dimples may be crack

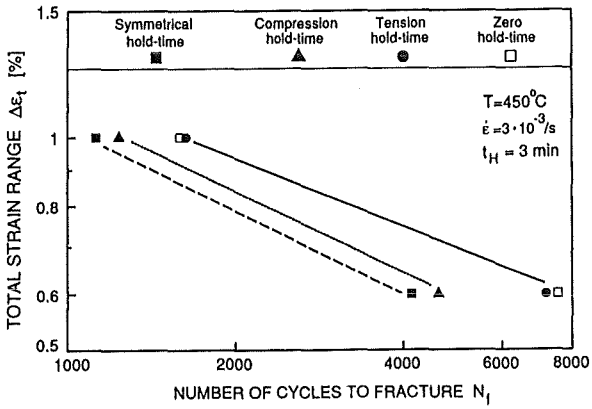

Fig. 1: Number of cycles to fracture versus strain range for different hold-time loading conditions for S-GRIM specimens of MANET I.

initiators, which decrease the number of cycles to fracture significantly, more than found in tension hold-time tests.

For the second heat of DIN 1.4914, MANET II, the Al/N - ratio has been raised to a higher level in order to avoid creep instabilities, mainly at higher temperatures. Fatigue tests on MANET II are on the way to examine, to what extend this improvement of chemical composition has an influence on lifetime. This is of general interest, especially for hold-time experiments, if creep damage is involved in the failure mechanism.

First results on S-GRIM specimens for a test temperature of 550°C are plotted in Fig. 2. There from it is obvious, that the numbers of cycles to fracture for MANET II (open circles) are about 30% lower as compared to MANET I (closed circles).

2. Thermal fatigue of MANET

2.1 Thermomechanical fatigue of MANET I

Thermomechanical and isothermal strain controlled fatigue (TMF and LCF) experiments had been performed in air on hollow hourglass samples of MANET I in the tempered condition of 750°C/2h. The cyclic load behaviour of a TMF data set can be simulated by tensional LCF data at the lower temperature

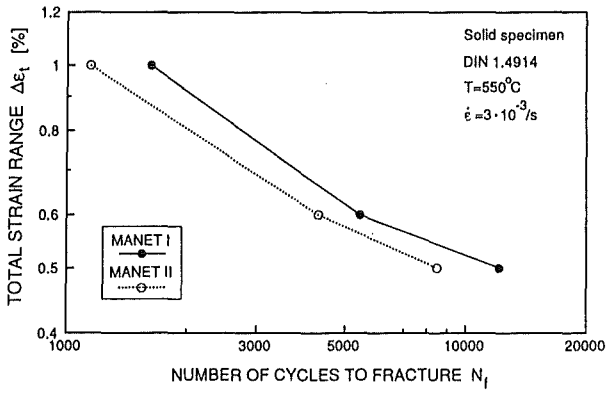

Fig. 2: Number of cycles to fracture versus total strain range for S-GRIM specimens of MANET I and MANET II (T = 550°C).

as well as by compressional LCF data at the higher temperature of a TMF experiment. But the number of cycles of TMF data are very different from LCF data. As an extrapolation method, to extend the LCF data set, a two parametric allometric function from [1] gives a good agreement. To define a criterion for the prediction of number of cycles to failure N_f a combination of two equations is utilized, calculating plastic strain ε_{pl}-values and from these the N_f values.

The calculated load range values are correlated with ε_{pl}-values by another equation from [2]. The resultant prediction is very good. Finally gives a failure criterion the last equation. This equation will be solved iteratively by increasing ε_{pl} from ε_{pl} (N=1) to ε_{pl} (N=infinity). The cutting point of this curve with the predicted one gives the requested N_f value.

A preliminary comparison between predicted and experimental N_f values from TMF experiments seems to be encouraging.

2.2 Thermal fatigue of MANET II

At present the ferritic-martensitic Cr-steel MANET II is under investigation. This steel has the German Steel Denomination Nr. 1.4914. The MANET II material has the Heat Nr. 50805.

Hollow hourglass shaped as well as cylindrical specimen were fabricated from MANET II perpendicular to the rolling direction and in the centerline of the sheet - and than heat treated.

MANET II samples had been thermally fatigued by triangle temperature cycles with constant heating and cooling rates $\dot{T} = \pm 5.8$ K/s in a range of a fixed low temperature T_L (200°C) and a variable high temperature T_H (600°C to 700°C).

Due the fact, that the fatigue testing device is no enabled to control neither the total mechanical strain range $\Delta\varepsilon_{t,m}$ nor the stress range $\Delta\sigma$, quantities like $\Delta\sigma$, $\Delta\varepsilon_{t,m}$ and the plastic mechanical strain $\Delta\varepsilon_{p,m}$ change with number of cycles. Hence only the measured values at $N_f/2$ are taken for any comparison.

The small thermal elongation of the ferritic - martensitic steels causes total mechanical strain ranges of both kinds of samples between 0.3% and 0.6% during triangular thermal fatigue experiments. From the data sets of thermally cycled cylindrical and hourglass samples of MANET II the total mechanical strain ranges $\Delta\varepsilon_{t,m}$ at $N_f/2$ are plotted versus the number of cycles to failure N_f in Fig. 3. By increasing ΔT, $\Delta\varepsilon_{p,m}$ at $N_f/2$ increases and leads to smaller N_f-values. This effect is mainly driven by the ΔT-influence on the plastic mechanical strain $\Delta\varepsilon_{p,m}$ at $N_f/2$, which is plotted versus N_f for both kinds of MANET II-samples in Fig. 4. The $\Delta\varepsilon_{p,m}$-values at $N_f/2$ range from 0.015% up to 0.2%.

With increasing ΔT the amount of plastic mechanical strain range increases due to the growing compressional creep contribution at each high temperature cycle.

In fig. 5 are compared the total stresses $\Delta\sigma_t$ at $N_f/2$ from both

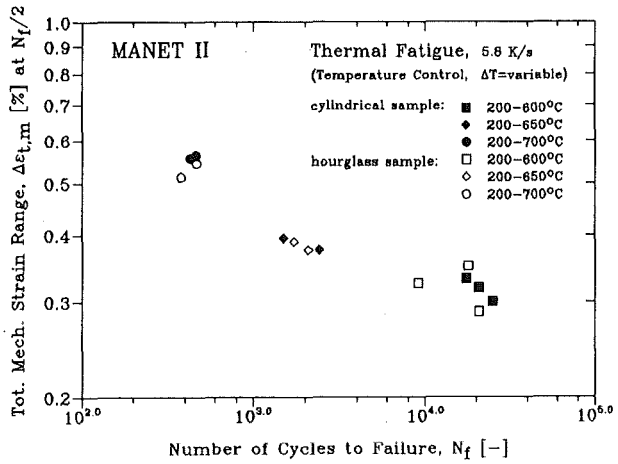

Fig. 3: Comparison of thermal fatigue data of cylindrical and hourglass shaped samples of MANET II in a $\Delta\varepsilon_{t,m}$ at $N_f/2$ versus N_f diagram.

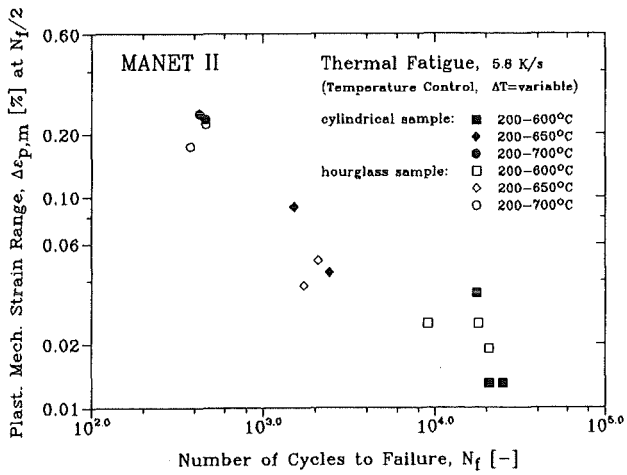

Fig. 4: Comparison of thermal fatigue data of cylindrical and hourglass shaped samples of MANET II in a $\Delta\varepsilon_{p,m}$ at $N_f/2$ versus N_f diagram.

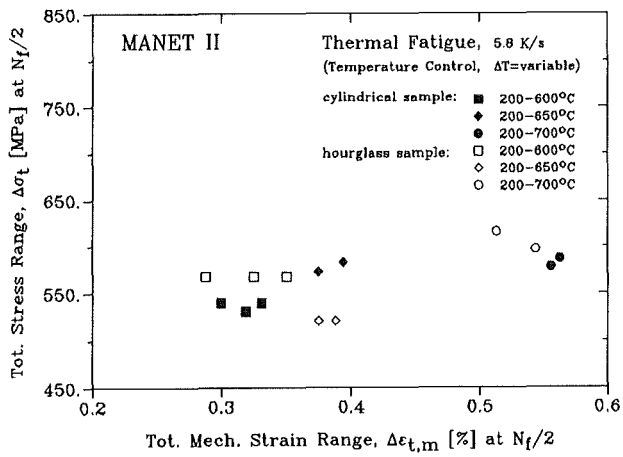

Fig. 5: Comparison of thermal fatigue data of cylindrical and hourglass shaped samples of MANET II in a $\Delta\sigma_t$ at $N_f/2$ versus $\Delta\varepsilon_{t,m}$, at $N_f/2$ diagram.

kinds of MANET II-samples, obtained during thermal fatigue. The $\Delta\sigma_t$-values at $N_f/2$ of MANET II increase up to a maximum value of about 600 Mpa with increasing ΔT and $\Delta\varepsilon_{t,m}$ at $N_f/2$.

Generally can be stated from this comparison, that the sample geometry has a neglectible influence on thermal fatigued MANET II data, if the gauge length is 8 mm, as it is applied in case of thermal fatigue experiments.

Literature:

[1] J. Hartung:
Statistik: Lehr- und Handbuch der angewandten Statistik, 8th edition, Oldenbourg Verlag, München, Wien, pp. 654-660, 1991.

[2] F. Wolter:
unpublished internal report No. 31.02.02 P15A, July 1993.

[3] C. Petersen:
Thermal Fatigue on MANET II, 6th International Conference on Fusion Reactor Materials, Stresa, Italy, 27.09.-01.10.1993, Pap.: ICFRM6/L006, to be publ. in J. of Nucl. Materials.

[4] C. Petersen and F. Wolter:
Thermal and Thermomechanical Fatigue of a Martensitic 10.6% Cr-Steel, Proceedings of MATEC 93, Paris-Marne la Vallee, France, 06.-07.12.1993.

[5] I. Alvarez-Armas, A. F. Armas and C. Petersen:
Thermal Fatigue of a 12% Chromium Martensitic Stainless Steel, Fatigue Fract. Engng. Mater. Struct., Vol. 17, No. 6, pp. 671-681, 1994.

[6] F. Wolter and C. Petersen:
Thermal and Thermomechanical Fatigue of a Martensitic 10.6% Cr-Steel, published in Proceedings of the Annual Meeting on Nuclear Technology '94, Stuttgart, Germany, 17.-19.05.1994.

[7] C. Petersen and F. Wolter:
Prediction of thermomechanical fatigue on MANET I, 18th SOFT, Karlsruhe, Germany, 22.08.-26.09. 1994. Pap.: PB - 128, to be published in J. of Nucl. Materials.

Staff:

C. Petersen
M. Pfeifenroth
D. Rodrian
W. Scheibe
R. Schmitt
H. Schneider
W. Schweiger
(F. Wolter)

MANET 3.4 Pre- and Post-Irradiation Fracture Toughness

The use of ferritic-martensitic steel alloys as structural material for the first wall and blanket of a future fusion device is advantageous because of their small tendency for swelling, irradiation creep and high temperature irradiation embrittlement (caused by helium). But like all materials with body centered cubic lattice ferritic-martensitic alloys show a low temperature embrittlement. This negative effect is worsened by neutron irradiation. A possible application of ferritic-martensitic alloys within fusion technology primarily depends on their irradiation induced embrittlement behaviour. So the aims of the investigations in subtask 3.4 MAN-303B are

- the characterisation of radiation embrittlement dependent on irradiation temperature and exposure dose,
- a reduction of the ductile-to-brittle transition temperature (DBTT) by variation of the chemical contents and material structure of different alloys,
- the characterisation of the radiation hardening recovery (self annealing behaviour) of irradiated steels.

The embrittlement studies are carried out using results of sub-size Charpy impact tests with miniaturised notched-bar specimens. The radiation recovery is economically measured by hardness tests on the available parts of Charpy specimens after different annealing treatments.

Experimental details

The impact tests were carried out in high precision instrumented impact test facilities developed at IMF-II. Two installations are available for the experiments, one of which was installed in a Hot Cell for examining irradiated specimens. Technical data: impact velocity: 3.85 m/sec, sampling rate: 1 MHz, semi-automatic specimen warming, cooling and loading system with a test temperature range of - 180°C to+600°C and PC-controlled test execution. The type of specimen used is specified in the European Standard under the term of KLST (3 mm×4 mm×27 mm, notch depth 1 mm).

Within the experiment FRUST/SIENA KLST specimens fabricated of MANET-I steel with different heat treatments were irradiated in the HFR in Petten at temperatures of 290°C, 370°C, 390°C, 420°C and 470°C to doses of 5 dpa, 10 dpa and 15 dpa. This irradiation experiment is completed and most of the specimens have been tested.

Within the low dose experiment MANITU (sometimes referred to as SIENA-II) several 9–12% CrMoV(Nb) steels including MANET and 7–10% CrWVTa low activation alloys including OPTIFER are irradiated at temperatures of 250°C, 300°C, 350°C, 400°C and 450°C to exposure doses of 0.2 dpa, 0.8 dpa and 2.4 dpa in the HFR. The purpose of this programme is to select the most promising alloys as well as to fill the parameter gaps of FRUST/SIENA.

Results

The irradiation induced embrittlement is characterised and represented by the rise in transition temperature and decline in the upper shelf energy which are referred to as DDBTT and DUSE.

On the basis of the great number of specimens irradiated and tested at various conditions it was possible to describe the impact characteristics of MANET-I type steel as a function of heat treatment, irradiation temperature and dose.

In the unirradiated condition normalisation treatment slightly improves the impact characteristics of MANET-I type alloy. The best properties are achieved by normalisation for two hours at 980°C. After irradiation the influence of normalisation temperature was within the normal scatter of results, i.e. no difference in behaviour can be recognised between the test materials normalised at 950°C and 980°C, respectively. The transition temperature (DBTT) decreases essentially as a linear function of the tempering temperature in the range between 600°C and 780°C (in the range between 750°C and the tempering limit at 780°C a slight deviation from this linearity is found). The relationship between the upper shelf energy (USE) and the tempering temperature can be fitted by a quasi exponential relationship. Further, the Charpy results have shown, that the irradiation induced shifts of the impact properties (DDBTT and DUSE) are not influenced by the tempering treatment. This leads to the more general assumption that these shifts are independent of the initial material constitution (within the same material composition).

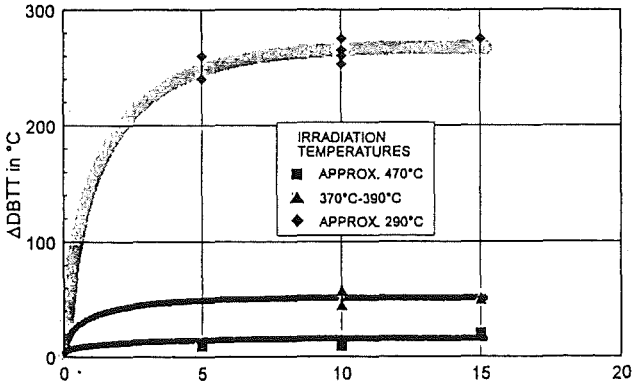

Fig.1

In MANET-I type steel quasi saturation in the deterioration of impact properties is occurring at a dose range of approx. 10–15 dpa (see Fig. 1). For a more precise determination of the dose dependence experiments at radiation doses below 5 dpa would be necessary. This is one of the objectives of the MANITU program. If it turns out that saturation starts at even lower dose levels there would be no practical benefit from recovery treatments. Nevertheless first results of self

annealing tests have turned out that a post-irradiation heat treatment, e.g. 450°C for 30 minutes, leads to a remarkable recovery in hardness and impact properties.

On the basis of the findings mentioned above, the DDBTT and DUSE values were combined to one data set, independent of the different tempering temperatures. The influence of irradiation temperature on the DDBTT levels is now plotted in Figure 2. The curve drawn through the measurement points is well evidenced in the upper temperature range, where the zero line is practically reached above an irradiation temperature of approx. 500°C. As the results with the DUSE levels show the same, one can state that at irradiation temperatures above approx. 500°C there is practically no radiation induced deterioration in the impact characteristics. On the other hand, while the increase in DDBTT values is still moderate for irradiation temperatures down to 370°C there is a remarkable rise between 370°C and 290°C. This might be explained by the fact that self-annealing of irradiation-induced defects can no longer take place at the lower temperatures. For a better understanding of the Charpy properties especially at irradiation temperatures below 370°C we certainly need further experiments. But a comparison with tensile test results already leads to the hypothesis, that a plateau of embrittlement is reached at an irradiation temperature below 340°C. This would correlate with Charpy impact tests of another 1.4914 type steel (wrapper tube alloy) irradiated at temperatures of 260°C, 310°C and 350°C to exposure doses of 2 – 3 dpa. Based on the above assumptions the shaded curve has been incorporated in Fig. 2.

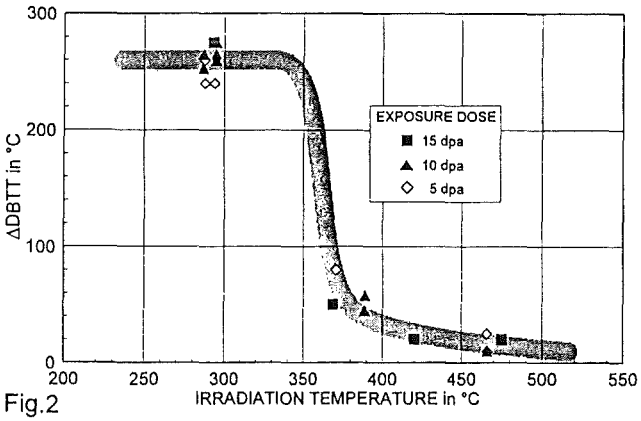

Fig.2

As mentioned above a comprehensive test matrix has been set up for the irradiation programme MANITU to account for the impact behaviour in the low dose as well as the low temperature irradiation area. By the inclusion of materials like F82H, OPTIFER, GA3X and ORNL 9Cr-2WVTa it will at the same time be possible to investigate the potential of ferritic steels with a reduced Cr content for an alleviation or even solution of the DBTT-problem.

Conclusions

The results of the FRUST/SIENA programme have shown that the irradiation induced embrittlement with MANET-I type steel becomes a problem below temperatures of 370°C. Appropriate heat treatments can improve the absolute values of DBTT and USE but do not affect the radiation induced shifts. So the next step is to examine, within MANITU, whether or not the other fusion relevant alloys come up with better before- and/or post-irradiation properties.

However, the very next step within the Long-term Materials Development Programme should be the start of a new irradiation experiment including a few structural materials selected on the base of the first results from MANITU. The irradiation parameters should be chosen as fusion-relevant as possible, i.e. high neutron fluence for high dose levels and especially low irradiation temperatures. With the results of these examinations (together with MANITU) we should be able to complete the Assessment Phase I concerning the ferritic-martensitic steels.

Literature:

[1] C. Wassilew †, K. Ehrlich, Effect of Neutron Irradiation on the Dynamic Fracture Toughness Behaviour of the 12% Cr Steel MANET-I Investigated Using Subsize V-notch Specimens, J. Nucl. Mat. 191-194 (1992), 850-854.

[2] C. Wassilew †, M. Rieth, B. Dafferner, Effect of Neutron Irradiation on the Dynamic Fracture Toughness Behaviour of the 12% Cr Steel MANET-I, in: Proceedings of the Workshop on Ferritic/Martensitic Steels, Vol. II, JAERI Tokyo, 26-28 October, 1992.

[3] M. Rieth, B. Dafferner, C. Wassilew †, Ein modulares Softwarepaket für die Analyse, Auswertung und Verwaltung von instrumentierten Kerbschlagbiegeversuchsdaten, in: Proceedings of the Annual Meeting on Nuclear Technology, Köln, Germany, 25-27 May, 1993.

[4] M. Rieth, B. Dafferner, C. Wassilew †, Ein flexibles System zur Durchführung, Auswertung und Analyse von instrumentierten Kerbschlagbiegeversuchen, in: Proceedings of the Annual Meeting on Nuclear Technology, Köln, Germany, 25-27 May, 1993.

[5] M. Rieth, B. Dafferner, C. Wassilew †, Der Einfluß von Wärmebehandlung und Neutronenbestrahlung auf die Kerbschlageigenschaften des martensitischen 10,6% Cr-Stahls MANET-I (Effect of Heat Treatment and Neutron Irradiation on the Charpy Impact Properties of the Martensitic 10.6% Cr Steel MANET-I), KfK Report 5243, Kernforschungszentrum Karlsruhe, June 1993.

[6] M. Rieth, B. Dafferner, C. Wassilew †, Der Einfluß der chemischen Zusammensetzung verschiedener Hüllkastenwerkstoffe vom Typ 1.4914 auf die Kerbschlageigenschaften vor und nach Neutronenbestrahlung

(Influence of the Chemical Composition of Different 1.4914 Type Wrapper Tube Materials on the Charpy Properties before and after Neutron Irradiation), in: Proceedings of the Annual Meeting on Nuclear Technology, Stuttgart, Germany, 17-19 May, 1994, pp. 347-350.

[7] M. Rieth, B. Dafferner, C. Wassilew †, Ein empirisches Modell der Kerbschlageigenschaften des Martensitischen 10,6% Cr-Stahls MANET-I in Abhängigkeit von Wärmebehandlung und Neutronenbestrahlung, in: Proceedings of the Annual Meeting on Nuclear Technology, Stuttgart, Germany, 17-19 May, 1994.

Staff:

B. Dafferner
A. Drasl
W. Kunisch
H. Ries
M. Rieth
O. Romer

MAT 5 Ion-Beam Irradiation Fatigue and Creep Fatigue Tests

The Dual Beam Facility of KfK, where α-particles (≤40 MeV) are focused onto a target, was developed as a research tool for materials within the European Fusion Technology Programme. This high energy Dual Beam Technique allows the simulation of fusion neutrons by the systematic variation of hydrogen, helium, and damage production in thick metal and ceramic specimens as well as the simulation of Tokamak relevant thermal and mechanical loads in proposed plasma-facing materials.

A specific feature of next step tokamak fusion devices are the plasma burn and off-burn periods. Depending on the operating conditions and the thermal conductivity of plasma facing structural components, these oscillating temperature gradients will cause thermal fatigue or creep fatigue which under neutron irradiation are considered to be one of the main lifetime-limiting failure modes. After several years of development novel experiments can be performed at the cyclotron facility of KfK, which allows a close simulation of realistic fusion conditions by simultaneous irradiation and fatigue loading. Detailed results on in-beam fatigue experiments at 420°C under fusion relevant loading conditions are published in the previous annual report.

A comparison of in-beam fatigue tests with unirradiated control and with conventional postirradiation tests has e.g. shown, that at least in MANET steels any fatigue life reduction in irradiated specimens can be linked to irradiation induced hardening. The importance of irradiation hardening is further confirmed by recent investigations showing a strong correlation between the irradiation induced strength and the deterioration of impact properties. Therefore, we have focussed in this reporting period the experimental activities mainly on postirradiation tensile tests to generate complete data sets on the temperature dependencies of the strength and ductility behavior as well as on the influence of helium and hydrogen. In addition to displacement damage helium and hydrogen has been introduced because for the next generation of fusion reactors production rates of about 100 appm He/yr and 400 appm H/yr are expected in typical structural alloys. The material used in this investigation was the ferritic/martensitic 12% Cr steel MANET I in the tempered condition.

1. Tensile properties after irradiation

A large number of sheet tensile specimens was simultaneously implanted between 80 and 500°C appm helium and 500 appm hydrogen at the Dual Beam Facility of KfK. The irradiations were performed in helium gas using a degraded 104 MeV a-particle beam to adjust the helium production rate and a degraded 30 MeV proton beam to adjust the hydrogen and damage generation rates. Special emphasise was put on faily low helium, hydrogen and damage production rates. After irradiation the specimens were tensile tested together with unirradiated control specimens at test temperatures equal to the irradiation temperature in a high vacuum furnace at a constant nominal strain rate of $\dot{\varepsilon}=1.2\times10^{-4}$ S^{-1}. In figs. 1 and 2 the tensile properties of specimens simultaneously implanted with α-particle and protons are shown and compared with only α-particle implanted specimens. These figures represent by far the most complete data sets with respect to the temperature dependeny of tensile properties after irradiation. The main conclusions are:

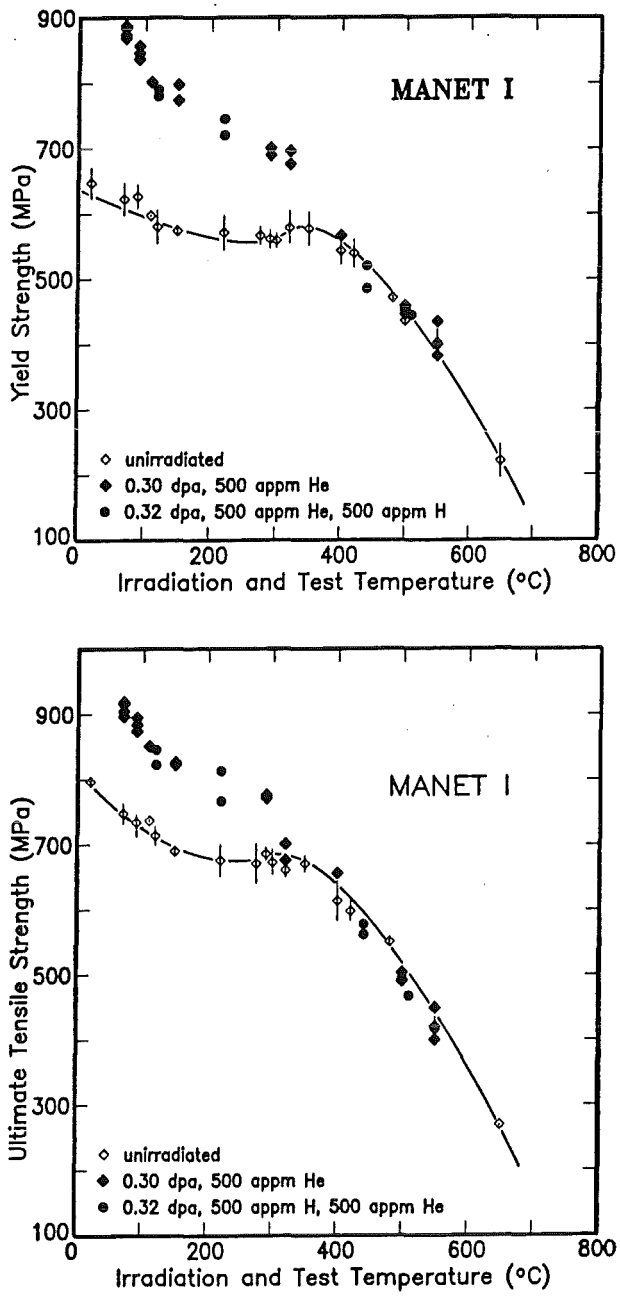

Fig. 1: Temperature dependency of the yield stress (a) and the total tensile stress (b) for MAANET I before (open symbols) and after irradiation (closed symbols).

Differences between helium implanted specimens and specimens simultaneously implanted with helium and hydrogen could not be observed. Therefore, synergistic effects between hydrogen, helium and irradiation induced

defects, if any, do not play a significant role on strength, ductility and embrittlement in the investigated parameter range.

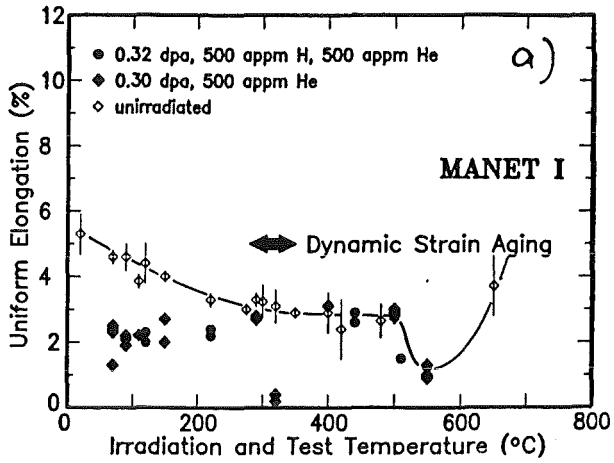

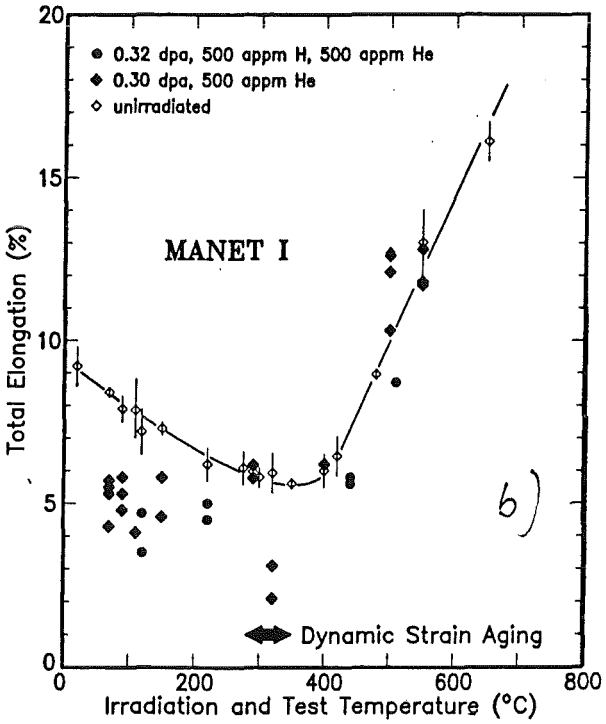

Fig. 2: Temperature dependency of the uniform elongation (A) and the total elongation (b) before and after irradiation.

The irradiation induced yield strength change (200 MPa at 100°C) decreases moderately with increasing temperature up to about 350°C and then changes rapidly into softening (about 50 MPa above 450°C). Although the dpa-dose was limited to 0.3 dpa, the irradiation induced hardening $\Delta\sigma_{Irr}$ is obvious. By analyzing various strengthening contributions the authors have shown, that a barrier model describes well the observed hardening in He-implanted specimens. It became also obvious, that $\Delta\sigma_{Irr}$ is mainly governed by the displacement damage. In that picture neutron irradiation induced hardening in the presence of helium occurs by the same process that occurs during dpa damage alone: Helium tends only to stabilize these defects.

Apart from the temperature region of dynamic strain aging (DSA), both uniform and total elongation were observed to be moderately sensitive to the implanatations (fig. 2). The reduction in total elongation was found to be less than 20% above 450°C and less than 55 % in the low temperature hardening region. Even in the temperature region of DSA there is no indication of a change in the fracture mode. Under all conditions investigated the rupture mode remains always ductile and transcrystalline. However, significant changes in ductility occurred between 280 and 350°C, where DSA was observed. In that temperature region, yield strength is close to ultimate tensile strength and uniform elongation drops from 3 to 0.3%. This small uniform elongation means, that little work hardening occurs, i.e. that total elongation is dominated by plastic deformation during the necking of the gauge length. In contrast to strength properties, helium generally has a significant effect on ductility and embrittlement below about 450°C: From a comparison with various neutron irradiation experiments it turns out, that at least below about 5 dpa the observed ductility reduction in helium containing specimens is governed by the helium concentration rather than by the dpa dose.

Fig. 1 and 2 also show, that below about 200°C, where neutron irradiated specimens are not available, $\Delta\sigma_{Irr}$ and the ductility reduction increase only moderately with decreasing temperature. Irradiation experiments around 200°C should therefore sufficiently describe also many low temperature properties.

Broad TEM investigation on irradiated and tensile tested samples confirm the general consensus of published data, that martensitic/ferritic steels like MANET show superior resistance against void swelling and high temperature He-embrittlement. The He-related swelling is less than 0.05% at all temperatures investigated and even after implantation of 3500 appm He, the bubble radius remained well below the critical radius for vacancy driven cavity growth.

2. In-beam fatigue tests at 250°C

While in-beam fatigue tests without and with 2 min hold times have been completed at 400–450°C, first in beam results on continuously push-pull (R=1) fatigue tested specimens at 250°C are available. In contrast to all conventional postirradiation tests the build-up of irradiation hardening with increasing dpa dose seems to be retarded at that temperature. Obviously during the cyclic motion of dislocation a fraction of irradiation induced point defects annihilates or is swept on inner surfaces. The first results at 250°C confirm the general trend, that radiation hardening is the main life time controlling mechanism.

Literature:

[1] K. K. Bae, K. Ehrlich and A. Möslang, "Tensile behavior and microstructure of the helium and hydrogen implanted 12 % Cr-Steel MANET", Journ. Nucl. Mater. 191 - 194 (1992) 905.

[2] R. Lindau and A. Möslang, "Fatigue tests on a ferritic-martensitic steel at 420°C: Comparison between in-situ and postirradiaiton properties"; ICFRM-6 conference, Stresa, Sept 27 - Oct. 1., 1993, accepted for Journ. Nucl. Mater.

[3] K. Ehrlich, S. Kelzenberg, A. Möslang, L. Schäfer and M. Schirra, in "Assessment of vanadium alloys for ITER application" eds.: W. Van Withenburg and V. van der Schaaf; ECN-Report ECN-RX--93-082 (1993).

[4] D. Preininger, "Plastische Instabilität - Theorie und Anwendung"; Hauptversammlung der DGM; Juni 1993, Friedrichshafen; Proceedings.

[5] K. Ehrlich, S. Kelzenberg, A. Möslang and M. Schirra, "Vanadium alloys: Assessment of mechanical properties and long term activation for ITER applications"; KTG-Tagung Stuttgart, May 17 - 19, 1994; Inforum Verlag; ISSN 0720-9297 (1994) p. 489.

Staff:

S. Baumgärtner
G. Bürkle
R. Lindau
A. Möslang
D. Preininger

Test Blanket Development

Introduction:

Within the European Fusion Technology Program blanket development is divided into work for the ITER basic machine and work for the DEMO-reactor. After establishing two European working groups KfK has concentrated its efforts on the development of DEMO relevant test blankets to be tested in ITER. In the DEMO-reactor, the potential of a fusion machine to produce electricity shall be tested for the first time. Consequently the test blankets have to be designed for DEMO relevance in terms of breeding rate, temperatures and pressure. Structural materials, maintainability, reliability and safety have to satisfy the more stringent requirements of power production in comparison with driver or shielding blankets for the ITER machine. These boundary conditions cannot be satisfied in full scale in the test positions available in ITER. Therefore the definition of test objects and the testing program are further important objectives of KfK besides the proof of DEMO relevance of the KfK blanket design alternatives.

The European Test Blanket Development Groups mentioned above deal with two development lines, one with helium cooled solid breeder, the other one with either selfcooled or water cooled liquid metal breeder. Both KfK designs, the selfcooled lithium-lead blanket and the helium cooled (breeder out of tube) solid breeder blanket are accepted alternatives within the European test blanket development program. A part of the work defined by the partners - KfK, CEA, ENEA and JRC Ispra - consists of common work, relevant to all blanket designs, whereas the design work itself is independent for the time being. It is foreseen to reduce the number of European DEMO relevant blanket alternatives from four to two in 1995, one solid breeder and one liquid metal breeder design, which will finally be tested in ITER.

The Solid Breeder Blanket Tasks (BS)

The solid breeder design work (Subtask BS DE-D) includes also small scale thermomechanical and fabricability tests and safety oriented studies. The KfK solid breeder material program (Subtask BS BR-D) has concentrated, in agreement with the European partners, on lithium orthosilicate. This subtask includes preparation, characterization, irradiation and postirradiation examination as well as measurement of the physical, chemical and mechanical properties. Of special interest are the in and out of pile tritium release studies, performed at KfK and within the common breeder development program in several European reactors. The behaviour of irradiated beryllium, especially the influence of large neutron fluences and high temperatures on swelling, embrittlement and tritium trapping as well as the inpile compatibility of beryllium with ceramic and structural material is being investigated in subtask BS BE-D.

The main non nuclear testing facility to prove the feasibility of KfK's solid breeder design is the helium loop HEBLO, in which elements as well as canister sections can be tested (Subtask BSNN-D).

The Liquid Metal Blanket Tasks (BL)

The design activities (Subtask BL DE-D) concentrate on a solution featuring an inboard / outboard selfcooled blanket with a helium cooled first wall, the so-called Dual Coolant Concept.

Of great importance to the development of the selfcooled blanket is the knowhow and the data base of magneto-hydrodynamic (MHD) behaviour of liquid metal flow aquired in theoretical and experimental studies of subtask BL MHD-D. The test facility MEKKA and the cooperation with Argonne National Laboratory play a central role in the MHD development.

In addition to design and MHD activities KfK studies the physico-chemical behaviour (Subtask BL PC-D), especially corrosion of structural materials in the lithium lead eutectic (Pb-17Li) and the behaviour of impurities (Polonium) including methods of clean-up. The Pb-17Li loops TRITEX and PICOLO are the main testbeds for the experimental studies.

A critical issue for selfcooled liquid metal blankets is the development and qualification of electrically insulating coatings to reduce the MHD pressure drops in the blanket. This work including the assessment of irradiation effects is being performed in subtask BL EI-D.

Safety and reliability studies are being performed in subtask BL SA-D.

A. Fiege

BS DE-D 1 Solid Breeder Test Blanket Design

1. Demo Blanket Design Work

The first design of the European Demo B.O.T. (Breeder Out of Tube) was based on the use of Li_4SiO_4 pebbles placed in gaps between beryllium plates [1]. Subsequently the beryllium plates were replaced by beryllium pebbles. The breeder and neutron multiplier material was arranged in a mixed bed of Li_4SiO_4 and beryllium pebbles cooled by tubes containing flowing high pressure helium [2,3]. This allows to cope better with the problems caused by neutron irradiation at high fluences in beryllium: differential swelling and embrittlement problems are eliminated and the swelling of the beryllium pebbles causes an increase of the pebble contact surface with consequent increase of the pebble bed thermal conductivity and decrease of the bed temperature.

The present design represents a further improvement of the concept with beryllium pebbles. The cooling tubes are replaced by cooling plates. This solution allows a considerable simplification of the blanket and the separation of the beryllium from the Li_4SiO_4 pebbles.

1.1 The design

Fig. 1 shows a vertical cross section across the right side of the torus. The general arrangement of the inboard and outboard blanket is similar to the two previous designs, however, the breeder and multiplier material in form of pebbles is cooled by plates placed in toroidal radial planes rather than by tubes. The walls of the boxes can withstand the full pressure of the cooling helium although normally operating at the pressure of the tritium purging gas (0.1 MPa).

Fig. 2 shows an isometric view of a poloidal portion of the outboard blanket segment. One can clearly see the two independent cooling systems containing high pressure helium. The helium gas purging the tritium produced in the blanket is brought to the front of the blanket by a small tube in each pebble bed (beryllium or Li_4SiO_4) slab and moves in the blanket in radial direction.

Fig 3 shows a horizontal cross section of the outboard blanket segment at the equatorial plane of the torus (left) and a vertical cross section of the same (right). The flow of the cooling helium is alternately in opposite directions, both in the first wall and in the blanket, to ensure better temperature uniformity. Between the cooling plates there are, alternatively beds of 0.3–0.6 mm Li_4SiO_4 pebbles or binary beds of 2 mm Be pebbles with the space between the larger Be pebbles filled with 0.1–0.2 mm Be pebbles. In the present design the Li_4SiO_4 pebbles are separated from the beryllium ones. This avoids the problem which could occur, in case of chemical reactions between the two, at high lithium burn-ups, although tests on unirradiated material show that beryllium and Li_4SiO_4 are compatible up to 700°C. If irradiations at high lithium burn-ups should prove that there are no compatibility problems between these two materials, then the mixed bed solution can be chosen with very little change in the design: the number of cooling plates would decrease and the tritium breeding ratio would slightly increase, due to the smaller amount of structural material and the decrease of the heterogeneity effect on the neutron economy. Fig. 4 shows a horizontal cross section of the inboard segment. The cooling tubes arrangement is analogous to that of the outboard blanket.

Figs. 2, 3 and 4 show how simplified the blanket has become by replacing the cooling tubes with cooling plates (cp. with Fig. 7 of Ref. 3). Fig. 3 shows schematically the arrangement of the plate cooling channels in the radial-toroidal planes. No high leak tightness is required between the parallel running coolant channels. High tightness is required only at the borders of the cooling plates. But even then, operation with small leakages is allowed, as the box, as in the previous design, can operate at the full helium coolant pressure (see Ref. [3]).

Fig. 5 shows in detail the arrangement of the helium cooling channels in the first wall and in the cooling plates. The upper part of the picture shows how the blanket cooling plates are welded to the first wall, while the lower one shows a detail of the cooling channels of the cooling plates. Due to the higher thermal conductivity of the Be pebble bed, its thickness is greater than that of the Li_4SiO_4 bed. Both the first wall and the blanket cooling plates are manufactured by diffusion welding. We were encouraged to use this solution by the recent excellent results obtained by KfK in collaboration with the Forschungsinstitut für Kerntechnik und Energieumwandlung, Stuttgart. Plates of MANET (the structural material foreseen for the BOT blanket) with dimensions up to 320 mm and appropriate thickness, provided with coolant and inspection channels, were fabricated and successfully tested. Bending tests showed that the strength was almost the same as that of the base material. Leak tests up to 15 MPa internal pressure showed no leak.

1.2 Results of the design calculations

The power distribution, the local tritium production and the tritium breeding ratio have been determined by means of three-dimensional Monte Carlo calculations using the MCNP code. Due account in the calculations was taken of the heterogeneity effects.

The thermohydraulic computations allowed to calculate the blanket temperatures and the helium coolant pressure drops. The heat transfer parameters used in the calculation have been measured using the actual materials (Li_4SiO_4 and Be pebble beds in helium) [4]. Fig. 6 shows the temperature distribution in radial direction in the first wall and in the blanket in a radial-toroidal plane at the equatorial region of the outboard blanket. This is the region of the maximum heat flux to the first wall and of the highest power densities in the blanket. The figure shows the temperatures at the radial-toroidal plane placed at the center of the Li_4SiO_4 pebble bed (upper diagram) and of the beryllium bed (lower diagram).

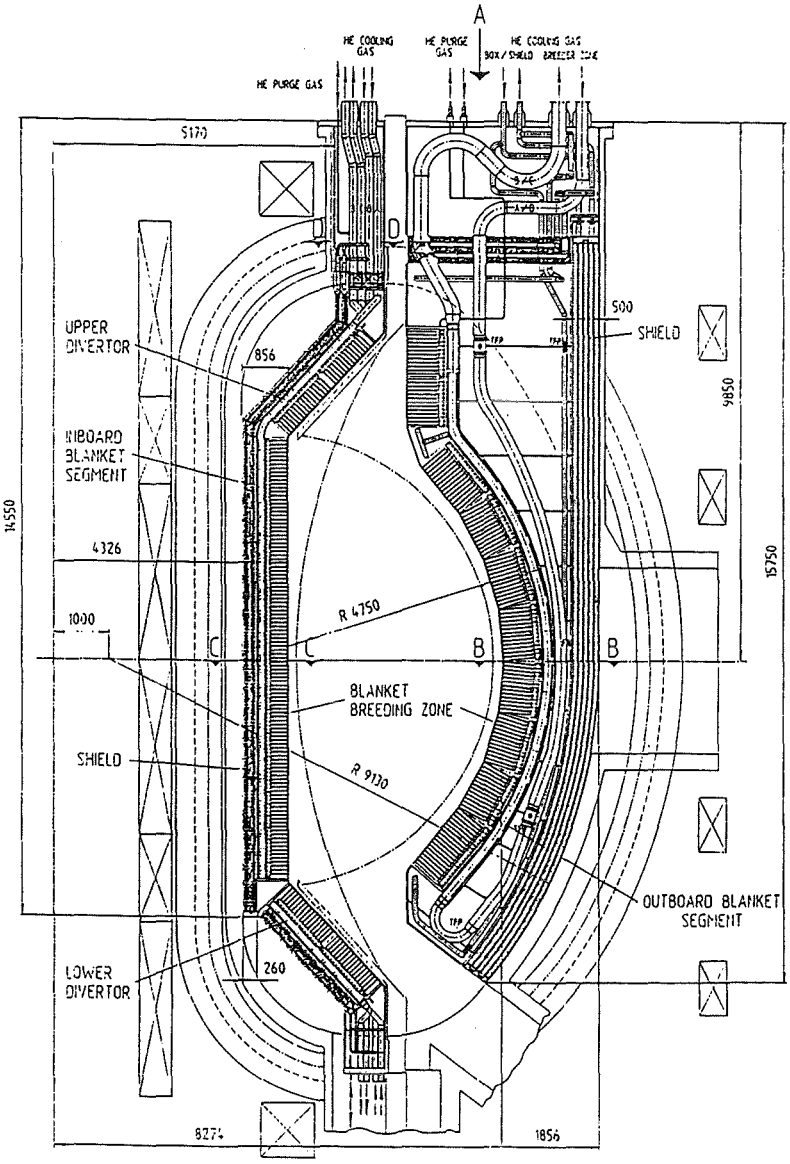

Fig. 1:
Vertical cross section across the right side of the torus.

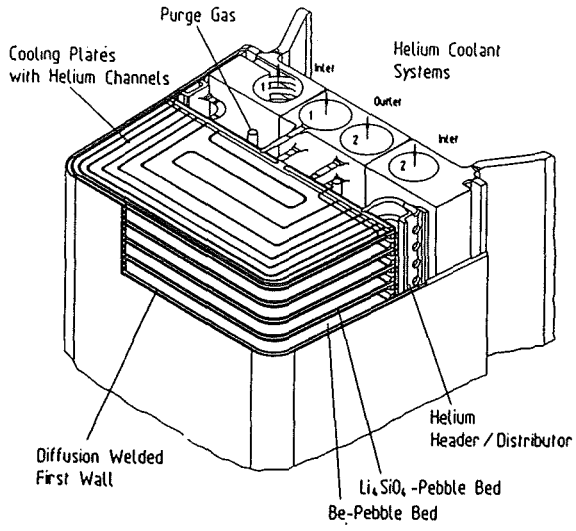

Fig. 2: Isometric view of a poloidal portion of the outboard blanket segment around the torus equatorial plane.

The tritium inventory in the Li_4SiO_4 pebbles was calculated on the base of in situ tritium release experiments [5], while the EOL (End Of blanket Life) tritium inventory was determined by the neutronic calculations, minus the tritium released from the beryllium during operation, which was determined with the code ANFIBE [6]. The tritium losses through the heat exchangers to the steam turbine circuit were determined with the same assumptions as in Ref [7]. Table 1 shows the main results of the calculations.

1.3 Conclusions

The design has been simplified and the possible difficulties arising from compatibility problems between beryllium and Li_4SiO_4 at high Li burn-ups have been eliminated. The remaining issues are common to both European Solid Breeder Blankets [3], namely behavior of Li_4SiO_4 and Be pebbles up to high neutron fluences. These are being investigated by the EXOTIC-7 irradiation in HFR and will be in the nearest future

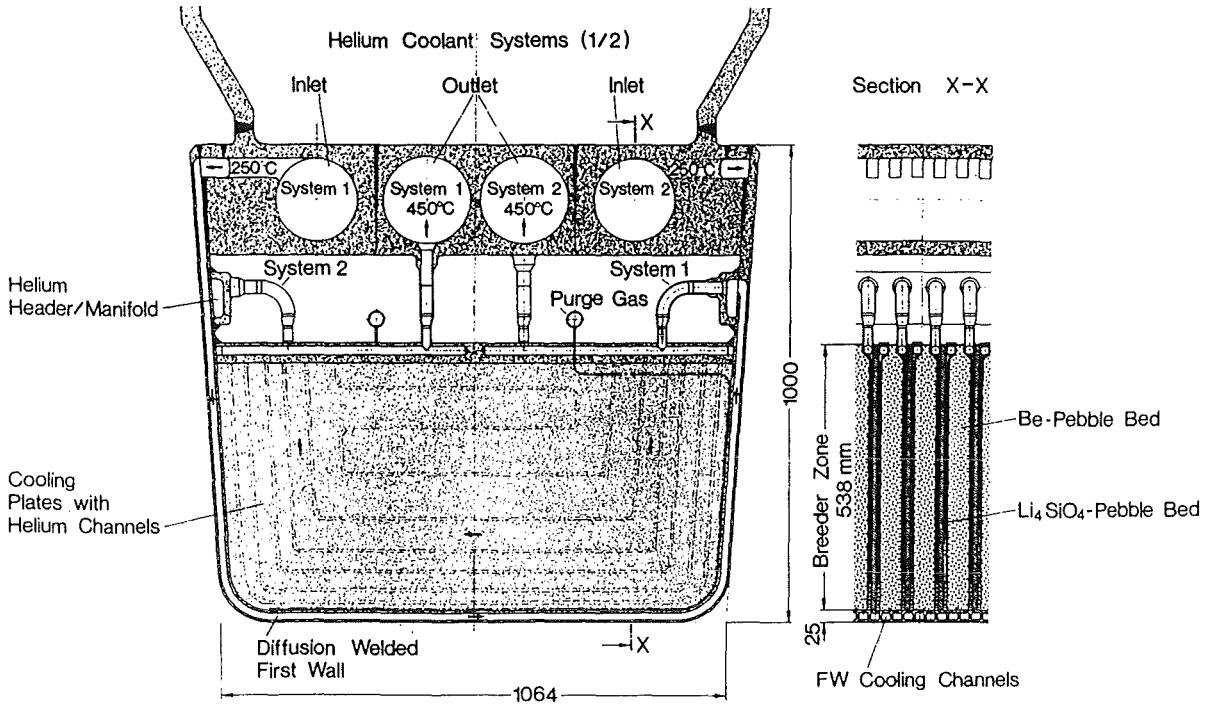

Fig. 3: Horizontal cross section of the outboard blanket segment at the equatorial plane of the torus (left) and vertical cross section of the same (right).

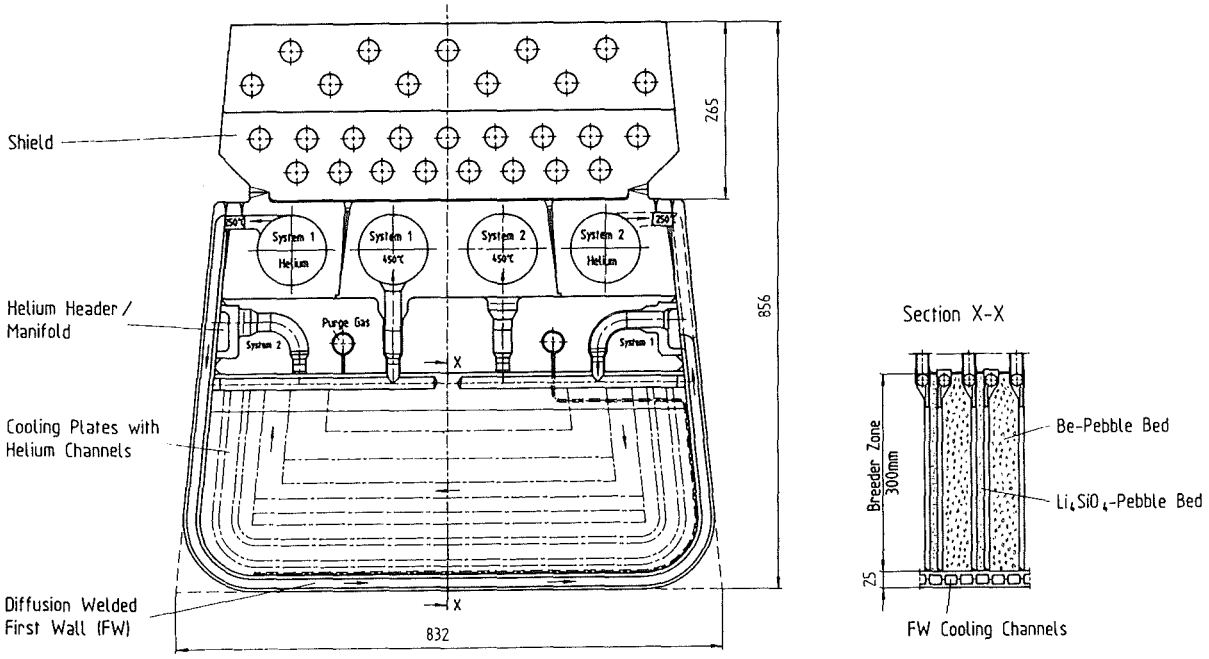

Fig. 4: Horizontal cross section of the inboard blanket segment at the equatorial plane of the torus (left) and vertical cross section on the same (right).

by the irradiation foreseen in the fast reactor Phenix. Further work is also necessary in the field of tritium control [3].

Literature - Part 1:

[1] M. Dalle Donne et al., KfK 4292, Oct. 1991.

[2] M. Dalle Donne et al., Proc. 17th Symp. on Fusion Technology, Rome, 14 - 18 Sept. 1992, Vol. 2, 1326.

[3] M. Dalle Donne et al., Status of EC Solid Breeder Blanket Designs, ISFNT-3, Los Angeles, June 27, 1994.

[4] M. Dalle Donne et al., Heat Transfer and Technological Investigations, to appear in J. Nucl Mat.

[5] H. Kwast, R. Conrad et al., The Behavior of Ceramic Breeder Materials, ICFRM-6 Sept. 27, Stresa, Italy.

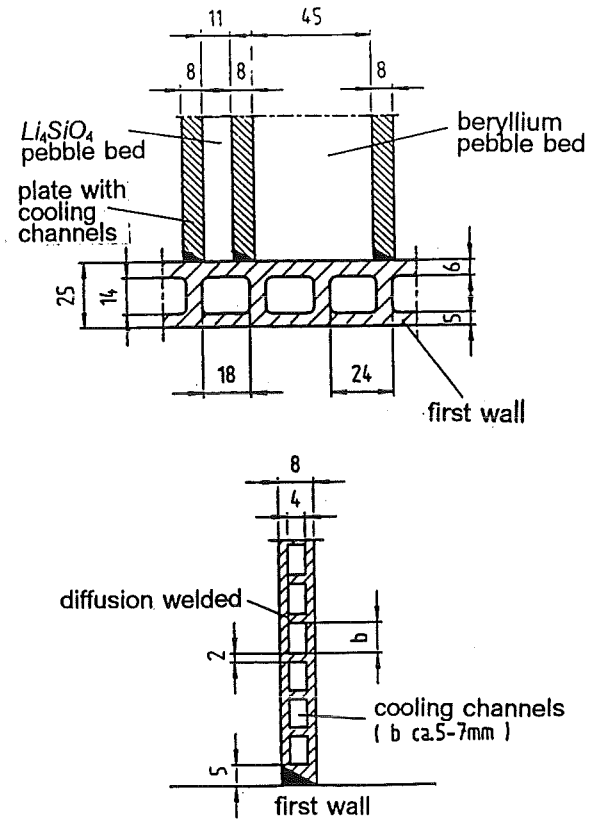

Fig. 5: Poloidal-radial cross section: detail showing the arrangement of the helium cooling channels in the first wall and in the cooling plates.

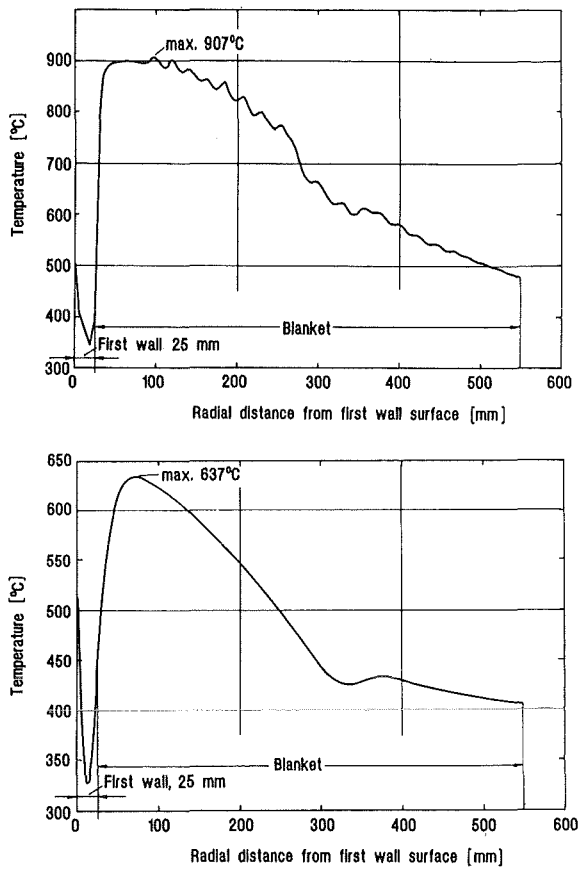

Fig. 6: Temperature distribution at the radial-toroidal plane placed at the center of the Li_4SiO_4 pebble bed (upper diagram) and of the beryllium pebble bed (lower diagram) in the blanket region of maximum power densities and maximum heat flux to the first wall. The little temperature undulations in the Li_4SiO_4 pebble bed are given by the presence of blind channels in the cooling plate.

[6] M. Dalle Donne, F. Scaffidi-Argentina, in KfK 5271, Dec. 1993.

[7] M. Futterer, X. Raepsaet and E. Proust, Tritium Permeation through Helium-Heated Steam Generators, ISFNT-3, Los Angeles, June 27, 1994.

Staff - Part 1:

M. Dalle Donne
U. Fischer
K. Müller
P. Norajitra
G. Reimann
H. Reiser

Table 1: Main characteristics of BOT DEMO Solid Breeder Blanket

Breeding and multiplier material		Separated beds of Li_4SiO_4 and beryllium pebbles
Li^6 enrichment		25 at%
Total blanket power		2500 MW (+ 300 MW in divertors)
Coolant helium pressure	outboard inboard	8 MPa 8 MPa
Coolant helium pressure drop (F.W., blanket, feeding tubes)	outboard inboard	0.30 MPa 0.30 MPa
Coolant helium temperature:	inlet outlet	250°C 450°C
Max. steel temperature		520 °C
Max. temp. in beryllium		640°C (BOL) 515°C (EOL)
Max. temp. in breeder material Min. temp. in breeder material		900°C 350°C
Real tridimensional tritium breeding ratio (without ports) Accounting for 10 outboard ports		1.13 (BOL) 1.11 (EOL) 1.07 (BOL) 1.05 (EOL)
Peak lithium burn up		7.25 at%
Peak fluence in beryllium		16300 appm He
Tritium purge system pressure		0.1 MPa
Tritium inventory in breeder mat.		10 g
Tritium inventory in Beryllium (EOL)		1280 g
Tritium losses to steam/water system		22 curie/d

2. Electromagnetic Forces and Stresses caused by Plasma Disruptions

One of the crucial problems in the blanket design is to demonstrate the capability of the structure to withstand the mechanical effects of a major plasma disruption. The Test Blanket Advisory Group (1990) gave the following specifications for a reference disruption in Demo: "a linear decay of the plasma current from 20 MA to zero in 20ms" and "one disruption during blanket segment life". The only mechanical requirement was that "the blanket segment may be deformed but it must remain removable through the port".

The Karlsruhe Nuclear Center is performing design and experimental work for the European BOT (Breeder Out of Tube) Helium Cooled Solid Breeder Blanket [1,2]. This paper discusses methods and results of the mechanical assessment of this blanket design during the Demo reference disruption.

2.1 Electromagnetic analysis

The electromagnetic calculation of the eddy currents and of the resultant magnetic forces has been performed by means of a 3-D eddy current computer program commonly used for NET/ITER applications [3].

As a complete finite element method model of the Demo reactor has been achieved, all the most relevant parts of the electromagnetic system can be taken into account in the calculation. The vacuum vessel, the 48 outboard and 32 inboard blanket segments are part of the developed electromagnetic model (see Figure 1). Each blanket segment is electrically insulated from the other segments and components of the reactor. Particularly, a fine discretization of the outboard and inboard blanket segments has been realized to account for the complex design of the components. The vacuum vessel - with a toroidal electrical resistance of 20 $\mu\Omega$ - has been taken into account by means of a coarse mesh in order to simulate the influence of the large toroidal eddy current that flows in it. The presence of the external magnetic field coil systems (TF and PF coils) is also considered in the calculation.

The fine mesh used in the blanket model allows an accurate description of the magnetic body forces that act on the different parts of these structures. Figure 2 shows the normal component (expressed in term of pressure) of the magnetic force acting on the first wall for the outboard and the inboard blankets. The interaction of eddy currents with the large toroidal field produces the typical observed behaviour; the load results in an internal or external pressure for the different regions of the first wall.

The effect of the magnetic steel MANET on the forces has been investigated too. The martensitic steel MANET has been chosen as structural material, because it is able to withstand the high neutron fluence in Demo (70 d.p.a.) without appreciably swelling and has good thermal-mechanical properties - lower thermal expansion and higher strength - in comparison with AISI 316L steel. Because it is used as structural material in the region surrounding the plasma, the magnetic flux distribution outside and inside the blanket structure can be significantly modified. When a plasma disruption occurs, as eddy currents are induced in the structure, electromagnetic forces rise whose magnitude can be greater than in the case without ferromagnetic structural material.

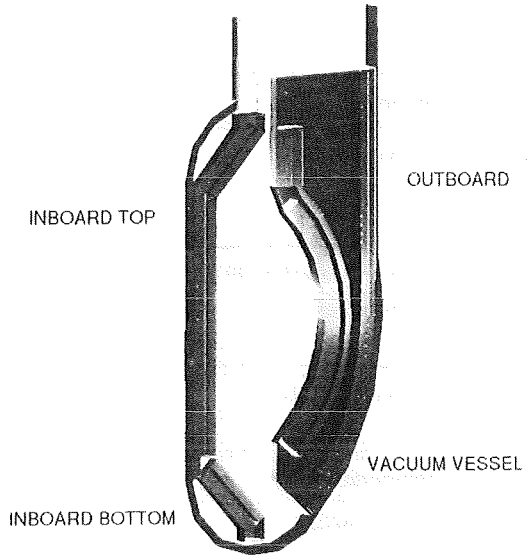

Fig. 1: FEM model for the electromagnetic analysis.

A computer code that allows electromagnetic calculations in presence of saturated magnetic materials is being developed [4]. Figure 3 gives the resultant forces and torques on the structure for different horizontal sections, with comparison between the case of MANET and a non-magnetic steel. These quantities are calculated on the geometrical center of each section and refer to the lower half of the section.

Forces in presence of magnetic structural material change mostly only their module values but not their direction. The largest increase of module values occurs for the box back wall and the vertical shield. However, this increase is limited to 20% in the first wall of the box, where the largest forces are acting and the highest stresses are expected.

2.2 Stress analysis

On the basis of the calculated force distribution, a dynamic stress analysis of the outboard and inboard segments has been performed. Shell elements have been used to model the whole structure with the exception of the vertical shield where solid elements have been used. The blanket segments have been constrained (fully built-in) on the upper flange. The support of neighbouring segments has been simulated by means of suitable boundary conditions on the vertical shield

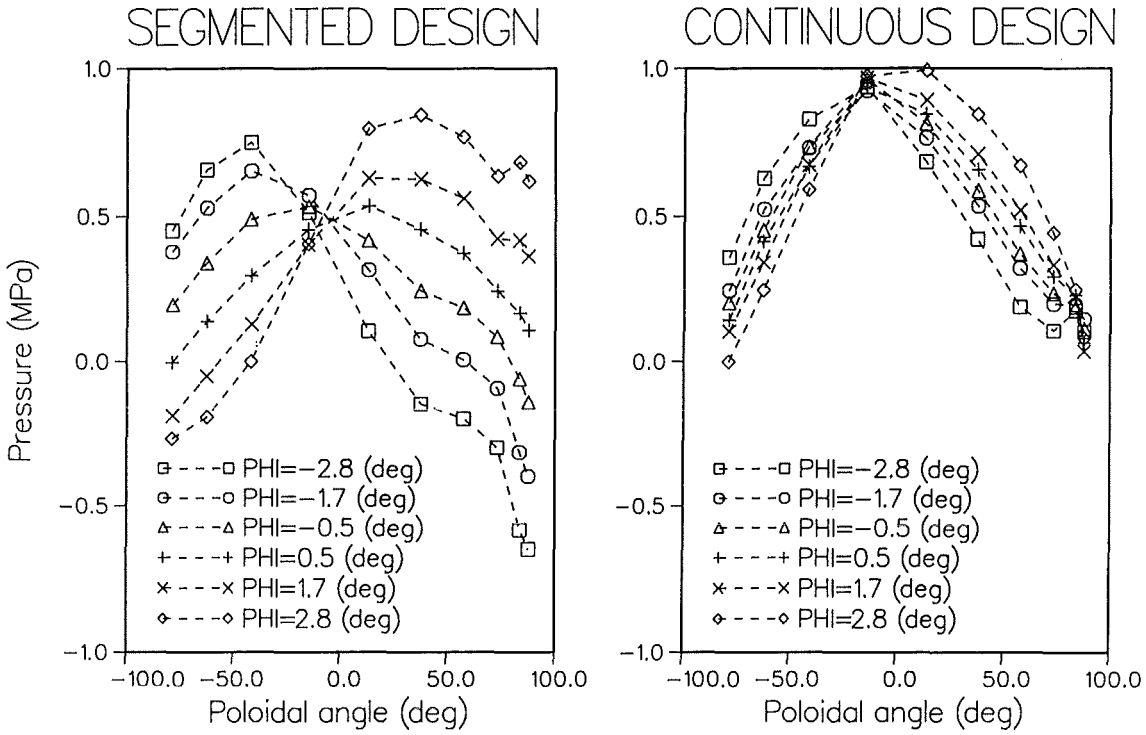

Fig. 2: First wall load.

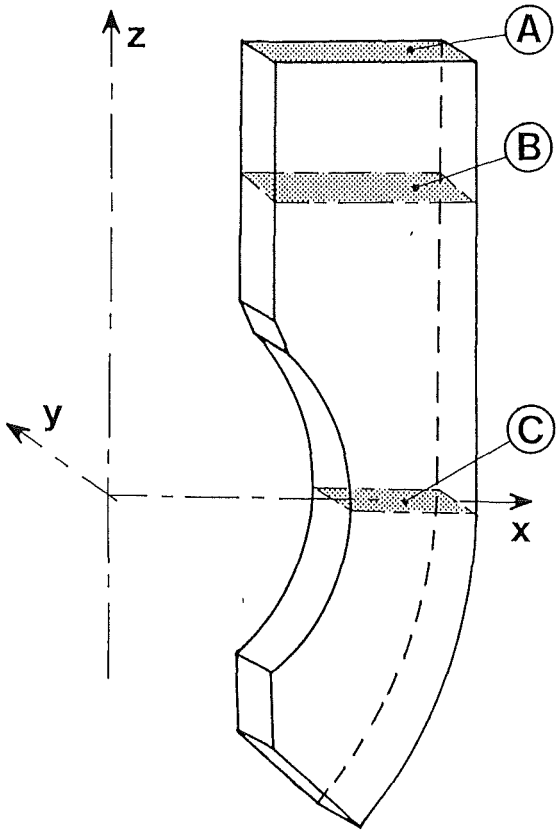

	MANET		NON MAGNETIC STEEL	
Sect.A x=8.315 y=0.0 z=9.950				
F_x = 1.292	T_x = -1.427	F_x = 1.494	T_x = -0.448	
F_y = -3.117	T_y = -1.421	F_y = -2.861	T_y = -6.370	
F_z = -0.081	T_z = 26.219	F_z = -0.042	T_z = 23.799	
Sect.B x=8.315 y=0.0 z=7.500				
F_x = -0.197	T_x = 10.524	F_x = 0.167	T_x = 10.418	
F_y = -2.050	T_y = 0.462	F_y = -1.960	T_y = -4.247	
F_z = 0.450	T_z = 17.880	F_z = 0.240	T_z = 16.226	
Sect.C x=9.202 y=0.0 z=0.0				
F_x = 0.273	T_x = 6.242	F_x = 0.571	T_x = 6.573	
F_y = 3.133	T_y = -7.003	F_y = 2.856	T_y = -7.031	
F_z = 0.675	T_z = -29.549	F_z = 0.625	T_z = -26.478	

Force (F) in MN
Torque (T) in MNm

Fig. 3: Magnetic load on the outboard blanket.

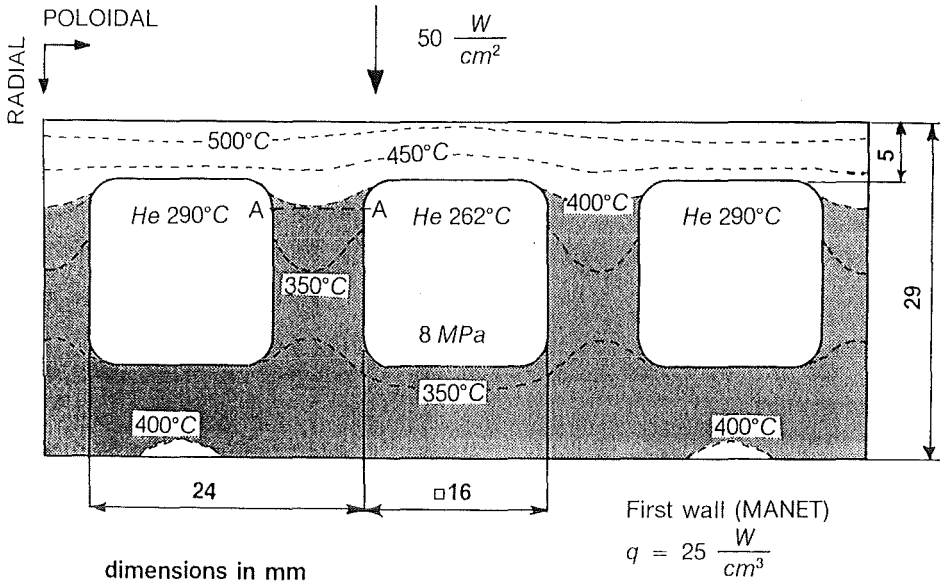

Fig. 4: Temperature disstribution in the first wall /8/.

region. In fact, all the 48 outboard and 32 inboard boxes are tied together to form two rigid cylinders.

Because of the mentioned constraints of the structure, the calculated displacements are relatively low. The maximum displacement (8 mm) is less than the gap between adjacent boxes and between each box and the vacuum vessel (20 mm). The maximum calculated Von Mises stress lies considerably below the yield stress of the structural material at high temperature (560 MPa at 350°C).

The results obtained by stress analysis have been verified according to [5] taking into account the presence of thermal, pressure and self-weight loads acting on the structure. The total load caused by the reference disruption has been classified into Category 2 ("unlikely and design faults"). The results show that the outboard and inboard structures can withstand the mechanical stress caused by the reference disruption remaining below the elastic limit. Moreover, the investigation has demonstrated that also the mechanical requirements for loads of Category 1 ("normal conditions and anticipated faults") can be met at least for the outboard structure [6].

The martensitic steel MANET-I presents a degradation of the fracture toughness properties at irradiation temperatures less than 400°C [7]. Figure 4 shows the temperature distribution in the outboard blanket first wall at the torus equatorial plane in which the power densities are the highest [8]. The shaded region shows the temperature range in which a degradation of the toughness properties occurs. As the maximum temperatures in the remaining structure are considerably lower than in the equatorial region, nearly all the structural material of the blanket has temperatures between 300°C and 400°C.

Application of the design criteria [5] results in a calculated critical crack dimension of 4 mm [9]. If this value is sufficient to assure the respect of the fast fracture limits, it remains a critical issue depending on the assumed cyclic thermal loading in the structure. In the case of pulsed operation further investigations are necessary.

2.3 Faster disruptions

Further calculations [9] have been performed to consider the effects of faster (centered of 5 and 2 ms) disruptions. Figure 5 (left) presents the currents which flow in the outboard segment. As the electrical time constant of the blanket segment is relatively low in comparison with the disruption time, faster disruptions produce very large currents. The stresses caused by such disruptions are unallowable for the actual design.

Figure 5 (right) shows the corresponding behaviour of a modified design ("continuous design") in which a first wall connection among neighbouring modules allows eddy currents to flow in toroidal direction. The increase of the current is now limited by the greater time constant associated with the connected structure. The force distribution in the two designs differs very much. In the second case the large toroidal current which flows in the first wall shields the remaining blanket structure. The stress analysis shows the advantages of the continuous solution; allowable stresses for all the considered disruptions result from the calculation.

2.4 Conclusions

The electromagnetic calculations and the stress analysis performed for the European B.O.T. Blanket demonstrate the capability of the inboard and outboard blanket segments to

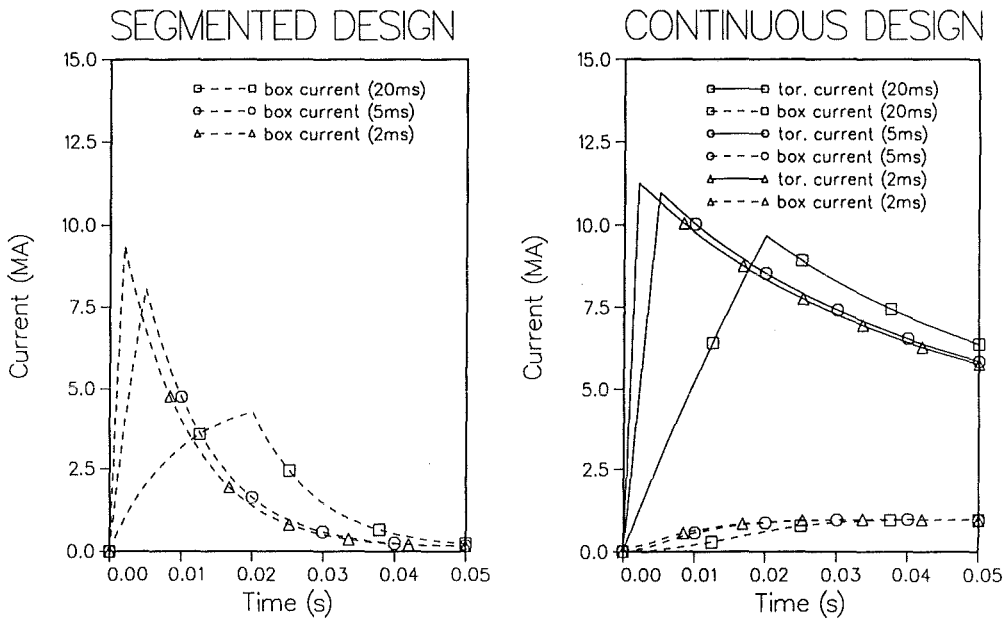

Fig. 5: Eddy currents for faster disruptions.

meet the structural requirements for the Demo reference plasma disruption.

As the toughness properties of the martensitic steel MANET - used as structural material - degrade under irradiation, a fracture mechanics assessment for the components has been performed.

Unallowable stresses can be produced during faster disruptions. In this case, a continuous design has been analyzed. A comparison with the segmented design shows a better performance of the continuous design at least for centered disruptions.

Acknowledgement

This work has been performed in the framework of the Nuclear Fusion Project of the Kernforschungszentrum Karlsruhe and is supported by the European Commission within the European Fusion Technology Program.

Literature - Part 2:

[1] M. Dalle Donne et al., KfK 4929 (1991).

[2] M. Dalle Donne et al., " European DEMO Solid Breeder Blanket: the concept based on the use of cooling plates and beds of beryllium and Li_4SiO_4 pebbles", presented at the 18th SOFT, Karlsruhe (1994), to be published.

[3] R. Albanese, G. Rubinacci, IEE Proceedings, 135 (1988) 457-462.

[4] P. Ruatto, Proc. of The 2nd International Workshop on Electromagnetic Forces and Related Effects on Blankets and Other Structures Surrounding the Fusion Plasma Torus, UTNL-R-0302, Tokai, Japan, September 1993, pp.169-177

[5] E. Zolti, D. Munz, R. Matera, V. Renda and M. Acker, "Interim Structural Design Criteria for Predesign of the NET Plasma Facing Components", The NET Team, NET/IN/86-14 (1986).

[6] L.V. Boccaccini, Proc. 17th Symp. Fusion Technology, 2 (1992) 1291-1295.

[7] M. Rieth, B. Dafferner, C. Wassilew †, KfK 5243 (1993).

[8] P. Norajitra, Kernforschungszentrum Karlsruhe, personal communication.

[9] L.V. Boccaccini, P. Norajitra, P. Ruatto, "Analysis of mechanical effects caused by plasma disruptions in the European BOT Solid Breeder Blanket Design with MANET as structural Material", presented at the 3rd ISFNT, Los Angeles (1994), to be published.

Staff - Part 2:

L. Boccaccini
M. Dalle Donne
P. Ruatto

BS BE-D 1 Beryllium

Beryllium Swelling in The European BOT DEMO Blanket

The ANFIBE code developed at KfK is capable to describe the behaviour of the helium produced in beryllium under neutron irradiation and thus calculate the beryllium swelling as a function of temperature and helium content [1-3]. This kind of calculations have been performed for a reference design of the BOT DEMO blanket assuming that the beryllium temperature does not change during the blanket life [4]. However, the temperature of the beryllium pebbles varies quite considerably duringthe irradiation. Experimental evidence has shown that the effective thermal conductivity and the heat transfer coefficient bed/containment wall are affected by the constraint on the pebble bed exerted by the containment walls. If the bed tends to expand, due for instance to increased temperature, and it is constrained by the containment walls, the contact surfaces of the highly heat conducting beryllium pebbles increases. Consequently the bed thermal conductivity and the heat transfer coefficient increase too and the pebble bed temperature decreases. An analogous effect has the neutron induced swelling: the increased pressure of the helium bubbles formed during the irradiation causes the beryllium to creep, thus the contact surfaces of the pebbles increase, which results in a decrease of the bed temperatures. The experiments performed at KfK have allowed to quantify these effects [4].

It was therefore decided to perform more realistic calculations of the beryllium swelling, accounting for these temperature variations, for the region of the blanket where the highest swelling rates are expected, i.e. for the outboard blanket region around the equatorial plane. A computer code has been developed to numerically solve the two dimensional (in poloidal and radial direction: there is symmetry in toroidal direction in the central region of the pebble bed) heat conduction differential equation, accounting for the variations of temperature caused by beryllium volume swelling and relative thermal expansion pebble bed/containing wall. The calculations have been performed at various times during the blanket operation up to the blanket end of life (EOL). At every time step, iterative calculations have been performed: starting from the temperature calculated in the previous time step and the known fluence, the beryllium swelling is obtained by interpolation of tabulated values obtained by ANFIBE calculations as a function of irradiation temperature and fluence. Then the bed temperature is calculated again on the basis of the new volume swelling values. The calculation is repeated until two successive temperature distributions differ for less than 0.5°C.

Fig. 1 shows the BOL temperature distribution in the beryllium pebble bed confined between two cooling plates in the equatorial region of the outboard blanket (see also Fig. 2.5.1 of Ref. [4]), while Fig. 2 shows the temperature for the same bed for the blanket EOL. The peak bed temperature decrease from 637°C to 501°C.

At present a first version of the code based on the above-mentioned assumptions is available, and is being validated by comparison with a large number of experiments. First results using this code are given below.

Figs. 3 and 4 show the beryllium swelling in the considered pebble bed slab with and without taking into account of the temperaturevariations due to swelling respectively. The peak beryllium swelling decrease from 11% to 8.3%. In both cases the volume swelling is considerably smaller than the void fraction in the pebble bed (about 20%) so that the flow of the helium purging the tritium produced in the beryllium is not impeded.

Literature:

[1] M. Dalle Donne, F. Scaffidi-Argentina, C. Ferrero, C. Ronchi: Modelling He-Induced Swelling in Beryllium During Fast Neutron Irradiation. KfK Report 5271, Karlsruhe, December 1993.

[2] M. Dalle Donne, F. Scaffidi-Argentina, C. Ferrero, C. Ronchi: Modelling of Swelling and Tritium Release in Irradiated Beryllium. Journal of Nuclear Materials 212-215 (1994) 954-960.

[3] F. Scaffidi-Argentina, M. Dalle Donne, C. Ferrero, C. Ronchi: Helium Induced Swelling and Tritium Trapping Mechanisms in Irradiated Beryllium: a Comprehensive Approach, in: Proc. of the 3rd International Symposium on Fusion Nuclear Technology, (Los Angeles, 1994). To appear in: Nuclear Engineering and Design.

[4] M. Dalle Donne, et al.: European DEMO BOT Solid Breeder Blanket. KfK Report 5429, Karlsruhe, November 1994.

Staff:

M. Dalle Donne
F. Scaffidi-Argentina

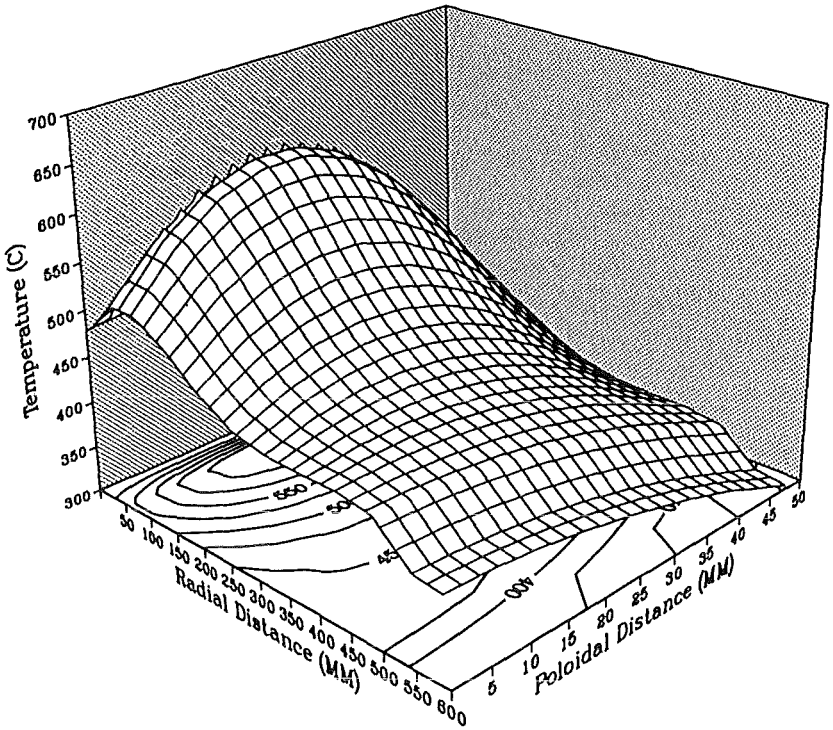

Fig. 1:
Temperature distribution in a radial-poloidal slab containing the beryllium pebble bed in the equatorial region of the outboard blanket at blanket BOL.

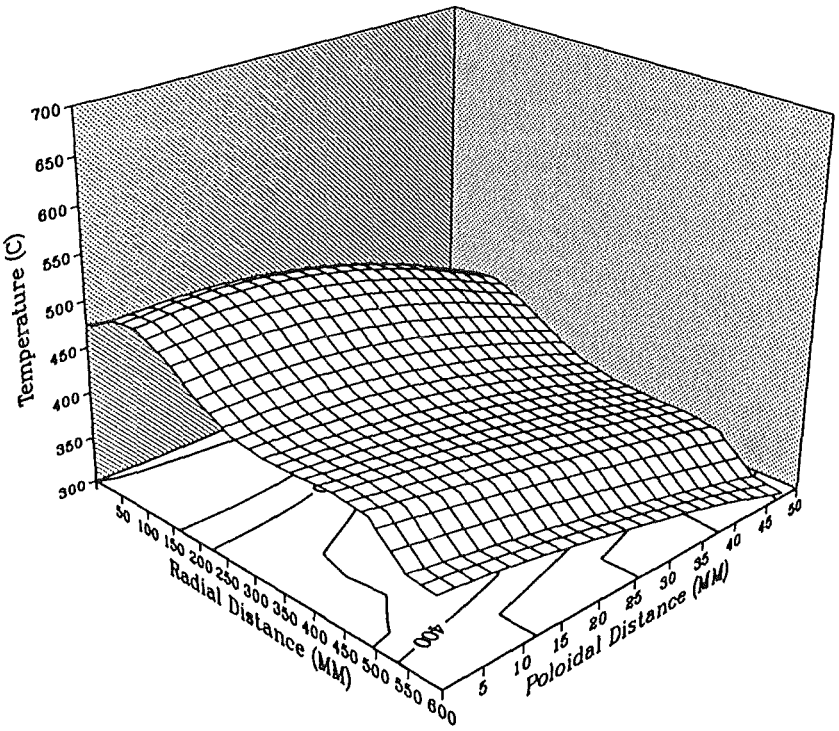

Fig. 2:
Temperature distribution in a radial-poloidal slab containing the beryllium pebble bed in the equatorial region of the outboard blanket at blanket EOL.

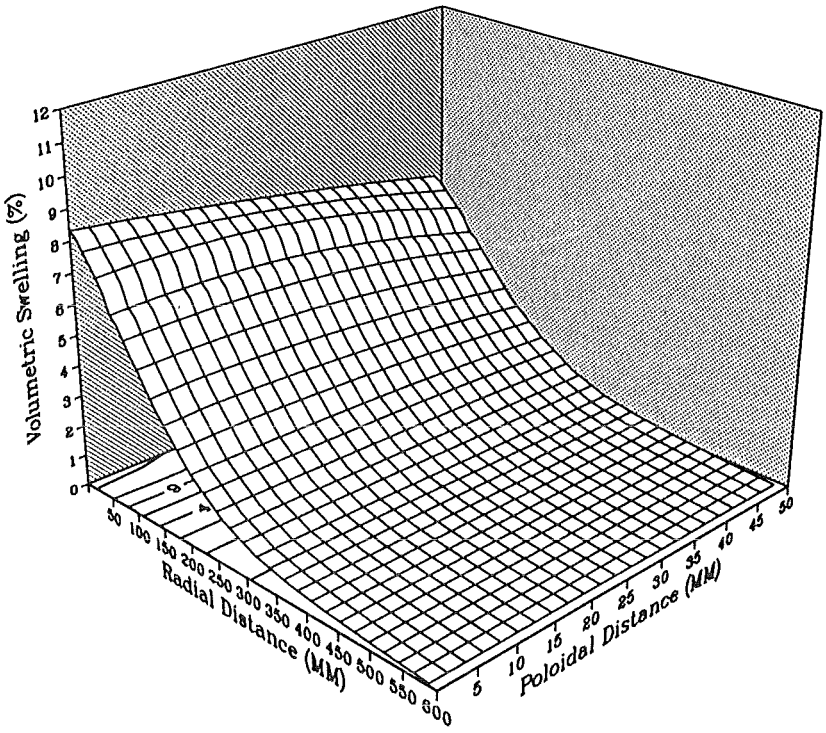

Fig. 3:
Beryllium volume swelling distribution at blanket EOL.

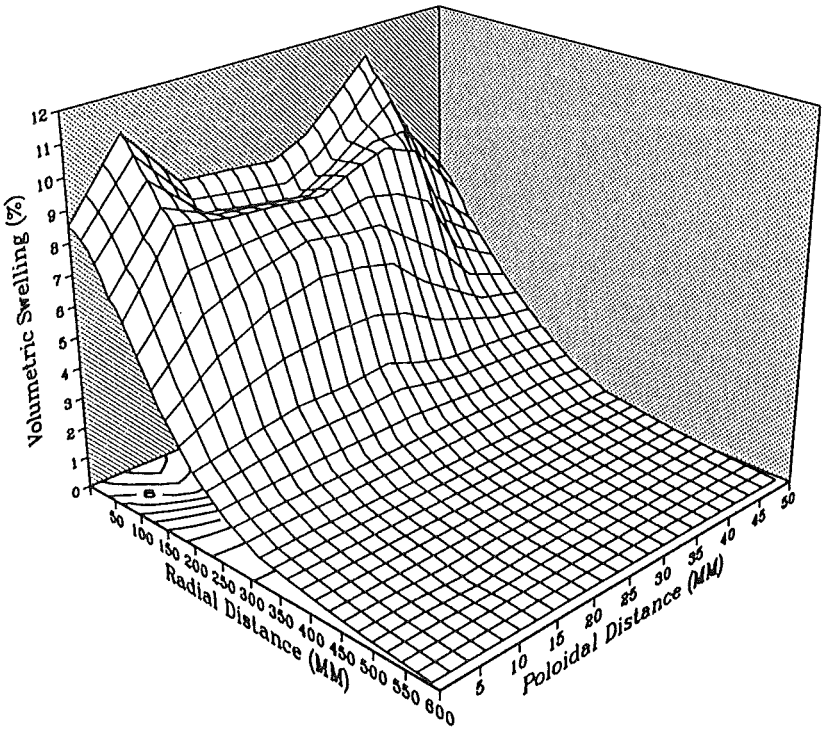

Fig. 4:
Beryllium volume swelling at blanket EOL without accounting for the temperature variations caused by beryllium swelling.

BS BR-D 1/D 2 Preparation and Characterization of Ceramic Breeder Materials

Differential thermal analysis (DTA) and calorimetry of Li_4SiO_4

Two Li_4SiO_4 samples with different lithium enrichments were analyzed by DTA and calorimetry in order to check the single-phase character and a possible influence of the isotope effect on the transformation and melting temperatures. Rods of $^{nat}Li_4SiO_4$ (heat T-5035) and Li_4SiO_4 with 50% ^6Li enrichment (heat T-5036) were prepared by Schott through as-casting.

Results

Heat T-5035: second-order transformations at 660°C and 723°C; eutectic temperature with second, SiO_2 richer phase at 1024°C; liquidus temperature at 1224°C. Heat T-5036: second-order transformations at 662°C and 726°C; a eutectic temperature was not observed; liquidus temperature at 1224°C.

Isotope effects of Li in Li_4SiO_4 could not be detected. A mass loss of the samples could not be established during DTA heating with 5K/min up to 1024°C; 0.8% mass loss was observed up to 1280°C. A eutectic temperature at 1024°C was observed in heat T-5025 during first heating; a two-phase character with SiO_2-richer phase is assumed for the as-received state of the sample. Heat T-5036 was single-phase before first heating. The congruent melting point of Li_4SiO_4 at 1255°C was not observed in both samples because a Li_2O-evaporation above 1024°C results in a displacement of the single-phase composition to SiO_2-richer concentrations.

The second-order transformation temperatures can be determined more precisely by high temperature calorimetry which gives 667°C and 725°C for $^{nat}Li_4SiO_4$.

Staff:

H. Kleykamp
W. Laumer

BS BR-D 3 Irradiation Testing and Post Irradiation Examination

Since 1984 irradiations have been performed in different reactors with mostly thermal neutron flux in order to study the material behavior of ceramic breeder materials and their tritium release behavior. The only irradiation performed of breeder material in the neutron spectrum of a fast reactor is the KNK II irradiation ELIMA 1. From January 1988 until the final shutdown of the KNK II reactor in August 1991, 24 pins with lithium metasilicate and lithium orthosilicate samples, placed in two sample holders in the MTE 2 Material Testing Element, were irradiated.

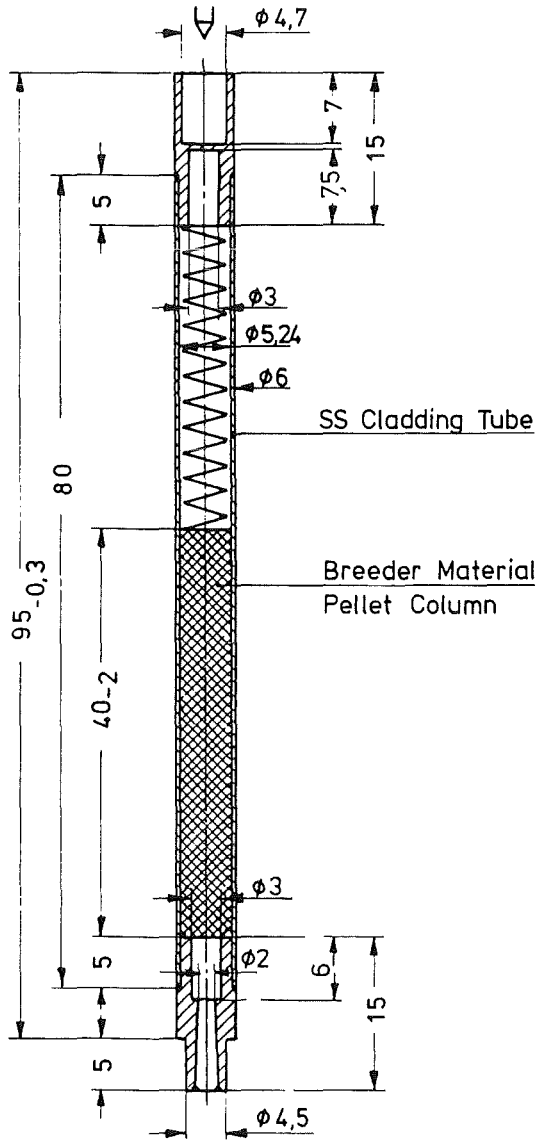

Fig. 1: Sample rod of ELIMA 1 irradiation experiment.

MTE 2 accomodated twelve breeder material samples (Fig. 1) each in an open sample carrier and in a sealed sample capsule with heat pipe at level IV above the 600 mm core height. The open sample carrier (Fig. 2, left) was operated as a low temperatrure insert at 400 to 450°C and the sealed high temperature capsule (Fig. 2, right) at 600 to 700°C. It is evident from table 1 that Li_2SiO_3 and Li_4SiO_4 were exposed to irradiation both as disks and pellets, with high and low density variants used of 65% and 90% of the theoretical density.

The layout of the irradiation experiment and preparatory work for it were carried out in 1986/87. After the long delay which had been caused by difficulties in the licensing procedure and by interruptions in reactor operation, the interest in the specimen material used has descreased because the material does no longer fully satisfy the specifications as defined today. Therefore, only a part of the sample capsules will be subjected to post irradiation examination in the Hot Cells. Unfortunately, the reactor was operated only at 60% of its nominal power for almost the entire period of irradiation; full reactor power was attained for a short time only. However, in this partial load mode the sample temperatures were not very much affected. The summed up irradiation time is 144 full power days (FPD).

The axial distributions of the temperatures and neutron dose in the two sample carriers have been plotted in Fig. 3. The fast neutron dose is identical for the two carriers. The temperature plot in the open sample carrier is given by the in-pile sodium temperature and does not depend on the reactor power. For the sealed heat pipe capsule 2 a sample temperature of about 680°C was calculated for 100% reactor power; a value of about 620°C should be anticipated in case of 60% reactor power.

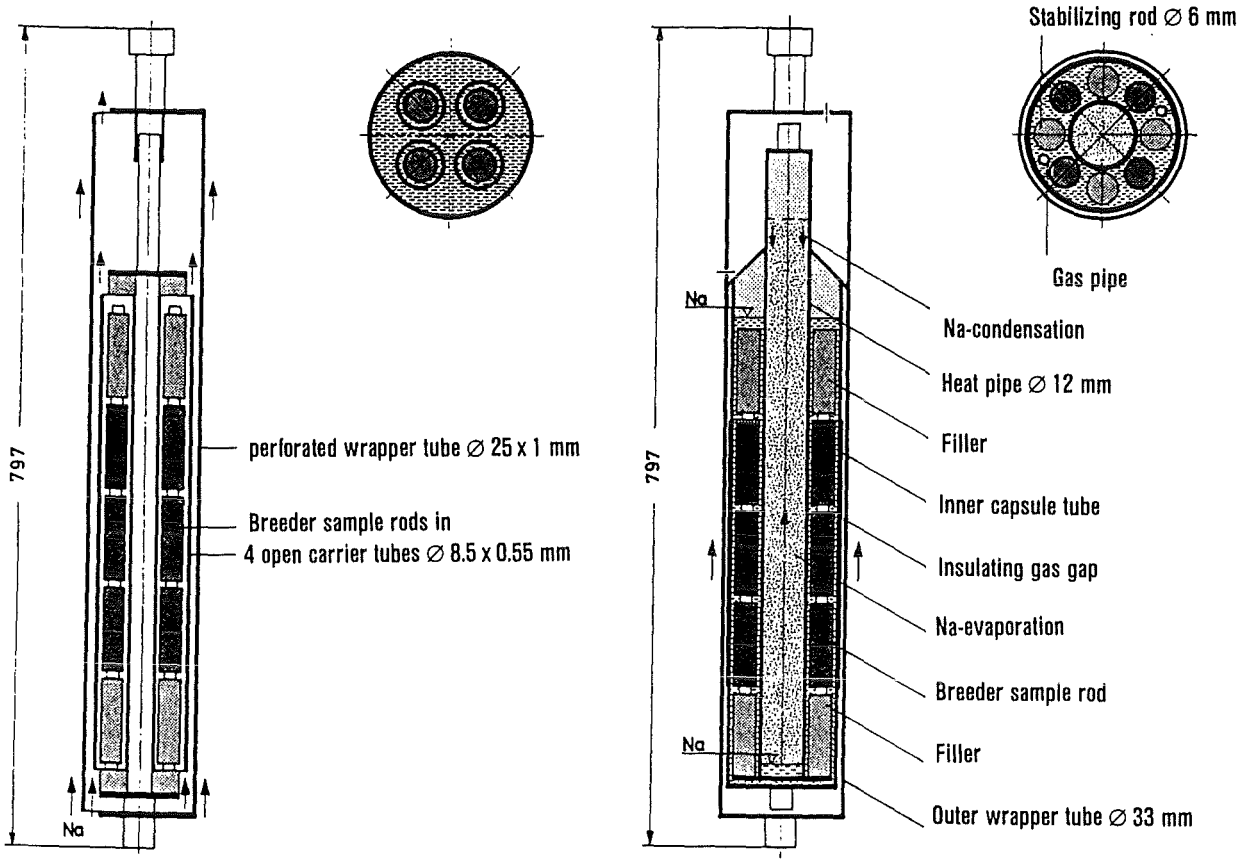

Fig. 2: Open sample carrier and heat pipe capsule of ELIMA 1 irradiation experiment.

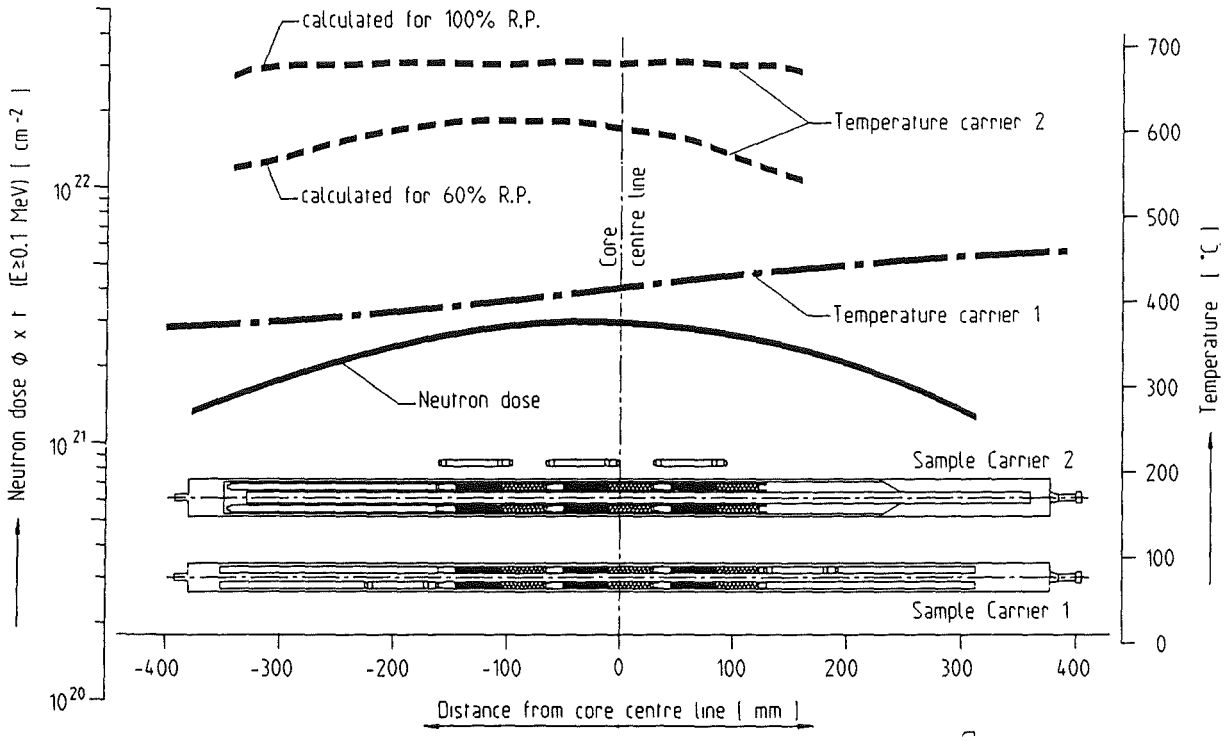

Fig. 3: Temperature and neutron dose of the breeder material samples from the ELIMA 1 experiment.

Table 1: Design and operational data of KNK-irradiation experiment ELIMA 1

Breeder material		Li_2SiO_3	Li_4SiO_4
		Pellets 5 mm high and Disks 2,5 mm thick	
Density	% th.D.	65/90	
Pellet diameter	mm	4,84	
Hight of sample stack	mm	40	
Cladding dimensions	mm	6 ⌀x0,38	
Cladding material		1.4970	
Number of sample rods		12	12
Fast neutron flux ϕ_f	n/cm^2s	max. ca. $2{,}5 \cdot 10^{14}$ temporarily $4 \cdot 10^{14}$	
Total heat generation *)	W/cm^3	5,8/8,2	7/10
Tritium production rate *)	10^{12} at/cm^3s	4,6/6,6	6,3/8,8
Temperature of samples	sample carrier 1	400...450 °C	
	sample carrier 2	ca. 620 °C (temporarily ca. 680 °C)	
Irradiation tim e	FPD	144	
Neutron dose $\phi_f \cdot t$	n/cm^2	ca. $3 \cdot 10^{21}$	
Neutron induced damage rate	dpa	ca. 2	
Damage rate by $t + \alpha$	dpa	up to ca. 1	
Total tritium production	Ci/sample	ca. 2 to 2,5	

*) temporarily; otherwise 60 % of that value

The Experiment COMPLIMENT can be considered as a screening test for the irradiation behaviour of different ceramic blanket materials.

Five ceramic blanket materials $LiAlO_2$, Li2O, Li_2ZrO_3, Li_2SiO_3 and Li_4SiO_4 provided by the European partners were irradiated in parallel in the HFR and the OSIRIS reactor in order to study the influence of the neutron energy spectrum on the irradiation characteristics of the Li-ceramics, Table 2 [1,2].

In total 72 samples have been irradiated at 2 different irradiation temperatures (700+950 K). The specimens were mostly in pellet form, but also some Li-orthosilicate samples of sintered granulate and molten spheres were provided by KfK.

The irradiation damage by fast neutrons and (a+t)-reactions reached about 2 dpa, still rather low compared with the 20 dpa foreseen for the DEMO plant.

PIE Results of Compliment

PIE work was done in the fusion ceramic laboratory (FKL) of KFK Hot Cells. It consisted in decladding of the specimens, T-release measurements, Hg-porosimetry, ceramography, fractography and x-ray analysis of lattice parameters. Ultimate compressive strength and Young's modulus were measured to characterize changes of the mechanical properties during irradiation. Many results of this work have been documented in [1,2,3]. In this contribution an assessment of these PIE results will be given. The main outcome of PIE with regard of the main performance criteria is summarized in Tab. 2. As concerns T-release Li_2O and Li_2ZrO_3 had the lowest residence time, followed by Li_4SiO_4 and $LiAlO_2$. Li_2SiO_3 had the highest residence time [4]. High swelling rates and a bad compatibility excludes the use of Li_2O.

Considering all the performance criteria the Li_4SiO_4 and Li_2ZrO_3 seem the best candidates. With regard to the fabrication know how at KFK the orthosilicate was finally chosen for the KFK Ceramic Breeder Concept. [5]. Because of the better swelling and thermal cycling accomodation, pebbles instead of pellets were chosen. In this respect Tab. 3 is much important, it summarizes the results of COMPLIMENT samples with orthosilicate pebbles concerning their mechanical stability.

The molten spheres (MS) exhibit the better performance compared with the sintered ones (SS). But the low temperature irradiation (400−450°C) in OSIRIS resulted also in about 40% dust for the molten spheres. Frequent thermal cycling of the OSIRIS reactor during irradiation is believed as the cause of these failures. Disposing of only a small amount of irrdiated molten spheres, thermal cycling experiments could not yet be performed. Therefore only compressive strength of single orthosilicate spheres could be measured before and after irradiation. Results of these measurements in comparison with results concerning the stability of pellets are shown in fig. 4. In contrast to a steep decrease of compressive strength of pellets (densities between 62 and 90% TD) at low Li-burnups the strength of pebbles (density 98% TD) is only slightly decreased (3−17%) by the irradiation.

Generally, a considerable reduction of the compressive strength has been found for all pellet materials depending on the Li-burnup and the irradiation temperature. Li_4SiO_4 exhibits the largest decrease, the lowest one has been

Table 2: PIE-results for different Li-compounds from the irradiation experiment COMPLIMENT

	stability of micro-structure	swelling	chem. reactivity	mech. stability	compr. strength pebbles	Tritium release[2)]	compatibility with cladding[3)]
$LiAlO_2$	o	+	-	o	/	medium	
Li_2O	Δ	Δ	Δ	Δ	/	fast	Δ
Li_2ZrO_3	+	o	o	o	/	fast	Δ
Li_2SiO_3	+	o	o	+	/	slow	+
Li_4SiO_4	o	+	+	+	/	medium	+
Molten Sheres (MS) of Li_4SiO_4	-	-	o	[1)]	o	medium	o

- not measured
+ high
o medium
Δ low

1) > 500 °C good, low cycling rates
2) H. Werle et al. [4]
3) W. Dienst et al. [7]

Table 3: Stability of Li-Orthosilicate pebbles after irradiation in COMPLIMENT

	ELIMA/HFR, Petten		DELICE / OSIRIS, Saclay	
	Matrix I 400-450 °C	Matrix II 650-700 °C	Matrix III 400-450 °C	Matrix IV 650-700 °C
Sample No. Colour Dust	MS 173 black < 1 %	MS 174 grey < 1 %	MS 175 grey ~ 40 %	MS 176 grey/dark < 1 %
Sample No. Colour Dust	SS 113 grey/black ~ 45 %	SS 114 grey/dark ~ 5 %	SS 115 grey ~ 60 %	SS 116 grey/dark ~ 5-10 %

MS = Molten spheres (Schott) = sintered spheres (KfK)

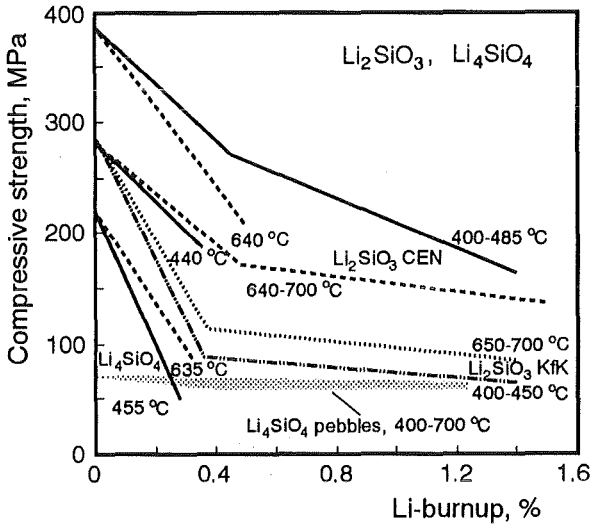

Fig. 4: Compressive strength of Li_4SiO_4 pebbles in comparison with sintered pellets as function of Li-burnup.

observed in Li_2ZrO_3, at all irradiation temperatures and in $LiAlO_2$, at 650−700°C. In all cases the steepest decrease in strength occurs at Li-burnups ≤0,4 at-%. This seems to be primarily caused by the formation of cracks and microcracks due to thermal stresses during irradiation. The influence of the irradiation temperature on the strength decrease seems to be different. The strength reduction of $LiAlO_2$, is rather large at 470°C, but much smaller above 650°C. On the other hand, the strength reduction of Li_2ZrO_3, below 490°C is significantly smaller than at temperatures above 650°C. The relative reduction of the Young's modulus under irradiation is smaller than that of the compressive strength. It depends primarily on the actual values of the density after irradiation.

Literature:

[1] K. R. Kummerer et al.
Fusion Technology (1990) p. 827 - 831

[2] P. Weimar, H. Steiner
2nd Intern. Workshop on Ceramic Breeder Blanket Interaction, Paris, Sept. 22 - 24 (1993)

[3] P. Weimar, H. Steiner, H. Zimmermann, L. Dörr
18th SOFT Karlsruhe, Aug. (1994)

[4] L. Dörr, D. Schild, H. Werle
18th SOFT Karlsruhe, Aug. (1994)

[5] M. Dalle Donne et al.
18th SOFT Karlsruhe (1994)

[6] H. Zimmermann
KfK 4525 (1989)

[7] W. Dienst et al.
ICFRM Stresa (1993)

Staff:

L. Dörr
H.E. Häfner
K. Heckert
E. Kaiser
D. Knebel
K. Müller
R. Pejsa
O. Romer
H. Steiner
P. Weimar
F. Weiser
H. Ziegler
H. Zimmermann

BS BR-D 4 Tritium Release

In assessing the performance of ceramic breeders, tritium release is an important aspect. KfK concentrates on lithium orthosilicate and metazirconate pebbles. Purged inpile tests and out-of-pile annealing tests of samples from purged and closed-capsule irradiations are performed.

Purged inpile tests

In the joint European, low-burnup, inpile test CORELLI-2, performed October to December 1993 in the SILOE reactor at CEN Grenoble, 0.2 – 0.6 mm Ø Li_4SiO_4 pebbles and, for the first time, a mixed bed of 2 mm Ø Be+ 0.1 – 0.2 mm Ø Be + 0.1 – 0.2 mm Ø Li_4SiO_4 pebbles have been tested by KfK. The inpile results are being evaluated, the irradiated samples will be sent to KfK for PIE.

In the second joint European medium-burnup (3% total Li) inpile test EXOTIC-6, performed at the HFR Petten from May 1991 to March 1992, reference breeder materials of the participating laboratories were tested [1]. Both KfK samples, Li_4SiO_4 and Li_2ZrO_3 pebbles survived the 200 FPD irradiation without visible damage. Because of the pretty large radial temperature difference (up to 180°C) between the center and the boundary of the samples, a careful estimation of the temperature distribution is required to determine relevant tritium residence times [2]. The residence times of both samples determined in this way were found to be in acceptable agreement (factor three) with previous low-burnup inpile tests (TRIDEX). In addition, there were no indications that the residence times increased with burnup up to 3% [2].

The joint European, high-burnup (up to 10% total Li), inpile test EXOTIC-7 is being performed in the HFR Petten. Small (0.1 – 0.2 mm Ø) Li_4SiO_4 pebbles and mixed beds of Be and small Li_4SiO_4 pebbles are tested by KfK. The ceramic samples have been prepared from lithium enriched to about 50% in Li^6.

Out-of-pile annealing

The extensive annealing studies of the large variety of samples from the joint European, closed-capsule, fast/thermal neutrons irradiation COMPLIMENT (damage ≤3 dpa, lithium burnup ≤4 %) have been finished. The most important results are [3,4]:

- In contrast to comparable previous irradiations, a large fraction of the samples, especially also the sintered and from the melt prepared Li_4SiO_4 pebbles decomposed during the low-temperature (425°C), thermal irradiation (burnup 1 – 4%). A tentative explanation are steep temperature gradients caused by reactor trips. Further DEMO-relevant irradiations are required.
- Tritium release kinetics is not significantly affected by
  - specific inventory (indicates first order release)
  - lihtium burnup (up to 4%)
  - type or radiation damage (fast neutrons, charged particles)
- The gamma activity of all samples was mainly due to steel contaminations and sample impurities.

Li_4SiO_4 pellets from ELIMA-1, irradiated in the fast spectrum of the KNK-II (144 FPD, total damage 3 dpa) and in addition the KfK samples of EXOTIC-6 are currently under investigation.

A closed capsule irradiation of mixed Be/Li_4SiO_4 pebble beds performed in the HFR Petten is nearly finished. The samples will be sent to KfK to study neutron-induced swelling and embrittlement of Be and tritium release of Be and Li_4SiO_4.

Literature:

[1] H. Kwast et al., Fusion Technology 1992, p. 1409.

[2] H. Kwast et al., "The Behaviour of Ceramic Breeder Materials with Respect to Tritium Release and Pellet/Pebble Mechanical Integrity", ICFRM-6, Stresa, 1993.

[3] L. Dörr, D. Schild, H. Werle, KfK 5355 (1994)

[4] L. Dörr, D. Schild, H. Werle, "Tritium Release and Gamma Activity of Various Lithium Ceramics Irradiated by Fast and Thermal Neutrons (COMPLIMENT Experiment)", presented at SOFT-18, Karlsruhe, August 1994.

Staff:

L. Dörr
T. Eberle
J. Lebkücher
M. Möschke
D. Schild
H. Werle

BS BR-D 8 Characterization of Lithium Orthosilicate: Adsorption of Water

Tritium bred in a lithium orthosilicate ceramic is essentially released as water. At constant rate of formation and release a stationary concentration will build up on the surface, which will determine the tritium inventory on the ceramic surface. At the temperature of operation of a blanket water may also lead to the formation of lithium hydroxide, which can contribute to tritium entrainment and eventually to corrosion of structural components.

The spherical Li_4SiO_4 material used in this investigation had a theoretical density of 99.9% and a specific surface area of 0.095 ± 0.010 m^2/g. By thermogravimetry a mass loss of less than 0.5% was observed when samples were heated up to 1000 K.

To perform water adsorption measurements on Li_4SiO_4 spheres a flow system, which permits water partial pressures as low as 1 mbar to be generated, was build. Water could be measured with high accuracy and precision using several different methods. The adorptive material, i.e. spherical lithium ceramics, was placed in one of two specially designed platinum reactors. To achieve the desired experimental adsorption temperatures conventional high frequency heating was employed.

Using the frontal analysis of gas chromatography adsorption isotherms were determined at temperatures and water vapor pressures ranging from 653 to 1093 K and 1 to 10 mbar, respectively. On the basis of the experimentally obtained isotherms, isobars were calculated that give the number of mols of water adsorbed per mol of lithium orthosilicate as a function of temperature at four different water pressures (1, 3, 5, and 10 mbar). In addition, isosteres giving the water vapor as a function of the inverse temperature at four surfaces coverages, i.e. $q = 0.005$, 0.010, 0.015, and 0.020, were determined. From the fact that the adsorption and desorption isotherms at a given temperature agreed rather well it is concluded that chemical processes played only a minor role under the employed experimental conditions.

The results suggest that water is adsorbed dissociatively on an energetically heterogeneous lithium ceramic surface. The data base obtained constitutes a good basis to estimate the tritium inventory at the surface of Li_4SiO_4 (cr) as function of temperature and water vapor concentration in the purge gas of a solid breeder blanket.

Staff:

S. Huber
R.-D. Penzhorn

BS NN-D 1 Helium Blanket Test Loop

The test involving temperature transients, performed on a beryllium plate with brazed-in coolant tubes, was ended according to schedule after 1000 cycles. No change in the transient temperature developments in the test object was observed during the test. This suggests that the contact between the steel tubes and beryllium did not change in the course of testing. The test object is represented once more in Fig. 1.

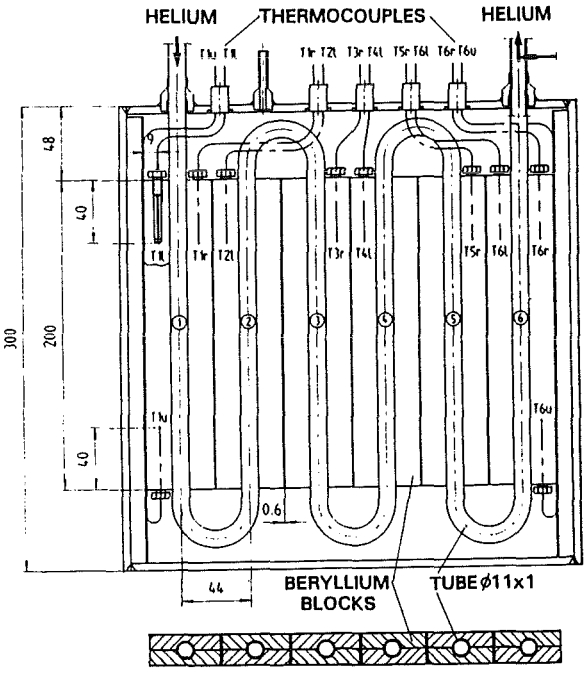

Fig. 1: Beryllium plate with brazed in helium tubes as test object in the HEBLO facility.

The beryllium test object was sent to the manufacturer, Heraeus, for post-test examinations. In a first step, a 40 mm piece each was cut from top and bottom in the manufacturer's shop and scrapped. Then slices of 5 mm thickness were cut off the top end for metallographic examinations and another slice, 10 mm in height, from both ends which served as shear specimens for strength examinations.

The results of the shear tests (Fig. 2) have been surprising because all four beryllium pieces from the interior exhibited only very uniform shearing stresses of slightly more than half the stresses measured in all preliminary tests on satisfactorily brazed specimens (180 – 200 N/mm²). Shearing took place in all specimens between the braze and the beryllium plate within the intermetallic phase. The low values of the shear stresses of the edge plates can possibly be explained by an elevated temperature near the autoclave wall during brazing resulting in enhanced embrittlement.

A second test involving temperature cycles will start in HEBLO in the near future. It will relate to the processes and stresses in a breeder material pebble bed passed by coolant coils. The

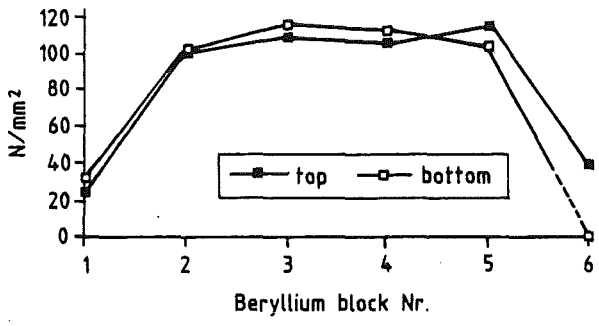

Fig. 2: Results of shear tests.

underlying concept had been until 1993 the reference concept for the helium cooled solid blanket. The layout of the test section is shown in Fig. 3. The bed (90 mm in diameter, 250 mm in height) consists of beryllium spheres of 2 mm diameter, with the spacings filled with a mixture of very small beryllium and Li_4SiO_4 ceramic pebbles of 80 – 200 µm diameter. Thus, the bed is similar to that in the highly loaded blanket front zone. Three hair-needle shaped coolant pipes run through the bed; their diameters and spacings are similar to those in the blanket. The bed can be loaded up to 500 N/cm² at the maximum through a pneumatically driven piston. In a middle plane of the bed thermocouples are installed on the surfaces of the coolant tubes and at different spacings between the tubes. This should allow the thermal conductivity of the bed and the heat transfer to the tubes to be measured, also as a function of the bed constraint. However, the actual purpose of the experiment is the determination of the bed behavior, i.e. the amount of abrasion and the amount of broken spheres at the end of endurance testing. Moreover, it is intended to record during the test any changes - e.g. regarding the thermal properties of the bed and the pressure drop in the purging gas.

The bed in the test section consists of material reprocessed from an earlier test bed used for thermal conductivity measurements. It was filled into the test section in a beryllium handling workshop of an industrial firm with great care and with all safety precautions taken. The test run in the HEBLO facility can start in October 1994.

Staff:

M. Dalle Donne
H. Lehning
K. Müller
D. Piel
G. Reimann
H. Reiser

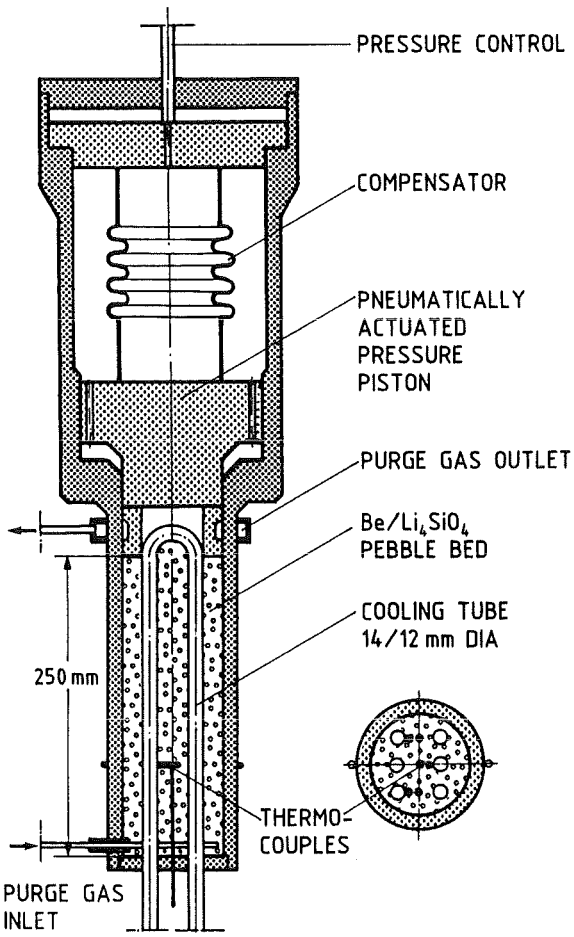

Fig. 3: Test section with a beryllium/Li_4SiO_4 pebble bed passed by cooling coils.

BS NN-D 2 Non Nuclear Tests

1. Thermal Cycling Tests on Li_4SiO_4 and Beryllium Pebbles

The European B.O.T. Demo-relevant solid breeder blanket is based on the use of mixed beds of Beryllium and Li_4SiO_4 pebbles [1] or, alternatively, on separate beds of beryllium and Li_4SiO_4 pebbles [2]. It is important to show that during blanket operation not too many pebbles break and powder is formed which could reduce or impede the flow of the gas purging the tritium produced in the Li_4SiO_4. Particularly dangerous for the pebble integrity are the rapid temperature changes which could occur, for instance, by a sudden blanket power shut-down. A series of thermal cycles tests have been thus performed for various mixed beds of beryllium and Li_4SiO_4, and for beds of Li_4SiO_4 pebbles. The present paper reports on the results of these investigations.

1.1 Experimental apparatus

Fig. 1 shows schematically the experimental apparatus. The test section containing the pebbles is heated in a furnace until the tube wall of the test section (Fig. 2) is heated to 600°C and then is automatically moved to a water bath until this temperature is reduced to 230°C. Then the test section is taken to the furnace again and the process is repeated many times. At regular time intervals, generally every 50 - 100 cycles, the pressure drop of the helium flowing through the pebble bed to be tested is measured. Fig. 2 shows the test section. The pebble bed is contained in a curved tube. The bed is kept in position by perforated plates fixed to small rods and supported by springs. The tube wall temperature and the center temperature of the bed are measured by means of two thermocouples.

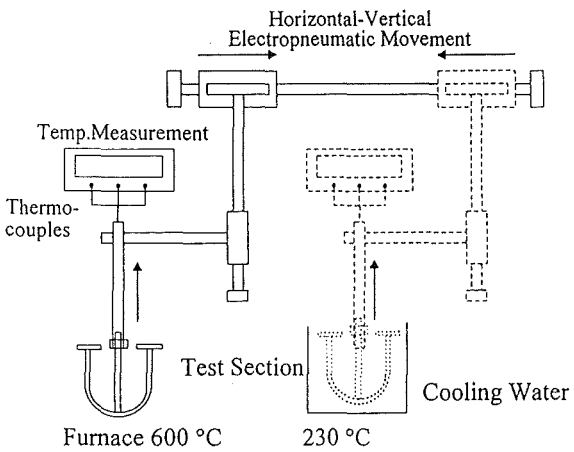

Fig. 1: Experimental apparatus for the thermal cycle tests

Fig. 3 shows a typical temperature profile measured during the test. The temperature at the pebble bed center follows the wall temperature with a considerable delay, so that temperature variations are smaller and much slower than at the wall. Fig. 4 shows the variation of the pressure drop of the flowing helium across the pebble bed. The breaking of the

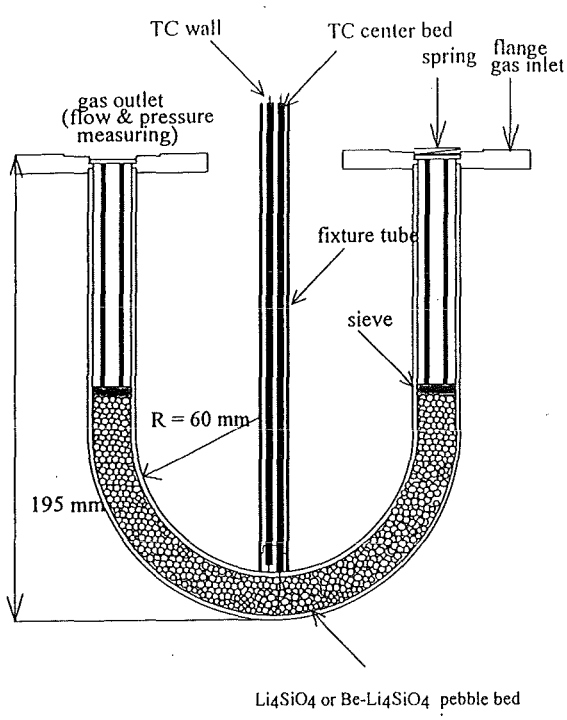

Fig. 2: Test section for the thermal cycle tests.

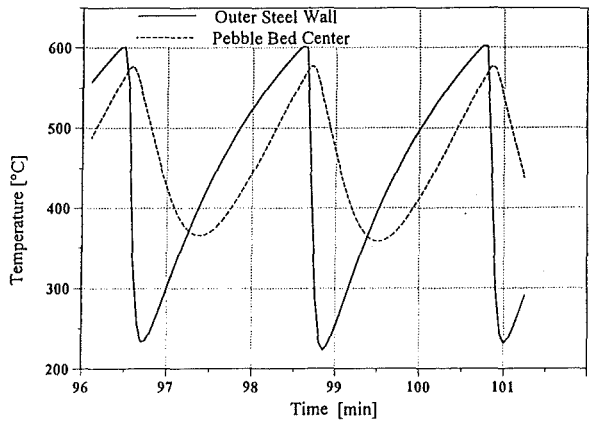

Fig. 3: Typical temperature profiles during thermal cycle tests (Li_4SiO_4 pebbles).

Li_4SiO_4 causes an increase of the pressure drop. However, generally after 300−500 cycles, the pressure drop remains approximately constant, indicating that no further break-up of the pebbles occurs.

Experiments were performed up to 1000 cycles for (i) mixed beds of beryllium (Ø=2 mm, packing factor: ψ=0.78) and Li_4SiO_4 (Ø=0.1−0.2 mm, ψ=0.18) pebbles and (ii) beds of Li_4SiO_4 (Ø=0.3−0.6 mm, ψ=0.64) pebbles. The tests were made with Li_4SiO_4+2.2 wt % SiO_2 with natural lithium or with lithium with 50% ^6Li. Both types of Li_4SiO_4 pebbles were produced by melting and spraying (density 97−99% of theoretical) by the firm Schott Glaswerke, Mainz, starting in

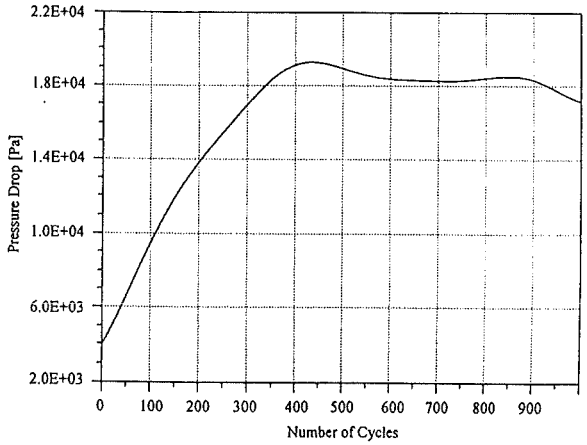

Fig. 4: Pressure drop across the pebble bed (mixed bed Be-Li_4SiO_4) during a thermal cycle test.

the first case with Li_4SiO_4 and SiO_2 powders and, in the second, with Li_4SiO_4, SiO_2 and $^6Li_2CO_3$ powders.

1.2 Results

Results of preliminary experiments have been published [3]. The present experiments have been performed with a greater number of cycles (1000) and with a more frequent recording (every 0.1 seconds) of the temperatures, which allowed a more accurate measurement of the temperature rates of change. Furthermore, the tests have been performed with a minimum tube wall temperature of 230°C, which is more relevant for the blanket application than the temperature of 70°C used in the previous tests.

Examination of the pebbles after the tests showed that no beryllium pebbles were broken, however a fraction of the Li_4SiO_4 were. As in previous tests, it was noticed that the broken particles were on the periphery of the bed in the region nearest the tube inner wall, where the rates of change in temperature are the highest.

The temperatures of the pebble bed during the cooling phase, when the rates of change in temperature are the highest, were calculated for the test part, where the greatest amount of broken particles was reached (constant pressure drop across the bed), by considering the pebble bed as a homogeneous solid. The flow of helium through the bed was so slow that the transfer of heat in radial direction was given by conduction only [4]. The heat conduction Fourier equation in cylindrical coordinates was solved for the cooling phase with a numerical procedure, taking as boundary conditions the measured wall and bed center temperatures. The resulting heat diffusivities for the Be-Li_4SiO_4 mixed bed and the bed of Li_4SiO_4 were 1.73 10^{-6} and 0.34 10^{-6} m^2/sec, respectively, in very good agreement with the measured thermal conductivity data for these beds [3] and the well known heat capacities of these materials.

The determination of the amount of broken particles at the end of the test allowed to calculate the critical radius beyond which the particle are broken. Fig. 5 shows the results of the calculations, namely the temperature rate of change versus the local bed temperature during the cooling phase at various radial distances from the bed center, including the critical radius, for the bed of Li_4SiO_4 pebbles. The line for r_{cr}=critical radius gives the combination of temperature gradient and temperature at which the breaking of the pebbles would have occurred. The results with pebbles with 50% ^6Li enrichment were practically identical to those with natural Li. The same holds for the two mixed Be-Li_4SiO_4 beds with natural and enriched ^6Li. Fig. 6 shows the same diagram for the critical radius of the two pebble beds (Be-Li_4SiO_4 and Li_4SiO_4). Also here one can notice that the curves for r_{cr} differ very little, although the diffusivity in the Be-Li_4SiO_4 bed is 5 times greater and the percentage of broken particles is higher than in the case of the bed with Li_4SiO_4 only. This shows that what breaks the particles is not the outside pressure of the constraining steel walls, but it is rather the temperature rate of change over the time. Indeed, the smaller Li_4SiO_4 pebbles in the mixed Be-Li_4SiO_4 bed are affected much less by the wall pressure than the bigger ones of the Li_4SiO_4 bed. In the mixed bed the structure of the bed is made up by the bigger beryllium pebbles which take the major part of the wall pressure. Nevertheless, with or without beryllium pebbles the breaking characteristics of the Li_4SiO_4 pebbles are about the same.

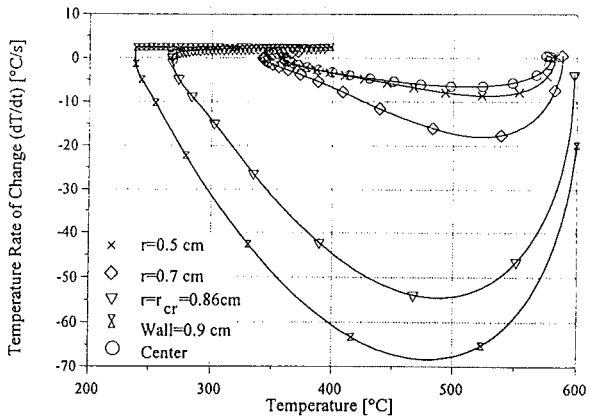

Fig. 5: Local temperature rate of change versus local temperature for various radial distances from the cylinder symmetry axis (Li_4SiO_4 pebble bed). r_{cr}=radius beyond which the particle are broken.

With the present experimental data is not possible to establish with certainty which is actually the critical temperature gradient. However, there are indications from irradiation experiments, that Li_4SiO_4 becomes brittle for temperatures in the range 400–450°C. Indeed, irradiation experiments performed in the OSIRIS reactor, in presence of temperature shocks given by reactor scrams, showed that a considerable portion of the particles irradiated at temperatures of 400–450°C were broken, while the particles irradiated at 650–700°C were intact [5]. From Fig. 6 one can

see that the temperature range 400 – 450°C corresponds to a temperature gradient of about – 50°C/sec.

Fig. 6 shows also the peak temperature rates of change expected in the region of maximum power density and highest first wall heat flux of the BOT DEMO solid breeder blanket [1] by the worst accident (sudden loss of power production by constant helium cooling flow). These are considerably lower than the values corresponding to the critical radius.

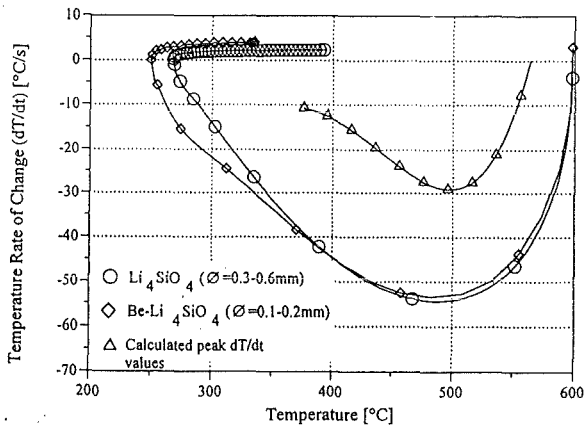

Fig. 6 Comparison of the curves dT/dt versus T at $r = r_{cr}$ for the tested beds with the curve calculated for a sudden loss of power by constant helium cooling flow in the region of maximum power density and highest first wall heat flux of the BOT DEMO blanket.

1.3 Conclusion

The performed thermal cycle tests have shown that the Li_4SiO_4 pebbles, although they tend to become more brittle at lower temperatures, can withstand temperature rates of change considerably higher than the peak values expected in the BOT DEMO blanket. This holds for unirradiated pebbles. These experiments should be repeated for pebbles irradiated up to the maximum burn-up foreseen in the BOT DEMO blanket, i.e. 7.25% [2] or 10% [1].

Literature:

[1] M. Dalle Donne et al., Status of EC Solid Breeder Blanket Designs and R&D for DEMO Fusion Reactors, Proc. ISFNT-3, Los Angeles, June 27, 1994.

[2] M. Dalle Donne et al., European DEMO BOT Solid Breeder Blanket: The Concept Based on the Use of Cooling Plates and Beds of Beryllium and Li_4SiO_4 Pebbles. 18th SOFT, August 22 - 26, 1994, Karlsruhe Germany.

[3] "Thermal Cycle Tests", in Nuclear Fusion Project Annual Report of the Association KFK/EURATOM, Oct. 1992 - Sept. 1993, KfK 5288, EUR 15466, Dec. 1993, p. 110 - 111.

[4] M. Dalle Donne and G. Sordon, Fus. Technol. 17, (1990) 597.

[5] P. Weimar, and H. Steiner, Results of the Destructive Examination of the Breeder Samples of the COMPLIMENT Irradiation Experiment,. Int. Workshop on Ceramic Breeder Blanket Interactions, Paris, Sept. 22, 1993.

Staff:

M. Dalle Donne
R. Huber
P. Norajitra
B. Schmitt
G. Schumacher
A. Weisenburger

BS NN-D3 Tritium Extraction from a Solid Breeder DEMO Blanket

The principle of a tritium extraction system (TES) being developed at KfK has been outlined in the preceeding report. It can be summarized as follows:

Tritium is expected to appear in two chemical forms (HT and HTO) in the blanket purge gas. Therefore, two specific process steps are applied for its recovery, i.e. a cooler to freeze out Q_2O (Q=H,T) at 173 K, and a molecular sieve bed to adsorb Q_2 at 78 K. For continuous tritium removal from the blanket these components must be available at least twice as shown in Figure 1: while the first cooler/molecular sieve is being loaded, the second unit is in the deloading/regeneration mode. (In the case of the molecular sieve beds, three units are needed because of capacity and cycle time reasons.)

A first layout of the tritium extraction system was developed in cooperation with Linde AG/München. It was especially designed to cope with large purge gas streams ($5-10^6$ mole He/d+0.1% H_2). This layout is described in the following.

At the inlet of the primary loop (see Fig. 1), a precooler PC1 is used to cool the purge gas to 308 K; the gas is then further cooled to 173 K in the main cooler C1 whereby the Q_2O-content is almost completely condensed and frozen out at the surface of the cooling tubes; the residual concentration is <0.015 ppm. The operation time of cooler C1 is 10 days. The purge gas is then directed to a second cooler C2, while the ice collected in the first one is thawed. 24 hours later, the tritiated water (about 12 ℓ with a tritium inventory of about 48 g) is drained into a water collector which is connected with a secondary loop ("*Q_2O loop*", see below).

The purge gas is further cooled down to 80 K by the second precooler PC2 and then passed through the adsorber bed MS1 where the molecular hydrogen is adsorbed on a 5 A molecular sieve. Residual moisture and gaseous impurities are also retained on the MS. The operation time of the bed in the adsorption mode is 6 hours.

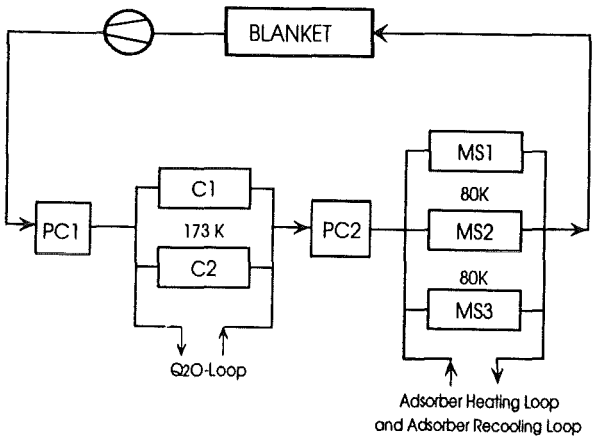

Fig. 1: Block Diagram of the Tritium Extraction System (Primary Loop)

An Adsorber Heating-Loop (Fig. 3) is used to warm up the adsorber within 6 hours to 160 K to release about 98% of the hydrogen isotopes.

Again 6 hours are needed to record the adsorber bed by using an additional Adsorber Recooling Loop. Thus, three adsorber beds are operated in parallel, according to the 6-hour steps adsorption, warmup, and recooling.

If the adsorption capacity should decrease, the molecular sieve beds must be regenerated by increasing the warmup temperature to about 500 K to desorb the accumulated impurities and/or the residual moisture. As this cannot be carried out within one of the usual 6 h periods, either a forth adsorber bed is needed for replacement, or an interruption of 2–3 days will be necessary in the availability of the TES.

Q_2O-Loop (Fig. 2)

The Q_2O collected in the cooler is liquefied by warmup to about 300 K and then drained into an evacuated water collector. The corresponding container is used also to reduce the total gas pressure in the cooler which increases during warmup. It is equipped with an electrical heater allowing a slow evaporation of the water.

The gas is now transferred to a water gas shift reactor (WGSR) where it is converted to CO_2 and Q_2 by addition of CO and by the use of a copper chromite catalyst (T=200°C, conversion rate >99.5%). The hydrogen isotopes are removed from the

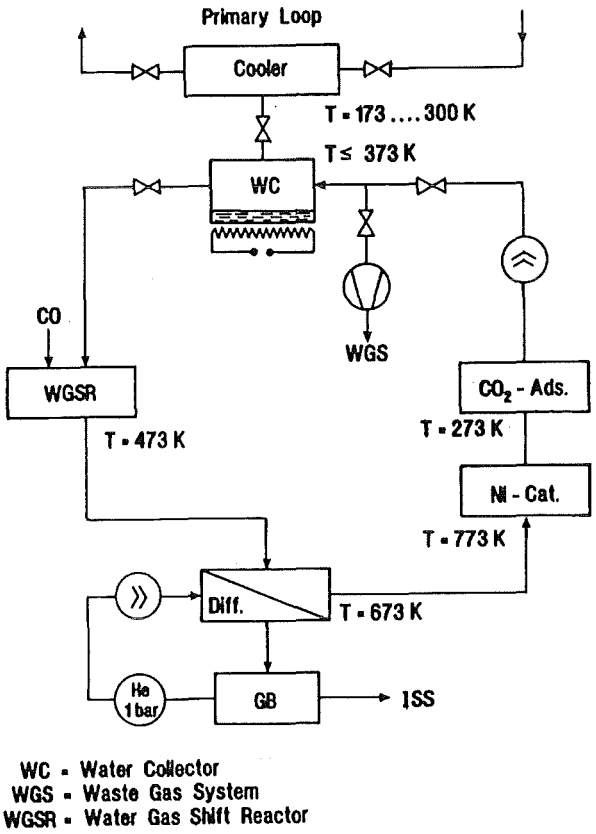

Fig. 2: Q_2O-Loop

gas stream by a Pd/Ag diffusor and stored on a metal getter bed.

The nickel catalyst bed has the task to crack tritiated methane that can be formed with a small yield by the reaction

$$CO + 3Q_2 \rightarrow CQ_4 + Q_2O \ .$$

The CO_2 adsorber down-stream of the nickel catalyst is used to remove the CO_2 formed by the water gas shift reaction.

Q_2-Loop (Fig. 3)

As described above, each molecular sieve bed is connected with the Adsorber Heating Loop which is also called *Q_2-Loop* in analogy to the Q_2O-Loop. The upper part of the Q_2-Loop includes an electrical heater H500, the circulation pump P500, and two buffer vessels B500a/b, each with a volume of 30 m³.

At the beginning of a warmup cycle, the vessel B500a must be cooled to 160 K and filled with 0.3 bar of very well purified helium. This gas is pumped through the adsorber with a gas flow rate of 1600 Nm³/h. With increasing temperature of the bed, first to co-adsorbed helium is released (max. 15 Nm³), and then the hydrogen isotopes (≤26 Nm³). The resulting pressure in the loop will be ≤1.3 bar (if the temperature of 160 K and 50% void volume of the molecular sieve material are considered). At the end of a 6 h deloading phase, the next adsorber is connected with the heating loop, and another warmup phase is started with 0.3 bar helium contained in vessel B500b.

With the help of pump P600, the He-Q_2-mixture contained in vessel B500a is sent through an uranium getter bed with a flow rate of 15 Nm³/h. The bed is operated at room temperature to ensure a selective and effective sorption of the hydrogen isotopes. The amount of uranium needed to store all H_2/HT of a 6 hour operation cycle is about 500 kg.

The first 15 Nm³ of gas leaving the getter bed are fed into the purified purge gas at the TES exit. The remaining hydrogen-free gas is collected in the buffer vessel B600 and lateron pumped back into vessel B500a.

The second getter bed is used when the first one is deloaded by heating. The released hydrogen isotopes are transferred directly into the Isotope Separation system (ISS).

Staff:

H. Albrecht
E. Hutter

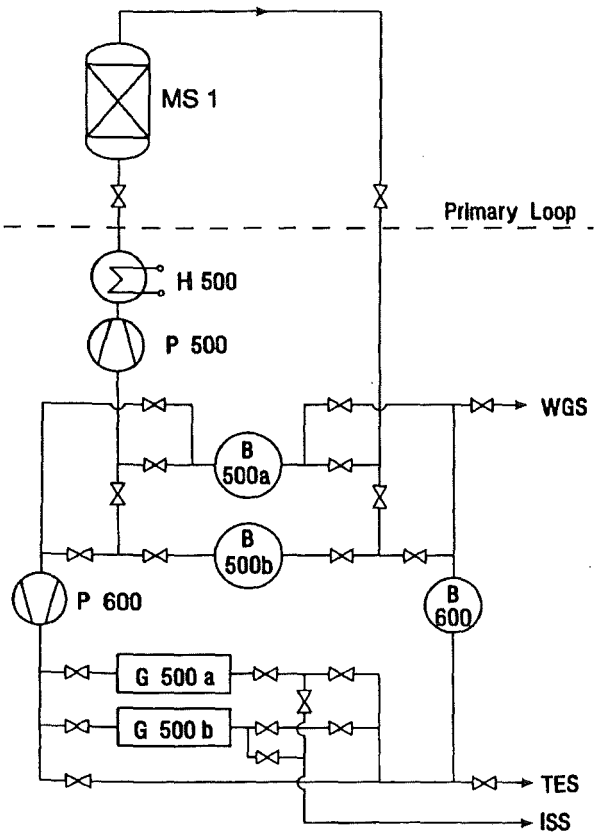

Fig. 3: Adsorber Heating Loop (Q_2-Loop)

BL DE-D 1 Liquid Metal Test Blanket Design

The subjects of this task are the design of liquid metal blankets for the application in a DEMO reactor, the development and the design of blanket test modules in NET/ITER, and, for both cases, the conceptual design of suitable external loops for heat and tritium extraction.

This work is part of the European Blanket Development Programme where four blanket concepts are developed with the intention to select in 1995 the two most attractive concepts for further development [1].

The design work has been concentrated on a "Dual Coolant Blanket" concept [2, 3] where the First Wall (FW) is cooled by helium and the breeding zone by the circulating liquid metal breeder ("self-cooling"). A perspective view of an outboard blanket segment is shown in Fig. 1.

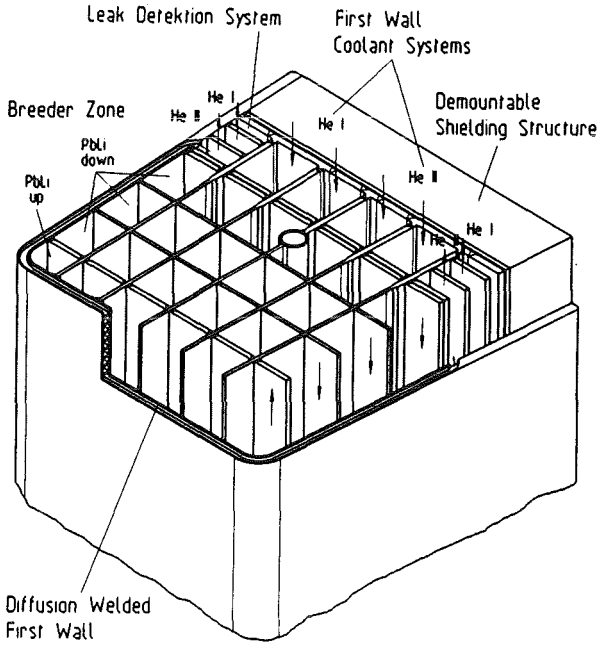

Fig. 1: Perspective view of an outboard blanket segment

The FW consists of two plates with integrated cooling channels which are bonded by diffusion welding. Several test welds have been carried out successfully; the results are described in this report under Task MANET 2.3.

As a next step the bending of the diffusion-welded FW panel into the U-shaped box will be investigated.

An important detail of the Dual Coolant Blanket concept is the joint between the U-shaped poloidal sections of the FW. According to the safety and reliability criteria which admit no single welds between plasma and helium or Pb-17Li, electron beam double welds are envisaged for this purpose. The gap between the two welds additionally serves for leak detection.

An investigation has been started in collaboration with an industrial manufacturer to demonstrate the feasibility of the EB double weld. Additionally, the quality of the weld has to be assessed in order to obtain a data base for the probabilistic assessment of EB welds (see Task BL SA-D1). The main results at the current state of the investigations are:

- the feasibility of the EB welding has been demonstrated
- the welding process has no influence on the leak detection gap between the two parts of the weld; thus it is possible to use single pass welding, which is an essential requirement with regard to the assembly of the blanket
- the nondestructive investigations are currently under way and are expected to confirm proper quality of the weldments
- a further test welding will be performed using a specimen with cooling channels. The purpose is to confirm the possibility of nondestructive testing under geometrical constraints, as well as to confirm that the welding procedure is not influenced by the presence of cooling channels in the joined sections.

Parallel to these investigations, a numerical analysis of the welding procedure was performed [4,5]. As a result, time dependent temperature and stress fields were obtained. Also, residual stresses were calculated and the effect of post-weld heat treatment was considered. Welding and residual stresses may be responsible for the initiation and propagation of cracks in the weld and are therefore essential for a reliability analysis (see Task BL SA D1).

The spatial power density distribution needed for the thermal analysis results from the neutronics analysis. The maximum power density occurs in the poloidal mid-plane of the outboard blanket and amounts to 25 MW/m^3 in the structural material and 19 MW/m^3 in the Pb-17Li. For the plasma facing blanket surface an average heat flux of 0.4 MW/m^2 and a local peak value of 0.5 MW/m^2 was assumed.

The thermohydraulic layout for inboard and outboard blankets has been completed. The total power generated is 30 MW in an outboard segment and 0.6 MW in an inboard half-segment. The inlet and outlet temperatures of the helium (250/350°C) and the Pb-17Li (275/425°C) have been selected using arguments like: sufficient margin to the DBTT of the martensitic steel and the melting point of the Pb-17Li, limitation of the maximum structural and Pb-17Li interface temperature, attractive thermal efficiency of electrical power generation, etc. The helium pressure is 8 MPa. The pressure drop of the helium flow amounts to 0.148 MPa in the outboard and 0.122 MPa in the inboard blankets.

For the calculation of the temperature and stress distribution in the structures, the FE code ABAQUS was used. The analysis was carried out for a radial/toroidal section of the outboard blanket with a poloidal height of one helium channel pitch (see Fig. 2). The alternating direction of the helium flow in neighbouring channels were taken into account by an iterative adjustment of the poloidal interface temperature

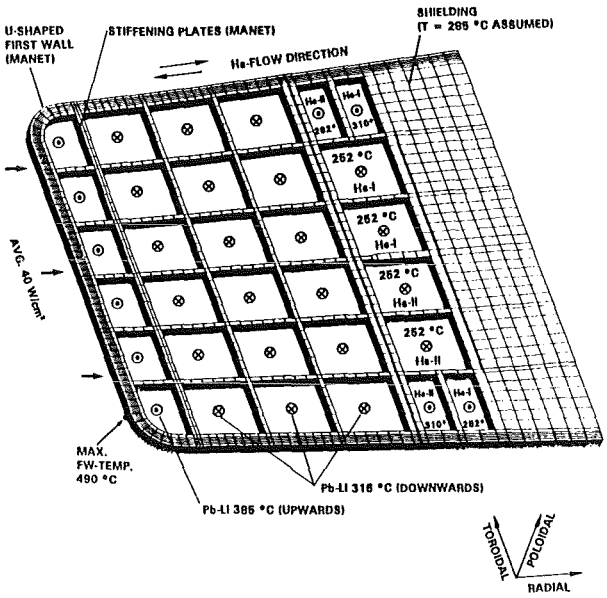

Fig. 2: FE Mesh Used in 3-D ABAQUS Calculations.

for a surface heat load of 0.4 MW/m². The maximum temperature occurs at the edge of the plasma facing surface of the blanket segment and amounts to 490°C. At the peak thermal load of 0.5 MW/m² the maximum structural temperature reaches 520°C.

In the stress calculations a quasi plane strain condition was applied for the poloidal surfaces of the model which means that these planes remain plane and parallel. For the breeder zone (Pb-17Li) the same pressure of 8 MPa was assumed as for the helium system. This is a conservative upper limit of the internal load which is reached only in case of a leak between the helium and the Pb-17Li systems. The temperature field for 0.4 MW/m² was used. The calculated primary von Mises stress amounts to 120 MPa. This value is below the limits for yield, rupture and 20 000 h creep stress allowed for MANET at 490°C according to ASME (217 MPa in case of bending). The total von Mises stress (primary plus secondary distribution is shown in Fig. 3. The maximum stress occurs at the location of the temperature maximum and amounts to 441 MPa. This is well below the allowable stress of 494 MPa according to ASME.

The global thermomechanical behaviour has been investigated in an additional two-dimensional ABAQUS analysis for a radial/poloidal section of the outboard blanket segments. These investigations show that the influence of the helium pressure and the gravity load on the global displacements is negligible. The maximum thermal stress and the stress distribution in the first wall depend strongly on the support conditions of the segment and the temperature of the backward shield plate. A relatively cool shield plate increase the bending of the free hanging blanket. This causes a reduction of the thermal stresses. If bending is restricted by an additional support, e.g. by connecting the shield plates of the segments to a rigid toroidal shell, a hot shield causes an increased poloidal strain and also a reduction of the secondary stresses. The quasi plane strain conditions assumed

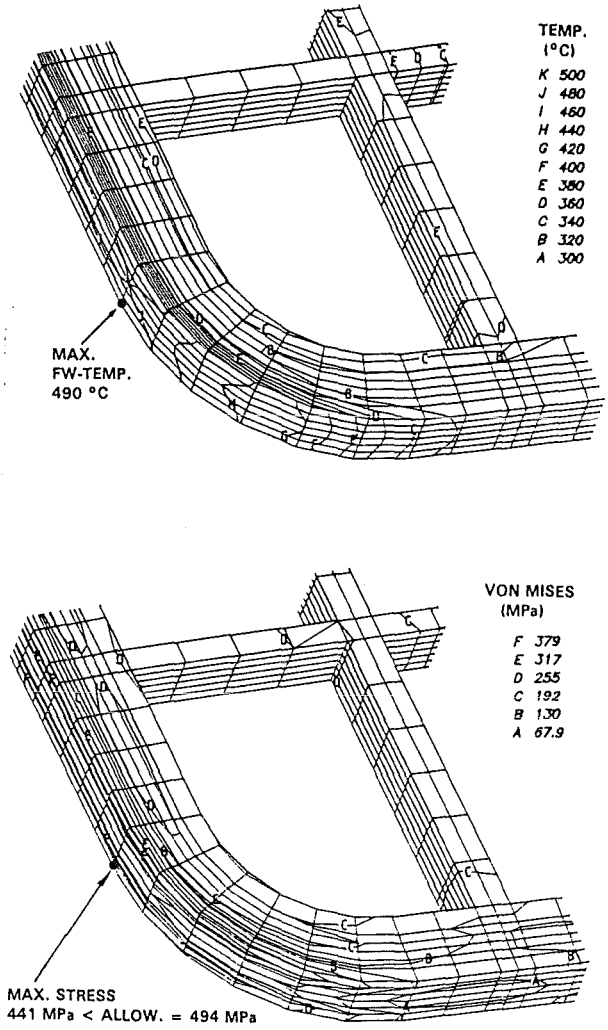

Fig. 3: Temperature (Top) and Stress Distribution (Bottom) in the Blanket Structure.

in the three-dimensional calculation for the radial/toroidal section was confirmed to be reasonable in the case that bending of the segment is suppressed. By optimizing the boundary conditions a reduction of the main compressive stresses of up to 28% can be reached. The resulting von Mises stress need to be determined in additional three-dimensional calculations.

The shield temperatures assumed in the two-dimensional calculations were in all cases lower than the mean value of the minimum and maximum temperature of the blanket structure. This allows the conclusion that also under operational transients the temperature difference between the shield and the structure, and consequently also the thermal stresses will not be larger than under the steady state conditions described above.

The investigations of the magnetohydrodynamic (MHD) issues of this concept are described under Tasks BL MH-D1 and BL EL-D1.

Literature:

[1] S. Malang, L. Anzidei, M. Dalle Donne, L. Giancarli, E. Proust, European Blanket Development for a DEMO Reactor, 11th TMTFE, New Orleans, Louisiana, USA, June 19-23, 1994.

[2] G. Kast (comp.), Nuclear Fusion Project, Annual Report of the Association KfK/Euratom, October 1992 - September 1993, KfK 5288, Dec. 1993.

[3] S. Malang, L. Barleon, E. Bogusch, P. Norajitra, H. Reiser, J. Reimann, K. Schleisiek, Conceptual Design of a Dual Coolant Liquid Metal Breeder Blanket, 18th SOFT, Karlsruhe, Aug. 22-26, 1994.

[4] L. Cizelj, H. Riesch-Oppermann, An Analysis of Electron Beam Welds in a Dual Coolant Liquid Metal Breeder Blanket, Kernforschungszentrum Karslruhe, KfK 5360, 1994.

[5] L. Cizelj, H. Riesch-Oppermann, Wleding Stresses in the First Wall of a Dual Coolant Liquid Metal Breeder Blanket, SOFT 18, Karlsruhe, 1994.

Staff:

L. Cizelj
U. Fischer
H. Gerhardt
S. Malang
K. Müller
P. Norajitra
J. Reimann
H. Reiser
H. Riesch-Oppermann
K. Schleisiek

BL PC-D 2 Active and Inactive Impurities and Clean-up of Molten Pb-17Li

1. Adjustment of lithium concentrations

The lithium concentration in a blanket will change because of different effects. The melting point of the mixture increases, causing the risk of blocking. Also the tritium breeding ratio and transport properties of tritium by the molten mixture change. The lithium concentration, therefore, has to be adjusted. While lead can be added in case of an Li-enrichment (e.g. because of segregation effects [1]), lithium cannot because of the large density difference. The two intermetallic compounds LiPb and Li_3Pb were fabricated in an argon glove box. Both compounds were used to add Li to mixtures of Li and Pb [2]. The dissolution rate of LiPb and Li_3Pb is 0.14 $g/cm^2 \cdot h$ at 300°C (stirred mixture). Therefore it is easy to adjust a desired Li-concentration. It is even possible to produce the eutectic mixture from pure lead in smaller facilities by adding Li_3Pb. This was done stepwise in a thermal convection loop with originally pure lead. Fig. 1 shows the increase of the lithium concentration in this loop [2].

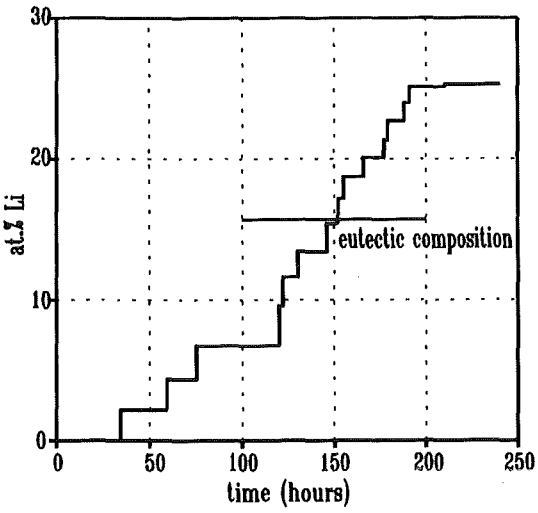

Fig. 1: Li concentration in Thermal Convection Loop 6 while adding Li_3Pb

2. Purification of Pb-17Li

Most of the investigations are done with the facility TRITEX. This is a pumped Pb-17Li loop from ferritic steel [3], now running in experimental phase 6. The main modification to phase 5 is a completely new designed Cold Trap. The photo shows the arrangement at the loop. The first part at the right is an air cooled section. There, seven chambers at fixed temperatures contain wire coils for deposition, each with 130 cm^2 surface. The second part is an isothermal deposition area with more than 1 m^2 ferritic steel wire mesh. The temperature in this part is kept constant within 1 degree.

TRITEX will run for 2000 to 4000 hours with constant conditions. After this, the Cold Trap will be analyzed. From the results, a model for the design of a technical Cold Trap will be developed.

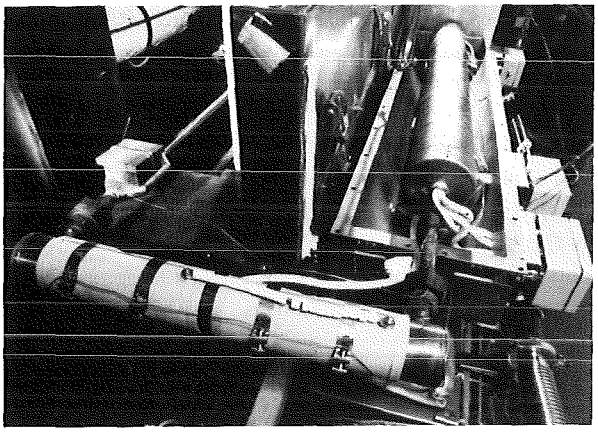

Fig. 2: Arrangement of Cold Traps in TRITEX during experimental phase 6

Literature:

[1] H. Feuerstein et al., Intern. Conf. on Liquid Metal Systems, Karlsruhe, Germany, March 16-18, 1993

[2] H. Feuerstein et al., Paper presented at the 18th SOFT Conference, Karlsruhe, August 22-26, 1994

(3) H. Feuerstein et al., J. of Nuclear Materials 155-157 (1988) 520

Staff:

J. Beyer
S. Bucké
H. Feuerstein
L. Hörner
S. Horn
H. Reinhard
D.A. Wirjantoro

BL EI-D 1 Electrical Insulation and Coatings

1. Direct Electrical Insulation

The oxidation of the aluminide layers on MANET steel produced by means of the "Hot-Dip" procedure was performed under reduced partial pressures of oxygen. The oxidizing atmosphere was Argon containing H_2 of a partial pressure of about 5 kPa, this gas was saturated with H_2O at room temperature [3]. The kinetics of oxidation at 900°C were slower than in air as oxidizing medium [1,2]. The oxide layers gained in the low oxygen atmosphere were of higher purity compared to the reaction product of the oxidation with air. The long lasting process step of oxidizing the aluminide layers made the thermal treatment

The oxide layers were of sufficient thickness after a reaction time of about 100 h, however, the integral measurements of the electrical resistance of coated specimens in contact with Pb-17Li at 400°C indicated that the layers contained some spots of low resistance. Such spots seemed to occur at edges and similar regions of the specimens.

Some specimens provided by ENEA in the particular size designed for thermal cycling tests in Pb-17Li within the LIFUS 2 facility at Brasimone were aluminized by means of hot-dipping and subsequently oxidized. These specimens which are not designed for in-line measurements of the electrical resistance will be used for the first tests. The aim of these tests is the detection of cracks or spalling of of coatings due to the thermal cycling in Pb-17Li.

Vanadium alloys (V-5Cr-5Ti and V-1Si-3Ti) were reproducibly coated with aluminide layers of sufficient thickness. Such aluminized V alloy samples were exposed to sodium at 500 to 550°C in the presence of nitrogen atmosphere or of dissolved sodium azide (NaN_3). The reactions of the aluminide with dissolved nitrogen were incomplete in all cases, the effect of temperature on the results indicated that the formation of aluminum nitride layers might occur at still higher temperatures. The solubility of V in liquid lithium was evaluated from corrosion tests [4].

The electrochemical measurements of the chemical activity of Al in iron aluminides at high temperatures are completed. Some chemical analyses are still necessary to relate the thermodynamic data to exact compositions of the alloys. The results will then be evaluated in respect to the thermodynamics of the self-healing in contact with Pb-17Li alloy containing traces of oxygen and documented.

Literature:

[1] H. Glasbrenner, H.U. Borgstedt
"Preparation and characterisation of Al_2O_3 / Fe_xAl_y layers on MANET steel", J. Nucl. Mater. 212-215 (1994) 1561-1565.

[2] H.U. Borgstedt, H. Glasbrenner, Z. Peric
"Corrosion of insulating layers on MANET steel in flowing Pb-17Li", J. Nucl. Mater. 212-215 (1994) 1501-1503.

[3] H.U. Borgstedt, H. Glasbrenner
"The development of a direct insulating layer for liquid metal cooled fusion reactor blanket", Intern. Symp. on Fusion Nuclear Technology 3, Los Angeles, 27.6.-1.7.1994.

[4] C. Guminski, H.U. Borgstedt
Solubility of vanadium in the liquid alkali metals lithium and sodium", Z. Metallkde. 85 (1994) November issue

Staff:

H.U. Borgstedt
H. Glasbrenner
Z. Peric
H. Kleykamp
W. Laumer

2. Irradiation Behaviour of Insulating Coatings

2.1 Neutron irradiations

During plasma operation, the insulator placed between the circulating metal coolant and the surrounding steel structure to limit the MHD pressure drop is subjected to a neutron flux of about 1×10^{15} n/(s cm²), an applied electrical field of 1 kV (DC)/cm and a temperature up to 450°C. A full power lifetime of 20 000 h results in a neutron damage in Al_2O_3 of 45 dpa.

To investigate the behaviour of Al_2O_3 under such conditions, irradiation experiments will be carried out in the HFR Petten. In the first test series, four highly pure (99.8%) bulk plates of 14 mm diameter and 0.5 mm thickness will be used. They are on both sides covered with vapor-deposited metal electrodes to be connected with the electrical leads for voltage, guard and current. The probes are separately placed inside inner capsules, which are filled with He or are evacuated. These inner capsules are placed inside outer capsules, which are cooled by reactor water. By changing the gas-mixture inside the gaps between inner and outer capsules the temperatures of the inner capsules can be controlled. The outer capsules will be inserted in a special rig of the type TRIO-131, which will be placed into one of the experimental in-core positions of the HFR-Petten.

The irradiation will start early in 1995. At the end of 1995 a damage of about 7 dpa will be reached.

Staff:

J. Aberle
K. Schleisiek
G. Schmitz

3. Irradiation Behaviour of Insulating Coatings

Among the properties of importance the electrical behaviour of insulating ceramic materials under irradiation plays a central role in various control and diagnostic components as well as in the selection and design of blanket and vacuum current breaks.

Well known in the literature is the radiation induced conductivity (RIC), which is due to the excitation of electrons from the valence into the conduction band by X- and γ-Rays or charged paricles. RIC has often been found to be in a wide range proportional to the density of this energetic ionizing particles and immediately disappears when the particle current is turned off. Even under intense neutron irradiation where the ionizing dose rates usually are much smaller compared to charged particle irradiations, RIC is orders of magnitude above the thermal induced conductivity at elevated temperatures. Recently, E. Hodgson discovered an additional considerable increase in the conductivity, called radiation induced electrical degradation (RIED), during electron irradiation when an electric field is applied. In contrast to RIC, RIED has found to be of permanent character.

The prime objectives of the present investigations are: Firstly, to contribute to a clarification of the present uncertainties on whether Al_2O_3 and AlN can suffer quickly a permanent loss of their electrical resistivity, when an electrical field is applied during irradiation. Secondly, to produce well defined data on the in-situ and postirradiation conductivities σ and σ_0 under fusion relevant loading conditions up to damage levels far beyond those ones, which typically could be reached by electron irradiations.

3.1 Experimental

Ceramic specimens have been cut from plates made of polycrystalline AlN (99.6%), Al_2O_3 (99.9%, Vitox) and Al_2O_3 (99.2%, Wesgo). The main impurities analysed with chemical methods are: Fe (0.08%) and O (0.34%) in aluminium nitride, MgO (0.09%), CaO (0.03%), Na_2O (0.03%) and Fe_2O_3 (0.03%) in Vitox-alumina, as well as MgO (0.31%), CaO (0.095%), Na_2O (0.027%) and Fe_2O_3 (0.076%) in Wesgo-alumina. All numbers are given in weight-%. To ensure well defined measurements of the volume conductivity, a guarded circuit design with three electrodes was used (fig. 1). The substrate consisted of a hollow fatigue specimen with a square cross section developed for in-beam creep-fatigue experiments and was made of the European ferritic/martensitic reference steel MANET.

The setup shown in Fig. 1 served several vital functions: (i) The solid state bonding between ceramic and MANET-steel removes effectively the heat deposition of the α-particle beam and minimizes thermal gradients. Even in the alumina samples with its very low thermal coefficient of linear expansion the calculated temperature gradient amounted to less than 3 K during these irradiations. (ii) The solid state bonded leads guaranteed constant and small (<1 Ω) contact resistance. (iii) An isolated, calibrated tiny thermocouple

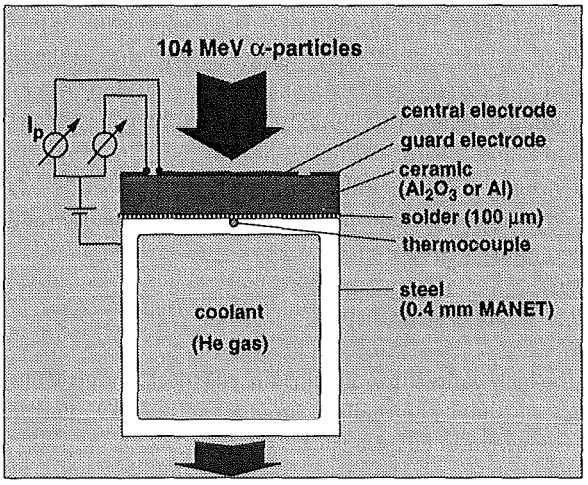

Fig. 1: Cross section of the experimental setup showing a ceramic specimen brazed onto a MANET steel and equipped with electrodes, leads, and a thermocouple.

brazed between ceramic and MANET substrate allowed to measure directly the temperature in the centre of the beam spot.

All irradiations were performed using the high enery Dual Beam Facility of KfK, where α-particle beam has been used.

Table 1:
Irradiation conditions under which the conductivity measurements were performed

Ceramic thickness	(0.25 - 0.47) mm
E-field (DC)	100 k V/m
α-particle energy	104 MeV
Displacement rate (O/N-lattice)	(6 - 8) x 10^{-8} dpa/s
Ionizing dose rate	< (4.5 - 6) x 10^5 Gy/s
Beam size	Ø 0 4 mm
α-particle beam current	(1.3 - 1.7) μA
Vacuum (total pressure)	(5 ± 4) x 10^{-6} mbar

In this work all dpa-rates are calculated with TRIM-91-Cascade assuming sublattice specific threshold energies of E_d (Al) = 20 eV and E_d (O) = 65 eV for alumina, and E_d (Al) = E_d (N) = 50 eV for AlN. The displacement damage rate given in table 1 represent only the damage of the O- and N-sublattice. The total displacement damage rates including the Al-atoms would be 3.6 times that of the O-sublattice in alumina and twice that of the N-sublattice in aluminium nitride.

Standard methods have been used to measure the DC resistance or conductivity of the ceramic specimens. Of special

importance for elevated temperature irradiations under an electric field is the avoidance of significant errors due to carbon layers which may grow during the extended measuring periods at the specimen surface leading to short-circuiting currents. Therefore, the gap resistivity R_g between central and guard electrode has to be far above the interesting volume resistivity $R_p = U_p/I_p$, where $U_p = (20-40)$ V is the applied voltage and Ip the measured current through the central electrode.

3.2 Results and discussion

In the high purity Vitox-alumina the electrical conductivities σ and σ0 show the highest irradiation induced electrical breakdown ever observed (Fig. 2).

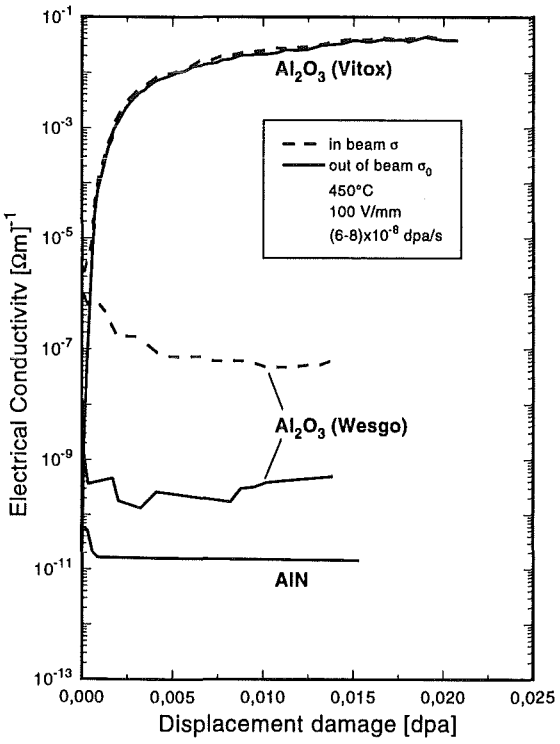

Fig. 2: Electrical volume conductivity during (σ) and after ($σ_0$) 104 MeV α-particle irradiation in high vacuum.

The $σ_0$ measurements were always taken three minutes after turning off the α-particle beam. Because the resistivity between the central electrode and the guard ring kept a high value of $R_g = (6 \pm 2) \times 10^{11}$ Ω during the 115 hours of irradiation, any surface layers formed during irradiation and leading to short-circuit currents can unambiguously be ruled out. Therefore, σ and $σ_0$ represent volume conductivity, that is, significant RIED occurs. After irradiation $σ_0$ still shows an Ohmic behaviour in Vitox-alumina and in contrast to unirradiated ceramics almost no temperature dependency (fig. 3).

The irreversible nature of RIED is confirmed. It is important to note, that the saturation level near 4×10^{-2} (Ωm)$^{-1}$, reached

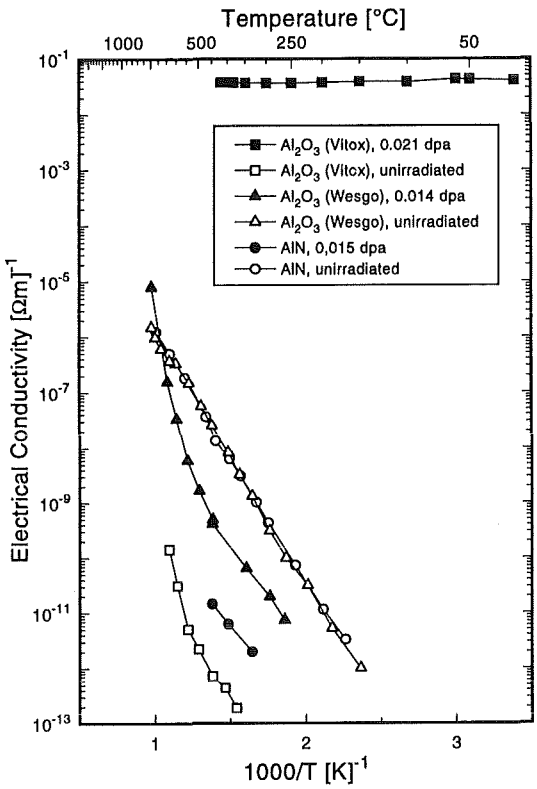

Fig. 3: Temperature dependency of the conductivity $σ_0$ before and after irradiaiton at 450°C. All measurements were performed in high vacuum.

already after 0.015 dpa, is above the critical value of about 10^{-3} (Ωm)$^{-1}$ necessary to avoid MHD pressure drop with 10 μm coatings in flowing liquid metal coolants.

In contrast to Vitox-alumina no RIED at all has been observed up to damage levels of about 0.015 dpa in Wesgo-alumina and AlN (figs. 3 and 4). The initial $σ_0$ values even decrease during the early stage of irradiation. Consequently, these grades reveal a much higher resistance to damage acccumulation.

At a given temperature, the difference between the in-situ conductivity σ and the out-of-beam conductivity $σ_0$ is due to RIC. In general, RIC is strongly correlated with the Gy-production and in our experiments ranges typically from 10^{-6} to 10^{-7} (Ωm)$^{-1}$. Therefore, the total conductivity $σ_0$ during irradiation can be either governed by RIC (e.g. in Wesgo-alumina) or by RIED (e.g. in Vitox-alumina).

The general consensus of the present data, that RIED sensitivity is at least greatly retarded in Al_2O_3 grades with higher amounts of impurities, is a promising result for coating developments, but has to be confirmed also at much higher dpa-doses. Further irradiation experiments are also necessary to investigate the nature of RIED and the electrical behaviour of suitable coatings.

Literature:

[1] A. Möslang, E. Daum and R. Lindau, "Irradiation-induced electrical conductivities of AlN and Al_2O_3 at 450°C"; 18th SOFT, Karlsruhe, 22 - 26 Aug., 1994.

(2) A. Möslang, "Wirkung hochenergetischer Teilchen in keramischen Werkstoffen"; KfK-Report 5367 (1994).

Staff:

S. Baumgärtner
G. Bürkle
D. Hecker
A. Möslang

BL MH-D 1 Liquid Metal MHD

In designing self-cooled liquid metal blankets, the magnitude of the MHD pressure drop and the heat transfer characteristics represent important design issues. MHD research is related both to a poloidal-toroidal blanket concept [1] and the Dual-Coolant Blanket [2], compare BL DE-D1.

Velocity distribution in U-bends partly parallel to the magnetic field

Mercury experiments were performed [3] with a U-bend where the magnetic field is perpendicular to the "radial" ducts and parallel to the "toroidal" duct in between. For heat transfer from the First Wall (FW) of the toroidal duct (Fig. 1) the velocity distribution is of prime importance.

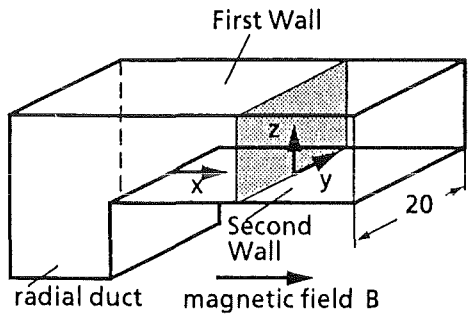

Fig. 1: Coordinates in toroidal duct

Measurements of mean velocities and velocity fluctuations were performed with hot wire anemometry (HWA) and electric potential probes (EPP). Theoretically, the flow distributions were predicted for inertialess MHD flow with the Core Flow Approximation.

Figure 2 shows HWA velocity distribtuions for different values of the Hartmann number Ha and Interaction parameter N. For hydrodynamic flow (Ha=N=0) a recirculation zone exists close to the "Second Wall". With increasing N this recirculation zone disappears and the liquid from the core is pushed towards the FW, as predicted by theory. Therefore,heat transfer from the FW should be considerably enhanced compared to a slug type velocity profile as assumed previously.

In the core a pair of vortices exists with axis parallel to the magnetic field as shown by the EPP signals in Fig. 3. Such vortices would be additionally beneficial for heat transfer.

Pressure drop in poloidal-radial manifolds

Significant pressure drop due to 3D electric currents were expected for this flow geometry. Screening tests for a variety of geometric and MHD parameters were carried out [4] using mercury as liquid metal. Fig. 4 shows the test section and characteristic results. The normalized pressure drop decreases with increasing Interaction parameter. The pressure drop in the middle channel is generally the highest. A very conservative extrapolation of the results to blanket conditions (linear increase of pressure drop with channel number) results in a value far below the maximum tolerable value.

Pressure drop in 2D flow geometries

Flow ducts with constant dimensions in the direction of the magnetic field (2D geometries) are favourable for blanket designs because no additional pressure drops are expected for high values of Ha and N for changing flow direction and/or combining/dividing flow. Figure 5 shows the 2D duct geometry at the bottom of the Dual-Coolant Blanket (compare BLDE-D1). For very low values of the Interaction parameter N, considerable additional pressure drops Δp occur due to the occurence of recirculation zones /5/. For $N>20$ this pressure drop has disappeared which means that for blanket relevant conditions ($N=2000$) the resulting MHD pressure drop can be assessed with sufficient accuracy using relationships for developed flow.

Pressure drop in multichannel U-bends parallel to the magnetic field

A set of experiments in multi-channel radial-toroidal-radial U-bends using NaK has been performed in the MEKKA facility. The electrical coupling of the U-bends can cause unequal pressure drops or flow rates in the individual channels.

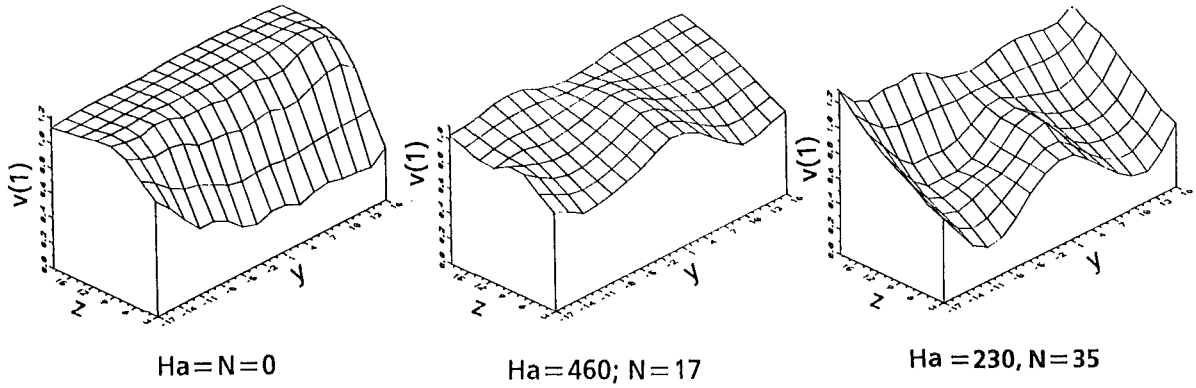

Fig. 2: Velocity distribution (HWA) in the toroidal duct (x=20 mm)

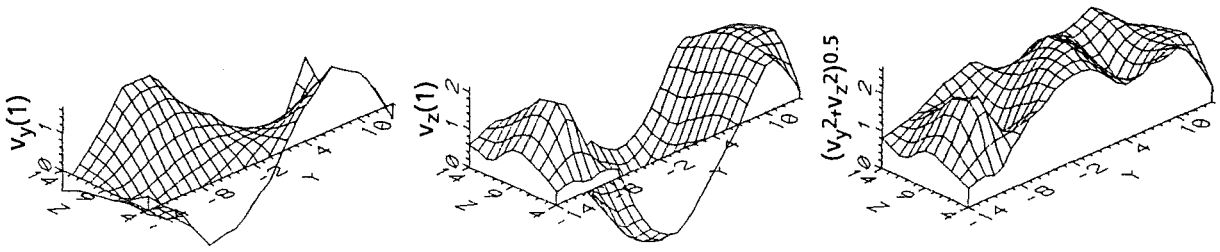

Fig. 3: Velocity components perpendicular to x (EPP) (x=35mm, Ha=255, N=38)

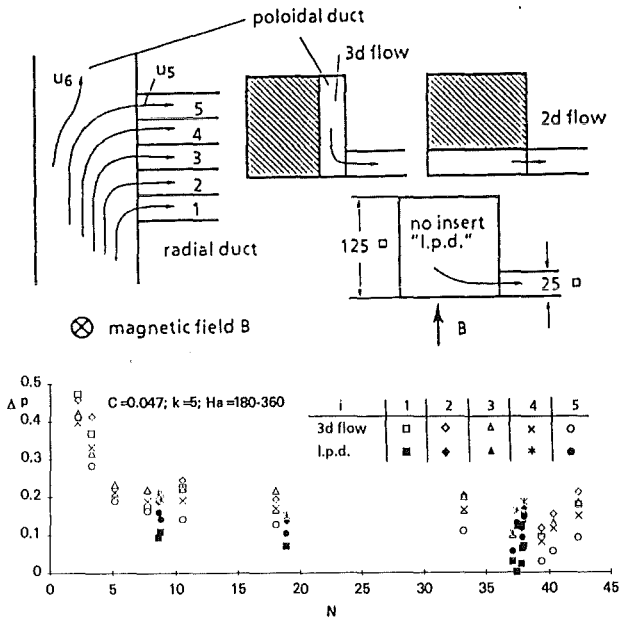

Fig. 4: Manifold test sections and characteristic pressure drop results

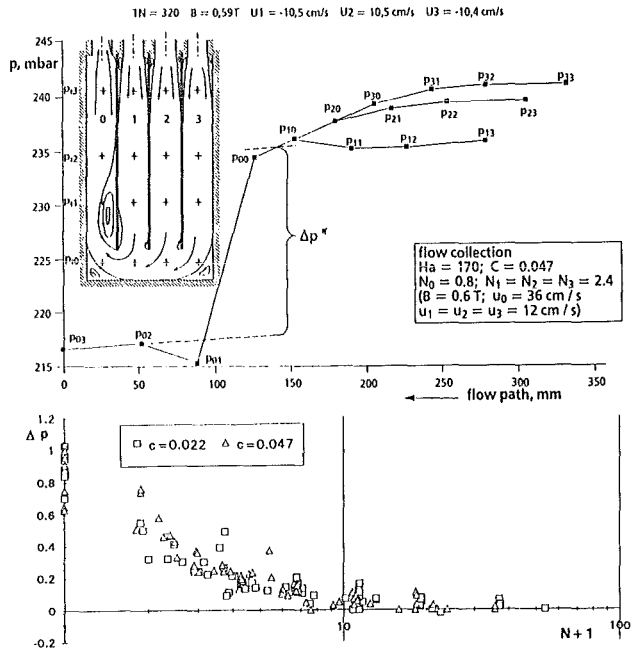

Fig. 5: Duct geometry at bottom of Dual-Coolant Blanket: pressure distribution and normalized pressure drop

One test section was electrically conducting in all parts to study multi-channel effects (MCE, fig. 6a). In this configuration a linear increase of the pressure drop with increasing amount of coupled channels was measured in the highly pressure loaded center channel. The additional pressure drop due to inertia effects was found to scale with $N^{-1/3}$, this inertial part of the pressure drop can be of the order of the inertialess pressure drop. With increasing amount of coupled channels the intertial part of the pressure drop increases (fig. 6b [6]). In multi-channel U-bend experiments performed in Riga using an InGaSn-alloy a full suppression of MCE was measured if the radial channels were completely electrically separated up to the first wall [7]. A second test section was built in which only the dividing walls in the radial duct parts were electrically separated (all other walls were conducting) in order to judge about the minimum requirements necessary for an electrical separation. The pressure measurements showed that MCE`s are still present, because electrical currents can short circuit through the Hartmann walls. All other effects like the linear increase of the pressure drop with the number of coupled ducts and the $N^{-1/3}$-dependence of the inertial part of the pressure drop remained unchanged. The effect of the separation of the dividing walls lead to a reduction of the pressure losses of about 30% (see fig. 7, [8]).

MHD heat transfer and pressure drop in an electrically insulated channel

A heat transfer-experiment at fusion relevant parameters was carried out in the MEKKA-facility [9, 10] in which the side wall of a rectangular (80 mm×40 mm) test section is heated over a length of 0.5 m using a direct contact heater, which allows a homogeneous heat flux up to 20 W/cm² (Fig. 8). The liquid metal contacting surfaces of the test section made of stainless steel are electrically insulated by a temperature resistant painting.

Hartmann Numbers up to 5000 (2 Tesla), Interaction parameters 320–22000, Péclet numbers 44–2200 based on the half-width in the field direction (a=40 mm), and

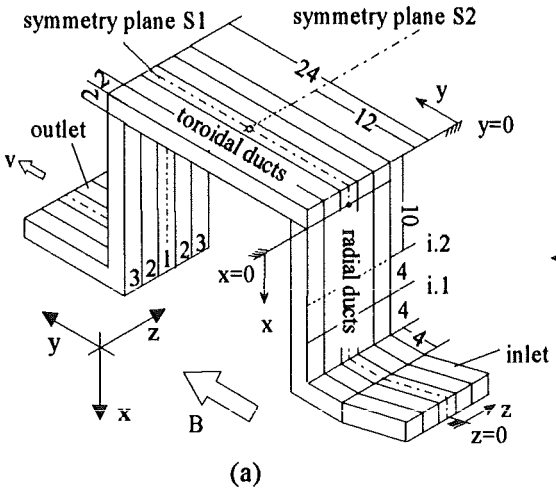

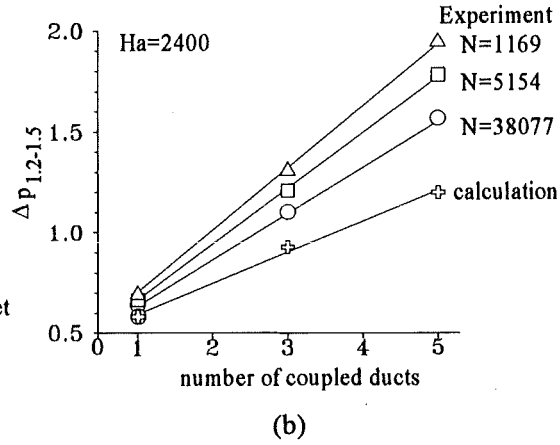

Fig. 6a,b: a) Investigated multi-channel geometry

b) Dimensionless pressure drop in an electrically coupled radial-toroidal-radial U-bend

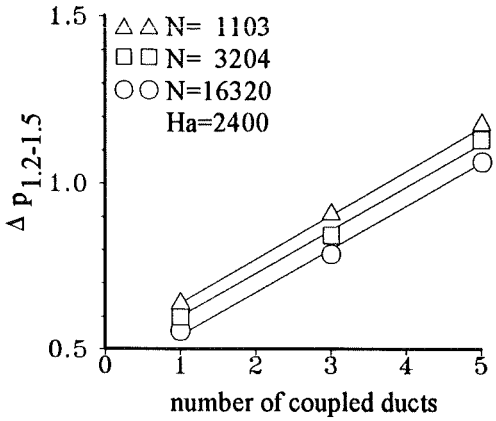

Fig. 7: Measured pressure drop in a partially decoupled radial-toroidal-radial U-bend

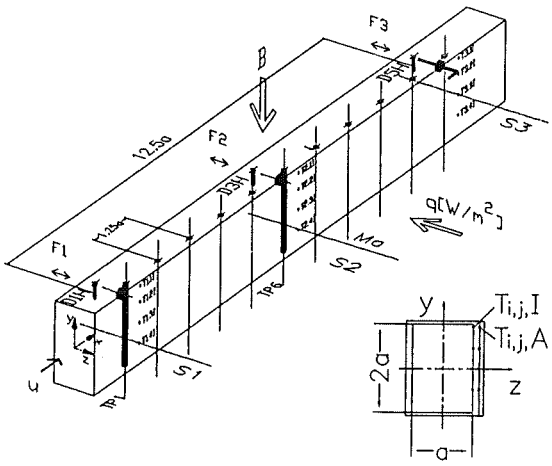

Fig. 8: The MHD/heat transfer test section

velocities between 0.04 and 2.5 m/s, were achieved. The working fluid was NaK (sodium potassium eutectic).

The experiments showed that due to the nonperfect insulation the pressure drop without turbulence promoters (TP) is about 8 times higher than predicted for perfect insulation.

Even in the case of the smooth channel without any TP a vortex structure is found for Pe>140 increasing the heat transfer by a factor of 2.8 for the highest Hartmann - and Péclet number measured. After inserting 2 mechanical TP`s strong oscillations are observed improving the heat transfer by a factor 7 for Pe=2200. A cost (increased pressure drop) benefit (increase of heat transfer) analysis shows the efficiency of the chosen mechanical TP`s (Fig. 9).

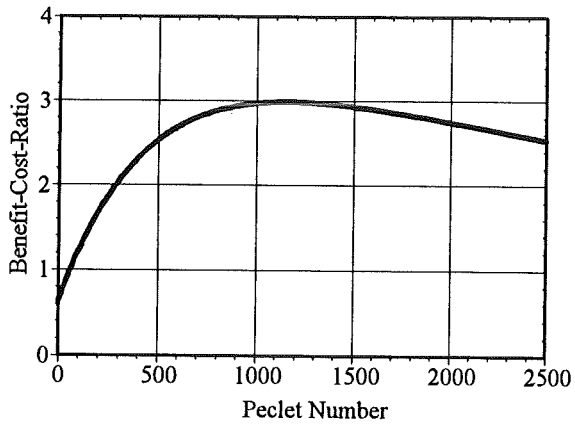

Fig. 9: Cost-benefit of turbulence promoter

Supplementary experiments conducted in the insulated duct of the horse track Gallium-Indium-Tin (eutectic) loop GALINKA confirmed the predicted low pressure drop in an insulated duct and showed the existence and the high stability of two-dimensional vortices with the vorticity axis

parallel to the field in rectangular ducts with electrically insulating walls.

MHD - Theoretical Work for blanket relevant flows

The flow through many basic elements of fusion blankets (bends, expansions, contractions, changes of cross section, etc.) is three-dimensional (3D). For flows in strong magnetic fields one has to distinguish between two different types of 3D flows. For flows in bends or expansions, where the mean flow direction changes only in the plane perpendicular to the magnetic field it has been shown that 3D effects in both conducting and insulating ducts are insignificant [11, 12]. Ideally, the coolant should flow in the radial-poloidal plane of a blanket as shown in figure 10. This allows to avoid pressure loss due to 3D effects.

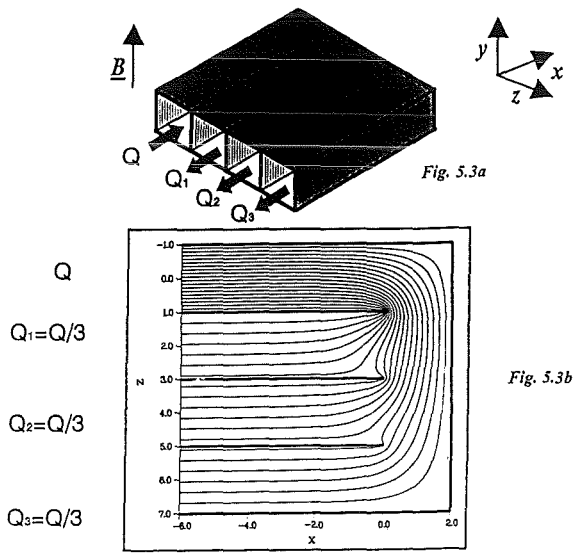

Fig. 10: Flow in a non-symmetric 180° turn with manifold related to the lower part of the Dual Coolant Blankt Concept. Duct walls are insulating.

For bends and expansions in the plane of the field 3D effects are more pronounced [11, 13]. For flows in insulating expansions in the plane of the field a numerical code is being developed, which treats the flow in the core and in the side layers (core and side layers are flow subregions) simultaneously. This code will be applied to the flow in an expansion with manifold.

For MHD flows exhibiting vortex type flow pattern a model has been developed which accounts for vorticity production caused by non-homogeneous electrical conductivity of the channel walls as well as for vorticity dissipation due to Joules' and viscous effects. By choosing a special distribution of the wall conductivity it is possible to create initial velocity profiles which loose their stability and show time dependent vortex type flow pattern once parameters exceed critical limits (see figure 11, [14]). These exact limits and further the implication of the time dependent flow on heat transfer are under current investigation.

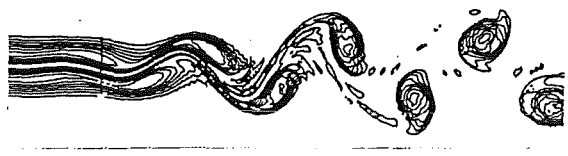

Fig. 11: Formation of vortex type MHD flow caused by a highly conducting strip aligned with the mean flow direction

Literature:

[1] Reimann, J.; Barleon, L.; Bucenieks, I.; Bühler, L.; Lenhart, L.; Malang, S.; Molokov, S.; Platnieks, I.; Stieglitz, R. (1994): MHD Investigations Related to a Self-cooled Pb-17 Li Blanket with Poloidal Radial-Toroidal Ducts. Third Int. Symp. on Fusion Nuclear Technology (ISFNT3), Los Angeles, USA, June 27-July 1.

[2] Malang, S.; Barleon, L.; Bogusch, E.; Norajitra, P.; Reiser, H.; Reimann, J.; Schleisiek, K. (1994): Conceptual Design of a Dual Coolant Liquid Metal Breeder Blanket. Contributions on 18th Symp. Fusion Technology, Karlsruhe, Germany, Aug. 22-26.

[3] Reimann, J.; Bucenieks, I.; Flerov, A.; Molokov, S.; Platnieks, I. (1994): MHD-Velocity Distributions in U-Bends Partly Parallel to the Magnetic Field. 2nd Int. Conf. on Energy Transfer in Magnetohydrodynamic Flows, Aussois-France, Sept. 26-30.

[4] Reimann, J.; Bucenieks, I.; Flerov, A.; Heller, L.; Platnieks, I. (1994): Experiments on Pressure Drop of MHD Flows in Manifolds. 2nd Int. Conf. on Energy Transfer in Magnetohydrodynamic Flows, Aussois-France, Sept. 26-30.

[5] Reimann, J.; Bühler, L.; Stieglitz, R.; Stumpf, F.; Mack, K.J.; Platnieks, I. (1994): Influence of a Magnetic Field B on Liquid Metal Flow through a T-Junction Perpendicular to B. 2nd Int. Conf. on Energy Transfer in Magnetohydrodynamic Flows, Aussois-France, Sept. 26-30.

[6] Stieglitz, R. (1994): Magnetohydrodynamische Strömungen in Ein- und Mehrkanalumlenkungen; Dissertation Universität Karlsruhe; KfK-5376.

[7] Reimann, J. et al. (1993): MHD-flow in Multi-channel U-bends: Screening tests and theoretical analysis; KfK-5102.

[8] Stieglitz, R.; Barleon, L.; Reimann, J.: Mack, K.-J. (1994): MHD-Flows in partially decoupled parallel U-bends at high Hartmann number; 18th Symposium on Fusion Technology (SOFT); August 22-26, Karlsruhe.

[9] Barleon, L., Mack, K.J., Kirchner, R., Frank, M., Stieglitz, R. (1994): MHD Heat Transfer and Pressure Drop in Electrically Insulated Channels at Fusion Relevant Parameters. 18th Symp. on Fusion Technology (SOFT), August 22-26, Karlsruhe.

[10] Barleon, L. , Mack, K.J., Kirchner, R., Stieglitz, R. (1994): Heat transfer in MHD-flow at high Hartmann number and improvement by turbulence promotion. Proc. 2nd Int. Conf. on "Energy Transfer in Magneto-hydrodynamic Flows", Sept. 26-30, Aussois, France.

[11] Burr, U., Bühler, L. (1994): Wärmeübertragung in dreidimensionalen magnetohydrodynamischen Strömungen. KfK- 5329.

[12] Molokov, S. (1994): Liquid metal flows in manifolds and expansions of insulating rectangular ducts of in the plane perpendicular to a strong magnetic field. KfK- 5272.

[13] Molokov, S., Bühler, L. (1994): Liquid metal flow in a U-bend in a strong uniform magnetic field. J. Fluid Mech. 267, 325-352.

[14] Bühler, L. (1994): Instabilities in 2D MHD flows. 2nd international conference on energy transfer in magnetohydrodynamic flows. Sept. 26-30, Aussois, France.

Staff:

L. Barleon
L. Bühler
E. Höschele
R. Kirchner
H. Kreuzinger
L. Lenhart
K.J. Mack
J. Reimann
R. Stieglitz
R. Vollmer

BL SA-D 1 Reliability Assessment

The reliability of the blankets, the He Cooled Breeder Blanket as well as the Dual Coolant Concept (see BSDE-D1 and BLDE-D1), has been evaluated by fault tree analysis. The TOP events are defined as the unavailability of the entire blanket systems when they ought to be available. The main basic events are disturbances in the coolability mainly caused by leakages of the coolants which result in shutdown of the plant. Especially critical are leakages from the blanket into the vacuum. The determinant events for both concepts are failures of the different welds. A typical example is the failure of the EB double welds which connect the blanket sections. A leakage of both welds would immediately cause a plant shutdown. The other welds in the blankets, including the diffusion welds, are less critical, they are considered in the sense that a weld failure would endanger the integrity of the structure.

According to the assumptions concerning reliability of the welds three cases are defined because of the similarity of the concepts. The cases are identical for both blanket concepts. In order to account for the large uncertainties in the assumptions the mean time to repair (MTTR) is selected as parameter.

Case 3 is the most conservative one based on the assumption that the EB double weld at the FW is classified with the same failure rate ($1 \cdot 10^{-8}$/mh) as a conventional single weld. A failure of a diffusion weld in the FW panel is set equal to a damage of the structure so that a blanket exchange is required. The specific failure rate of the diffusion welds is taken as $1 \cdot 10^{-9}$ /mh. The specific failure rate for the longitudinal welds is assumed as $1 \cdot 10^{-9}$ /mh. In both cases a leak is tolerable; only in combination with a damage of the integrity of the structure an undesired event has to be supposed.

Case 2 is based on the same assumptions as Case 3 except the diffusion welds, where only those are considered which are neighbouring the EB double welds.

Case 1 is equivalent to Case 2 except the very conservative assumption on the EB double welds. In this case the specific failure rate is reduced by the factor 10 to the more realistic value of $1 \cdot 10^{-9}$ /mh.

Helium Cooled Solid Breeder Blanket

The calculated availabilities for the blanket are shown in Fig. 1. As expected the results for Case 3 show the lowest availability. Exclusion of those diffusion welds which have no importance for the leaktightness of the blanket (Case 2) leads to a significant increase of the availability. Case 1 would result in the highest availability of all cases under consideration and is judged as the most probable case.

The Dual Coolant Concept

Fig 2 shows the results of the analysis for the Dual Coolant Concept. The relation between the three cases is similar to the Solid Breeder Blanket but the availabilities are in general somewhat higher. This is mainly a consequence of the flow leading system between the horizontal cooling plates and the He manifolds in the Solid Breeder concept.

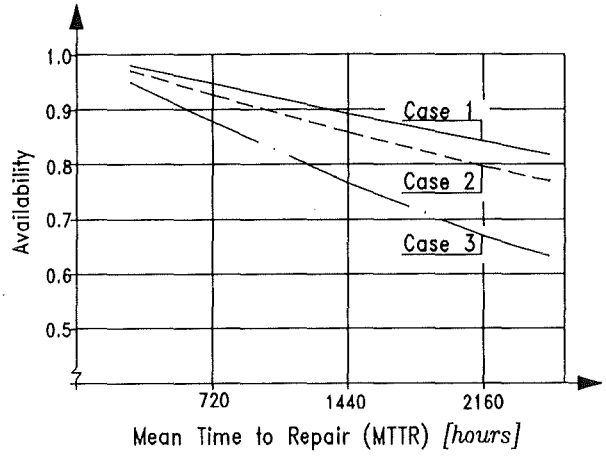

Fig. 1: Availability of the Solid Breeder Blanket depending on MTTR

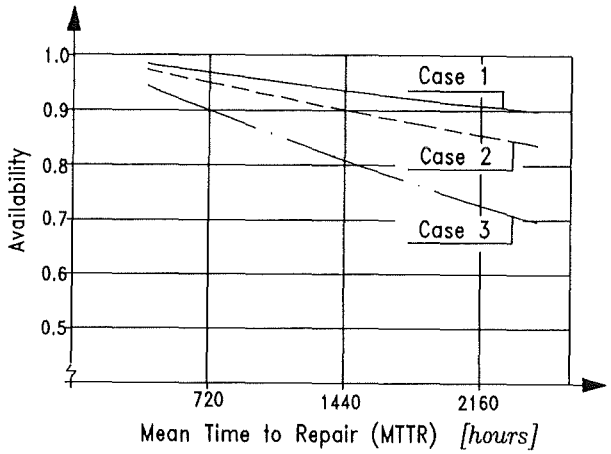

Fig. 2: Availability of the Dual Coolant Blanket depending on MTTR

Conclusions

In general, at this time there are no indications that availability aspects will give rise to particular problems with these blanket designs.

Difficulties and uncertainties in the reliability analysis arise mainly from the lack of completeness in the design and from the novel feature of components and systems without adequate operating experience. The preliminary results from the experimental verification so far support the assumptions which have been made. But work must continue and further R&D is necessary.

Staff:

H. Schnauder

BL SA-D 2 Safety Analysis of Self-cooled LM Breeder Blankets

The European Blanket Coordination Group has established the procedure for the "DEMO Blanket Selection Exercise" to be started in 1994. This blanket selection will be based on a number of status reports for each of the European blanket concepts under development. In this context the work reported herein was devoted to safety analyses for the Dual Coolant Blanket concept pursued by KfK, according to the safety and reliability criteria developed earlier for the blanket selection exercise. The hazard potential and accidents related to the Dual Coolant Blanket have been assessed [1] under the following topics: (1) toxic inventories, (2) energy sources for mobilization, (3) fault tolerance, (4) release of radionuclides, and (5) waste management.

Toxic inventories

Radioactive inventories in the different regions of the blanket (inboard, outboard, first wall, breeding zone and shield) as well as in the cooling systems have been assessed and are summarized in Table 1 in two categories, i.e., tritium and activation products.

The tritium inventory in the breeder (Pb-17Li) is determined by the recovery process and is moderate (30 g). A considerable amount of tritium (≃4 g/d) will permeate into the helium coolant. This is assumed to be permanently removed, so that the tritium concentration in the helium can be kept low, say <1 wppm, corresponding to a total inventory of <9 g. The tritium inventory in the intermediate NaK circuits depends on the achievable permeation barrier factor of between 50 and 1000 resulting in a total amount of 4−42 g with a greater likelyhood towards the upper value, since a high permeation barrier factor is aimed at. Tritium losses to the steam circuit (ferritic steel without any permeation barrier) are estimated to be 0.12 g/d (1200 Ci/d). Thus, barrier factors in the order of 120 need to be achieved in order to reduce the losses to 10 Ci/d. With another loss of 10 Ci/d via the helium cooling system, the total tritium losses of 20 Ci/d (0.002 g/d) would accumulate to 1.7 g of tritium in the entire water/steam system, which is acceptable. The tritium inventory in the recovery system is governed by the inventory in the cold traps and amounts to 2.5 g per circuit, i.e., 200 g for 80 circuits, corresponding to approximately one half of the daily production. The structural material will accumulate about 19 g of tritium with a weight concentration in the first wall of 72 wppb (compare Table 1).

Activation products inventories have been assessed based on the calculations performed under BL DE-D1. The specific activity in the Pb-17Li after decay times of 0 s, 1 h, 1 d, 1 month, 1 yr amounts to 2.4×10^{14}, 1.1×10^{13}, 5.2×10^{12}, 1.4×10^{11}, 2.1×10^{10} Bq/kg, respectively. Accounting for a radial activation profile and for the actual residence time the circulating liquid metal spends in the flux region, a dilution factor of 10 has been estimated, leading to the values quoted in Table 1. Activation products in the first wall helium coolant are introduced by corrosion and sputtering. They have to be permanently removed, in order to avoid accumulation somewhere in the circuit components. Therefore, the contents are considered to be small, i.e., $<1.5\times10^{11}$ Bq. The specific activity in the first wall (including impurities as specified for MANET) after decay times of 0 s, 1 h, 1 d, 1 month, 1 yr is 5.7×10^{14}, 4.9×10^{14}, 3.5×10^{14}, 3.1×10^{14}, 2.1×10^{14} Bq/kg, respectively. It decays much slower than in Pb-17Li. In the breeding zone and shield the radioactivities are considerably smaller. The specific activity in the insulation layers has not been evaluated explicitly, but an estimation showed that it is negligible after a few minutes.

Table 1: Radioactive inventories in blanket and related systems

Blanket region or system	Tritium (g)	Activation Products after shutdown (Bq)	
		0 s	1 year
Breeder material	30	6×10^{20}	5.3×10^{16}
Primary first wall coolant (Helium)	< 9	1.5×10^{11}	0.5×10^{11}
Intermediate coolant (NaK)	4-42	neglibile	negligible
Steam system	< 1.7	negligible	negligible
Tritium recorvery system	200	negligible	negligible
Structural material (total)	19	1.5×10^{20}	5.2×10^{19}
First wall	7.2	5.2×10^{19}	1.9×10^{19}
Breeding material	11.5	9×10^{19}	3.3×10^{19}
Shield	0.3	4.4×10^{18}	5.5×10^{17}
Insulating layers	negligible	2.1×10^{19}	4.5×10^{11}

Energy sources for mobilization

Potential energy sources in upset or accidental conditions are seen in (a) plasma disruptions, (b) continued plasma operation after cooling disturbances, (c) decay heat, (d) work potential of pressurized coolants, and (e) exothermic chemical reactions.

(a) Plasma disruptions can cause local evaporation of first wall material or mobilization of adhesive dust. This is a problem of first wall protection and dust processing that is common to all fusion reactors and not specific to a particular blanket system. The energy source is essentially the energy stored in the plasma, typically ≃1 GJ.

(b) Continued plasma operation after a sudden cooling disturbance would cause any first wall to melt within tens of seconds. The energy source is simply the time integral of fusion power from the cooling disturbance to complete shutdown. This time integral is inherently small (by plasma poisening) or otherwise a matter of plasma control and of hypothetical scenario conventions, and again not peculiar to a specific blanket concept.

(c) The decay heat is the governing feature in managing cooling disturbances like LOCA, LOFA and, in particular, loss of site power or loss of heat sink. The decay heat in the entire blanket amounts to 53.2 MW after shutdown and declines after 1 h, 1 d, 1 month, and 1 yr to 10.8, 1.56, 1.22, 0.57 MW, respectively.

(d) The first wall cooling system contains ≈9000 kg of helium at 8 MPa, ≈300°C. The work potential relative to ambient conditions is ≈13 GJ. Adiabatic expansion of the helium from two outboard first wall cooling circuits (≈2100 kg), which are connected within a subsystem, would pressurize the vacuum vessel in the event of an in-vessel pipe rupture to ≈0.47 MPa absolute. This is above the expected design pressure (≈0.2 MPa) and, hence, would require an extra expansion volume.

(e) Chemical reactions may occur between Pb-17Li and air or water in various accident scenarios. These processes were found to be moderate, since in Pb-17Li/water reactions only the lithium reacts and the kinetics is controlled by the small lithium mass fraction of only 0.7%. For NaK/water reactions see section below.

Fault tolerance

The following analyses of electromagnetic forces and temperature transients have been performed in order to show whether this blanket system is tolerant against conceivable transients and accidental conditions.

Electromagnetic forces and induced stresses caused by disruptions have been analyzed with the CARIDDI code. The 3-D model covers one quarter of the blanket segment using poloidal and toroidal symmetry. Preliminary results indicate that the maximum von Mises stresses ranging up to 73 MPa are uncritical.

Temperature transients have been studied for instantaneous loss-of-coolant scenarios with leaks in one of the three primary coolant circuits per blanket segment (2 helium circuits for the first wall and one Pb-17Li circuit for the breeding zone), and in the intermediate NaK circuit. A LOCA in a first wall helium circuit means at most an instantaneous loss of helium at t=0 in one of the two helium loops. Plasma shutdown is assumed to occur at t=1 s. A 3-D model representing two adjacent first wall cooling channels (one being intact and the other one failed) has been adopted in the FE analyses with FIDAP. Transient temperatures in the first wall exceed the steady state values for a few seconds by up to 100°C before they decline and stabilize at a low level. The temperature transients do not endanger the integrity of the structure [2].

A LOCA in the Pb-17Li circuit can cause (a) a loss of liquid metal flow in the blanket in case of an ex-vessel leak, or (b) a drainage of the Pb-17Li from a blanket segment in case of a major in-vessel leak. For (a) the decay heat in the structure plus Pb-17Li would lead to temperature rises, which stabilize at $t_{Pb\text{-}17Li} < t_{He} + 160°C$, if the first wall cooling remains intact (t_{He}=helium coolant temperature). For case (b) with all Pb-17Li removed but with the first wall cooling systems operating, an estimation revealed a maximum structure temperature $t_{structure} < t_{He} + 100$ °C. At $t_{He} = 350°C$ this is slightly above the normal operating temperature. These transients do not endanger the integrity of the structure.

A LOCA in the intermediate NaK circuit with the consequence of substituting the NaK in the steam generator tube gaps by the cover gas, e.g. argon, would reduce the heat transfer coefficient in the steam generator by 1 to 2 orders of magnitude, leading to a strong temperature increase of Pb-17Li at the steam generator outlet. In order to avoid excessive temperatures in the blanket, the plasma has to be shut down within approximately 60 s after drainage of the NaK. This scenario does not present a safety concern, but the temperature transients need further attention with regard to design limits of the structural material.

Pb-17Li/NaK or NaK/water leaks may be postulated for the double-wall steam generator. While the first type would lead to a limited LOCA in the Pb-17Li circuit, the second type would involve chemical NaK/water reactions which are exothermic and mostly violent. Such leaks had been assessed in an earlier study on the grounds of industrial experience in sodium technology with the result that a fast propagation of a single inner tube failure (defined as design basis accident) can be precluded. Confirming tests are proposed.

Tritium and activation products release

The release rates in accidental situations are hard to quantify at this stage of analyses. As a first approach one may take the radioactive inventories contained in the largest amount of fluid within the blanket system (Pb-17Li, helium and NaK) which could be liberated by a single failure (like a guillotine break) into either the vacuum vessel or other compartments of the containment. These escaped inventories will then have to be multiplied by a mobilization factor to obtain the potential gaseous or suspended release into the vacuum vessel or containment. Table 2 summarizes the escape fractions, mobilization factors, and the resulting single failure releases into the vacuum vessel or containment which have been estimated for this blanket design.

Waste generation and management

Only the decommissioning waste has been considered. The total amount of radioactivity in the blanket structure

Table 2: ACCIDENTAL TRITIUM AND ACTIVATION PRODUCTS RELEASE INTO VACUUM VESSEL AND CONTAINMENT IN CASE OF LOCA

	Total Inventory	Fraction escaping into		Mobilization factor	Single Failure Release into	
		Vacuum vessel	Containment		Vacuum vessel	Containment
Tritium	(g)				(g)	(g)
Breeder material (Pb-17Li)	30	≈0.035	≈0.027	1	1.1	0.8
Prim. FW coolant (helium)	9	0.24	0.24	1	2.2	2.2
Intermediate coolant (NaK)	42	0	1/80	1	0	0.5
FW structural material	7.2	0-0.01	0	1	0.07	0
Activation products	(Bq)				(Bq)	(Bq)
Breeder material (Pb-17Li)	6×10^{20}	≈0.035	≈0.027	10^{-3}	2.1×10^{16}	1.6×10^{16}
Prim. FW coolant (helium)	1.5×10^{11}	0.24	0.24	1	4×10^{10}	4×10^{10}
Intermediate coolant (NaK)	negligible	0	1/80	10^{-3}	0	negligible
FW structural material	5.2×10^{19}	1	0	$<-10^{-5}$	5.2×10^{14}	0

(MANET) sums up to 1.5×10^8 TBq at shutdown. The contact γ-dose rate per kg of steel in the first wall ranges up to 1.1×10^5 Sv/h, declining slowly so that the IAEA low level waste (LLW) limit of 2×10^{-3} Sv/h is reached only after 10^5 years. The total amount of radioactivity in Pb-17Li is 6×10^8 TBq at shutdown. After a cooling time of 1 year the nuclide Hg-203 is the major contributor to the specific activity, and Po-210 yields the highest ingestion dose rate. The contact γ-dose rate of Pb-17Li reaches the LLW limit (if no purification is considered) after 300 years and the hands-on limit of 2.5×10^{-5} Sv/h after about 7000 years.

Literature:

[1] K. Kleefeldt, W. Kramer: Contribution to the dual coolant blanket report, Report to be published.

[2] F. Dammel: Dual coolant liquid metal breeder blanket for DEMO: Transient thermal analyses for the first wall, KfK Internal Report in preparation.

Staff:

F. Dammel
T. Jordan
K. Kleefeldt
W. Kramer
K. Schleisiek

Development of ECRH Power Sources

1. Introduction

At present, gyrotron oscillators are mainly used as high power millimeter wave sources for electron cyclotron resonance heating (ECRH) and diagnostics of magnetically confined plasmas in controlled thermonuclear fusion research. Long-pulse and CW gyromonotrons utilizing open-ended cylindrical resonators which generate output powers of 100–400 kW per unit, at frequencies between 28 an 84 GHz, have been used very successfully for plasma formation, ECRH and local current density profile control by noninductive current drive (ECCD) in tokamaks [1] and stellarators [2]. Gyrotron systems with total power of up to 4 MW are in use. The confining toroidal magnetic fields in present day fusion machines are in the range of Bo=1–3.5 Tesla. As experimental devices become larger and operate in higher magnetic fields (Bo=5T) and higher plasma densities ($n_{eo}=1-2\cdot10^{20}/m^3$) in steady state, present and forthcoming ECRH requirements call for gyrotron output powers of at least 1 MW, CW at frequencies ranging from 140–170 GHz [3]. Since efficient ECRH and ECCD needs axisymmetric, narrow, pencil-like mm-wave beams with well defined polarization, single mode emission is necessary in order to generate a TEM_{00} Gaussian beam mode at the plasma torus antenna.

2. Development of High-Power Fusion Gyrotrons

2.1 0.6 MW $TE_{10,4}$ Gyrotron with radial output coupling, advanced quasi-optical mode converter and depressed collector

Radial output coupling of the rf power of a gyrotron into a Gaussian (TEM_{00}) mode has three significant advantages for high-power operation. First, the linearly polarized TEM_{00} mode is directly usable for low-loss transmission as well as for effective interaction with the fusion plasma and no further mode converters are needed. Second, the converter separates the electron beam from the rf wave path, so that the electron collector is no longer part of the output waveguide as in the case of an axially arranged tube. Hence, the collector can be designed especially for handling the high electron beam power. In addition, energy recovery by potential depression becomes possible. Third, the influence of rf power reflected from the output window and the load is expected to be significantly reduced, especially for modes rotating in the opposite direction from the design mode.

Some of the main parameters of the $TE_{10,4}$ mode gyrotron are summarized in Table 1. The tube arrangement with a quasi-optical (q.o.) mode converter is shown in Fig. 1 [4].

The rotating $TE_{10,4}$ cavity mode is converted to a linearly polarized Gaussian beam by an advanced mode conversion system designed according to [5,6]. It consists of a helically cut quasi-optical aperture antenna with a deformed feed waveguide and three beam-forming mirrors. The rotating mode is converted by the feed waveguide section into a mode mixture that assures an almost sidelobe-free radiation pattern when launched through the antenna aperture. After being refocused by a quasi-parabolic mirror that corrects the phase in the transverse plane, an astigmatic Gaussian beam is obtained. Two further mirrors remove the astigmatism and direct the rf beam through the output window. The beam radius at the window is 25 mm ($1/e^2$ drop of power density). The single disk window (100 mm diameter, $d=4.4\ mm=9\lambda_g/2$) is made of pyrolytic boron nitride which has a permittivity of about 4.7. The transmission capacity of the edge cooled disk is estimated to be around 500 kW for up to 0.3 s.

The operating mode can be identified by measuring the frequency of the output signal. A contiguous filterbank receiver with a spectral resolution of 100 MHz is used for this purpose. In addition, instantaneous frequency measurement during a single pulse is performed with a set-up employing a

Table 1: Parameters of the 140 GHz $TE_{10,4}$ gyrotron with q.o. mode converter and depressed collector employing a triode-type MIG with an Osmium coated impregnated tungsten emitter.

U_{cath} = 80 kV	R_{cav} = 8.11 mm
U_{mod} = 25 kV	L_{cav} = 16 mm
I_{beam} = 25 A	Q_{diff} = 1150
J_{cath} = 6 A/cm²	α = 1.1
B_{cath} = 0.187 T	B_{cav} = 5.5-5.6 T
R_{cath} = 19.8 mm	R_{beam} = 3.65 mm
θ_{cath} = 26.6°	beam thickness = 0.5 mm

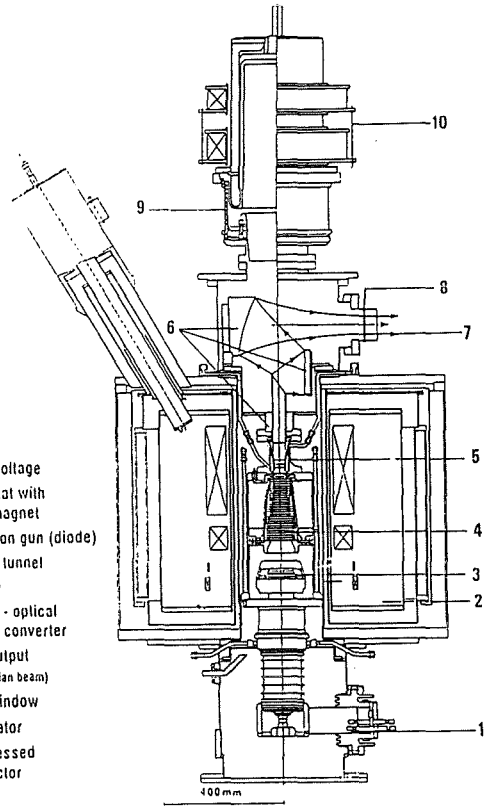

Fig. 1: Schematic layout of a $TE_{10,4}$ mode gyrotron with quasi-optical mode converter and depressed collector.

frequency-time analyzer. Purity of the TEM_{00} output mode is measured with a thin dielectric transmission target monitored by an infrared camera (Joel JTG-3210) and power measurements are made using an octanol-filled static calorimeter. The maximum efficiency working point is at $U_{cath}=79$ kV, $I_{beam}=23$ A, $P_{out}=0.50$ MW (32% output efficiency, 38% electronic efficiency). The maximum power working point is at $U_{cath}=83$ kV, $I_{beam}=27$A, $P_{out}=0.6$ MW (27% output efficiency, 12 ms pulse length). The mode purity of the TEM_{00} output mode was measured to be 94.5%. Fig. 2 shows the measured power distribution at a distance of 0.83 m from the output window. In a next series of experiments the pulse duration will be increased to approx. 0.2 s. Proof of principle experiments using a single-stage depressed collector, biased via a variable resistor, yielded an increase of the output-efficiency up to 48 % (U_{col} =31 kV voltage depression). Fig. 3 shows body current and output power versus the collector depression voltage U_{coll}.

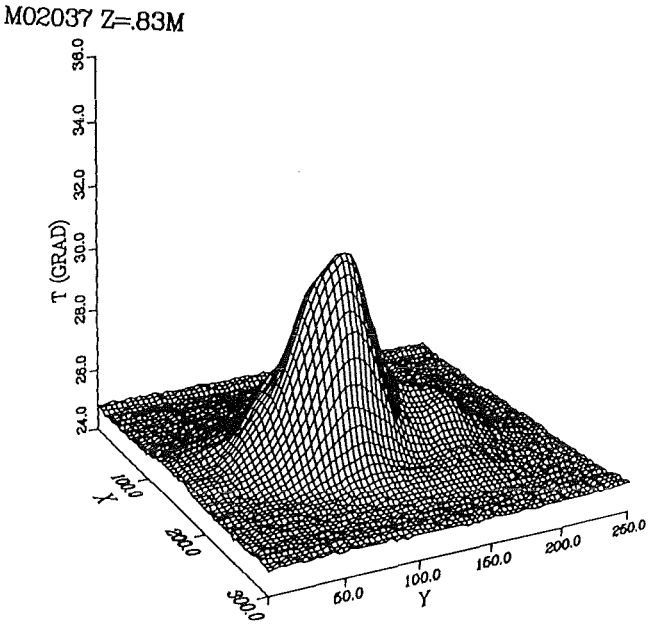

Fig. 2: Measured 3-dimensional power density distribution of TEM_{00} gyrotron output.

In addition, the gyrotron was operated in the $TE_{12,4}$ mode at a frequency of 154.7 GHz by increasing the magnetic induction to 6.1 T. At this frequency the single disk tube output window has the next minimum of the reflection coefficient (electrical window thickness $10\lambda_g/2$).

The $TE_{12,4}$ mode was excited at $U_{cath}=80$ kV and $I_{beam}=25$ A, by changing the compression ratio from $b_c=29$ to 25, to give a slightly higher beam radius, $R_{beam}=3.96$ mm. A maximum output power of 0.35 MW and an rf-output efficiency of 18% was achieved which are in good agreement with theoretical predictions including velocity spread (self-consistent calculations). The improved quasi-optical mode converter works well also for this mode and frequency.

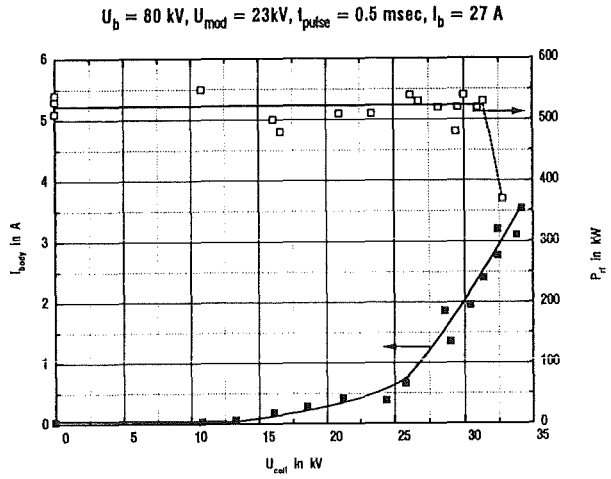

Fig. 3: $TE_{10,4}$ gyrotron operation with depressed collector ($U_{cath}=80$ kV, $I_{beam}=27$ A).

The present development status at KfK of high power gyrotrons for fusion plasma applications is summarized in Table 2.

Table 2: Present development status of high power mm-wave gyrotron oscillators at KfK.

Frequency [GHz]	Mode cavity	Mode output	Mode Purity [%]	Power [kW]	Efficiency [%]	Pulse Length [ms]
140.8	TE_{03}	TE_{03}	98	300	34	0.5
			98	120	26	500
132.6	$TE_{9,4}$	$TE_{9,4}$		420	21	5
140.2	$TE_{10,4}$	$TE_{10,4}$	99	690	28	5
147.4	$TE_{11,4}$	$TE_{11,4}$		350	19	5
140.1	$TE_{10,4}$	TEM_{00}	94.5	600	27	12
				540	42(CPD)	8
154.7	$TE_{12,4}$	TEM_{00}		350	18	10

CPD : Collector Potential Depression

2.2 1MW $TE_{22,6}$ gyrotron with radial output coupling and compact quasi-optical mode converter

In order to generate an output of 1 MW or even more at long pulses up to CW, modes of higher order than $TE_{10,4}$ have to be used. A 1 MW $TE_{22,6}$ gyrotron (pulse length 0.1 s) with radial output coupling and compact quasi-optical mode converter is currently under construction at KfK [7,8]. The diode-type magnetron injection gun for this tube was designed in collaboration with IAP Nizhny Novgorod and has been manufactured and successfully tested using the retarding field method with a scaling factor of k=10. The experimental results of relative transverse energy t_{tr} and velocity spread $\delta\beta_{tr}$ as functions of the scaled beam current are plotted in Fig.4 together with theoretical predictions. It should be noted that the experiments were performed in a superconducting magnet system for which the gun is not optimized.

$TE_{22,6}$ - gun (diode type): tests and calc. done at IAP

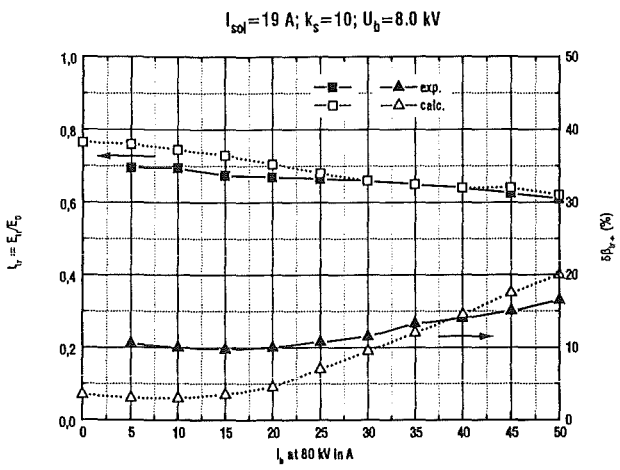

Fig. 4: Experimental values of relative transverse energy t_{tr} and velocity spread $\delta\beta_{tr}$ for the $TE_{22,6}$ gun (diode type) and comparison with theoretical predictions (for non-optimum magnetic field).

First experiments on rf generation with the electron beam of this MIG where also performed by KfK and IAP staff at IAP (Fig. 5). At a beam current of I_b=40 A more than 0.6 MW output power were generated in the $TE_{22,6}$ mode at 140.04 GHz and approximately 0.76 MW in $TE_{23,6}$ at 143.77 GHz. Modes of the type TEm,6 with m=20 to 26 were excited in the frequency range between 132 GHz and 151 GHz.

Some of the main design parameters for the $TE_{22,6}$ mode gyrotron are summarized in Table 3.

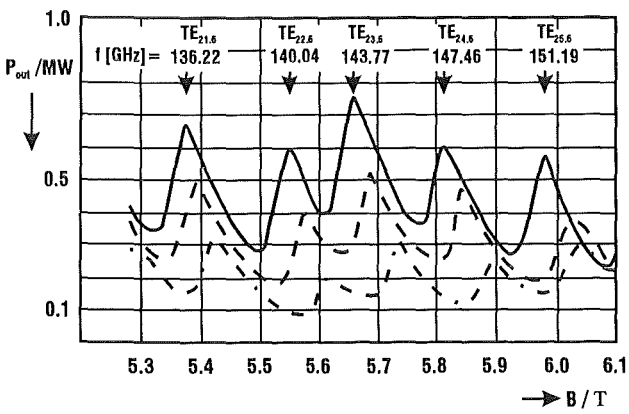

Fig. 5: Stepwise tuning of the $TE_{22,6}$ gyrotron by variation of the magnetic induction B. Output power versus B in different modes with same radial, but increasing azimuthal index for beam currents I_b = 17A (-.-.-), 25A (----) and 40A (—) at U_{cath}=80 kV.

A Denisov-type q.o. launcher for a high order mode like $TE_{22,6}$ utilizing a periodically perturbated, mode converting feed waveguide is either so long that it will be difficult to integrate it into the tube or it needs to be operated very close to cutoff where spurious rf oscillations may cause problems. For this reason here the type of feed waveguide deformations proposed in [9] will be used.

Table 3: Design parameters of the 1 MW, 140 GHz, $TE_{22,6}$ gyrotron with q.o. converter and depressed collector employing a diode-type gun with LaB_6 emitter.

U_{cath} = 80 kV	R_{cav} = 15.57 mm
I_{beam} = 40 A	L_{cav} = 15 mm
J_{cath} = 3.6 A/cm²	Q_{diff} = 1000
B_{cath} = 0.187 T	α = 1.4
R_{cath} = 45.2 mm	B_{cav} = 5.5 T
θ_{cath} = 21.5°	R_{beam} = 7.93 mm

2.3 1.5 MW coaxial cavity gyrotron

Microwave sources in the 2 MW-power region are needed for economically attractive ECRH on future next step fusion experiments like ITER and W7-X. A coaxial 1.5 MW gyrotron ($TE_{28,16}$; 140 GHz) with inverse magnetron injection gun is under development at KfK, in collaboration with the IAP, Nizhny Novgorod. The coaxial geometry allows measures to reduce mode competition in very big cavities ($D/\lambda \geq 25$) and also reduces the voltage depression of the electron beam dramatically (from 8 to 1 kV) which leads to higher efficiency. The design parameters of the inverse electron gun are given in Table 4. This construction allows fixing and cooling of the inner rod inside the resonator.

Table 4: Parameters of the inverse electron gun for a coaxial cavity gyrotron.

U_{cath} = 90 kV	$R_{cav} \approx$ 29.8 mm
$I_{beam} \leq$ 50 A	$R_{cav}/Ri \approx 4$
$\eta \geq$ 33 %	$R_{beam} \approx$ 10 mm
P ≈ 1.5 MW	$Q_{diff} \approx$ 2000
a ≈ 1.3	$Q_{ohm} \approx$ 75000
$\delta v\perp \leq$ 30 %	$p_{max} \leq$ 1.5kW/cm²

In a first step a short pulse gyrotron (300 µs) with an axial rf-output will be built.

A photograph of the inverse electron gun with LaB_6 emitter is given in Fig. 6. First experiments with that gun are being performed at Nizhny Novgorod.

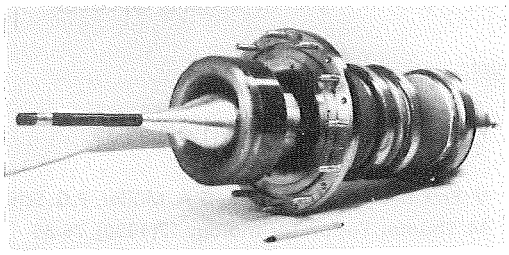

Fig. 6: Inverse electron gun.

The maximum pulse length is limited by the heat load capability of the collector, which is part of the output waveguide. The aim of this experiment is to study mode competition and cavity output purity. In a second step a radial Gaussian mode output using a dual-beam quasi-optical mode converter with two output windows will be installed, allowing a longer pulse length since a different collector will be used.

3. Collective Thomson Scattering Diagnostics with Gyrotrons

In 1993, first mm-wave scattering experiments from thermal, collective electron density fluctuations in the W7-AS plasma were performed at IPP Garching in a collaboration of IPP, IPF Stuttgart, IAP Nizhny Novgorod and KfK. The aim of these experiments is to measure the ion temperature or, more generally, the energy distribution of the different ion species in the plasma. This diagnostic could ultimately be used to get information on the energy spectrum of alpha particles generated in fusion reactions. For the measurements two installations orginally envisaged for ECRH at 70 GHz and 140 GHz were used. KfK provided the diagnostics equipment to measure the linewidth and the frequency drift during the gyrotron pulses. A notch filter with appropriatly 100 MHz bandwidth suppressed the stray radiation. First scattering spectra were measured which clearly showed that the thermal part of the density fluctuations could be detected with sufficient resolution. After these encouraging results both the 70 and 140 GHz scattering system are being modified for better spectral resolution.

4. Broadband Window

Frequency agile sources for future electron cyclotron wave systems demand for high-power millimeter wave windows with a broad transmission passband. The development of such windows has been continued at KfK [10,11,12,13] . Different techniques for anti-reflection treatment of window discs can be used to increase the bandwidth. Figure 7 shows the reflectivity as a function of frequency for an untreated window disk. This window has a relative bandwidth below 1 %. With dielectric antireflection layers on both sides the bandwidth of this disk could be increased to more than 12 % (Figure 8). Although the resulting three-layer window meets most of the bandwidth requirements it is not suitable for transmission of highly energetic mm-wave beams. Thus our present investigations concentrate on antireflection techniques which promise higher transmission capacities.

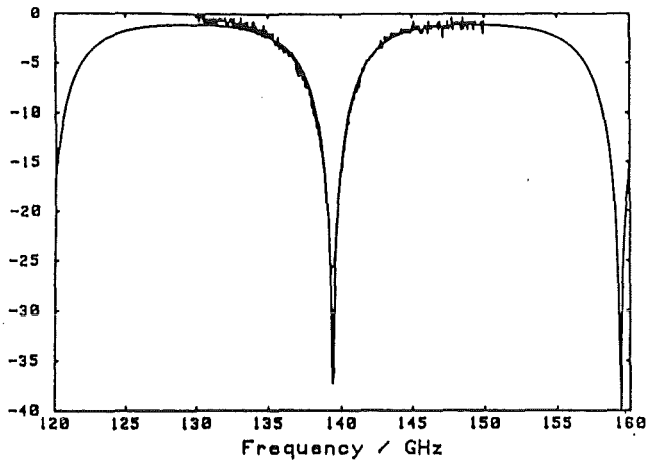

Fig. 7: Reflection spectrum in dB (measured and calculated) of a single disk window from magnesium titanate ceramics [11,13].

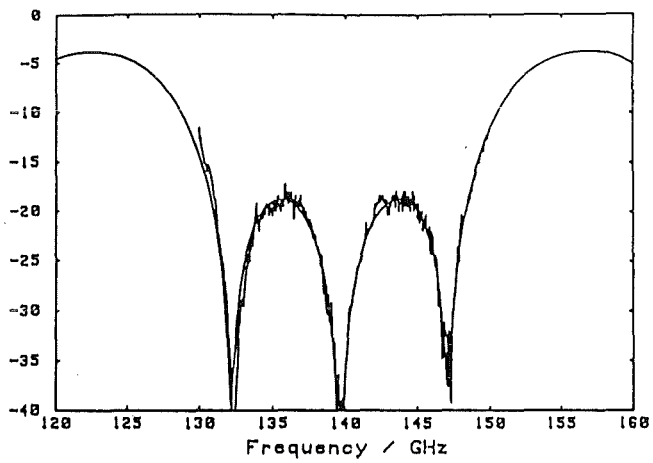

Fig. 8: Reflection spectrum in dB (measuered and calculated) of the disk of Fig. 1. This time both sides of the disk are antireflection coated [11,13].

Literature:

[1] R. Prater, J. Fusion Energy 9(1990), 19-30.

[2] V. Erckmann, W. Kasparek, G.A. Müller, P.G. Schüller, M. Thumm, Fusion Technology 17(1990), 76-85

[3] M. Thumm, Archiv Elektrotechn.77(1994)51-55

[4] M. Thumm et al., Proc. 2nd Int. Workshop on Strong Microwaves in Plasma, Moscow/Nizhny Novgorod/ Moscow, 1993, Vol. 2, Institute of Applied Physics, N. Novgorod, 1994, 670-689

[5] G.G. Denisov et al., Int. J. Electronics, 72 (1992), 1079-1091

[6] J. Pretterebner, A. Möbius, M.Thumm, Proc. 17th Int. Conf. on Infrared and Millimeter Waves, 1992, Pasadena, SPIE 1929, 40-41

[7] G. Gantenbein, Dr.-Ing. Thesis, University of Karlsruhe, 1993, KfK Report 5229, Sept. 1993

[8] G. Gantenbein et al., Proc. 16th Int. Conf. on Infrared and Millimeter Waves, 1991, Lausanne, Switzerland, SPIE 1576, 264-265

[9] J. Pretterebner, A. Möbius, Proc. 16th Int. Conf. on Infrared and Millimeter Waves, 1991, Lausanne, SPIE 1576, 531-532.

[10] H.-U. Nickel, U. Ambrosy, M. Thumm, 1992, Vacuum windows for frequency tunable high-power millimeter wave systems, 17th Conf. on Infrared and Millimeter Waves, Pasadena, California, USA, Conference Digest, SPIE Vol. 1929, 462-463.

[11] H.-U. Nickel, H. Massler and M. Thumm, 1993, Development of broadband vacuum windows for high-power millimeter wave systems, 18th Int. Conf. on Infrared and Millimeter Waves, Colchester, United Kingdom, Conference Digest, SPIE Vol. 21-04, 172-173.

[12] C.C. Shang, M. Caplan, H.-U. Nickel and M. Thumm, 1993, Electrical analysis of wideband and distributed windows using time-dependent field codes, 18th Int. Conf. on Infrared and Millimeter waves, Colchester, United Kingdom, Conference Digest, SPIE Vol. 2104, 178-179.

[13] H. Maßler, 1993, Untersuchung von Oberflächenstrukturen zur Vergrößerung der Bandbreite von Hochleistungsfenstern für Millimeterwellen, KfK-Report 5249.

Staff:

W. Baumgärtner
E. Borie
H. Budig
G. Dammertz
P. Grundel
O. Höchtl (Uni Karlsruhe)
A. Hornung
C. Iatrou (EC-Fellowship)
S. Illy
S. Kern (Uni Karlsruhe)
M. Kuntze
A. Möbius
N. Münch
H.-U. Nickel (Uni Karlsruhe)
B. Piosczyk
M. Pereyaslavets (Minerva Fellowship)
G. Redemann
M. Thumm
R. Vincon
A. Wien (Uni Karlsruhe)

High Power Windows

In the ceramic window of a gyrotron for fusion power applications thermal stresses occur due to the dielectric losses. These stresses are responsible for failure and finite lifetime of the ceramic materials. The most important failure modes are for temperatures below the creep region: spontaneous failure, subcritical crack growth under static load, and cyclic fatigue. These values characterise the qualification of a candidate material from the mechanical point of view. Data for a number of fusion-relevant ceramics were investigated. The strength of a selection of first choice materials is represented in fig. 9. The superiority of sapphire is evident.

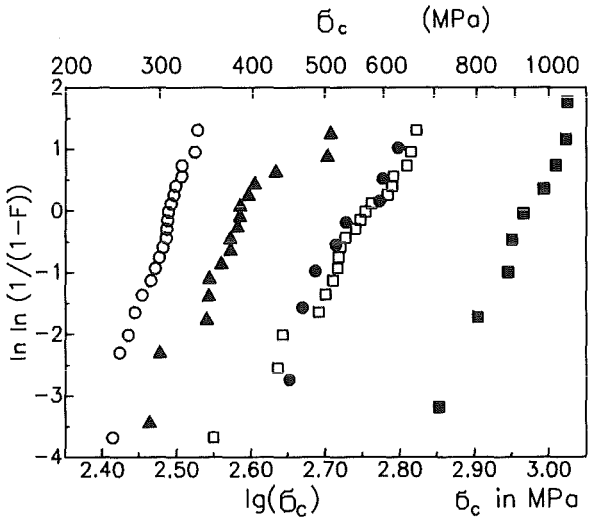

Fig. 9: Comparison of first choice materials for HF-windows. Weibull-representation of bending strengths: triangles: 99.99% Al_2O_3, solid circles: Al_2O_3+5%ZrO_2, open squares: Al_2O_3+10%ZrO_2, open circles: AlN, solid squares: saphhire.

Staff:

T. Fett

The concept of a single disk sapphire window cooled with boiling liquid nitrogen is being pursued at KfK [1]. The disk of 140 mm diameter and about 2 mm thickness is embedded in a 90 mm diameter waveguide and cooled at atmospheric pressure (77 K) in an annular space around the edge. The material used for the window is monocrystalline Al_2O_3 (sapphire).

The main topics for investigations are:

- Design calculations,
- Heat transfer experiments for verification of the calculations, and
- Calorimeter experiments for loss factor evaluation and for the study of technical problems such as fog formation and freezing in an open system.

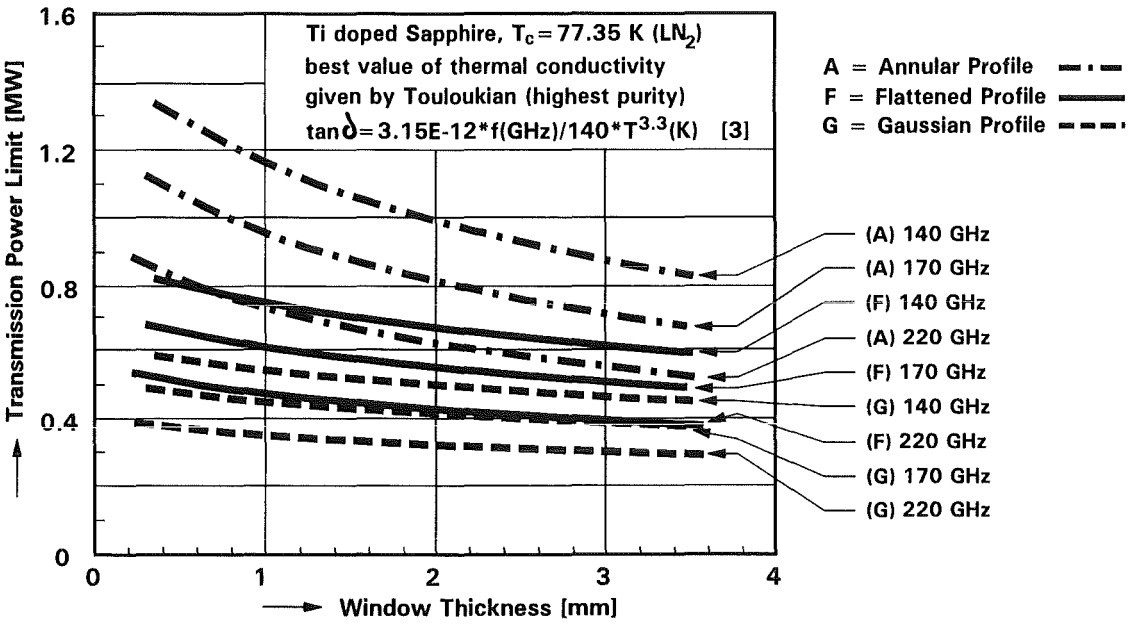

Fig. 10: Transmitted power as a function of disk thickness for different frequencies.

Earlier design calculations done with the loss factor $\tan\delta = 3.15 \times 10^{-12} \times T^{3.3}$ (at 140 GHZ) as determined for laser grade (Ti-doped) material, yield continous wave transmission capabilities of 500 kW for a Gaussian mode beam, 700 kW for a flattened profile, and 1 MW for an annular power distribution [2,3]. In the meantime further parameter studies have been performed for higher frequencies and for lower temperatures [4]. The dependence of the transmission power on frequency is shown in Figure 10. An increase in frequency from 140 GHz to e.g. 170 GHz (ITER performance) causes a loss in transmission power of about 16%; at 220 GHz the loss would amount to 37%.

Transmission of 1 MW, cw millimeter waves through a circular, single disk sapphire window with Gaussian field distribution at 140 GHz and at higher frequencies with even more sophisticated field distributions require cooling temperatures below 77 K (LN2). Lowering the operational temperature to about 30 K (the boiling temperature of Neon) is expected to increase the capability of such windows by a factor of about 5. Respective calculations as shown in Figure 11 have been done for relatively low grade material (Hemex grade sapphire). Further improvement is expected for laser grade sapphire.

In order to extend our future investigation in this temperature range, we have made available a cryorefrigerator with about 150 W of cooling power at 30 K.

In any case, operational temperatures below 77 K will have the very stringent implementation that such window will have to be operated in an evacuated wave guide. In order to avoid such complications for near future experiments, efforts are made for designing LN_2 cooled high power windows to be used in open wave guides.

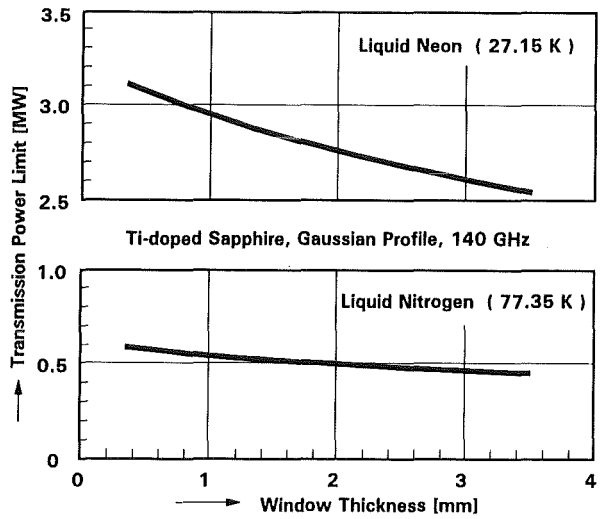

Fig. 11: Transmitted power as a function of disk thickness for LN_2 and LNe cooling

For verification of the design calculations various heat transfer experiments were carried out with an electrically heated copper simulator and an original sapphire window. The main results of these experiments are:

- The chosen experimental device has proved excellent and the concept of the edge-cooled single-disk window in liquid nitrogen at atmospheric pressure is feasible.

- The computer code used has proved reliable in calculation the temperature distribution in the window. The experiments with an electrically heated copper disk

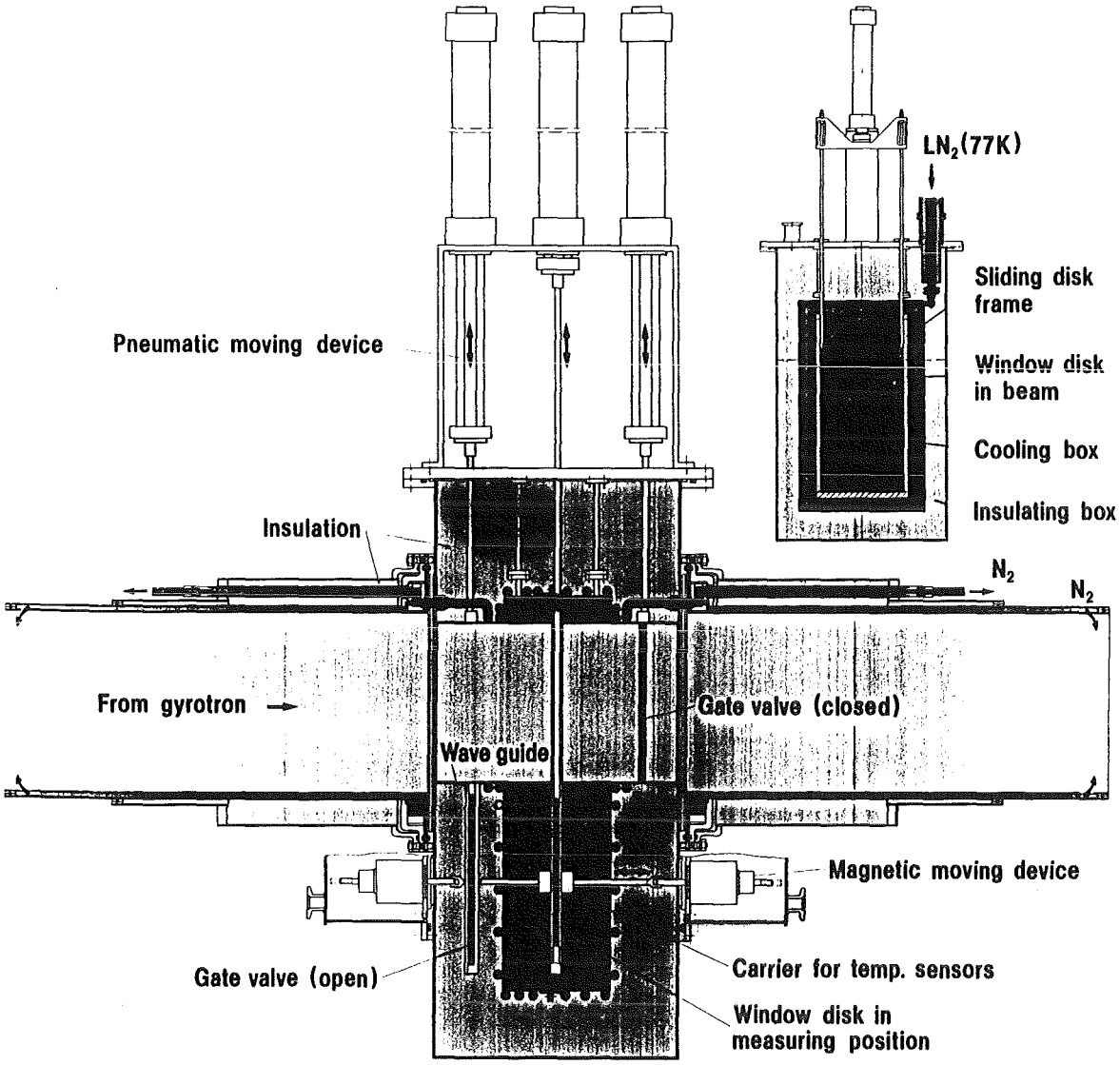

Fig. 12: Test equipment for high power transmission (140 GHz) through a LN_2 cooled sapphire window at open atmosphere

showed a very good agreement of the measured with the calculated temperature distribution.

- The discrepancies in the tests with the sapphire disk have the reason that the thermal conductivity of the material used is not of best quality as assumed.

- By atmospheric evaporative cooling 1300 W can be removed from the edge of the window. Thus, it is not the heat removal at the edge which limits the transmittance power of the window, but the radial conduction of heat in the disk which already at 150 to 300 W leads to thermal runaway.

Another series of experiments were performed with a liquid nitrogen cooled sapphire disk operated in the pulsed beam of a Russian high-power gyrotron at Garching. The test facility acts as a calorimeter such that the energy absorbed during a shot is obtained from measurements of the temperature increase after the shot. Such experiments also allow to study the problems (e.g. mist in the wave guide and frost at the window) of high power transmission through normal atmosphere at temperatures between 80 K and 300 K.

The experimental set-up is shown in Fig. 12. The window is embedded in an insulated Cu box cooled by LN_2 flow. Mounted on a pneumatically actuated slide, the window is moved to in-beam position during the pulsed gyrotron operation. After the shot, it is moved into the "calorimeter position" where the increase of temperature is detected by six thin film sensors pressed with magnetic actuators to different positions of the window. The absorbed energy is mainly derived from the steady state temperature stabilizing within about two seconds. Two gate valves closing the beam channel when the window is in the calorimeter position serve to prevent excessive convection of cold gas. The sequence of all actuators is

controlled electronically and it can be triggered by the gyrotron.

During the first experiment series in December 1993 140 GHz gyrotrons pulses with power ranging up to 500 kW and 500 ms pulse length could be transmitted. Longer pulses caused electric arcing or breakdown. There are some indications that this might be caused by fog formation and icing within the waveguides, which starts during extended operation at 80 K. The temperature increase of the window was in the range of 3 K. This is less than expected. Experiments with improved gas flow to get less condensation of moisture are going on.

Literature:

[1] H.E. Häfner, E. Bojarsky, P. Norajitra, H. Reiser, Cryocooled Windows for High Frequency Plasma Heating.17th Symposium on Fusion Technology, Roma/Italy, September 1992.

[2] G.G. Denisow, A.Sh. Fix, P. Sushilin, *Russian Proposals for Power Distributions in Windows,"* Institute for Applied Physics, Niszhny Novgorod, 1992.

[3] R. Heidinger, *Dielectric Measurements on Sapphire for Electron Cyclotron Wave Systems,* 6th Int. Conf. on Fusion Reactor Materials, Stresa/Italy, 1993.

[3] H.E. Häfner, P. Norajitra, K. Müller, M. Thumm, *Conceptual Design and Thermodynamics of Cryogenically Cooled Windows for ECR Plasma Heating,* 18th Symposium on Fusion Technology, Karlsruhe, August 1994.

Staff:

H.E. Häfner
K. Heckert
A. Hofmann
K. Müller
N. Münch
H.-U. Nickel, Univ. Karlsruhe
P. Norajitra
R. Vouriot

The new installation of the low temperature laserflash equipment, which has been developed as a prototype during a thesis will be finished in the next weeks.

Staff:

G. Haase
B. Schulz

Appendix I: Allocation of Tasks

Task No.	Title	FZK Departments
Plasma Facing Components and Plasma Engineering		
PPM 1	Characterization of Graphites and CFCs	IMF I, HVT/HZ
PPM 3	Numerical simulation of Off-normal Plasma Material Interaction	INR
PPM 4	Ceramics for Heating and Current Drive Systems	IMF I
PPM 6	Erosion, H-Retention, Gas Interaction	INR, IRCH
PDT 1	First Wall Mock-ups and Tests	IATF, IMF II
Superconducting Magnets		
MCOI	Model Coil	ITP
MCON	Full-Size 40 kA Conductor	ITP
MTOS	TOSKA Upgrade for Model Coil Testing	ITP, HIT, HVT-EA, HPE
MBAC	High Field Operation of NbTi at 1.8 K	ITP, HIT, HPE
Vacuum and Fuel Cycle		
TPV 2	Optimization of Cryogenic Vacuum Pumping of Plasma Exhaust	HIT, ITP
TEP 2	Permeation und Catalytic Cracking	IRCH
TEP 3	Tritium Storage and Transportation	IRCH
TRIT-1	**Tritium Supply and Management: Calorimetric Measurements**	HIT, HVT, IRCH
Nuclear Engineering / Basic Blanket		
NDB 1	Neutronics Data Base	INR, TU Dresden
T 16	Preparation of Neutronics Experiments and Measuring Technologies	INR
Remote Handling / Maintenance		
RHB 1	RH Common Subsystems	IAI
RHT 1	Articulated Boom Transporter	HIT, HVT, IAI, IRS
T 43	Remote Pipe Welding and Cutting (former task RST 2)	HIT

Safety and Environment

SEA 3	Analysis of Reference Accident Sequences	IRS
SEP 2	Environmental Impact of Tritium and Activation Products	INR

Long Term Program for Materials Development

LAM 2	Nuclear Data Base for Low Activation Materials Development	IMF I
LAM 3	Development of Low Activation Martensitic Steel	IMF I, IMF II
MANET 1.1	Characterization and Optimization of MANET-II-Steel	IMF I, IMF II
MANET 2.3	Diffusion Welding	IMF III
MANET 3.2	Pre- and Post-Irradiation Fatigue Properties of MANET Steel	IMF II
MANET 3.4	Pre- and Post-Irradiation Fracture Toughness	IMF II, HVT/HZ
MAT 5	Ion-Beam Irradiation Fatigue and Creep Fatigue Tests	IMF I

Test Blanket Development

BS - Solid Breeder Test Blankets

BS DE-D 1	Solid Breeder Test Blanket Design	IMF III, INR
BS BE-D 1	Beryllium	INR
BS BR-D 1/D 2	Preparation and Characterization of Ceramic Breeder Materials	IMF I
BS BR-D 3	Irradiation Testing and Post Irradiation Examination	IMF I, IMF III, HVT/HZ
BS BR-D 4	Tritium Release	INR, HVT/HZ
BS BR-D 8	Characterization of Lithium Orthosilicate: Adsorption of water	IRCH
BS NN-D 1	Helium Blanket Test Loop	IMF III, INR
BS NN-D 2	Non Nuclear Tests	IMF III, INR
BS NN-D 3	Tritium Extraction from a Solid Breeder DEMO Blanket	HIT, IRCH

BL - Liquid Metal Test Blankets

BL DE-D 1	Liquid Metal Test Blanket Design	IMF II, IMFIII, INR, IATF, IRS
BL PC-D 2	Active and Inactive Impurities and Clean-up of Molten Pb-17Li	HIT
BL EI-D 1	Electrical Insulation and Coatings	IMF I, IMF III, IRS
BL MH-D 1	Liquid Metal MHD	IATF
BL SA-D 1	Reliability Assessment	IRS
BL SA-D 2	Safety Analysis of Self-cooled LM Breeder Blankets	IRS

Development of ECRH Power Sources

ITP, IMF II, IMF III

Appendix II: Table of ITER / NET Contracts

Theme	Contract No.	Working Period
I_C vs. Strain Test on Nb_3Sn Strands	ERB 5000 CT 930036 NET	10/93 – 9/94
Investigation of Cryo-Cascade-Concept for ITER and Definition of Test Requirements	ERB 5000 CT 930041 NET	11/93 – 6/94
ITER Coil and Model Coil Design and Analysis	ERB 5000 CT 930046 NET	11/93 – 6/94
Quench Analysis for Magnet Safety Assessment	ERB 5000 CT 940027 NET	9/94 – 5/95
ITER Shielding Analysis	ERB 5000 CT 940039 NET	9/94 – 8/95

Appendix III: FZK Departments Contributing to the Fusion Project

FZK Department	FZK Institut/Abteilung	Director	Ext.
Institute for Materials Research	Institut für Material- und Festkörperforschung (IMF)	I. Prof. Dr.K.-H. Zum Gahr II. Prof. Dr. D. Munz III. Dr. J. Haußelt	3897 4815 2518
Institute for Neutron Physics and Reactor Engineering	Institut für Neutronenphysik und Reaktortechnik (INR)	Prof. Dr. G. Keßler	2440
Institute for Applied Thermo- and Fluiddynamic	Institut für Angewandte Thermo- und Fluiddynamik (IATF)	Prof. Dr. U. Müller	3450
Institute for Radiochemistry	Institut für Radiochemie (IRCH)	Prof. Dr. H.J. Ache	3200
Institute for Reactor Safety	Institut für Reaktor-sicherheit (IRS)	Prof. Dr. D. Cacuci	2550
Central Engineering Department	Hauptabteilung Ingenieur-technik (HIT)	Dr. H. Rininsland	3000
Institute for Technical Physics	Institut für Technische Physik (ITP)	Prof. Dr. P. Komarek	3500
Central Experimental Engineering Department	Hauptabteilung Versuchstechnik (HVT)	Dr. Schubert	3114
- Hot Cells	- Heiße Zellen (HVT-HZ)	DI. Enderlein	3650
- Tritium Laboratory Karlsruhe	- Tritiumlabor Karlsruhe (TLK)	Dr. R.D. Penzhorn	3239
Remote Handling Laboratory	Handhabungstechnik-Labor (HT)	Dr. Scholl	2942
Central Safety Department	Hauptabteilung Sicherheit (HS)	DP. W. Koelzer	2660
Institute for Applied Informatics	Institut für Angewandte Informatik (IAI)	Prof. Dr. H. Trauboth	5700
Institute for Nuclear and Atomic Physics of the Technical University Dresden		Prof. Dr. K. Seidel	035101/8982

Appendix IV: Fusion Project Management Staff

Head of the Research Unit	Dr. J. E. Vetter	ext. 5460
Secretariate:	Fr. I. Sickinger	ext. 5461
	Fr. I. Pleli	ext. 5466
	Fr. V. Lallemand	ext. 5466
Project Budgets, Administration, Documentation	BW G. Kast	ext. 5462
Studies, ITER / NET Contacts	Dr. J.E. Vetter	ext. 5460
Superconducting Magnets, Gyrotron Development	DI H. Knuth	ext. 5468
Tritium Technology Structural Materials	Dr. H.D. Röhrig	ext. 5463
Blanket Technology, Remote Handling	DI A. Fiege	ext. 5465

Address: Forschungszentrum Karlsruhe GmbH
Nuclear Fusion Project Management

Post Office Box 3640, D-76021 Karlsruhe / Germany

Telephone No: 07247-82- Extensions ....

Telefax No: 07247 - 82 - 5467

Telex No: 17 724 716